

CURVED AERODYNAMIC SHOCK WAVES

SANNU MOLDER

**DEPARTMENT OF MECHANICAL ENGINEERING
MCGILL UNIVERSITY
MONTREAL**

**A THESIS SUBMITTED TO MCGILL UNIVERSITY IN
PARTIAL FULFILLMENT OF THE REQUIREMENTS OF THE
DEGREE OF DOCTOR OF PHILOSOPHY**

©S.MOLDER, 2012

JANUARY 2012

TABLE OF CONTENTS

ABSTRACTS.....	VII, IX
ACKNOWLEDGEMENTS	XI
CHAPTER 1 INTRODUCTION.....	1
CHAPTER 2 CURVED SHOCK THEORY (CST).....	5
2.0 Introduction	5
2.1 Morphology of axisymmetric shock shapes.....	7
2.2 Rankine-Hugoniot and Euler Equations	11
2.3 Constant property lines	14
2.4 The <i>curved shock equations</i>	15
2.4.1 Vorticity jump at the shock	23
2.5 Concluding comments.....	30
CHAPTER 3 APPLICATIONS OF CURVED SHOCK WAVE THEORY.....	31
3.0 Introduction.....	32
3.1 Shocks with planar symmetry, $S_b = 0$	32
3.1.1 Plane shock in uniform upstream – a limiting case.....	33
3.1.2 Shock with single curvature S_a in the flow plane, in a uniform upstream flow – planar flow ($S_b = 0$).....	33
3.1.3 The Thomas and Crocco points in planar flow.....	35
3.1.4 Polar streamline slope (l) in planar flow	38
3.2 Shocks with conical symmetry; $S_a = 0$	40
3.2.1 Acute conical shock in uniform flow; cone flow.....	41
3.2.2 Obtuse conical shock in uniform flow; M-flow	42
3.2.3 Polar streamline slope in conical flow.....	43
3.3 Shocks with compound (double) curvature; $S_a \neq 0$, $S_b \neq 0$	43
3.4 Vorticity.....	44
3.5 Normal shocks	45
3.5.1 Normal shocks in uniform flow.....	48
3.5.1.1 Blunt body with convex normal shock	48
3.5.1.2 Flow behind a normal shock at a concave Mach disk.....	50
3.5.1.3 Blunt leading edge with sweep.....	53
3.6 Shocks on a circular wedge-annulus (<i>unit ring-wedge</i>); $y=1$, $D_2 = 0$,	54
3.7 Shock surfaces with up- or downstream uniformity.....	56
3.7.1 Doubly curved Thomas and Crocco shocks.....	56
3.7.2 Polar streamline slope for flow behind a shock in uniform flow.....	60
3.7.3 Polar streamlines for uniform post-shock flow.....	60

3.7.4 Conditions behind a reflected shock	62
3.8 Curvature and strength of characteristics	62
3.8.1 Curvature of characteristics	62
3.8.2 Strength of characteristics	65
3.8.3 Reflection coefficient	66
3.9 Sonic line orientation	70
3.10 Concluding remarks	73

CHAPTER 4 CONICAL FLOW AND TAYLOR-MACCOLL

EQUATION(S).....	75
4.1 Introduction	76
4.2 The Taylor-Maccoll Equations	78
4.2.1 The first order equations	78
4.2.2 Mach number variables	79
4.3 Conical flows with uniform upstream and downstream flows	80
4.3.1 Cone flow and W-flow	81
4.3.2 Busemann flow, experiments and CFD results	82
4.3.2.1 Description of Busemann flow	83
4.3.2.2 Busemann flow theory and intake performance	84
4.3.2.3 Streamlines and radials in Busemann flow	87
4.3.2.4 Numerical analysis of Busemann flow	88
4.3.2.5 Characteristics and a centered axisymmetric compression fan	90
4.3.2.6 Inflection point on the Busemann streamline	93
4.3.2.7 Wind-tunnel tests on Busemann flow	96
4.3.2.8 Busemann tests in the gun-tunnel at Mach 8.33	96
4.3.2.9 Busemann tests in the wind-tunnel at Mach 3.00	98
4.3.3 M-flow experiments and CFD results	102
4.3.3.1 Characteristics on M-flow contour	105
4.3.3.2 M-flow experiments in the gun tunnel and CFD results	107
4.3.3.2(A) The 145 deg shock	109
4.3.3.2(B) The 153.7 deg shock	111
4.3.3.2(C) The 170.3 deg shock	113
4.4 Concluding remarks	116

CHAPTER 5 HYPERBOLIC SHOCK WAVE..... 119

5.1 Introduction	119
5.2 Geometry of the concave hyperbolic shock	120
5.3 Flow properties behind a curved shock	123
5.4 Streamlines behind hyperbolic shock	124
5.5 Orientation of sonic line behind the shock	125
5.6 CFD results	131
5.7 Conclusions	135
APPENDIX 5A	135

CHAPTER 6 SHOCK DETACHMENT.....	137
6.1 Introduction	137
6.2 Preliminaries	139
6.2.1 The Unit Ring Wedge (URW) and splitter tube	139
6.2.2 Curved Shock Theory (CST)	140
6.3 Shock detachment from a sharp leading edge	141
6.3.1 Detachment by excessive flow turning – δ_{max} criterion	142
6.3.2 Shock detachment by overpressure	143
6.3.2.1 Shock detachment by global choking	144
6.3.2.2 Shock detachment by local choking	145
6.4 Analysis of detachment by local choking	145
6.4.1 Pressure gradient at leading edge of curved surfaces	146
6.4.2 Mach number gradient and choking length L^*	150
6.4.3 Curved surface length required for choking, L^*	153
6.4.4 Local choking on a flat plate	154
6.4.5 Planar flow over a curved surface	155
6.4.6 Flow in a URW with a conical surface	157
6.4.7 Flow in a URW with curved surface	159
6.5 Computational examples	160
6.5.1 Grid-independence	160
6.5.2 Local and global choking	161
6.5.3 Attachment/detachment hysteresis by CFD	162
6.5.4 CFD vs. CST	163
6.5.5 Abruptness of detachment	165
6.6 Conclusions	166
 CHAPTER 7 CLAIMS, CONCLUSIONS, DISCUSSION AND RECOMMENDATIONS.....	 169
7.1 Claims.....	169
7.2 Conclusions	170
 REFERENCES.....	 175

ABSTRACT

Curved shock theory (CST) has been extended to apply to axisymmetric shocks in non-uniform flow. A general formula has been derived for the vorticity jump across a doubly curved shock in non-uniform flow. Influence coefficient forms of equations for the gradients and vorticity show the effect of changing pre-shock conditions. CST has been applied to a series of simple shock flows and to the orientation of the sonic surface at the rear face of a doubly curved shock. This orientation is significant in determining the occurrence of embedded shocks in the post-shock flow. Application of CST to curved, concave, normal shocks allowed the derivation of an explicit relationship between the shock's curvature and the length of down-shock subsonic flow. Investigations of conical flows by analysis, CFD and experiment all failed to demonstrate the existence of regular reflection of shocks at the centre line of axisymmetric flows. An analytically predicted conical shock, on the calculated streamline, does not extend all the way to the centre line but terminates in Mach reflection. It appears that the existence of an analytical Taylor-Mccoll (T-M) solution is not in itself a guarantee of the physical existence of a conical flow in all cases. The T-M equations predict the existence of an axisymmetric centered compression fan, analogous to the Prandtl-Meyer fan in planar flow. A free-standing conical shock is located downstream of the compression fan. Both features have been shown to exist by CFD as well as experiment. Busemann flow is the only flow where these wave structures can exist; it is possible to reflect an incident, centered compression as a conical shock. Discovery of an inflection point on the Busemann streamline has an important implication to spontaneous starting of Busemann intakes. Three types of flow can exist behind a doubly curved concave shock; characterized by the orientation of the sonic surface which, in turn, is determined by the pre-shock Mach number and the shock curvatures ratio. Shapes of special axial shock surfaces, with straight post shock streamlines (Crocco shocks), or vanishing streamwise pressure gradient (Thomas shocks) and shocks with specific sound reflectivity (zero, if desired), have been calculated and illustrated. Boundary layer generated noise abatement is a possibility. Local flow choking, near the leading edge, leads to shock detachment from a curved wedge with such detachment depending on freestream Mach number, the wedge

angle, the wedge curvature and the wedge length. These are new criteria for shock detachment with analogies extending to the transition from regular to Mach reflection of shock waves.

RÉSUMÉ

La théorie des ondes de chocs courbées (TOCC; Curved Shock Theory) a été généralisée aux chocs axisymétriques dans un écoulement non uniforme. Une formule générale a été dérivée pour les sauts de vorticit      travers un choc    double courbe dans un   coulement non uniforme. La forme coefficient d'influence des   quations des gradients et de la vorticit   d  montrent l'effet de la variation des conditions en amont. La TOCC a   t   appliqu  e    plusieurs   coulements simples avec chocs incluant l'orientation de la surface sonique    la face arri  re d'un choc    double courbe. Cette orientation est importante pour d  terminer l'existence d'ondes de choc int  gr  es    l'  coulement aval. L'application de la TOCC aux ondes de choc courb  es, concaves et normales permet de d  river une relation explicite entre la courbe du choc et la longueur de l'  coulement subsonique derri  re l'onde. L'  tude analytique, num  rique et exp  rimentale des   coulements coniques n'a pas permis de d  montrer l'existence de r  flexions r  guli  res des chocs    l'axe de sym  trie des   coulements. Un choc conique pr  dit analytiquement sur la ligne d'  coulement n'atteint pas l'axe central, mais se termine en r  flexion Mach. Il semble que l'existence d'une solution Taylor-McColl (T-M) ne garantit pas l'existence physique d'un   coulement conique. Les   quations T-M pr  disent l'existence d'un train d'ondes de compression axisym  trique, analogue au train d'ondes de Prandtl-Meyer dans un   coulement planaire. Un choc conique d  tach   est situ   en aval du train de compression. L'existence des deux caract  ristiques a   t   d  montr  e par CFD ainsi qu'exp  rimentalement. L'  coulement Busemann est le seul   coulement o   ces structures d'ondes peuvent exister : une compression centr  e peut   tre refl  t  e en onde de choc conique. La d  couverte d'un point d'inflexion dans la ligne d'  coulement de Busemann a une implication importante au d  marrage spontan   de diffuseurs Busemann. Trois types d'  coulements peuvent exister    l'arri  re d'un choc concave    double courbure : ils sont caract  ris  s par l'orientation de la surface sonique qui,    son tour, est d  termin  e par le nombre de Mach pr  -choc et le ratio de courbures du choc. Des formes de surfaces d'ondes de choc axiales particuli  res, avec   coulement droit en aval (chocs Crocco), ou avec un gradient de pression tendant vers z  ro dans l'axe d'  coulement (chocs Thomas) ainsi que des chocs avec une r  flectivit   acoustique sp  cifique (incluant nulle) ont   t   calcul  es et illustr  es. Une r  duction du bruit de couche limite est aussi possible.

X

L'étranglement local au bord d'attaque d'une pointe courbée mène au détachement de l'onde de choc, lequel dépend du nombre de Mach de l'écoulement libre, de l'angle, de la courbure et de la longueur de la pointe. Ce sont de nouveaux critères pour le détachement du choc avec des analogies pouvant s'étendre aux transitions des réflexions régulières aux réflexions Mach.

ACKNOWLEDGEMENTS

Although the Author initiated, monitored, analyzed and utilized the results; he did not participate in any of the experimentation. Gun-tunnel experiments on the full Busemann inlet and on M-flow were done by Julian Romeskie at the NRC under the supervision of Dr. Ray Mayer and William Rainbird. Experiments on the Busemann ring were done in the DRDC trisonic wind-tunnel under the direction of Dr. Francois Lesage.

The same is true of most of the CFD calculations. Dr. Rabi Bin-Tahir calculated Busemann flow details. Len Snow of the Applied Physics Laboratory of The Johns Hopkins University did the MOC calculations for M-flow and Dr. Evgeny Timofeev of McGill University made extensive calculations of M-flow and Busemann flow using Solver II. The experimenters and computational analysts tackled difficult and often frustrating flows with shocks and singularities – their contributions have added credibility to what would otherwise have been a purely theoretical effort.

The Author is greatly appreciative of Dr. George Emanuel of the University of Texas at Arlington for his diligence and persistence in steering and verifying the development of the Curved Shock Theory. We have exchanged over 500 e-mails in the last three years. Many errors were corrected, many mis-conceptions eliminated. His extensive knowledge of the subject and great perseverance eventually convinced the Author that some of his claims were over-enthusiastic.

Dr. Evgeny V. Timofeev not only directed the research but also made essential direct contributions. All the very careful Solver calculations of M-flow were done by Dr. Timofeev. His seminal expertise with Solver proved essential. His overall advice and encouragement are much appreciated.

Dr. V. Tanguay provided the French language version of the Abstract. Seyed Miri organized the multi-detailed structure of the manuscript. I did not have a good answer when, a few years ago, Dr. Susan Molder asked: “Why don’t you get a Ph.D. from McGill”? That’s when it started.

CHAPTER 1

INTRODUCTION

The first hypersonic X-51 scramjet powered long-duration flights.....that tie atmospheric and space propulsion will begin as early as May 25 at Edwards Air Force Base. According to the article (17 May 2011 issue of *Spaceflight Now*), scramjet propulsion is the future for spaceflight as even a partially successful test would hasten progress on spacecraft that could launch horizontally. Furthermore, this is "an example of the type of revolutionary propulsion thatwill be needed for future space operations." The article noted that "there is a bright future for a range of scramjet-powered vehicles" and "scramjet development will proceed no matter what happens in the near-term shift to commercial crew and cargo launch to the International Space Station."

A shortened version from *AIAA Daily Launch*, March 2011

Research and development of the scramjet type engine had its beginnings in the late 50's. A historical review of progress to 1990 is found in [Curran, 1997] and a more up-to-date international state-of-the-art summary is found in [Curran and Murthy (ed.), 2000]. The scramjet engine consists of three main components: the intake, the combustor and the exhaust nozzle. Each component has its very unique and challenging design problems. Scramjet intake design and development has been reviewed by Van Wie [2000]. A high performance intake is critical to obtaining even minimal scramjet engine performance. For the aerodynamicist, intake design challenges arise from shock losses, boundary layer losses and their interactions, from trade-offs between adequate compression and intake starting, from attainment of sufficient performance at off-design operation and from obtaining stable and predictable as well as tailored flows at on- and off-design conditions.

The contents of this thesis is applicable to the design of supersonic and hypersonic air intakes. Three aerodynamic features that occur in such intakes are treated in detail: Taylor-Maccoll flow of the Busemann type, doubly curved, concave shocks in internal flow and detachment of shocks from doubly curved leading edges. Wherever possible, the various flow features of interest are examined by analysis, computational fluid dynamics and experiment. Novel developments of curved shock theory are used extensively for the last two topics.

Simple flows behind flat shocks, behind conical shocks and in Prandtl-Meyer fans have been used as starting points to construct many operational intake flows, e.g. the Concorde SST and early MiG series of fighters. The resulting, essentially **external**, flows do not lead into the axial flow and **enclosed** flow paths most readily welcomed by a tubular combustor. Two flows which do not suffer from this ‘flatness’ but which are equally simple, **internal** flows, with enclosed circular exit flowpaths, are presented in Ch.4.

Even simple shocks take on compound curvature in intakes at off-design conditions. Such curved shocks are shown to produce post-shock streamline curvatures and pressure gradients that may not be compatible with adjacent surfaces. An extensive treatment of curved shock theory and vorticity development is presented in Ch. 2. Simple applications of the theory are in Ch. 3 and a concave, hyperbolic shock is examined with curved shock theory in Ch. 5, such a concave shock being representative of curved shocks in internal flow. Verification of analytical flows is provided by comparing the flows and surface contours generated by solutions of the Taylor-Maccoll equations against flows in the same contours as predicted by finite difference calculations and results of experiments in Ch.4. There is good reason to be suspicious of the influence of lateral surface curvature on shock detachment because it is a well-known fact that a shock on a cone detaches at a higher cone surface angle than the same strength shock on a wedge. The difference in surface deflection required for shock detachment is made up of the curving Taylor-Maccoll flow that exists between the conical shock and the cone. The intermediate case of lateral surface curvature on a ring-wedge should have an intermediate effect on shock detachment – by analytic continuity. Curving flow, although not of the Taylor-Maccoll type, also exists between a ring-wedge surface and its shock. In Ch. 6 it is demonstrated that local flow choking at the leading edges of curved ducts can cause premature shock detachment. This effect, when applied to shock reflection, would cause similar premature cessation of regular reflection on a curved wall.

All theoretical work is based on a thermally and calorically perfect compressible gas. Although all formulas contain the specific heat ratio as a variable, the numerical results are for $\gamma = 1.4$ throughout. All experiments have been conducted in steady flow of

air. Boundary layer corrections have been applied to the wind tunnel models, otherwise the flows are taken as inviscid.

CHAPTER 2

CURVED SHOCK THEORY (CST)

Contents

- 2.0 Introduction
- 2.1 Morphology of axisymmetric shock shapes
- 2.2 Rankine-Hugoniot and Euler Equations
- 2.3 Constant property lines
- 2.4 The *curved shock equations*
 - 2.4.1 Vorticity jump at the shock
- 2.5 Concluding comments

2.0 Introduction

A student of descriptive geometry, trying to visualize the shape of a function, can evaluate the function at several values of the independent variable. A slightly more sophisticated student gains a better picture of the function's shape by evaluating its derivative and slope. An even brighter student will take the second derivative to discover curvature and inflection points. So it is in the aerodynamics of shock waves where a basic level of understanding is obtained by examining the ratios of dynamic and thermodynamic variables across an oblique shock wave and a deeper grasp of the subject comes from an examination of variable gradients when the shock is curved.

Research focusing on shock curvature and the resulting flow property gradients has a long history and has been largely analytical. Crocco [1937] showed that, on a curved, planarly symmetric (planar) shock wave, there is a shock angle where the streamline behind the shock is straight, irrespective of shock curvature. This shock location is called the Crocco point. Thomas [1947] derived the curved shock equations for steady flow of an ideal gas with planar shocks in uniform flow. He found an expression for the curvature of the streamlines and the streamwise pressure gradient behind a curved shock. The shock angle where the pressure gradient along the streamline behind the shock is zero we call the Thomas point. Any influence of upstream vorticity was not considered. Lin and Rubinoff [1948] re-derived the equations of Crocco and Thomas to show that a normal shock can sit on a continuously curving surface only if the Mach number exceeds a certain supersonic value. Lin and Rubinoff stopped short of

considering axisymmetric flows. Thomas [1949a] extended the study of shock curvature to higher derivatives of shock and streamline shape, giving extensive graphs of the first-derivative relations. Algebraic complexities prevented Thomas from examining higher derivatives in detail. Today's computerized algebra manipulators such as Matlab and Maple could be used to advance Thomas' early efforts. Thomas [1949b, 1950] also considered the motion of a shock attached to the leading edge of a planar, curved surface and developed total differential equations for the first, second and third approximations for the surface pressure. These methods, although algebraically cumbersome, are more versatile than the Method of Characteristics because they can be used in flow regions where the flow is locally subsonic; however, they are approximations and not as straightforward in application as modern CFD methods. Truesdell [1952] derived the formula for the vorticity jump across a curved shock wave, but erroneously concluded that "when a uniform flow of any fluid breaks across a shock the pressure gradient cannot vanish on the rear side of the shock at any point where the shock is curved and oblique". A simple physical argument shows otherwise; so does the correct theory. Application of CST to the propagation and decay of spherical blast waves is found in Thomas [1957b]. Clutterham and Taub [1953] considered curvature of planar pseudo-stationary shocks in Mach reflection. Bianco, Cabannes and Kuntzmann [1960] used CST for axial flow to find pressure gradients at the nose of an axially symmetric body in supersonic flow. Gerber and Bartos [1960] presented coefficients for the curved shock equations for determining the orientation of constant property lines behind planar and axial shocks in steady, irrotational, uniform flow of an ideal gas. Truly unsteady (i.e. non-pseudo-steady) flow and shock motion was allowed by Pant [1969] in deriving gradient expressions for flow behind a moving shock. Molder [1970, 1971] presented numerical results for curved shocks in regular reflection (RR) and Mach reflection (MR) at a plane wall and [in 1972] some results for polar streamline directions behind the triple point of Mach reflection. Pant [1972] presented similar results for planar flow. Darden [1984] derived the spatial derivatives of flow properties behind curved weak shocks with applications to sonic boom problems. All of the above papers have assumed that the gas is both thermally and calorically perfect. Sedney [1961] accounted for vibrational relaxation on flow over a wedge. Hsu [1961] accounted for the effects of non-

equilibrium dissociation on gradient functions for flow behind a shock. Hornung [1976, 1998] described many interesting features of real gas effects on curved shocks and inferred real gas properties from measurements of shock curvature on plane wedges.

A series of papers by Truesdell [1952], Hayes [1957], Kanwal [1958, 1960] and Emanuel [1994] have treated the production of vorticity by a curved shock. Most of these make use of the equation of state and Crocco's thermodynamic relation when deriving the vorticity equation. Kanwal [1958] and others have shown that the jump in vorticity is independent of the energy equation and the form of the equation of state and can be derived from strictly kinematic basis.

The Curved Shock Theory (CST) is derived and embodied in the *curved shock equations*, which relate shock curvature directly to the gradients of flow properties near the shock. The equations are derived by applying the Rankine-Hugoniot and Euler equations of conservation to a perfect gas, in steady flow, across a doubly curved shock wave. Curved shock theory is introduced and further extended in this chapter to be applied in later chapters to investigate flow about doubly curved shock surfaces.

2.1 Morphology of axisymmetric shock shapes

Most of the curved shock equation applications referred to above are for simple shock curvature and a uniform upstream flow and so do not contain terms reflecting upstream vorticity, upstream flow non-uniformity and compound shock curvature. In applying to shock reflections, terms must be included which account for complex shock curvature since the reflected shock, advancing into non-uniform and rotational flow, becomes doubly curved; also one must account for

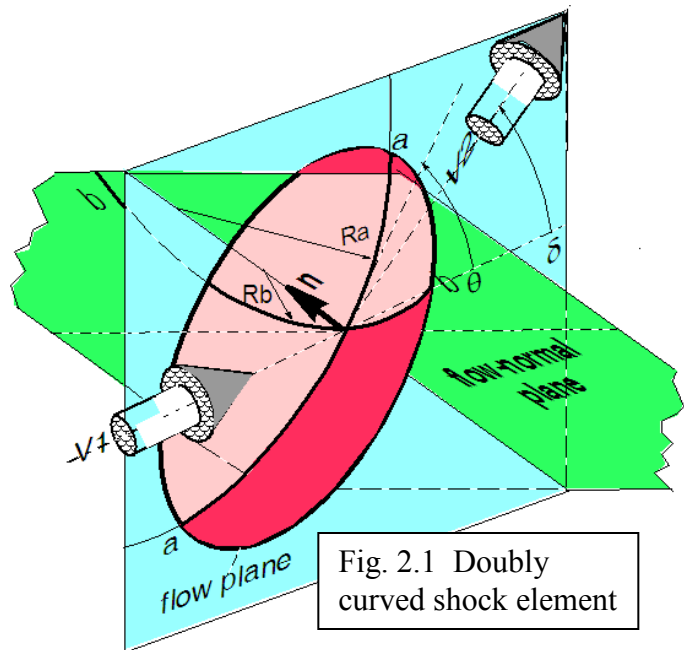


Fig. 2.1 Doubly curved shock element

the upstream flow being both rotational and possibly convergent. We present equations for pressure gradient, flow curvature and vorticity for flow behind a doubly curved shock in steady non-uniform flow where the upstream flow can have a pressure gradient, a streamline curvature, vorticity and be inclined to the axis. The equations are valid for shocks that possess planar and axial symmetry and, with some restrictions, also to shock surfaces in three-dimensional space.

Figure 2.1 shows an oblique, doubly curved shock element in supersonic flow separating the pre-shock state (1) from the post-shock state (2). The gas enters the shock with a velocity vector V_1 and leaves with a velocity vector V_2 . A vector \mathbf{n} is normal to the shock and points towards the upstream flow. The plane containing both \mathbf{n} and V_1 is useful in deriving the curved shock equations. Since the shock is normal to \mathbf{n} , the vector V_2 also lies in this plane. Kaneshige and Hornung, [1999] call it the **flow plane**. The coordinate plane (x,y) , lies in the flow plane and the x -axis is aligned with the freestream direction. In axial flow the x -axis is collinear with the axis of symmetry which may not be the freestream direction. The velocity vectors are inclined at δ_1 and δ_2 to the x -axis so that the net flow deflection through the shock is $\delta = \delta_2 - \delta_1$. The shock has a trace a-a in the flow plane that is inclined at an angle θ (the shock angle) to the incoming flow vector.

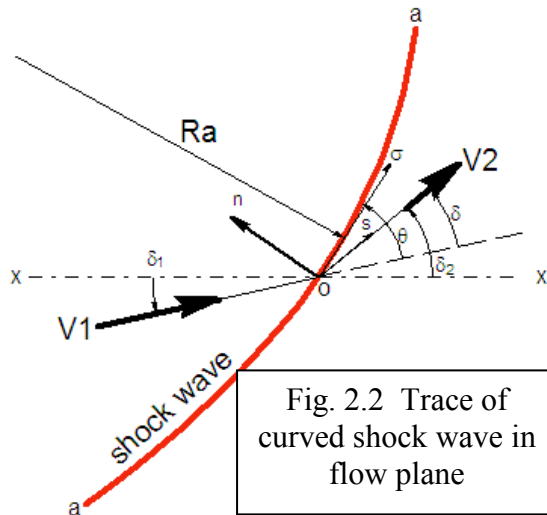


Fig. 2.2 Trace of curved shock wave in flow plane

The shock has a trace a-a in the flow plane that is inclined at an angle θ (the shock angle) to the incoming flow vector. Distance measured along the shock trace is σ and distances measured along and normal to the streamline are S and n . The shock trace has a **curvature** $S_a \equiv d\theta_2 / d\sigma$ and a **radius of curvature** $R_a \equiv -1 / S_a$ in the flow plane. The **flow-normal plane** is normal to both the flow plane and the shock surface. The shock has a trace b-b in the flow-normal plane. The b-b trace has a curvature S_b and a radius of curvature $R_b = -1 / S_b$. Shock curvature is positive when, moving along the shock trace so that the upstream is on the left, the shock angle increases. A positively

curved shock is always concave towards the upstream flow¹. In axisymmetric flow there is a third plane, the **transverse plane**. It is normal to the axis of symmetry and it contains the y -coordinate of the (x,y) coordinate system and specifically, the distance, y , from the shock to the axis of symmetry. In axial flow y is the radius of the circular trace of the shock in the transverse plane. In axial flow, the radius of curvature of the shock in the flow-normal plane is $y/\cos\theta$. We will have occasion to refer to the ratio of shock curvatures, $\mathcal{R} = S_a / S_b$.

A shock wave element in three-dimensional space is defined completely by its inclination to the pre-shock flow vector, θ , and the two shock curvatures S_a and S_b . The angle θ is measured counter-clock-wise from the pre-shock flow direction to the shock surface, in the flow plane. S_a and S_b are the curvatures of the shock traces in two mutually perpendicular planes – the flow plane and the flow-normal plane. Both sign and magnitude of S_a are defined by $d\theta/d\sigma$ where σ is distance measured along the shock trace while keeping the pre-shock flow on the left. In axial flow, S_b reduces to $-\cos\theta/y$ where y

is the perpendicular distance from the symmetry axis. The descriptive terms concave/convex are used exclusively with S_a to denote positive/negative S_a and the terms acute/obtuse are used to describe the location of the shock by its angle θ_s . For an axial shock, all four S_a/S_b combinations $+/+$ $-/+$ $-/-$ and $+/-$ are possible. For a hyperbolic shock (discussed in Ch. 5) lying on the x -axis, only two combinations are possible, $-/-$ for the right lobe and $+/+$ for the left lobe i.e. convex/acute and

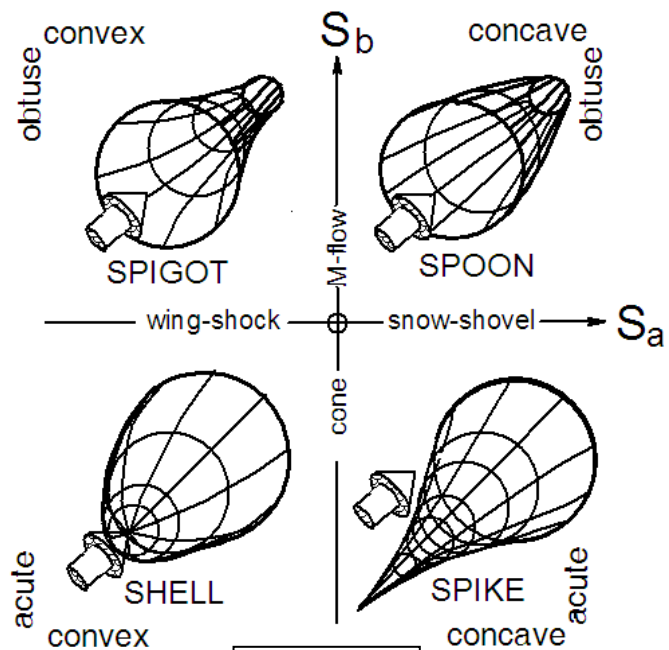


Fig. 2.3

Four types of curved shock surfaces and their limiting shapes

¹ This definition is unambiguous and does not depend on the chosen coordinate system.

concave/obtuse. The signs and values of S_a and S_b and $\mathcal{R} = S_a / S_b$ are important. *Concave, convex, acute, obtuse* are convenient descriptors. Because of axial symmetry we need to consider only ($0 < \text{acute} < \pi/2$) and ($\pi/2 < \text{obtuse} < \pi$) shock angles.

The four generic shock shapes are shown in the (S_a, S_b) -diagram in Fig.2.2. In the first quadrant, where S_a and S_b are both positive, the shock surface is concave and obtuse, resembling the inside surface of a spoon. In the second quadrant S_a is negative and S_b is positive (convex/obtuse); the shock surface resembles a spigot. In the third quadrant S_a and S_b are both negative convex/acute producing a water-melon-like shock surface as often seen on a blunt body. In the fourth quadrant S_a is positive and S_b is negative, (concave/acute) producing a spike or saddle-shaped shock surface. On the two axes of this figure the shock surfaces are of single curvature so that, on the positive S_a - axis the shock shape resembles a snow-shovel. On the positive S_b -axis the shock shape is conical, with the cone vertex pointing downstream. This conical flow, called M-flow, will be dealt with in Chapter four. On the negative S_a - axis the shock shape is found on the leading edge of a convex wing surface. On the negative S_b axis the shock shape is conical, with the cone vertex pointing upstream. To complete the picture, at the origin there is a plane (flat) shock with no curvature in either direction.

There are two geometric/mathematical principles that need to be stated, understood and used in deriving gradient relations at a surface of discontinuity involving conservation laws.

The first: For a conserved quantity (e.g. mass flux) that remains constant as it crosses a discontinuity the derivatives of this quantity, on the up- and downstream sides of the discontinuity, along the same direction on the surface of the discontinuity, must be equal.

The second: The above principle holds for both steady and unsteady motion of the discontinuity.

The first of these is the basis of Curved Shock Theory; it seems 'intuitively obvious'. Perhaps less obvious for unsteady flow - but it must still be so since the discontinuities

are infinitely thin so that quantities immediately upstream of the shock take no time to cross the shock. The second principle is not crucial to the development of CST however it is implicit wherever it is claimed that the CST results apply to unsteady discontinuity motion – mostly everywhere. A rigorous proof of the second principle would be necessary for the development of CST for time-dependent flows.

2.2 Rankine-Hugoniot and Euler equations

Across a stationary **normal** shock wave the relations expressing conservation of mass, momentum/force, energy and state are: [Liepmann and Roshko, 1956, p.56]

$$\rho_1 V_1 = \rho_2 V_2 \quad (2.1)$$

$$p_1 + \rho_1 V_1^2 = p_2 + \rho_2 V_2^2 \quad (2.2)$$

$$C_p T_1 + V_1^2 / 2 = C_p T_2 + V_2^2 / 2 \quad (2.3)$$

$$\frac{p_1}{\rho_1 T_1} = \frac{p_2}{\rho_2 T_2} \quad (2.4)$$

where the usual density, velocity, pressure and temperature symbols with subscript 1 refer to the flow entering the shock and the subscript 2 refers to the departing flow in Figure 2.1. For an **oblique** (acute or obtuse) shock the conservation equations are:

$$\rho_1 V_{1N} = \rho_2 V_{2N} \quad (2.5)$$

$$p_1 + \rho_1 V_{1N}^2 = p_2 + \rho_2 V_{2N}^2 \quad (2.6)$$

$$\rho_1 V_{1N} V_{1T} = \rho_2 V_{2N} V_{2T} \quad (2.7)$$

$$C_p T_1 + (V_{1N}^2 + V_{1T}^2) / 2 = C_p T_2 + (V_{2N}^2 + V_{2T}^2) / 2 \quad (2.8)$$

$$\frac{p_1}{\rho_1 T_1} = \frac{p_2}{\rho_2 T_2} \quad (2.9)$$

The additional subscripts N and T denote velocity components normal and tangential to the oblique shock. For the applications that follow it is important to affirm here that these equations relate flow properties immediately up- and downstream of the shock surface and they apply locally to plane as well as to smoothly curving shock waves, be

the shocks stationary or not, as long as velocities are measured with respect to the shock wave. Equation 2.7, when divided by Equation 2.5, becomes $V_{1T} = V_{2T}$.

The Euler equations are used to describe how the flow properties change on moving away from the shock surfaces, either upstream or downstream. They express the conservation of mass, momentum/force and energy in directions along (s) and normal (n) to a streamline. For our purposes we make the assumption that the flow is steady and homenergetic so that the stagnation enthalpy is constant along, as well as across, streamlines. In the natural, or intrinsic, streamline coordinates [Hayes and Probstein p.482, 1966] the Euler conservation equations are,

$$\text{mass:} \quad \frac{\partial}{\partial s} \rho V y^j + \rho V y^j \frac{\partial \delta}{\partial n} = 0 \quad (2.10)$$

$$\text{s-momentum:} \quad \rho V \frac{\partial V}{\partial s} + \frac{\partial p}{\partial s} = 0 \quad (2.11)$$

$$\text{n-momentum:} \quad \rho V^2 \frac{\partial \delta}{\partial s} + \frac{\partial p}{\partial n} = 0 \quad (2.12)$$

$$\text{energy (homenergetic flow):} \quad \frac{\partial h}{\partial s} + V \frac{\partial V}{\partial s} = 0 \quad \frac{\partial h}{\partial n} + V \frac{\partial V}{\partial n} = 0 \quad (2.13a,b)$$

$$\text{vorticity is defined as:} \quad \omega = V \frac{\partial \delta}{\partial s} - \frac{\partial V}{\partial n} \quad (2.14)$$

In these equations y is the normal distance from the x-axis of symmetry, δ is the inclination of the streamline from the x-axis and $h = C_p T$ is the static enthalpy. The equations apply to continuous steady flow, in smooth flow regions, between the shock waves. s is measured in the flow direction along the streamline and n is normal to it. j is 0 or 1 for planar or axial flow respectively. For the present theory, the flow has to be neither planar nor axial if y is taken as the local radius of curvature of the shock trace in the plane normal to the upstream velocity vector. With this, more general definition of y , what follows is applicable to doubly curved shock waves possessing at least left-right symmetry with an identifiable y and where s and n are local (intrinsic) coordinates fixed in the flow plane at the shock. The direction of the normal coordinate n is well defined

only at the shock wave but this poses no difficulties since we are concerned only with the flow immediately up- and downstream of the shock. Both (x,y) and (s,n) are in right-hand coordinate systems so that the corresponding positive z and t point ‘out-of-the page’. All lengths are eventually non-dimensionalised by a convenient length scale that need not be initially specified.

For future algebraic neatness and convenience we define the following normalized variables:

$$\text{the normalized pressure gradient,} \quad P \equiv \frac{\partial p / \partial s}{\rho V^2}$$

$$\text{the streamline curvature,} \quad D \equiv \partial \delta / \partial s$$

$$\text{the normalized vorticity,} \quad \Gamma \equiv \omega / V$$

and note that along a streamline in front of the shock $\left(\frac{\partial y}{\partial s}\right)_1 = \sin \delta_1$ and $\left(\frac{\partial y}{\partial s}\right)_2 = \sin \delta_2$

behind. With these definitions, the Euler Equations, 2.10 to 2.14, can be written:

$$\text{mass:} \quad \frac{\partial \delta}{\partial n} = -(M^2 - 1)P - j \frac{\sin \delta}{y} \quad (2.15)$$

$$\text{s-momentum:} \quad \frac{1}{V} \frac{\partial V}{\partial s} = -\frac{1}{\rho V^2} \frac{\partial p}{\partial s} = -P \quad (2.16)$$

$$\text{n-momentum:} \quad \frac{1}{\rho V^2} \frac{\partial p}{\partial n} = -\frac{\partial \delta}{\partial s} = -D \quad (2.17)$$

$$\text{energy:} \quad \frac{1}{\rho} \frac{\partial \rho}{\partial n} = -M^2 [D + (\gamma - 1)\Gamma] \quad \frac{1}{\rho} \frac{\partial \rho}{\partial s} = M^2 P \quad (2.18,19)$$

$$\text{vorticity:} \quad \frac{1}{V} \frac{\partial V}{\partial n} = D - \Gamma \quad (2.20)$$

where the Mach number, M , is defined from $M^2 = \rho V^2 / \gamma p$.

These relations are used to eliminate the derivatives of δ , V , p and ρ on the left hand side in favour of M , P , D and Γ , appearing on the right. In the above equations all variables have either the subscript 1 or 2 depending on whether application is to flow on the up- or downstream side of the shock. The parameter y needs no subscript since it has the same value when states 1 and 2 are on opposite sides of the same shock. The use of j to denote flow with planar or axial symmetry will not be carried unless needed. The

effect of dimensionality (planar vs. axial) is obtained by assigning a very large value to y when dealing with planar flows.

2.3 Constant property lines

The contour lines of constant flow property values provide an insight into flow with variable properties; the sonic line being the most useful of the constant property lines in interpreting compressible flow fields. Orientation of contours and their properties are derived from equations 2.15 to 2.20. As an example, the variation of pressure along a line l , inclined at an angle α to the streamline, is,

$$\frac{dp}{dl} = \frac{\partial p}{\partial s} \cos \alpha + \frac{\partial p}{\partial n} \sin \alpha$$

If the line is an isobar then $dp/dl = 0$ and the inclination of the isobar to the streamline is α_p , such that,

$$\tan \alpha_p = -\frac{\frac{\partial p}{\partial s}}{\frac{\partial p}{\partial n}} = -\frac{\rho V^2 P}{-\rho V^2 D} = \frac{P}{D} \quad (2.21)$$

Similarly for an isotach, a line of constant velocity,

$$\tan \alpha_v = -\frac{\frac{\partial V}{\partial s}}{\frac{\partial V}{\partial n}} = -\frac{-VP}{V(D-\Gamma)} = \frac{P}{D-\Gamma} \quad (2.22)$$

From the energy equation, for adiabatic flow,

$$C_p T + V^2 / 2 = C_p T_t \quad (\text{constant})$$

V is constant, along an isotach, T must be constant also, and, so is then the speed of sound and the Mach number. Thus the lines of constant velocity, temperature, speed of sound and Mach number are collinear in adiabatic flow. Equation 2.22 will be used in Chapters five and six to find the inclination of the sonic line behind a doubly curved shock. For an isochor, a line of constant density,

$$\tan \alpha_\rho = -\frac{\frac{\partial \rho}{\partial s}}{\frac{\partial \rho}{\partial n}} = \frac{P}{D + (\gamma - 1)\Gamma} \quad (2.23)$$

For an isocline, a line of constant flow inclination,

$$\tan \alpha_s = -\frac{\frac{\partial \delta}{\partial s}}{\frac{\partial \delta}{\partial n}} = \frac{D}{(M^2 - 1)P + \sin \delta / y} \quad (2.24)$$

The constant property line inclinations for V , T , M , ρ , and p are all expressible in terms of P , D and Γ . Eliminating P , D and Γ from Equations 2.21 to 2.23 gives,

$$\frac{\gamma - 1}{\tan \alpha_v} = \frac{\gamma - 1}{\tan \alpha_T} = \frac{\gamma - 1}{\tan \alpha_M} = \frac{1}{\tan \alpha_\rho} = \frac{2 - \gamma}{\tan \alpha_p}$$

This equation can be used to establish the relative inclinations of the various constant property lines in **adiabatic** flow, particularly in flow behind curved shocks where the flow is rotational. For **irrotational** flow, $\Gamma = 0$, so that,

$$\tan \alpha_v = \tan \alpha_\rho = \tan \alpha_T = \tan \alpha_M = \tan \alpha_p = P / D$$

showing that all constant property lines, except the isoclines, are collinear for irrotational flow. These results are useful in the interpretation of contours of constant properties on interferometer and CFD pictures. We will develop expressions for P , D and Γ in terms of shock curvatures S_a , S_b and upstream Mach number so that, in conjunction with the flow direction, equations 2.21 to 2.24 can be used to find the directions of the constant property lines near curved shock surfaces. Specifically, these relations can be used to find the orientation of the sonic line behind a curved shock and, more generally, the orientation of the trace of the sonic surface in the flow plane. All angles presented above are measured counter-clock-wise from the local streamline direction.

2.4 The *curved shock equations*

Consider a segment of a doubly curved shock wave inclined at an angle θ to the free stream flow direction, as shown in the first two figures in Section 2.1, above. The angle θ is measured in the plane that contains both the entering and leaving velocity vectors. It is also the minimum angle between the post-shock velocity vector and the shock wave. This is called the *flow plane*. This definition of shock angle is very general and makes the theory applicable to a curved shock segment at any orientation in flow with left-right symmetry. In the flow plane the curvature of the shock is $S_a = \partial \theta_1 / \partial \sigma$,

where σ is the distance measured along the shock trace in the flow plane and $\theta_1 = \theta + \delta_1$ is the *geometric shock angle* (as measured from the axis of symmetry). The curvature of the shock trace in a plane normal to the flow plane and normal to the shock surface is S_b . The corresponding radii of curvature are then $R_a = -1/S_a$ and $R_b = -1/S_b$. In axisymmetric flow, $y/R_b = \cos \theta_1$ so that $S_b = -\cos \theta_1 / y$, where y is the normal distance from the axis to the shock. In the flow plane the velocity components, normal and tangential to the shock, upstream (1) and downstream (2) of the shock are,

	<u>normal</u>	<u>tangential</u>
upstream:	$V_{1N} = V_1 \sin \theta$	$V_{1T} = V_1 \cos \theta$
downstream:	$V_{2N} = V_2 \sin(\theta - \delta)$	$V_{2T} = V_2 \cos(\theta - \delta)$

With these substitutions, the Rankine-Hugoniot Equations, 2.5 to 2.9, become:

$$\rho_1 V_1 \sin \theta = \rho_2 V_2 \sin(\theta - \delta) \quad (2.25)$$

$$p_1 + \rho_1 V_1^2 \sin^2 \theta = p_2 + \rho_2 V_2^2 \sin^2(\theta - \delta) \quad (2.26)$$

$$V_1 \cos \theta = V_2 \cos(\theta - \delta) \quad (2.27)$$

$$V_1 V_2 \sin \theta \sin(\theta - \delta) = a_*^2 - \frac{\gamma - 1}{\gamma + 1} V_1^2 \cos^2 \theta \quad (2.28)$$

Where a_*^2 is the sound speed at sonic conditions (a constant in adiabatic flow).

The *curved shock equations* are derived by taking derivatives of both sides of each of equations 2.25, 2.26 and 2.27 with respect to σ (the distance along the shock) and equating these pre- and post-shock derivatives for each equation. This is a subtle yet essential step. It is justified because the derivative of any quantity that does not change across the shock does not change also if the derivatives, on the up- and downstream sides, are taken with respect to distance, σ , along the same shock. Taking derivatives of the conservation of mass, Equation 2.25, gives,

$$\begin{aligned} & \rho_1 V_1 \frac{\partial \sin \theta}{\partial \sigma} + \rho_1 \sin \theta \frac{\partial V_1}{\partial \sigma} + V_1 \sin \theta \frac{\partial \rho_1}{\partial \sigma} = \\ & = \rho_2 V_2 \frac{\partial}{\partial \sigma} \sin(\theta - \delta) + \rho_2 \sin(\theta - \delta) \frac{\partial V_2}{\partial \sigma} + V_2 \sin(\theta - \delta) \frac{\partial \rho_2}{\partial \sigma} \end{aligned}$$

and similarly, for Equation 2.26, produces two differentiated conservation equations involving the shock curvature terms $\frac{\partial \sin \theta_1}{\partial \sigma}$ explicitly.

In front of the shock, the derivative of any quantity with respect to distance along the shock, can be expressed in terms of the two derivatives along and normal to the streamline,

$$\left(\frac{\partial \bullet}{\partial \sigma}\right)_1 = \left(\frac{\partial \bullet}{\partial s}\right)_1 \cos \theta + \left(\frac{\partial \bullet}{\partial n}\right)_1 \sin \theta \quad \text{for } \rho, V, T \text{ and } p$$

Similarly, behind the shock,

$$\left(\frac{\partial \bullet}{\partial \sigma}\right)_2 = \left(\frac{\partial \bullet}{\partial s}\right)_2 \cos(\theta - \delta) + \left(\frac{\partial \bullet}{\partial n}\right)_2 \sin(\theta - \delta) \quad (2.29a,b)$$

These are used to replace the σ -derivatives, in the just differentiated conservation equations, by s and n derivatives and then replacing all derivatives $\frac{\partial \bullet}{\partial s}$ and $\frac{\partial \bullet}{\partial n}$ by expressions involving $P_1, D_1, \Gamma_1, D_2, P_2, S_a$, and S_b .² This produces, with a few pages of algebraic manipulation, the *curved shock equations*,

$$\boxed{\begin{aligned} A_1 P_1 + B_1 D_1 + E_1 \Gamma_1 &= A_2 P_2 + B_2 D_2 + C S_a + G S_b \\ A'_1 P_1 + B'_1 D_1 + E'_1 \Gamma_1 &= A'_2 P_2 + B'_2 D_2 + C' S_a + G' S_b \end{aligned}} \quad (2.30 \text{ a and b})$$

where the coefficients A, B, E, C, G and their primed and subscripted variants (14 in all) are given by,

$$\begin{aligned} A_1 &= 2 \cos \theta ((3M_1^2 - 4) \sin^2 \theta - (\gamma - 1) / 2) / (\gamma + 1) \\ B_1 &= 2 \sin \theta ((\gamma - 5) / 2 + (4 - M_1^2) \sin^2 \theta) / (\gamma + 1) \\ E_1 &= 2 \sin^3 \theta ((\gamma - 1) M_1^2 + 2) / (\gamma + 1) \\ A_2 &= \sin \theta \cos \theta / \sin(\theta - \delta) \\ B_2 &= -\sin \theta \cos \theta / \cos(\theta - \delta) \\ C &= -4 \sin \theta \cos \theta / (\gamma + 1) \\ F &= -4 \sin^2 \theta \cos \theta \sin \delta_1 / (\gamma + 1) \\ G &= 4 \sin^2 \theta \cos \theta \sin \delta_1 / (\gamma + 1) / \cos(\theta + \delta_1) \end{aligned} \quad (2.30c)$$

² A very similar algebraic process, to obtain an expression for vorticity from Eqn. 2.27, is described in more detail in the next section.

$$\begin{aligned}
A'_1 &= M_1^2 \cos \delta \cos^2 \theta - (M_1^2 - 1) \cos(2\theta + \delta) \\
B'_1 &= -\sin(2\theta + \delta) - M_1^2 \sin \delta \sin^2 \theta \\
E'_1 &= (2 + (\gamma - 1)M_1^2) \sin \delta \sin^2 \theta \\
A'_2 &= (1 + (M_2^2 - 2) \sin^2(\theta - \delta)) (\sin \theta \cos \theta) / (\sin(\theta - \delta) \cos(\theta - \delta)) \\
B'_2 &= -\sin(2\theta) \\
C' &= -\sin(2\delta) / (2 \cos(\theta - \delta)) \\
F' &= \sin \theta \cos \theta \sin \delta_2 - \sin^3 \theta \sin \delta_1 / \sin(\theta - \delta) \\
G' &= -F' / \cos(\theta + \delta_1)
\end{aligned} \tag{2.30d}$$

where,

$$M_2^2 = \frac{(\gamma + 1)^2 M_1^4 \sin^2 \theta - 4(M_1^2 \sin^2 \theta - 1)(\gamma M_1^2 \sin^2 \theta + 1)}{[2\gamma M_1^2 \sin^2 \theta - (\gamma - 1)][(\gamma - 1)M_1^2 \sin^2 \theta + 2]}$$

and $\delta = \delta_2 - \delta_1$

Two extra variables F and F' , functions of G and G' , are introduced for future utility. The two Equations (2.30a,b) relate shock curvature, S_a and S_b to stream-wise pressure gradient, P , and streamline curvature, D , on the up- and downstream sides of a shock element while accounting for any upstream vorticity, Γ_1 . The equations, together with the coefficients (2.30c,d) constitute the tools for analyzing shock wave curvature and flow gradients on the up- (subscript 1) and downstream (subscript 2) sides of a curved shock. If we assume that the specific heat ratio (γ), the free stream Mach number (M_1), the flow inclination in front of the shock (δ_1) and the shock angle (θ) are known then all the coefficients can be calculated.³ Then, with five of the seven variables $P_1, D_1, \Gamma_1, D_2, P_2, S_a$, and S_b known, the remaining two can be calculated from the two ‘simultaneous’ *curved shock equations*, (2.30a,b). If the coordinate system is aligned with the free stream then the shock angle, θ , is measured with respect to the free stream direction and $\delta_1 = 0$ so that $\delta = \delta_2$. Various restricted forms of these equations have been presented by many authors, Crocco [1937], Thomas [1947], Pant [1972]. However, they have not appeared with the degree of generality that includes both upstream vorticity, Γ_1 , and transverse shock curvature, S_b . Both of these are essential in application to axial curved shock wave detachment and reflection. The detailed derivation of the curved

³ Although γ will appear explicitly in the equations, it will be used with a value of 7/5 throughout.

shock equations is not presented because it requires a large number of algebraic steps. To illustrate the derivation procedure, a very similar but simpler derivation of the vorticity equation is given in the next section.

In a situation where the upstream flow is non-uniform and rotational with pressure gradient P_1 , streamline curvature D_1 and vorticity Γ_1 and where the shock is doubly curved with curvatures S_a and S_b we can calculate the pressure gradient P_2 and streamline curvature, D_2 behind the shock directly from,

$$\boxed{\begin{aligned} P_2 &= \frac{B_2 (C'S_a + G'S_b - L') - B_2' (CS_a + GS_b - L)}{A_2 B_2' - A_2' B_2} \\ D_2 &= -\frac{A_2 (C'S_a + G'S_b - L') - A_2' (CS_a + GS_b - L)}{A_2 B_2' - A_2' B_2} \end{aligned}} \quad (2.30e)$$

where,

$$\begin{aligned} L &= A_1 P_1 + B_1 D_1 + E_1 \Gamma_1 \\ L' &= A_1' P_1 + B_1' D_1 + E_1' \Gamma_1 \end{aligned}$$

These are the most general expressions for pressure gradient and streamline curvature for flow behind a doubly curved shock facing a non-uniform upstream flow with pressure gradient P_1 , streamline curvature D_1 and vorticity Γ_1 ; the upstream non-uniformities being contained in the two expressions L and L' . Both L and L' become zero for a uniform upstream. The upstream flow inclination, δ_1 , is contained in the two coefficients G and G' . G and F as well as G' and F' are mutually redundant because they multiply S_b or $1/y$ respectively and one would use either the G 's or F 's depending on which of S_b or $1/y$ is being used to define the flow-normal shock curvature.

Both P_2 and D_2 can be written in the *influence coefficient form*,

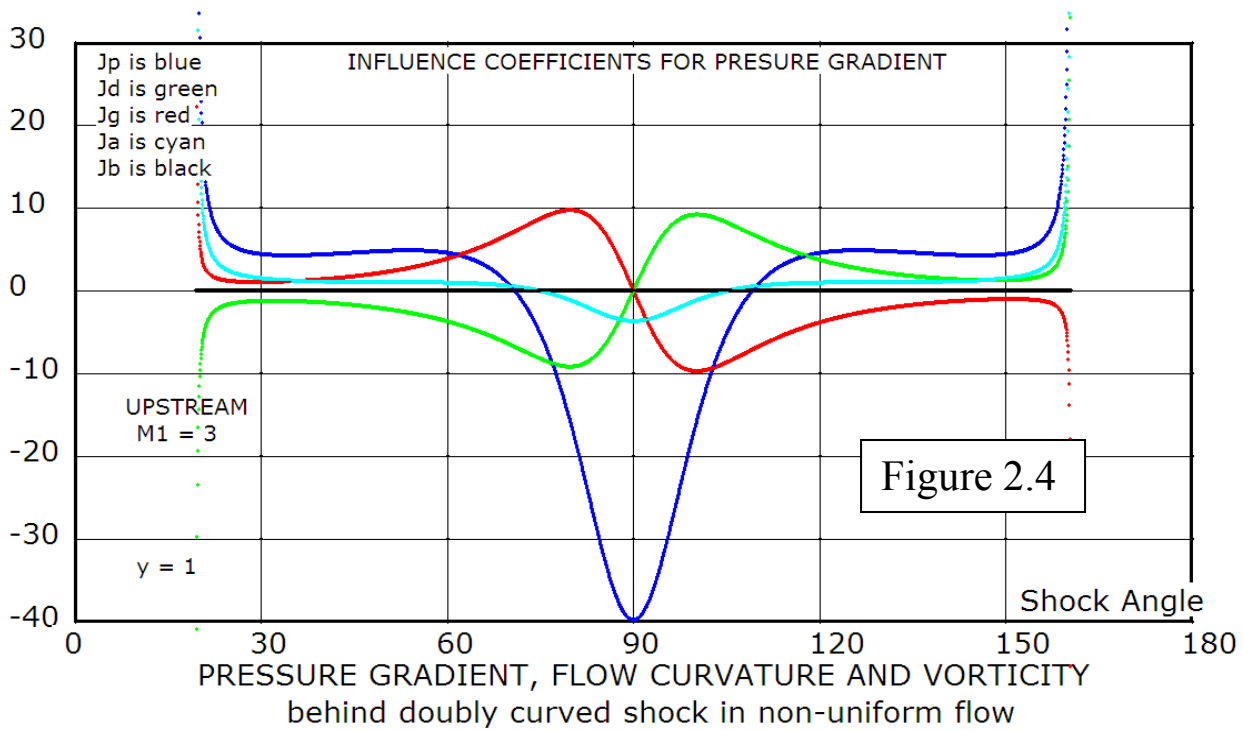
$$\boxed{\begin{aligned} P_2 &= J_p P_1 + J_d D_1 + J_g \Gamma_1 + J_a S_a + J_b S_b \\ D_2 &= K_p P_1 + K_d D_1 + K_g \Gamma_1 + K_a S_a + K_b S_b \end{aligned}} \quad (2.30 f)$$

where the *influence coefficients* are,

$$\begin{aligned}
J_p &= (A_1 B'_2 - A'_1 B_2) / [AB] & K_p &= (A_1 A'_2 - A'_1 A_2) / [AB] \\
J_d &= (B_1 B'_2 - B'_1 B_2) / [AB] & K_d &= (B_1 A'_2 - B'_1 A_2) / [AB] \\
J_g &= (E_1 B'_2 - E'_1 B_2) / [AB] & K_g &= (E_1 A'_2 - E'_1 A_2) / [AB] \\
J_a &= (B_2 C' - B'_2 C) / [AB] & K_a &= (A_2 C' - A'_2 C) / [AB] \\
J_b &= (B_2 G' - B'_2 G) / [AB] & K_b &= (A_2 G' - A'_2 G) / [AB]
\end{aligned} \tag{2.30 g}$$

and $[AB] = A_2 B'_2 - A'_2 B_2$.

These influence coefficient equations show explicitly how each of P_2 and D_2 are determined by the upstream quantities and the shock curvatures and the shock properties. The gas and shock properties (γ , M_1 , θ , δ_1) are sufficient to determine the *influence coefficients*. The influence of pre-shock flow convergence/divergence, as expressed by δ_1 , is unfortunately not as explicit, being embedded in J_a , J_b and K_a , K_b , through the



coefficients C , C' , G , G' . A similar influence coefficient equation will be derived for vorticity behind the shock in Section 2.3.1. Coefficients with subscripts p , d , and g are all zero for a uniform upstream flow.

Fig. 2.4 shows the influence coefficients for the post-shock pressure gradient, P_2 for both an acute and obtuse shock facing a Mach 3 air flow.⁴ The blue curve shows that for weak shocks the pre-shock pressure gradient is amplified in the same sense by a factor of about 4, whereas for a strong shock the incoming gradient is amplified by as much as 40 with a sense reversal⁵. At some intermediate values of shock angle of about 66 degrees and $180-66=114$ degrees the incoming pressure gradient has no influence on the post-shock gradient. The green curve shows that a pre-shock flow curvature, D_1 , causes an unlike sense contribution to the post-shock pressure gradient for the acute shock and a like sense contribution for the obtuse shock. Upstream vorticity's contribution (red curve) to post-shock pressure gradient is in the opposite sense to pre-shock flow curvature's but otherwise similar. The contribution of the flow-plane curvature, S_a , to the pressure gradient is shown by the cyan coloured curve. The effect is similar to that of pre-shock pressure gradient; sense reversal occurring near a shock angle of 75 and $180-75$ deg. The black curve shows that the lateral shock curvature, S_b , has no influence on the post-shock pressure gradient. This appears to be so because we have normalized the pressure gradient by y , so that the influence coefficient is calculated for a constant y of 1. The physical pressure gradient varies as $1/y = -S_b / \cos(\theta + \delta_1)$.

⁴ The curves, at the right and left extremes, are shown to approach $\pm\infty$ when the shock angle equals the Mach angle for both acute and obtuse shocks. This is due to the shock-tangential gradients becoming zero while the shock-normal gradients remain finite across a characteristic. The seeming infinities can be eliminated by first passing all the curved shock coefficients to their Mach wave limits before they are used as divisors. However, the infinities pose no problems when the theory is applied to finite strength shocks.

⁵ Note that in this case I_p represents P_2/P_1 , the ratio of the non-dimensional pressure gradients. To get the

ratio of the physical pressure gradients $\left(\frac{\partial p}{\partial s}\right)$, multiply by the dynamic pressure ratio, $\rho_2 V_2^2 / \rho_1 V_1^2$.

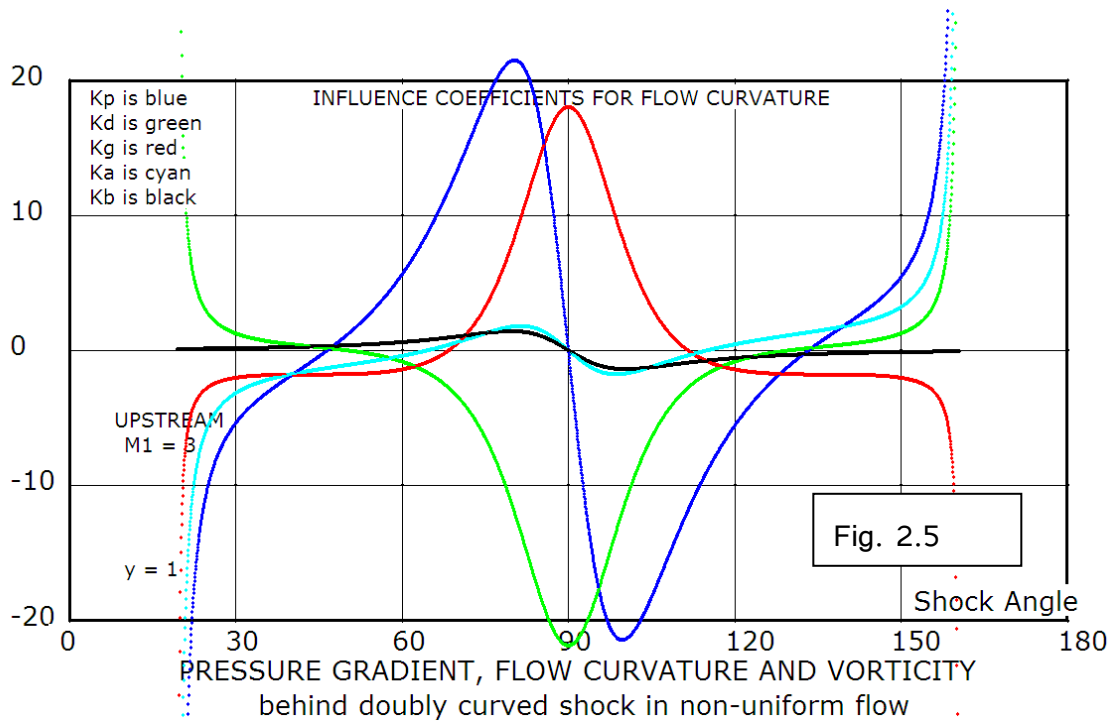


Fig. 2.5 depicts the influence coefficients for the pre-shock and shock curvature terms affecting the post-shock flow curvature, D_2 . The blue curve shows that a positive pre-shock pressure gradient contributes negatively to post-shock curvature for a weak acute shock and positively to a strong acute shock. The effect is anti-symmetric for an obtuse shock. The green curve shows that the pre-shock flow curvature causes a positive contribution to the post-shock curvature for weak shocks and a negative contribution for strong shocks, acute as well as obtuse. The contribution of pre-shock vorticity (red curve) is similar except with an opposite sense. Cyan and black curves show the anti-symmetric effects of the two shock curvatures S_a and S_b . The I_a curve crosses the horizontal axis at the Crocco point – to be discussed later.

The two graphs, presented above, are either symmetric or anti-symmetric for acute and obtuse shocks. This is because the freestream has been set to be parallel to the axis of symmetry ($\delta_1 = 0$). A finite value of δ_1 has no effect in planar flow. However, in axial flow, it leads to pre-shock flow convergence or divergence effects through the $(\sin \delta_1 / y)$ -term in Equation 2.15.

In most aeronautical applications the freestream is specified (and very often uniform) and the body shape is given as well and the post-shock conditions are to be determined. For such situations we would have the body slope behind the shock δ_2 , the body curvature D_2 and the distance from the axis of symmetry y . From these we can calculate the shock angle θ and the lateral (flow-normal) curvature of the shock, $S_b = -\cos\theta / y$. Substituting D_2 and S_b in (2.30 a and b) gives two equations for the pressure gradient behind the shock, P_2 , and the shock curvature in the flow plane S_a . Before considering other applications of the curved shock equations, we develop the equation for the vorticity behind the shock.

2.4.1 Vorticity behind the shock

Although the effect of pre-shock vorticity on the post-shock flow curvature and pressure gradient is included in the curved shock equations (2.30 a and b) the post-shock vorticity is not. The post-shock vorticity is required in the formula for the inclination of the sonic line behind the shock, Eqn. (2.2.2) and the constant density line, Eqn. (2.23).

The vorticity behind a curved shock, as given by Truesdell [1952], and more recently by Emanuel [1994] is,

$$\omega_2 = V_1 \frac{\rho_2}{\rho_1} \left(1 - \frac{\rho_1}{\rho_2}\right)^2 \cos\theta \times S_a \quad (2.31a)$$

The derivation of this relation uses the Crocco relation between vorticity and entropy and assumes a uniform upstream flow. The normalized version of (2.31a) is,

$$\Gamma_2 = \frac{\omega_2}{V_2} = \frac{V_1}{V_2} \frac{\rho_2}{\rho_1} \left(1 - \frac{\rho_1}{\rho_2}\right)^2 \cos\theta \times S_a \quad (2.31b)$$

Equation (2.31b) can be further simplified by using the oblique shock relations:

$$\Gamma_2 = \frac{2 \sin^2 \delta}{\sin(2\theta) \sin(\theta - \delta)} S_a \quad (2.31c)$$

This equation gives the normalized vorticity behind an acute or obtuse shock with curvature S_a when the **upstream flow is uniform and irrotational**. For both a normal shock and a Mach wave $\delta = 0$, and it is clear that neither one of these waves produces vorticity. The function has a maximum at an intermediate shock angle where maximum

vorticity is produced for a given shock curvature. The term multiplying S_a , later designated I_a , will be shown to be the *influence coefficient* for S_a in the general equation for Γ_2 . Also it will be shown that if the pre-shock flow is rotational then a term has to be added to each of (2.31a, b and c). For our purposes it is important to acknowledge that vorticity can either increase or decrease across a shock depending on the signs of $\cos\theta$ and S_a and that the vorticity behind the shock is influenced by upstream non-uniformity and vorticity and is therefore given by a more complicated relation than (2.31), to be derived below.

We seek an expression for vorticity behind a doubly curved shock for a shock that faces a flow that is curved, has a pressure gradient, is vortical and is converging or diverging towards or away from the line of symmetry – altogether a very high degree of generality. As for the previous derivations, the flow is steady and adiabatic of a calorically and thermally perfect gas. Results apply directly to flows that possess axial and planar symmetry and with some considerations of symmetry also to curved shock elements in three-dimensional flow. As for P_2 and D_2 , in the previous section, we derive the rational as well as the influence coefficient forms of the vorticity equation. The derivation is based on the shock-tangential momentum equation, the Euler equations and the definition of vorticity for the upstream (subscript 1) and downstream (subscript 2) flows. The following Euler relations are used to eliminate derivatives of velocity in favour of expressions containing streamwise pressure gradient, streamline curvature and normalized vorticity.

$$\begin{aligned} \frac{1}{V_1} \left(\frac{\partial V}{\partial s} \right)_1 &= -P_1 & \frac{1}{V_1} \left(\frac{\partial V}{\partial n} \right)_1 &= D_1 - \Gamma_1 & (2.11, 2.14) \\ \frac{1}{V_2} \left(\frac{\partial V}{\partial s} \right)_2 &= -P_2 & \frac{1}{V_2} \left(\frac{\partial V}{\partial n} \right)_2 &= D_2 - \Gamma_2 \end{aligned}$$

The geometric shock angle is $\theta_1 = \theta + \delta_1$. Taking derivatives of θ_1 with respect to σ gives the geometric shock curvature in the flow plane, S_a ,

$$S_a = \frac{\partial \theta_1}{\partial \sigma} = \frac{\partial \theta}{\partial \sigma} + \frac{\partial \delta_1}{\partial \sigma} \quad (2.32)$$

This can be written,

$$S_a = \frac{\partial \theta}{\partial \sigma} + \cos \theta \frac{\partial \delta_1}{\partial s} + \sin \theta \frac{\partial \delta_1}{\partial n}$$

But
$$\frac{\partial \delta_1}{\partial s} = D_1 \quad \text{and} \quad \frac{\partial \delta_1}{\partial n} = -(M_1^2 - 1)P_1 - \sin \delta_1 / y \quad (2.15)$$

So that,
$$\frac{\partial \theta}{\partial \sigma} = S_a + (M_1^2 - 1) \sin \theta P_1 - \cos \theta D_1 + \sin \theta \sin \delta_1 / y \quad (2.33)$$

Similarly, starting from $\theta - \delta = \theta_1 - \delta_2$, gives,

$$\frac{\partial(\theta - \delta)}{\partial \sigma} = S_a + (M_2^2 - 1) \sin(\theta - \delta) P_2 - \cos(\theta - \delta) D_2 + \sin(\theta - \delta) \sin \delta_2 / y \quad (2.34)$$

In these equations δ_1 and δ_2 are the geometric flow **inclinations** in front of and behind the shock. $\delta = \delta_2 - \delta_1$ is the flow **deflection** through the shock and θ is the corresponding aerodynamic shock angle. θ_1 is the geometric (physical) shock inclination. All inclinations are measured from the axis of symmetry, in the flow plane. For axial flow, y is the perpendicular distance from the shock to the axis of symmetry or, more generally, the radius of curvature of the shock trace in the transverse plane. For planar flow $y \rightarrow \infty$. Equations (2.11), (2.14), (2.33) and (2.34) are needed in the derivation of the vorticity equation. The derivation follows.

The momentum equation tangential to the shock is,

$$V_1 \cos \theta = V_2 \cos(\theta - \delta) \quad (2.35)$$

Taking derivatives of both sides of this equation with respect to the distance σ along the shock, gives,

$$V_1 \frac{\partial \cos \theta}{\partial \sigma} + \cos \theta \frac{\partial V_1}{\partial \sigma} = V_2 \frac{\partial \cos(\theta - \delta)}{\partial \sigma} + \cos(\theta - \delta) \frac{\partial V_2}{\partial \sigma}$$

Dividing through by V_1 and using equation (2.29a,b) gives,

$$\begin{aligned} \sin \theta \frac{\partial \theta}{\partial \sigma} - \cos \theta \left[\cos \theta \frac{1}{V_1} \left(\frac{\partial V}{\partial s} \right)_1 + \sin \theta \frac{1}{V_1} \left(\frac{\partial V}{\partial n} \right)_1 \right] &= \frac{V_2}{V_1} \left[\sin(\theta - \delta) \frac{\partial(\theta - \delta)}{\partial \sigma} \right] \\ - \cos(\theta - \delta) \frac{V_2}{V_1} \left[\cos(\theta - \delta) \frac{1}{V_2} \left(\frac{\partial V}{\partial s} \right)_2 + \sin(\theta - \delta) \frac{1}{V_2} \left(\frac{\partial V}{\partial n} \right)_2 \right] & \end{aligned} \quad (2.36)$$

Using equations (2.11), (2.14), (2.33) and (2.34) from above to replace the velocity and angle derivatives and replacing V_2 / V_1 by $\cos \theta / \cos(\theta - \delta)$ gives (2.37),

$$\begin{aligned}
& \sin \theta \left[S_a + (M_1^2 - 1) \sin \theta P_1 - \cos \theta D_1 + \sin \theta \sin \delta_1 / y \right] + \cos^2 \theta P_1 - \cos \theta \sin \theta \{ D_1 - \Gamma_1 \} = \\
& \cos \theta \tan(\theta - \delta) \left[S_a + (M_2^2 - 1) \sin(\theta - \delta) P_2 - \cos(\theta - \delta) D_2 + \sin(\theta - \delta) \sin \delta_2 / y \right] - \\
& \cos \theta \left[-\cos(\theta - \delta) P_2 + \sin(\theta - \delta) \{ D_2 - \Gamma_2 \} \right]
\end{aligned} \tag{2.37}$$

Dividing through by $\cos \theta$ and collecting coefficients of the physical variables P_l , D_l etc. for the *vorticity equation*:

$$\boxed{A_1'' P_1 + B_1'' D_1 + E_1'' \Gamma_1 = A_2'' P_2 + B_2'' D_2 + E_2'' \Gamma_2 + C'' S_a + G'' S_b} \tag{2.38a}$$

where,

$$\begin{aligned}
P_1 : A_1'' &= (M_1^2 - 1) \tan \theta \sin \theta + \cos \theta \\
D_1 : B_1'' &= -2 \sin \theta \\
\Gamma_1 : E_1'' &= \sin \theta \\
P_2 : A_2'' &= (M_2^2 - 1) \tan(\theta - \delta) \sin(\theta - \delta) + \cos(\theta - \delta) \\
D_2 : B_2'' &= -2 \sin(\theta - \delta) \\
\Gamma_2 : E_2'' &= \sin(\theta - \delta) \\
S_a : C'' &= \tan(\theta - \delta) - \tan \theta \\
1/y : F'' &= \tan(\theta - \delta) \sin(\theta - \delta) \sin \delta_2 - \sin \theta \tan \theta \sin \delta_1 \\
S_b : G'' &= -F'' / \cos(\theta + \delta_1)
\end{aligned} \tag{2.38b}$$

Equation (2.38a) can now be written,

$$L'' = A_2'' P_2 + B_2'' D_2 + E_2'' \Gamma_2 + C'' S_a + G'' S_b \tag{2.38c}$$

or

$$L'' = A_2'' P_2 + B_2'' D_2 + E_2'' \Gamma_2 + C'' S_a + F'' / y \tag{2.38d}$$

where

$$L'' = A_1'' P_1 + B_1'' D_1 + E_1'' \Gamma_1 \tag{2.38e}$$

Either one of the equations (2.38c) or (2.38d) can be used to solve for the post-shock vorticity, Γ_2 , in terms of the other variables. The two equations differ in their last terms depending on whether the transverse curvature of the shock is specified by S_b or y – a choice determined by the problem at hand. S_b and y are themselves interchangeable through $S_b = -\cos(\theta + \delta_1) / y$. Choosing (2.38c) and solving (2.38a) for Γ_2 gives the desired expression for the downstream vorticity,

$$\boxed{\Gamma_2 = \left[L'' - (A_2'' P_2 + B_2'' D_2 + C'' S_a + G'' S_b) \right] / E_2''} \tag{2.38f}$$

This is the generalized *vorticity equation* in a rational form for Γ_2 , the normalized vorticity behind a curved shock facing non-uniform flow. Together with equation (2.30f) it forms three equations for the three unknowns P_2 , D_2 and Γ_2 so as to completely define the non-uniform post-shock flow. For a uniform upstream (2.38f) reduces to,

$$\Gamma_2 = \left[\frac{C''}{E_2''} + \frac{[BC]}{[AB]} \frac{A_2''}{E_2''} - \frac{[AC]}{[AB]} \frac{B_2''}{E_2''} \right] S_a \quad (2.38g)$$

Fortunately P_2 and D_2 are decoupled from Γ_2 , leading to explicit solutions for all unknowns. P_2 and D_2 , appearing in the equations (2.30f), (2.38a) and (2.38f) are found from the two curved shock equations (2.30e) which are repeated here:

$$\begin{aligned} P_2 &= \frac{B_2(C'S_a + G'S_b - L') - B_2'(CS_a + GS_b - L)}{A_2B_2' - A_2'B_2} \\ D_2 &= -\frac{A_2(C'S_a + G'S_b - L') - A_2'(CS_a + GS_b - L)}{A_2B_2' - A_2'B_2} \end{aligned} \quad (2.30e)$$

Where the L -terms above are given by,

$$\begin{aligned} L &= A_1P_1 + B_1D_1 + E_1\Gamma_1 \\ L' &= A_1'P_1 + B_1'D_1 + E_1'\Gamma_1 \end{aligned}$$

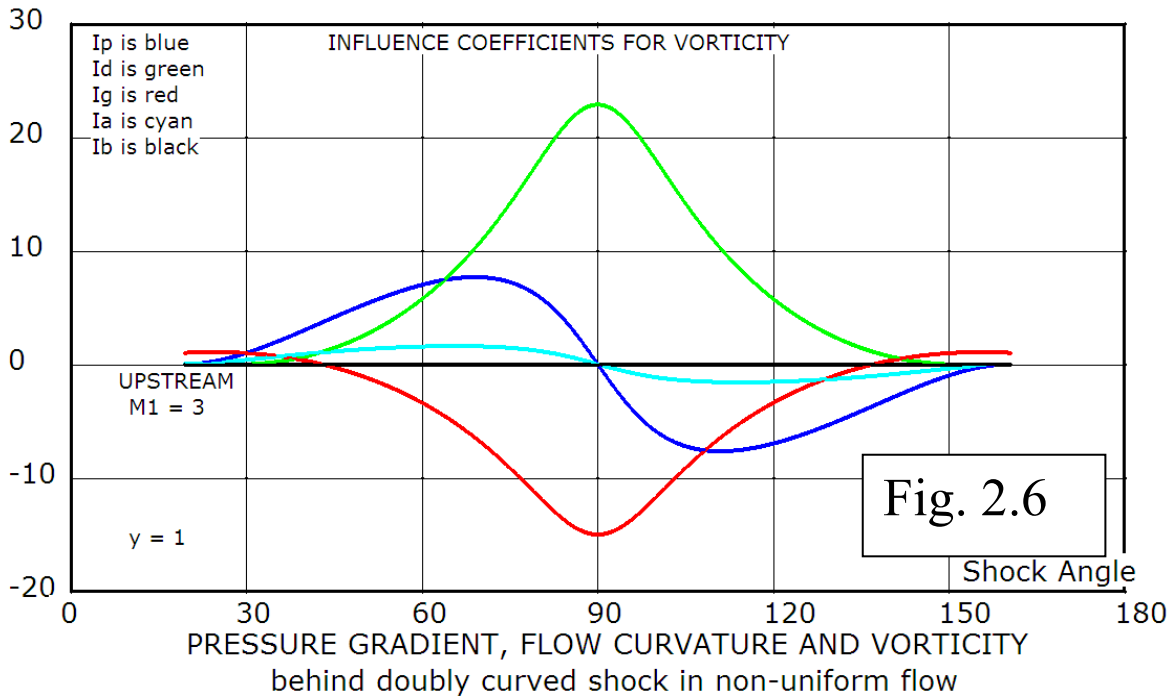
Note that L and L' contain the upstream gradients and that G and G' contain the upstream flow inclination δ_1 . Substituting P_2 and D_2 from Eqn. 2.39a into Eqn. 2.38f and collecting terms of the upstream gradients and the shock curvatures gives the *influence coefficient* form of the vorticity equation (2.38f),

$$\Gamma_2 = I_P P_1 + I_D D_1 + I_G \Gamma_1 + I_a S_a + I_b S_b \quad (2.40a)$$

where the I-coefficients, each multiplying their respective variables, appear in the full equation for Γ_2 as shown below,

$$\begin{aligned}
\Gamma_2 = & \left\{ [AB] A_1'' + (B_2 A_1' - B_2' A_1) A_2'' - (A_2 A_1' - A_2' A_1) B_2'' \right\} / \left\{ [AB] E_2'' \right\} P_1 \\
& + \left\{ [AB] B_1'' + (B_2 B_1' - B_2' B_1) A_2'' - (A_2 B_1' - A_2' B_1) B_2'' \right\} / \left\{ [AB] E_2'' \right\} D_1 \\
& + \left\{ [AB] E_1'' + (B_2 E_1' - B_2' E_1) A_2'' - (A_2 E_1' - A_2' E_1) B_2'' \right\} / \left\{ [AB] E_2'' \right\} \Gamma_1 \quad (2.40b) \\
& - \left\{ [AB] C'' + (B_2 C' - B_2' C) A_2'' - (A_2 C' - A_2' C) B_2'' \right\} / \left\{ [AB] E_2'' \right\} S_a \\
& - \left\{ [AB] G'' + (B_2 G' - B_2' G) A_2'' - (A_2 G' - A_2' G) B_2'' \right\} / \left\{ [AB] E_2'' \right\} S_b
\end{aligned}$$

The unprimed and single-primed coefficients $A \dots G$ are listed as equations (2.30 c and d); the double-primed are in Eq. (2.38b). This equation shows clearly what the role is of each upstream non-uniformity P_1 , D_1 and Γ_1 and of the shock curvatures S_a and S_b in determining the downstream vorticity. Note that the above derivation for vorticity does not need Crocco's thermodynamic relation between vorticity and entropy gradient, and that the resulting equations account for upstream flow non-uniformity and vorticity as well as flow inclination. Derivation of the



vorticity equation parallels those for the pressure gradient and streamline curvature but it is quite a bit simpler. That is the reason why the vorticity derivation is presented above and the others are not. The use of j to denote planar or axial symmetry has been dropped since the equations are uniformly valid for both geometries. For axial flow, y is the radius of the shock's curvature in the transverse plane, so that the flow is sensitive to dimensionality through the parameter y . In the calculations for planar flow, y is set to a very large number. Fig. 2.6 above depicts the influence coefficients for vorticity plotted against shock angle. The blue curve shows the influence of pre-shock pressure gradient P_1 , and we see that a positive pressure gradient causes a positive vorticity contribution for an acute shock and a negative contribution for an obtuse shock. The green curve shows that a positive pre-shock flow curvature, D_1 produces a positive contribution to vorticity. The red curve is for the effect of pre-shock vorticity itself and it is noted that the curve passes through zero at about 43 deg. and also at its supplement 180-43 deg. – the pre-shock vorticity is destroyed at these shock angles when the freestream Mach number is 3. At the Mach wave limits the influence coefficient has a value of 1, predicting that vorticity passes through Mach waves unchanged. All other curves are at zero so, at Mach wave conditions, there is no vorticity production due to pre-shock gradients or Mach wave curvatures. Stronger shocks tend to amplify and reverse the direction of vorticity. The cyan curve shows that positive vorticity is produced by a positive flow-plane shock curvature, S_a , for an acute shock and negative vorticity is produced by a positively curving obtuse shock. The black curve is for the effect of the transverse shock curvature, S_b and it shows that the influence coefficient for the transverse curvature is identically zero. This confirms the fact that the shock produces vorticity only by its flow-plane curvature and not by the transverse curvature so that flow behind a conical shock is irrotational. The $I_b S_b$ term can be dropped from equations 2.40a and 2.40b since I_b is identically zero. Seemingly opposing effects on the acute and obtuse shocks are generally due to different shock orientations rather than any differences in the underlying fluid mechanics.

2.5 Concluding comments

This chapter has presented the *curved shock theory* relating pressure gradient, streamline curvature and vorticity on the up- and downstream sides of a doubly curved shock surface in terms of the pre-shock Mach number, the shock angle and the two shock curvatures. Equations have been derived for constant property line inclinations for pressure, density, temperature and Mach number in terms of pressure gradient, flow curvature and vorticity.

In the next chapter we apply the *curved shock equations* to derive various results for doubly curved shocks as well as for characteristics and constant property lines for flows with planar and axial symmetry. For all examples, involving an oblique shock element, we first need to solve the Rankine-Hugoniot equations (2.25) to (2.28) to obtain one of M_2 , θ , and δ in terms of the other two and the upstream conditions. These three variables are required in order to calculate the coefficients of the *curved shock equations* (2.30 a and b). Most example flows have a uniform upstream so that all terms on the left hand sides of the two *curved shock equations* are zero and so is G , on the right hand side, if we choose to align the free stream with the x-axis ($\delta_1 = 0$). This is not the case when the equations are applied to the reflected shock in the shock reflection process, for then the flow in front of the reflected shock is inclined towards the axis and is possibly also non-uniform and rotational.

The very general *curved shock equations* have been derived above because they have not been presented with this degree of generality before. This is true especially for the vorticity equation as well as the influence coefficient form of the other equations for flow curvature and pressure gradient. Their full generality may not necessarily be used in the applications presented next in Ch. 3. The purpose of Ch. 3 is to show that the *curved shock equations* give results that make sense for limiting and simple shock geometries.

CHAPTER 3

APPLICATIONS OF CURVED SHOCK WAVE THEORY

Contents

- 3.0 Introduction
- 3.1 Shocks with planar symmetry, $S_b = 0$
 - 3.1.1 Plane shock in uniform upstream – a limiting case
 - 3.1.2 Shock with single curvature S_a in the flow plane, in a uniform upstream flow – planar flow ($S_b = 0$)
 - 3.1.3 The Thomas and Crocco points in planar flow
 - 3.1.4 Polar streamline slope (l) in planar flow
- 3.2 Shocks with conical symmetry; $S_a = 0$
 - 3.2.1 Acute conical shock in uniform flow; cone flow ($\mu < \theta < \pi / 2$)
 - 3.2.2 Obtuse conical shock in uniform flow; M-flow $\pi / 2 < \theta < (\pi - \mu)$
 - 3.2.3 Polar streamline slope in conical flow
- 3.3 Shocks with compound (double) curvature; $S_a \neq 0, S_b \neq 0$
- 3.4 Vorticity
- 3.5 Normal shocks
 - 3.5.1 Normal shocks in uniform flow
 - 3.5.1.1 Blunt body with convex normal shock
 - 3.5.1.2 Flow behind a normal shock at a concave Mach disk
 - 3.5.1.3 Blunt leading edge with sweep
- 3.6 Shocks on a circular wedge-annulus (*unit ring-wedge*); $y=1, D_2 = 0,$
- 3.7 Shock surfaces with up- or downstream uniformity
 - 3.7.1 Doubly curved Thomas and Crocco shocks
 - 3.7.2 Polar streamline slope for flow behind a shock facing uniform flow
 - 3.7.3 Polar streamlines for uniform post-shock flow
 - 3.7.4 Conditions behind a reflected shock
- 3.8 Curvature and strength of characteristics
 - 3.8.1 Curvature of characteristics
 - 3.8.2 Strength of characteristics
 - 3.8.3 Reflection coefficient
- 3.9 Sonic line orientation
- 3.10 Concluding remarks

3.0 Introduction

This chapter describes facts and tools for the analysis of curved shocks, presenting simple examples of CST results which point the way to more complicated applications. CST is shown to apply for a range of flow situations without pursuing any one example in great depth. Topics such as the flow behind a Mach disk deserve extended studies of their own. Comparison of CST results against known flows increases confidence in the correctness and applicability of the general CST equations.

CST, as derived in the previous chapter, is applied to flat shock waves, shocks with planar symmetry, shocks with conical symmetry and shocks with axial symmetry. For such cases, expressions are derived for pressure gradient, streamline curvature and vorticity on the post-shock sides of symmetric shocks. Application is also made to normal shocks in both a uniform and a non-uniform upstream flow. Results are produced for the stand-off distance of a shock from a bluff body and the stand-back distance of the sonic line from a Mach disk. Shapes of shocks with zero post-shock pressure gradient (isobaric) and straight post-shock streamlines (isoclinic) are calculated. Polar streamline slopes are illustrated for planar shocks, conical shocks and doubly curved shocks. CST formulae for curvature and strength of characteristics lead to an equation for the reflection coefficient of pressure disturbances from the back side of a shock. This, in turn, leads to the discovery of an axial shock surface shape, the back-side of which is uniformly and totally absorbing to impinging pressure pulses. Equations are presented, in terms of the CST coefficients, for the angle between the sonic line and the streamline for both planar and axial flow. These applications are presented here to lend credibility to the CST and to show how readily the CST is adapted to the analysis of various flow situations. About one-third of the examples are found in the literature [Lin & Rubinoff, 1948; Chernyi, 1961; Probstein & Hayes, 1966], while the rest are believed to be novel. Applications are selected on the basis of having some relevance to the design of air intakes for high Mach number air-breathing engines. Some findings are relevant to future study of RR→MR transition.

3.1 Shocks with planar symmetry, $S_b = 0$ occur on solid surfaces that also possess planar symmetry such as unswept wing leading edges and air intake ramps.

These types of shocks and associated flows are sometimes called *two-dimensional*. We avoid the use of *two-dimensional*, using instead the term *planar*, since axisymmetric flow, having two independent space variables, is also two-dimensional. The classical oblique shock and Prandtl-Meyer flows are examples in this category of planar flows.

3.1.1 Plane⁶ shock in uniform upstream – a limiting case

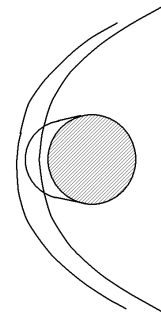
This application is just to demonstrate that the *curved shock equations* predict no flow gradients behind a plane (flat) shock in a uniform stream. In a uniform freestream flow all the gradients are zero and the left-hand-sides of the *curved shock equations* (2.30 a and b) both reduce to zero. For a plane shock both S_a and S_b are zero as well so that the *curved shock equations* reduce to,

$$\begin{aligned} 0 &= A_2 P_2 + B_2 D_2 \\ 0 &= A'_2 P_2 + B'_2 D_2 \end{aligned} \quad (3.1)$$

For any values of A_2 , B_2 , A'_2 and B'_2 , the only possible solution for these two equations is $P_2 = D_2 = 0$, i.e. the pressure gradient and flow curvature behind a plane shock, in a uniform irrotational stream, are both zero. Not an unexpected result. The *vorticity equation* (2.31 c) implies that the vorticity is zero behind a plane shock in uniform flow - also not surprising. For a flat shock, in a uniform pre-shock flow, the CST equations predict a uniform post-shock flow.

3.1.2 Shock with single curvature S_a in the flow plane, in a uniform upstream flow – *planar flow* ($S_b = 0$).

Such a shock and its associated flow exist at the curved leading edge of an unswept wing or a circular cylinder placed perpendicular to the flow direction. Again, because of the uniform, irrotational, freestream the left-hand sides of the *curved shock equations* are zero. The transverse curvature S_b is zero also



⁶ The term ‘plane’ or ‘flat’ is used to denote a surface with no curvature in any direction; for the case of a shock it means $S_a = S_b = 0$. The term ‘planar’ refers to flow and shocks with planar symmetry where the shock curvature $S_b = 0$ but $S_a \neq 0$ and ‘axial’ refers to flow that is axially symmetric. The term ‘conical flow’ implies flow that has no variation along any ray drawn from the apex of a coordinate cone. In axial conical flow $S_a = 0$. Conical shock means that the shock curvature in the flow plane, $S_a = 0$. Conical wall **surface** means that the surface curvature in the flow plane, $D = \partial\delta / \partial s = 0$.

but the curvature in the flow plane has a finite value, $S_a \neq 0$. Under these conditions the *curved shock equations* become,

$$\begin{aligned} 0 &= A_2 P_2 + B_2 D_2 + C S_a \\ 0 &= A'_2 P_2 + B'_2 D_2 + C' S_a \end{aligned} \quad (3.2a)$$

such that the pressure gradient and the streamline curvature behind the shock can both be expressed in terms of the shock curvature,

$$P_2 = \frac{B_2 C' - B'_2 C}{A_2 B'_2 - A'_2 B_2} S_a \quad D_2 = \frac{C A'_2 - C' A_2}{A_2 B'_2 - A'_2 B_2} S_a \quad (3.2b,c)$$

We abbreviate the above expressions by the following matrix notation. The square-bracketed matrix terms appear often in what follows.

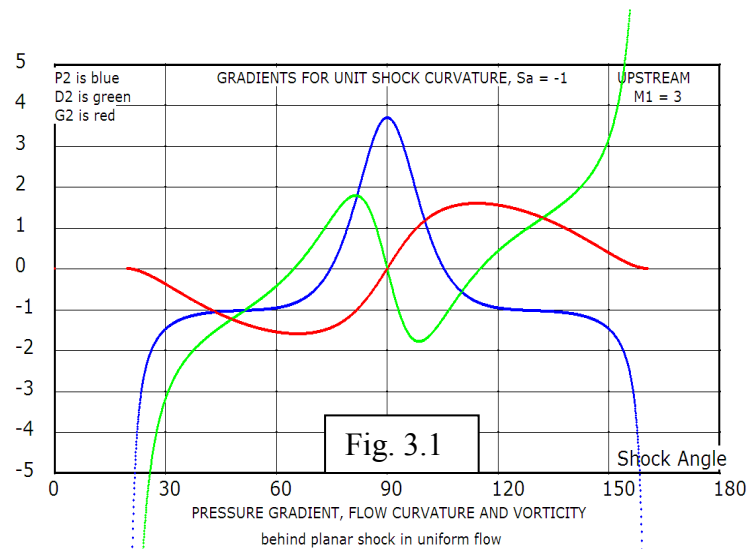
$$P_2 = \frac{[BC]}{[AB]} S_a \quad D_2 = \frac{[CA]}{[AB]} S_a \quad (3.2d,e)$$

The equation for downstream vorticity follows from Eqn. (2.28 g),

$$\Gamma_2 = \left[\frac{C''}{E_2''} + \frac{[BC]}{[AB]} \frac{A_2''}{E_2''} - \frac{[AC]}{[AB]} \frac{B_2''}{E_2''} \right] S_a$$

(3.2f) Equations 3.2a-e state that, immediately behind the shock, the pressure gradient along the streamline and the streamline curvature and vorticity are all linearly dependent on the shock curvature, S_a . The magnitude and sign of the dependence is determined by

the terms in the square brackets. These terms are functions of the freestream Mach number and the shock angle only, as in Eqns. (3.2 a, b and c). P_2 , D_2 and the vorticity Γ_2 are plotted, (where Γ_2 is denoted by G_2) in Fig. 3.1 for a freestream Mach number of 3 and a convex shock with curvature of $S_a = -1$.



For a convex, nearly normal shock, where $\theta \sim 90$ deg, the pressure gradient is positive and at weaker shock angles it is negative. Flow curvature is positive above and

negative below the line of symmetry for the strong shock and opposite to that for weak shocks. The points/angles on the shock wave where P_2 and D_2 are zero are the **Thomas and Crocco points** respectively. They are useful guide-posts in the landscape of changing flow-fields near curved shocks. As an example, in the search for reflected (embedded) shocks, behind curved incident shocks, it appears that where the flow is supersonic behind a convex shock it is also always expansive so that reflected shocks are not likely to form. For concave shocks, however, the flow is compressive, so that reflected shocks can form. This will become evident when considering hyperbolic shocks in Ch.5. It is the Thomas point that separates compressive and expansive flow-fields. In Ch.6 the concepts embodied in Thomas and Crocco points will be broadened to doubly curved shocks. The vorticity behind the shock is given by Eqn. (2.29 a,b,c); it is uniformly negative for acute convex shocks and positive for obtuse convex shocks. All of the above is consistent with our knowledge of qualitative aspects of flow behaviour behind strong shocks on bluff planar shapes.

3.1.3 The Thomas and Crocco points in planar flow

The Thomas and Crocco points, described qualitatively above, are set into mathematical terms in this section. First, for the Thomas point, from equation (3.2d) it is seen that $P_2 = 0$ occurs when $[BC] = B_2C' - B_2'C = 0$, and this condition yields an equation relating δ and θ ,

$$(\gamma + 1)\sin 2\delta = 8\sin 2\theta \cos^2(\theta - \delta) \quad (3.3a)$$

This equation has an explicit solution because it does not contain the freestream Mach number explicitly.

$$\tan \delta_r = \frac{\alpha - 2a^2b^2 \pm \sqrt{\alpha(\alpha - 4a^2b^2)}}{2a^3b} \quad (3.3b)$$

where $a = \sin\theta_T$, $b = \cos\theta_T$ and $\alpha = (\gamma+1)/8$. Having specified a θ_T and calculated δ_T , from (3.3b), the freestream Mach number can then be found from the usual oblique shock relation [Ames, NACA Rep. 1135; Eqn. 148 a]

$$\frac{1}{M_{1T}^2} = \sin^2 \theta_T - \frac{\gamma + 1}{2} \frac{\sin \theta_T \sin \delta_T}{\cos(\theta_T - \delta_T)} \quad (3.3c)$$

to obtain the condition $(M_{1T}, \theta_T, \delta_T)$ at which the pressure gradient along the streamline behind the shock is zero. There is a unique such condition for every Mach number. On a planar curving shock the zero streamline pressure gradient shock angle lies between the angle for maximum flow deflection and the normal shock – on the strong shock side, in subsonic downstream flow. In recognition of Thomas' [1947 and subsequent] early work on curved shock theory, we call θ_T the *Thomas angle*, or *Thomas point* on the shock. For a plane shock, the Thomas point, defined by $[BC] = B_2C' - B_2'C = 0$, is where the pressure gradient behind the shock is zero but the flow curvature is not. If both were zero then we would have just an uninteresting piece of flat shock that can occur at any combination of Mach number and shock angle. Thomas points are shown in green on the Mach number curves in the theta/delta polar diagram, Fig. 3.2, below. The Thomas point plays a key role in the discussion of shock detachment in Ch.6.

An approach similar to that for the Thomas point, but setting $[CA] = 0$, yields the equation,

$$\sin \delta = \frac{4}{\gamma + 1} \left[\sin 2(\theta - \delta) + (M_2^2 - 2) \sin^2(\theta - \delta) \sin 2\theta \right] \quad (3.4)$$

which, with the help of the oblique shock relations (2.25) to (2.28), relates M_1 and θ . Solving for θ gives a shock angle θ_C at which the streamline curvature behind the shock is zero. The angle is called the *Crocco angle* and its location is the *Crocco point*. No explicit solution has been found for (3.4) so that the Crocco angle has to be found iteratively, solving for θ_C as a function of the freestream Mach number.

G. Emanuel (private communication) has derived a cubic equation for $w = M_1^2 \sin^2 \theta_C$:

$$aw^3 + bw^2 + cw + d = 0 \quad (3.5)$$

where,

$$a = -\gamma(2\gamma - 1)$$

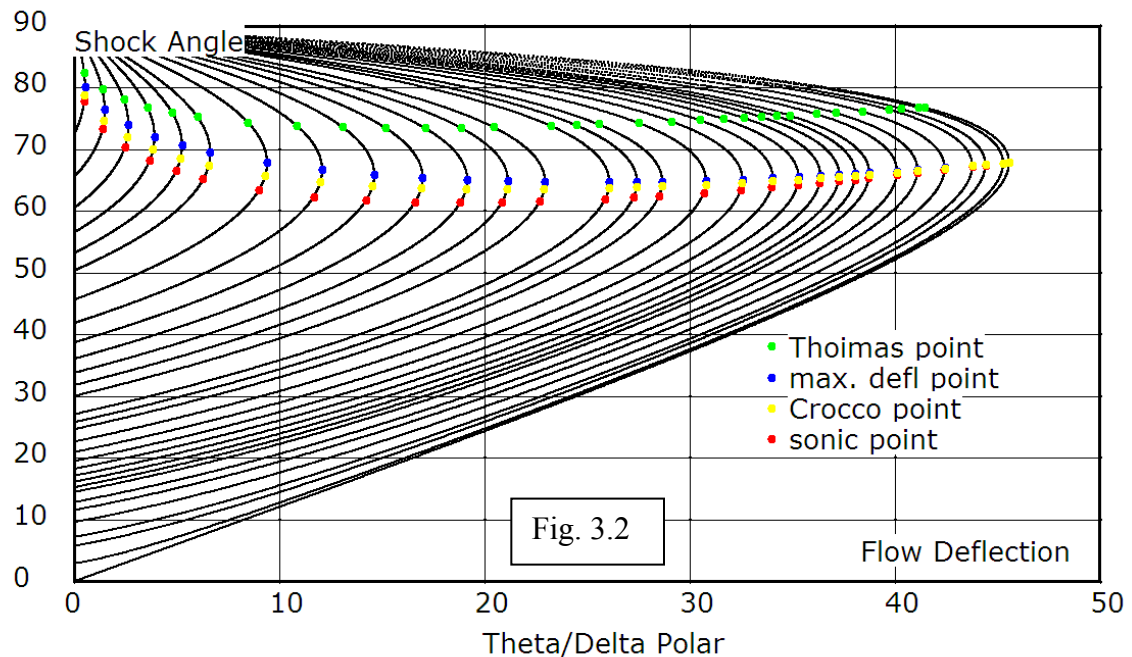
$$b = (\gamma + 1)(2\gamma - 1)M_1^2 / 2 + (2\gamma^2 - 13\gamma + 3) / 2$$

$$c = (\gamma + 1)(\gamma + 5)M_1^2 / 4 + (4\gamma - 5)$$

$$d = -(\gamma - 1)(\gamma + 1)M_1^2 / 4 + (\gamma - 5) / 2$$

Since the cubic has an exact solution it is more accurate and faster than any iterative solution.

For every freestream Mach number, in a planar flow, there is then a unique shock angle attached to each of: the maximum flow deflection, the post-shock sonic condition,



the Crocco point and the Thomas point. Figure 3.2 is for shock angle (theta) vs. flow deflection (delta) through the shock for a selection of Mach numbers 1.05, 1.1, 1.15, 1.2, 1.25, 1.3, 1.4, 1.5, 1.6, 1.7, 1.8, 1.9, 2, 2.2, 2.3, 2.4, 2.6, 2.8, 3, 3.2, 3.4, 3.6, 3.8, 4, 4.5, 5, 6, 8, 10, 20, 10000 (from left to right). The maximum flow deflection points and the sonic points are shown in blue and red, respectively. For a planarly symmetric (planar) curved shock wave the Thomas and Crocco points are shown in green and yellow respectively. The Crocco shock angle lies between the sonic shock angle and the maximum flow deflection angle for any Mach number (and any γ). The Crocco point, shown by the yellow points, is not just where the flow curvature behind the shock is zero;

it is a point where the flow curvature is zero but the shock curvature and pressure gradient are not. If all were zero then we would have just an uninteresting piece of flat shock that can occur at any combination of M_I and θ . The Crocco and Thomas shocks, here restricted to planar flow, are versions of the more general isoclinic and isobaric shocks when the flow is axial and the shock has double curvature. It will be shown that, for doubly curved shocks, both the Crocco and Thomas point locations are a function of the shock's surface curvature ratio as well as the freestream Mach number. Crocco and Thomas point definitions have been generalized, not to lie at specific shock angles, but at locations where the post-shock streamline is straight and where the post-shock flow properties are constant along the streamline.

The Thomas and Crocco points are convenient points of reference when dealing with flow gradients' behavior behind curved shocks. The Crocco condition $[CA] = 0$ has been suggested as a possible point of transition from RR to MR [Henderson, 1987]. Mathematically this is apparent from Eqns. (2.33 c, d) where, for a finite D_2 , the shock curvature and pressure gradient will become unbounded when $[CA] \rightarrow 0$. This is in line with Henderson's assertion: "...transition on concave, plane and convex surfaces are different,...". An infinite pressure gradient behind an attached or reflected shock, be it favorable or adverse, is bound to affect the shock as well as the boundary layer.

3.1.4 Polar streamline slope (l) in planar flow

In studying shock reflections and interactions the set of Rankine-Hugoniot conservation equations is often closed by statements regarding pressure and flow direction in the downstream flow. For example, for shock reflection at a plane wall we require that the flow be returned to the freestream direction by the reflected shock and for a three-shock, free-floating shock interaction (Mach reflection at a triple point) we require that the pressures and flow directions match across the slip layer [von Neumann, 1943]. These pressure/deflection conditions encourage the use of the Rankine-Hugoniot shock wave equations in pressure/deflection ($p - \delta$) polar form [Ames Res. Staff, NACA Rep. 1135, Eqn. 160], and the graphical representation of the shocks on a ($p - \delta$) plane.

$$\tan^2 \delta = \left(\frac{\xi - 1}{\gamma M_1^2 - \xi + 1} \right)^2 \frac{2\gamma M_1^2 - (\gamma - 1) - (\gamma + 1)\xi}{(\gamma + 1)\xi + (\gamma - 1)} \quad (3.6)$$

where ξ is the shock pressure ratio, p_2 / p_1

If the shock is curved then there is a value of P_2 and D_2 associated with every point on the shock polar and the flow 'direction' in the $(p - \delta)$ -plane can then be written as,

$$l = \frac{1}{\frac{\partial \delta}{\partial s}} \frac{\partial p}{\partial s} = \frac{1}{\rho V^2} \frac{\partial p}{\partial \delta} = \frac{P_2}{D_2} = \frac{[BC]}{[AC]} \quad (3.7)$$

This is the slope of the 'streamline'⁷ behind the planarly symmetric shock in the $(p - \delta)$ -plane, here denoted by the symbol l . A typical $(p - \delta)$ -polar with associated streamlines is shown in Fig. 3.3 [Molder, 1972]. The right-hand-side represents acute shocks, with

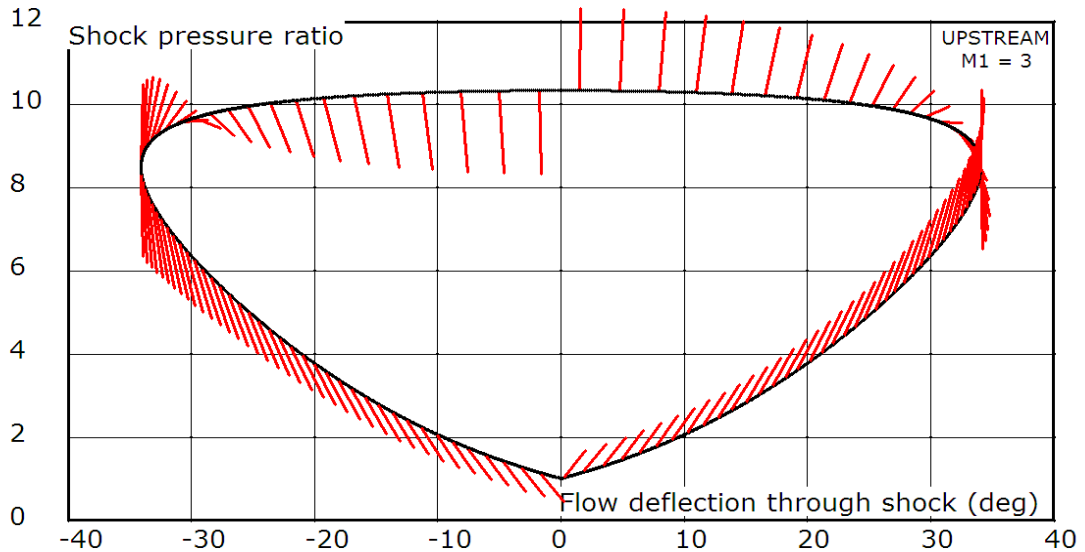


Fig. 3.3 SHOCK POLAR AND POLAR STREAMLINE DIRECTIONS behind planar shock in uniform flow

positive flow deflection and the left-hand-side represents obtuse shocks with negative flow deflection. For a weak acute shock l is positive, representing either P_2 and D_2 both positive or both negative for $S_a > 0$ or < 0 respectively. At the Crocco point (± 34 deg) the slope goes through $\pm\infty$ because $[CA] = 0$. At the Thomas point (± 31 deg) the slope

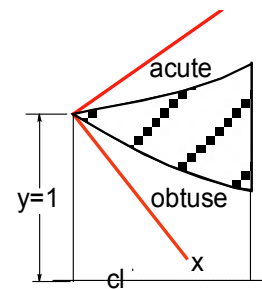
⁷ A true streamline exists only in physical space. In $(p - \delta)$ -space there is a curve that relates the pressure and flow direction as the flow moves along the true streamline.

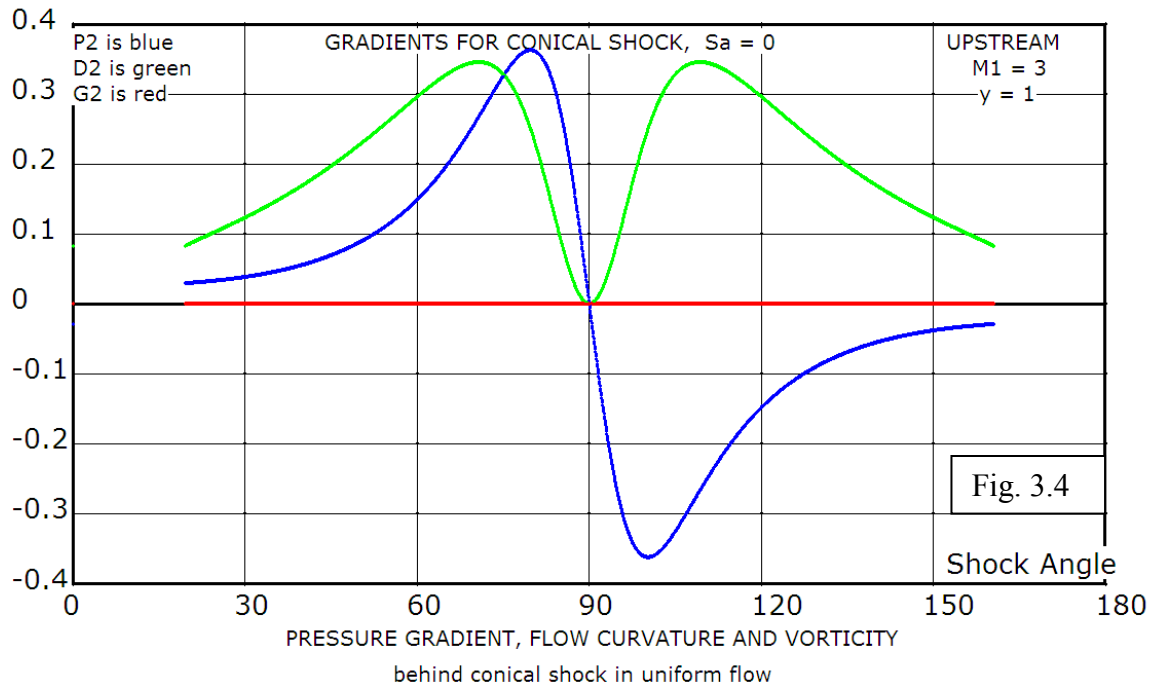
goes through another change of sign, this time through zero, because $[BC] = 0$. For a strong acute shock the streamline slope is positive because both pressure gradient and flow curvature are positive behind the shock. The polar streamline slope is independent of shock curvature in planar flow. For an obtuse shock, on the left side of the polar the streamline slopes are in the opposite sense because the flow curvatures have opposite signs. If the shock is the incident shock in regular reflection then P_2/D_2 , as given by (3.7), will have to equal P_3/D_3 in front of a reflected shock. This condition is applied in studies of regular shock reflection. For Mach reflection it means that the quantity $M^2 P/D$ has to match across the slip layer. Reasons for including the M^2 -term stem from the pressure invariance requirement across the slip layer. The polar streamline slope is a useful ‘higher level’ concept in relating reflection and interaction of curved shocks by requiring compatibility of streamline slopes between incident, reflected and Mach shocks.

This section has introduced the polar streamline slope and suggested its applications to shock interactions.

3.2 Shocks with conical symmetry; $S_a = 0$

The flow associated with a conical shock, either upstream or downstream of the shock, as governed by the Taylor-Maccoll equations [Owcharek,1964 p.482], will be treated further in Ch.4 under **CONICAL FLOW AND THE TAYLOR-MACCOLL EQUATION(S)**. In this section we use CST to develop the flow gradient terms for flow behind such **conical** shocks that face a uniform upstream flow, $P_l = D_l = \Gamma_l = 0$, where $S_a = 0$ and $S_b = -\cos(\theta + \delta_l)/y$. The freestream is parallel to the x-axis so that $\delta_l = 0$. This makes $G = 0$ so that the *curved shock equations* become,





$$\begin{aligned} 0 &= A_2 P_2 + B_2 D_2 \\ 0 &= A'_2 P_2 + B'_2 D_2 + G'_2 S_b \end{aligned} \quad (3.8)$$

with the solutions,

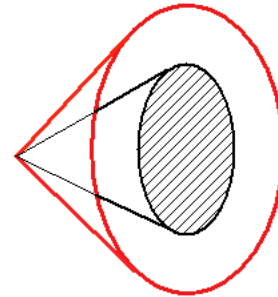
$$P_2 = -\frac{B_2 G'_2}{[AB]} \cos \theta / y \quad D_2 = \frac{A_2 G'_2}{[AB]} \cos \theta / y \quad (3.9)$$

These gradients are plotted in Fig. 3.4 for a Mach number of 3 and for streamlines that originate at a point on the shock that is located unit distance from the centre line, $y = 1$. Vorticity behind a conical shock is zero, as shown by the red line G_2 .

3.2.1 Acute conical shock in uniform flow; cone flow ($\mu < \theta < \pi/2$)

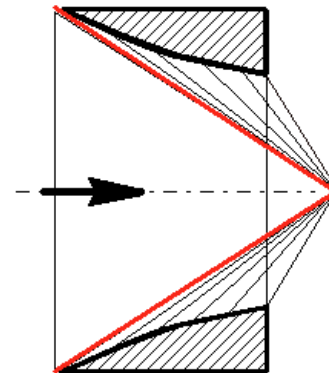
This section describes the classical flow behind the attached shock (in the first quadrant – left half of the Fig. 3.4) that envelops a solid axisymmetric cone in uniform supersonic flow at zero angle of attack. For this flow both P_2 and D_2 are positive, confirming that, in the flow behind an acute conical shock, the pressure increases as does the flow inclination. These are both conditions known to exist in flow over a circular cone

at zero angle of attack [Sims, 1964]. We note that both P_2 and D_2 become very large near the apex of the cone as $y \rightarrow 0$ in Eqns. (3.9). This is necessary for the flow, coming from the shock, to adjust to the cone surface conditions in a very short distance. Fig. 3.4 above shows P_2 and D_2 vs θ for Mach 3. The left half of this figure is for a cone with an acute shock angle. The right half is for an obtuse conical shock, producing M-flow to be discussed further in Ch. 4. Note that B_2 , A_2 and G' are never zero (except for a normal shock) so the flow gradients behind a conical shock are never zero and there is then no possibility of a Crocco or Thomas point on a conical shock.



3.2.2 Obtuse conical shock in uniform flow; M-flow; $\pi/2 < \theta < (\pi-\mu)$

For this less well-known obtuse conical shock (in the second quadrant), the lateral streamline curvature coefficient (Eqn. 3.9) is positive but the pressure gradient coefficient is negative while the shock curvature S_b is positive so that the pressure decreases but the streamline inclination increases along the streamline. P_2 and D_2 are plotted in Fig. 3.4. Gradients for both of these results are confirmed by the solution of the Taylor-Maccoll equations for axially symmetric conical flow in Ch. 4. From Eqn. (3.9) we see again that both the pressure gradient and the flow curvature become very large on approaching the axis of symmetry ($y \rightarrow 0$). This is the fundamental reason why oblique shocks cannot reach the centre line, as in the sketch above [Rylov, 1990] and it is proposed as a cause of the untimely $RR \rightarrow MR$ transition in all axial internal flows.



3.2.3 Polar streamline slope in conical flow

Using Eqns. (2.37) for conical flow gives the polar streamline slope,

$$\frac{P_2}{D_2} = -\frac{B_2}{A_2} \quad (3.10)$$

This is the slope of the streamline in the $(p-\delta)$ -plane for conical flow. It corresponds to Eqn.(3.7) for planar flow. Examining the nature of B_2 and A_2 shows that the streamline slope in the $(p-\delta)$ -plane is a function of freestream Mach number and shock angle only – and not of the shock curvature, S_b . Polar streamline directions are plotted in Fig. 3.5, on the right. We will present below an equation for the slope of polar streamlines for shocks with compound curvature.

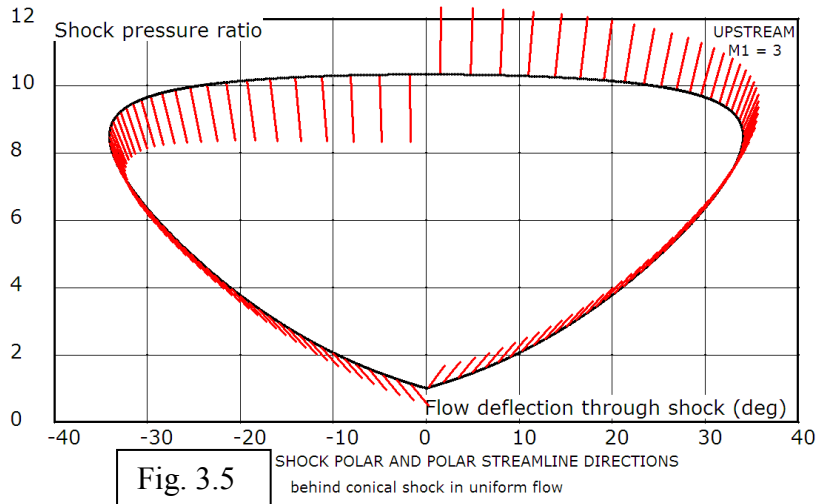


Fig. 3.5

3.3 Shocks with compound (double) curvature; $S_a \neq 0$, $S_b \neq 0$

This is the general case of a doubly curved shock with a non-zero surface curvature S_a in the flow plane and S_b in the flow-normal plane. For a uniform freestream, aligned with the coordinate axis, the *curved shock equations* reduce to,

$$\begin{aligned} 0 &= A_2 P_2 + B_2 D_2 + C S_a \\ 0 &= A'_2 P_2 + B'_2 D_2 + C' S_a + G' S_b \end{aligned} \quad (3.11)$$

with the solutions,

$$\begin{aligned} P_2 &= \frac{[BC]}{[AB]} S_a + \frac{B_2 G'}{[AB]} S_b \\ D_2 &= \frac{[CA]}{[AB]} S_a - \frac{A_2 G'}{[AB]} S_b \end{aligned} \quad (3.12 \text{ a,b})$$

The first of the two terms, on the right-hand-side, in each of the two expressions above is due to the curvature of the shock in the *flow plane*. The second term is due to the

curvature in the *flow-normal plane*. Flow behaviour due to the second term is sometimes called *convergence effects*. A *flow plane* [Hornung and Robinson, 1982] can always be identified on a doubly curved shock element, even in 3D space, as the plane that contains the incoming and outgoing velocity vectors [Figure 2.1]. The shock angle and S_a are measured in the flow plane and S_b from the shock trace in the transverse plane. This results in the definition of all quantities on the right-hand sides of Eqns. (3.2 a,b), leading to the determination of P_2 and D_2 . The polar streamline slope is now,

$$P_2 / D_2 = \frac{[BC]\mathcal{R} + B_2G'}{[CA]\mathcal{R} - A_2G'} \quad (3.12c)$$

where, $\mathcal{R} = S_a / S_b$, showing that the slope can have any value depending on the ratio of shock curvatures. These relations will be used throughout most of the subsequent developments concerning curved shocks facing a uniform stream.

3.4 Vorticity

In intrinsic coordinates, *primitive* vorticity is defined as,

$$\omega = V \frac{\partial \delta}{\partial s} - \frac{\partial V}{\partial n}$$

For dimensional homogeneity and ease of algebraic manipulation it is convenient to use a *normalized* vorticity,

$$\Gamma = \frac{\omega}{V} = \frac{\partial \delta}{\partial s} - \frac{1}{V} \frac{\partial V}{\partial n}$$

For a shock with flow-plane curvature S_a , in a rotational upstream flow with normalized vorticity Γ_1 , which is otherwise uniform, the influence coefficient form (2.40 a) of the vorticity equation reduces to,

$$\Gamma_2 = I_G \Gamma_1 + I_a S_a$$

If the pre-shock flow is rotational then the term $I_G \Gamma_1$ must be retained on the right hand side of (2.31b and c). This equation can be used to find the vorticity behind a curved shock in a boundary layer where the pre-shock velocity profile is known. In terms of primitive vorticity this can be written,

$$\omega_2 = \frac{V_2}{V_1} (I_G \omega_1 + V_1 I_a S_a)$$

So that, for a **conical shock** where, $S_a = 0$, facing uniform rotational flow, we can write a primitive vorticity ratio across the shock,

$$\frac{\omega_2}{\omega_1} = \frac{V_2}{V_1} I_G \quad (3.13)$$

where $I_G = \{[AB]E_1'' + (B_2E_1' - B_2'E_1)A_2'' - (A_2E_1' - A_2'E_1)B_2''\} / \{[AB]E_2''\}$.

The above illustrates the fact that the vorticity formulas (2.31a,b,c), for calculating the vorticity downstream of a curved shock, are applicable only if the upstream flow is uniform **and** irrotational.

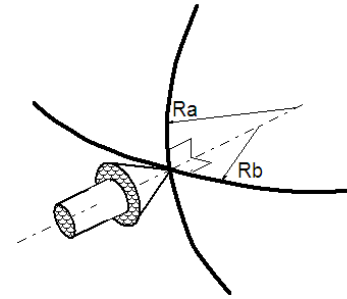
3.5 Normal shocks

This section contains an illustration of curved shock theory applied to a curved shock wave that is locally perpendicular to its upstream velocity vector. Typically, this normal shock and associated flow appear near the most forward part of a blunt object in supersonic flow ('shell-shock', Fig. 2.2) and behind the Mach stem in Mach reflection ('spoon-shock' in Fig. 2.2). For the blunt body case both curvatures S_a and S_b are negative and the corresponding radii of curvature, R_a and R_b , are positive, as shown in the sketch below. For a Mach disk both curvatures are positive. A less frequently encountered, saddle-shaped, normal shock, would have one negative and one positive curvature. Results of this section will be used to estimate the stand-off distance of a blunt body shock as well as the downstream extent of the subsonic region behind a concave, hyperbolic shock. Some results for normal shocks facing non-uniform flow are derived by allowing the upstream flow to have a pressure gradient and be curved as well so that $P_1 \neq 0$ and $D_1 \neq 0$. For a normal shock,

$$\delta_1 = \delta_2 \quad \delta = 0 \quad \theta = \pi/2 \quad (3.14)$$

Under these conditions the curved shock coefficients (2.30) become,

$$\begin{aligned}
 A_1 &= 0 \\
 E_1 &= \frac{2}{(\gamma+1)} [(\gamma-1)M_1^2 + 2] \\
 B_1 &= [\gamma + 3 - 2M_1^2] / (\gamma+1) \\
 A_2 &= 0 \\
 B_2 &= -[(\gamma-1)M_1^2 + 2] / [(\gamma+1)M_1^2] \\
 C &= 0 \\
 A'_1 &= (M_1^2 - 1) \\
 B'_1 &= E'_1 = B'_2 = G = 0 \\
 A'_2 &= -(M_1^2 - 1)[(\gamma-1)M_1^2 + 2] / [M_1^2(2\gamma M_1^2 - \gamma + 1)] \\
 C' &= -\frac{2}{(\gamma+1)} (M_1^2 - 1) / M_1^2 \\
 G' &= -\frac{2}{(\gamma+1)} (M_1^2 - 1) / M_1^2
 \end{aligned} \tag{3.15}$$

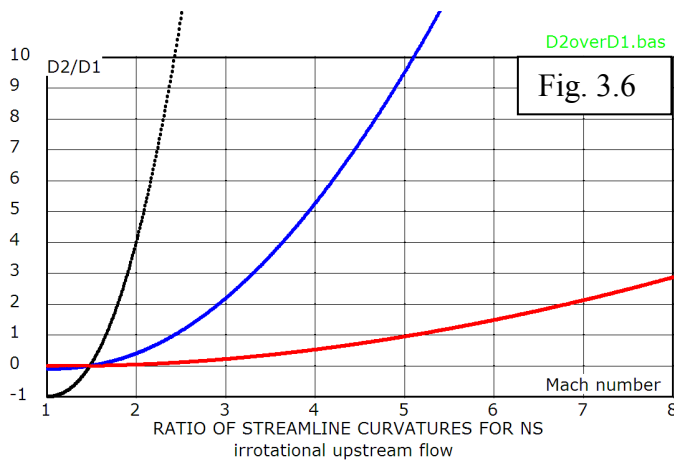


Traces of normal shock on flow- and flow-normal planes

For a **normal shock**, the *curved shock equations* reduce to,

$$\begin{aligned}
 B_1 D_1 + E_1 \Gamma_1 &= B_2 D_2 \\
 A'_1 P_1 &= A'_2 P_2 + C' S_a + G' S_b
 \end{aligned} \tag{3.16 a,b}$$

Note that the streamline curvatures, D , and the shock curvatures, S , appear separately in the above equations. The equations are thus decoupled which means that, for a normal shock, the streamline curvatures, D , and the shock curvatures, S , do not influence one another. Behind the shock, streamline curvature depends on freestream Mach number and upstream vorticity only, whereas pressure gradient depends on shock curvature. This brings about some surprising results for normal shocks at curved wall boundaries. If the



freestream is irrotational, which is a good assumption for a normal shock sitting on top of an airfoil in transonic flow, then $\Gamma_1 = 0$ and the first of these equations gives,

$$\frac{D_2}{D_1} = \frac{B_1}{B_2} = \frac{M_1^2(2M_1^2 - \gamma - 3)}{(\gamma - 1)M_1^2 + 2} \tag{3.17}$$

The black curve in Fig. 3.6 represents D_2/D_1 . To catch the rapid rise with Mach number, $(D_2/D_1)/10$ is shown by the blue curve and $(D_2/D_1)/100$ by the red curve. The normal shock is a strong amplifier of streamline curvature. From (3.17) we see further that if $D_1 = 0$ then $D_2 = 0$ also, implying that a straight streamline, entering a curved normal shock, remains straight irrespective of the shock curvature or pressure gradient or value of pre-shock Mach number as long as the pre-shock flow is irrotational. Not unreasonable, since consideration of axial symmetry has to lead to the same conclusion. If the term $\gamma + 3 - 2M_1^2 = 0$ then, for $\gamma = 1.4$, $M_1 = 1.485$ and $D_2 = 0$ for all values of D_1 . A normal shock at this Mach number, whatever its curvature, will straighten out a curved flow. A curious result. If $D_1 = D_2$ then M_1 must equal 1.662. This implies that only for this Mach number can a normal shock sit on a surface of constant curvature. Another curious and unexpected result. These anomalous results were studied by German aerodynamicists Zierrep [1958], Oswatitsch and Zierrep [1960], Gadd [1960] and others. Fung [1983] characterizes the problem by: "Such a flow is known to have a multi-valued normal pressure gradient and a stream-wise pressure gradient that is logarithmically singular". It seems that the anomaly appears only when a normal shock, at a specified pre-shock Mach number, is required to be attached to a curved wall with preset curvatures. In reality the shock is prevented from being influenced by wall curvature by the boundary layer and hence it is not constrained by Eqn. 3.18c. Away from the boundary layer the shock is free to set its own streamline curvatures according to Eqn. (3.16 a) so that no anomaly exists. No other physical descriptions have been proposed. The peculiar results are presented for awareness in case similar results appear for oblique shocks and shock reflections. From the second equation (3.16b),

$$P_2 = (A'_1 / A'_2) P_1 - (C' / A'_2) S_a - (G' / A'_2) S_b \quad (3.18 a)$$

Using the normal shock coefficients (3.15),

$$M_2^2 P_2 = -M_1^2 P_1 - \frac{2}{\gamma + 1} \{S_a + S_b\} \quad (3.18b)$$

$$P_2 = -\frac{M_1^2 (2\gamma M_1^2 - \gamma + 1)}{[(\gamma - 1)M_1^2 + 2]} P_1 - \frac{2}{\gamma + 1} \frac{(2\gamma M_1^2 - \gamma + 1)}{[(\gamma - 1)M_1^2 + 2]} \{S_a + S_b\} \quad (3.18c)$$

This can be used to obtain the pressure gradient, P_2 , behind the normal shock, in terms of the two principal radii of curvature of the shock surface and the pressure gradient in front of the shock⁸.

3.5.1 Normal shocks in uniform flow

With uniform upstream flow, Eqns. (3.16) and (3.18, b) reduce to,

$$D_2 = 0 \quad (3.19)$$

$$P_2 = \frac{2}{\gamma + 1} \frac{(2\gamma M_1^2 - \gamma + 1)}{[(\gamma - 1)M_1^2 + 2]} \left\{ \frac{1}{R_a} + \frac{1}{R_b} \right\} \quad (3.20)$$

The first of these states that behind a normal shock, in a uniform, irrotational free-stream, the streamlines are straight **no matter how the shock is curved**. The second states that the pressure gradient is proportional to the Gaussian curvature of the shock, $1/R_a + 1/R_b$. An exploding **spherical** shock, moving at Mach M_1 with radius R , has a post-shock pressure gradient given by (3.20) where $\{1/R_a + 1/R_b\}$ is replaced by $\{2/R\}$. For a **cylindrical** shock in the same situation, the $\{1/R_a + 1/R_b\}$ -term is replaced by $\{1/R\}$. For imploding shocks the gradients are negative. This equation will be applied below to find the first approximations to the shock stand off distance on a bluff body and the length of the subsonic region behind a Mach disk or Mach stem.

3.5.1.1 Blunt body with convex normal shock

We note that for a blunt body shock in a uniform freestream, where the shock curvature radii are both positive, the pressure gradient, P_2 in Eqn. (3.20) indicates an increasing pressure behind the normal shock. This is known to be the case for blunt body flow where the flow along the centre line, behind the shock, has a monotonically increasing pressure, eventually stagnating, on the body, at a pressure higher than that immediately behind the shock. From M_1 and p_1 we can readily calculate p_2 , the pressure

⁸ It is a result of differential geometry that the quantity $1/R_a + 1/R_b$ remains a constant on a curved surface no matter in what planes the radii lie as long as the planes are orthogonal. [Kreyszig, 1991]. This must be so since the orientation of coordinate planes can not influence the pressure gradient or any other physical variable at the shock surface.

behind the shock and p_{t2} , the pressure at the stagnation point (pitot pressure). This leads to a first approximation for the shock stand-off distance, Δ , from,

$$P_2 \approx \frac{p_{t2} - P_2}{\rho_2 V_2^2 \Delta} \quad (3.21)$$

This is a linear approximation to the pressure gradient over Δ and, for axial flow, can be written,

$$\frac{\Delta}{R} = \frac{(\gamma - 1)}{2\gamma} \left[\left(\frac{(\gamma + 1)^2 M_1^2}{4\gamma M_1^2 - 2(\gamma - 1)} \right)^{\frac{\gamma}{\gamma - 1}} - 1 \right] \quad (A)$$

and for planar flow

$$\frac{\Delta}{R} = \frac{(\gamma - 1)}{\gamma} \left[\left(\frac{(\gamma + 1)^2 M_1^2}{4\gamma M_1^2 - 2(\gamma - 1)} \right)^{\frac{\gamma}{\gamma - 1}} - 1 \right] \quad (B)$$

Another approach to obtaining the stand off distance is to assume that the average **velocity** gradient between the shock and the stagnation point is the same as the post-shock velocity gradient, i.e., $\frac{0 - V_2}{\Delta} = \left(\frac{\partial V}{\partial s} \right)_2$ so that $\frac{1}{\Delta} = -\frac{1}{V_2} \left(\frac{\partial V}{\partial s} \right)_2 = P_2$ and $P_2 \times \Delta = 1$

Using (3.20) for **axial flow**, where $2/R = 1/R_a + 1/R_b$ produces,

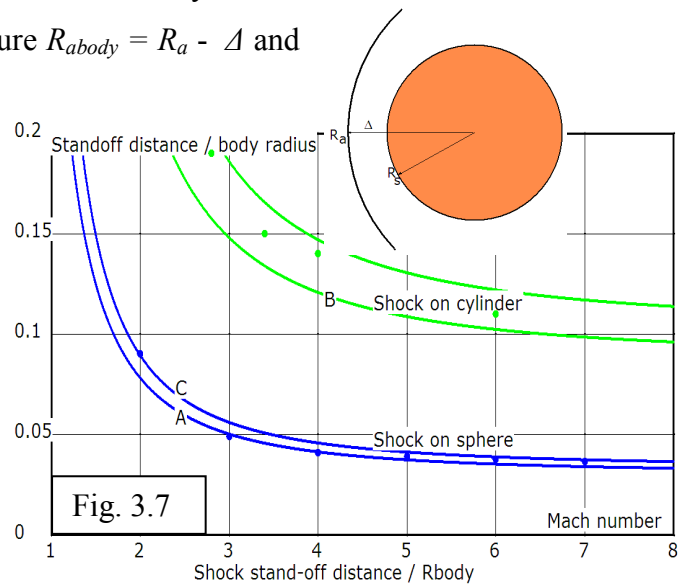
$$\frac{\Delta}{R} = \frac{\gamma + 1}{4} \frac{[(\gamma - 1)M_1^2 + 2]}{(2\gamma M_1^2 - \gamma + 1)} \quad (C)$$

A very similar result for **planar flow**, where $R_b = 0$ and $1/R = 1/R_a$, is,

$$\frac{\Delta}{R} = \frac{\gamma + 1}{2} \frac{[(\gamma - 1)M_1^2 + 2]}{(2\gamma M_1^2 - \gamma + 1)} \quad (D)$$

These formulas are plotted in Fig. 3.7. Most published data on the shock stand off distance is in terms of the body radius R_s and not the shock radius R_a , as used above. To facilitate comparison, we have plotted against body surface radius R_s , assuming that $R_s = R_a - \Delta$. This is a reasonable approximation especially for axial flow at high Mach numbers where the shock lies close to the body surface. Data points are from various sources found in [Liepmann and Roshko, Fig.4.15, 1956]. Except at low Mach numbers there is reasonable agreement with experiment and other theories.

We have here derived a simple equation for the stand off distance of a shock on a sphere or a cylinder from general curved shock wave theory. However, we started with the more general, doubly curved, normal shock having two differing curvature radii R_a and R_b , as in Eqn. (3.20). Such a shock would be carried by a nose cap body having two differing radii of curvature $R_{abody} = R_a - \Delta$ and $R_{bbody} = R_b - \Delta$, at least to the first approximation. If analytic continuation holds between the axial and planar results then the theory should predict shock stand-off distances for intermediate blunt bodies with elliptic cross-sections with differing curvature radii. Experimental results of stand off distance have not been found in the literature for such shapes.



For concave shocks Eqn. (3.20) indicates a negative post-shock pressure gradient. Normal shocks with negative (concave) curvature are discussed in the next section.

3.5.1.2 Flow behind a normal shock at a concave Mach disk

For an axisymmetric Mach disk with radius of curvature $R = R_a = R_b$, in a uniform freestream, Eqn. (3.20) gives a direct relationship between the radius of curvature of the disk and the pressure gradient behind the disk,

$$P_2 = \frac{4}{\gamma+1} \frac{(2\gamma M_1^2 - \gamma + 1)}{[(\gamma-1)M_1^2 + 2]} \left\{ \frac{1}{R} \right\} \quad (3.21)$$

Which can also be written in terms of M_2 ,

$$P_2 = \frac{4}{(\gamma+1)M_2^2 R} \quad (3.22)$$

P_2 is defined as,

$$P_2 = \frac{(dp/ds)_2}{\rho_2 V_2^2} = \frac{(dp/ds)_2}{\gamma p_2 M_2^2} \quad (3.23)$$

Eliminating P_2 and M_2 ,

$$\frac{dp}{p} = \frac{4\gamma}{(\gamma+1)} \frac{ds}{R} \quad (3.24)$$

In the isentropic flow behind the Mach disk the Mach number and pressure are related by, [Shapiro, 1954],

$$\frac{dM}{M} = -\frac{1 + \frac{(\gamma-1)}{2}M^2}{\gamma M^2} \frac{dp}{p} \quad (3.25)$$

Eliminating dp/p , and separating variables gives,

$$\frac{MdM}{1 + \frac{(\gamma-1)}{2}M^2} = -\frac{4}{\gamma(\gamma+1)} \frac{ds}{R} \quad (3.26)$$

Integrating, with the conditions that $M = M_2$ at $s = 0$ and $M = 1$ at $s = s^*$ gives,

$$\frac{s^*}{R} = \frac{\gamma+1}{4(\gamma-1)} \ln \left[\frac{2}{(\gamma+1)} \left(1 + \frac{(\gamma-1)}{2} M_2^2 \right) \right] \quad (3.27)$$

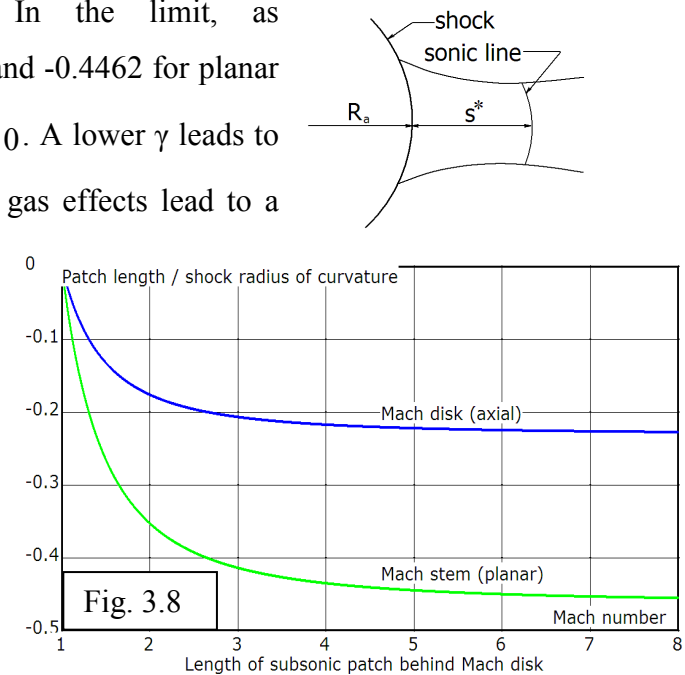
In terms of the freestream Mach number this becomes,

$$\frac{s^*}{R} = \frac{\gamma+1}{4(\gamma-1)} \ln \left[\frac{(\gamma+1)M_1^2}{2\gamma M_1^2 - (\gamma-1)} \right] \quad (3.28)$$

This equation gives the length of the subsonic patch, s^* , behind the axisymmetric Mach disk, in terms of the shock curvature radius (R is negative) and the freestream Mach number. The formula is plotted in Fig. 3.8 as a blue line. This is a unique result which could be useful in designing axial flows with convergent shocks. It points to the possibility of first constructing a shock structure in Mach reflection and then building the supersonic flow around it. Results of Eqn. (3.28) need to be compared against CFD and experiment.

For **planar flow** the shock has only a single curvature, R , where $1/R = 1/R_a$, showing that the subsonic region in planar flow is twice as long as in axial flow. This is reasonable since flow convergence for planar flow takes place from two sides whereas axial flow converges from all four sides, leading to sonic flow in a shorter distance. The planar flow equation is plotted in Fig. 3.8 as a green line. The above results will be used to provide the length of the subsonic region behind hyperbolic shocks in Ch. 5. The ratio of patch length to shock curvature reaches a finite limit for both a hypersonic freestream as well as a sonic freestream. In the limit, as $M_1^2 \rightarrow \infty$, $s^*/R \rightarrow -0.2231$ for axial flow and -0.4462 for planar flow. For both cases, as $M_1 \rightarrow 1$, $s^*/R \rightarrow 0$. A lower γ leads to a longer patch length suggesting that real gas effects lead to a

longer patch length for the same shock radius of curvature. As for the blunt body example above, Eqn. (3.20), used above to estimate the subsonic patch length for axial Mach disks and planar Mach stems, can also be used to estimate s^* for a concave shock having two differing curvatures. . In such a case the sonic surface would not be circular but somewhat elliptic in shape. For a **flat normal shock** where $R_a = R_b = \infty$,



$$P_2 / P_1 = -M_1^2 / M_2^2 \quad (3.29)$$

Since M_1 is always greater than M_2 , a flat normal shock amplifies and reverses the normalized pressure gradient. Shocks of equal but opposite curvature do so also and, not unexpectedly, a flat normal shock in uniform flow has no pressure gradient behind it. This concludes the application of *curved shock theory* to curved and plane **normal** shocks.

3.5.1.3 Blunt leading edge with sweep

A supersonic airfoil profile appears thinner to the approaching airflow if the wing is swept back. Making supersonic airfoil profiles appear thinner leads to a decrease in wave-drag. Sweep-back also lessens heat transfer to leading edges of hypersonic air intakes, promotes weaker leading edge shocks and leads to a higher compression efficiency of the internal intake flow. Flow near the leading edge of such swept leading edges is the same as that over a swept cylinder and, in any plane normal to the axis of the cylinder, behaves as if the cylinder were placed normal to an air flow with Mach number $M \sin \Lambda$ where M is the freestream Mach number and Λ is the sweep angle. If, in this *normal plane*, the leading edge curvature is, S_c , then the shock stand off distance, Δ , and curvature S_b can be found, with reasonable accuracy, from Billig's correlation [Billig, 1967]. For constant sweep at the leading edge of the shock $S_a = 0$ giving the curved shock equations,

$$\begin{aligned} 0 &= A_2 P_2 + B_2 D_2 + G S_b \\ 0 &= A'_2 P_2 + B'_2 D_2 + G' S_b \end{aligned} \quad (3.30)$$

such that behind the leading edge of the swept shock the pressure gradient and streamline curvature are given by (note that G is zero),

$$P_2 = \frac{B_2 G'}{[AB]} S_b \quad \text{and} \quad D_2 = \frac{-A_2 G'}{[AB]} S_b \quad (3.31)$$

This is a type of conical flow in that there is no variation of conditions along the leading edge. Not surprisingly, the polar streamline slope is the same as that for the cone [Eqn. (2.40)],

$$\frac{P_2}{D_2} = -\frac{B_2}{A_2} \quad (3.32)$$

Morphologically this flow lies on the negative S_b axis in Figure 2.2. If the sweep angle

varies along the leading edge so that at any point the lateral curvature is S_d and if $S_d \ll S_c$ then the local flow is again invariant in the spanwise direction so that along the shock ridge,

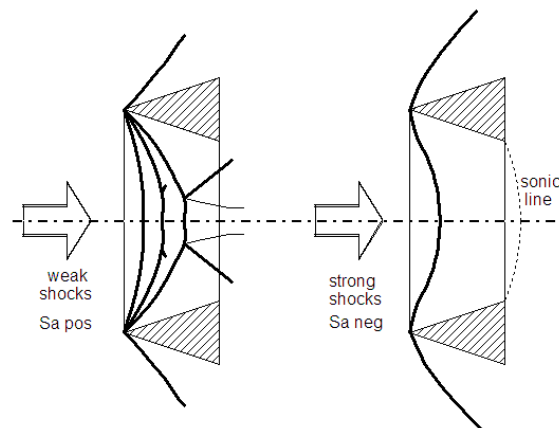
$$P_2 = \frac{[BC]}{[AB]} S_d + \frac{B_2 G'}{[AB]} S_c \quad \text{and} \quad D_2 = \frac{[CA]}{[AB]} S_d - \frac{A_2 G'}{[AB]} S_c \quad (3.33)$$

If the leading edge sweep is decreasing then $S_a > 0$ and the shock is ‘saddle’ shaped appearing in the fourth quadrant in Figure 2.2. If the leading edge sweep increases then $S_a < 0$ and the shock is ‘shell’ shaped, appearing in the third quadrant.

The above has shown how the pressure gradient and streamline curvature behind a swept leading edge shock can be found from the freestream Mach number, the sweep angle and the two leading edge curvatures. The shock on a swept blunt leading edge is three-dimensional in that it has two finite curvatures. However, there is locally no change in the shock angle in the cross-stream direction so that the trace bb (Fig. 2.1) is perpendicular to the freestream vector. This makes CST applicable locally for this 3D shock shape. The shock is a ridge in the flow plane. Equally well, CST would be applicable behind a left-right symmetric col-shaped shock. The critical feature that makes CST applicable in both of these cases is that $R_b = -1/S_b$ (Fig. 2.1) stays constant along the bb trace.

3.6 Shocks on a circular wedge-annulus; $D_2 = 0$, (a.k.a. *Unit Ring - Wedge*)

Conical flow does not generally flow over conical surfaces and conical surfaces do not always produce conical flow. In this section we find the flow gradients behind shocks attached to the leading edges of conical ducts (no streamwise surface curvature) and we find that the flow does not possess conical symmetry. The circular wedge, or conical duct, on the right, presents examples of flow over external and internal truncated conical



Attached weak and strong shocks on axisymmetric ring-wedge

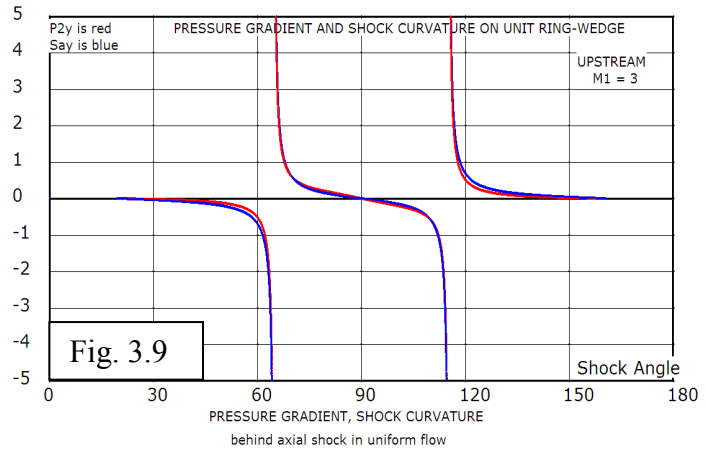
surfaces. An axisymmetric engine cowl leading edge is a typical example where attached shocks appear on the external as well as the internal surfaces and where the surfaces are not necessarily curved in the flow direction. For such flow the streamline curvature behind the shock, at the surface, is zero, so that $D_2 = 0$. The transverse shock curvature is $S_b = -\cos\theta / y$, where θ is the shock angle and y is the leading-edge radius of the ring-wedge.⁹ Note that for weak acute shocks (external flow), S_b is negative while, for obtuse angled shocks (internal flow), S_b is positive. For a uniform, parallel, irrotational, freestream and $D_2 = 0$, the *curved shock equations* reduce to,

$$\begin{aligned} 0 &= A_2 P_2 + C S_a \\ 0 &= A_2' P_2 + C' S_a + G' S_b \end{aligned} \quad (3.34)$$

From these we find the pressure gradient on the ring-wedge surface and the shock curvature at the leading edge,

$$P_2 = \frac{CG' \cos\theta / y}{|CA|} \quad S_a = \frac{-A_2 G' \cos\theta / y}{|CA|} \quad (3.35a,b)$$

$P_2 y$ and $S_a y$ are plotted in Fig. 3.9 showing the effects of varying the shock angle on a surface that has only lateral curvature. At the Crocco point, where $|CA| = CA_2' - C'A_2 = 0$, both the pressure gradient and the shock curvature become infinite and switch sign. Some authors have suggested that the shock will detach from the leading edge at this condition. [Guderley, 1962]. CFD will be used in Ch. 6 to simulate attached shock



behaviour at the leading edge of a ring-wedge at conditions corresponding to the Crocco point. This will be done by varying the freestream Mach number through the Crocco point on a fixed angle ring-wedge. Equally interesting would be to vary the axisymmetric ring-wedge angle through the Crocco point at constant Mach number. The

⁹ A ring-wedge with $y = 1$ is called a *unit ring-wedge*. This is the scale length referred to in Chapter 2.

latter is easier to do computationally than with a ‘solid’ model in a wind tunnel. Even computationally it may not be that easy because the Crocco point lies close to the shock detachment point. CFD results of flow over and inside the ring-wedge are presented in Ch. 6.

3.7 Shock surfaces with up- or downstream uniformity

In aeronautical flight application the flow conditions upstream of the shock are most often uniform, irrotational and the coordinate axis is aligned with the freestream so that $\delta_1 = 0$. In an airbreathing engine the combustor requirements may be such as to require uniform flow from the last shock in the intake. For shock reflections off a plane wall the flow emerging from the reflected shock must be parallel to the wall and must have no curvature so that $\delta_2 = 0$ and $D_2 = 0$. Also, for shock reflection, the polar streamline direction behind the incident shock must equal the polar streamline direction in front of the reflected shock. This makes it important to have analytical tools suitable for uniform flows on the upstream and downstream surfaces as well as for prescribed non-uniform conditions. Shocks with no downstream pressure gradient and with straight streamlines will be studied in what follows.

3.7.1 Doubly curved Thomas and Crocco shocks

Consider a shock in uniform, irrotational upstream flow that is doubly curved so that neither S_a nor S_b is zero. For these conditions the *curved shock equations* reduce to,

$$\begin{aligned} 0 &= A_2 P_2 + B_2 D_2 + C S_a \\ 0 &= A'_2 P_2 + B'_2 D_2 + C' S_a + G' S_b \end{aligned} \quad (3.36)$$

Solving these for pressure gradient and flow curvature,

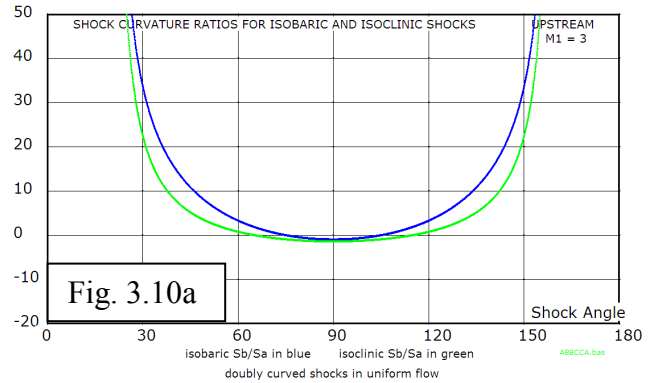
$$\begin{aligned} P_2 &= \frac{[BC]}{[AB]} S_a + \frac{B_2 G'}{[AB]} S_b \\ D_2 &= \frac{[CA]}{[AB]} S_a - \frac{A_2 G'}{[AB]} S_b \end{aligned} \quad (3.37 \text{ a,b})$$

If the pressure gradient behind the shock is zero then, setting $P_2 = 0$ in Eqn. (3.33 a)

gives,
$$\mathcal{R}_p \equiv \left(\frac{S_a}{S_b} \right)_p = - \frac{B_2 G'}{[BC]} \tag{3.37 c}$$

so that for this shock curvature ratio we can expect to find a space behind the doubly curved shock with relatively constant pressure. Such a point on the shock wave is called a Thomas or an *isobaric point* and the relation expressed by Eqn. (3.37 c) is the *isobaric condition*. For planar flow, where $S_b = 0$,

the isobaric condition occurs when either the shock is flat, $S_a = 0$, or at the Thomas point. Recall that, for planar flow, the Thomas and Crocco conditions are defined by $[BC] = 0$ and $[CA] = 0$ respectively. At the Thomas condition, where $[BC] = 0$ on a doubly

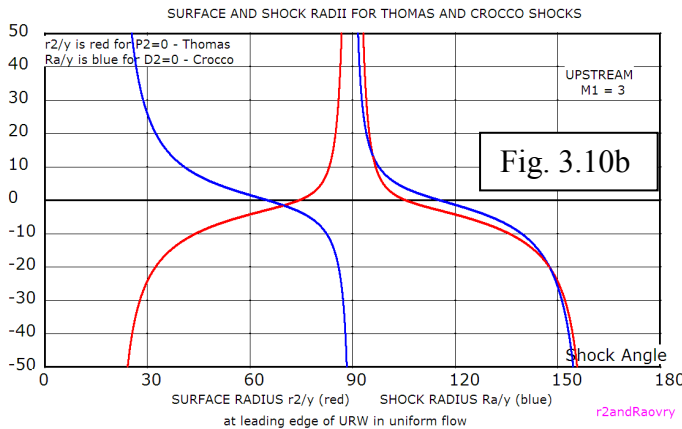


curved shock, the pressure gradient is not generally zero but equal to $\{B_2 G' / [AB]\} S_b$. It is only for a planar shock that the pressure gradient is zero at the Thomas condition.

From Eqn. (3.33 b), setting $D_2 = 0$ for straight streamlines behind the shock, gives,

$$\mathcal{R}_D \equiv \left(\frac{S_a}{S_b} \right)_D = \frac{A_2 G'}{[CA]} \tag{3.37d}$$

so that for this shock curvature ratio we can expect a space behind the doubly curved shock to have straight streamlines. Such a point on the shock wave is called a Crocco or an *isoclinic point* and the



relation expressed by equation (3.33d) is the *isoclinic condition*. For planar flow, where $S_b = 0$, the isoclinic condition occurs either when the shock is flat or at the Crocco point.

At a given γ , Mach number and shock angle the isobaric or isoclinic shock surface can be established by proper choice of shock curvature ratio as shown in Figures 3.10a and b. Fig. 3.10b shows what the URW leading edge radius of curvature r_2 must be to obtain a zero pressure gradient on the URW surface at any acute or obtuse shock angle. Similarly the shock radius of curvature, S_a , is plotted to show what the curvature must be to obtain a surface of zero curvature.

For shocks with axial symmetry in a parallel upstream flow,

$$S_a = \frac{d\theta}{d\sigma} = \frac{d\theta}{dy} \frac{dy}{d\sigma} = \frac{d\theta}{dy} \sin\theta$$

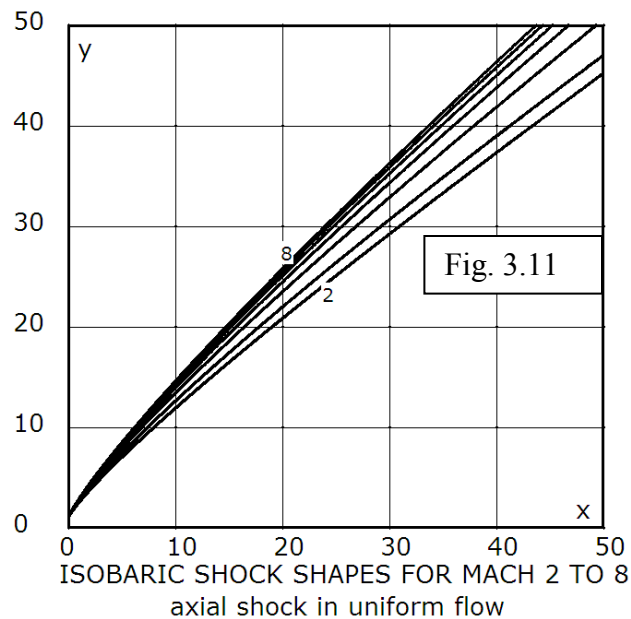
$$S_b = -\cos\theta / y$$

For an isobaric shock where $P_2 = 0$, using Eqn. (3.33 a),

$$\frac{dy}{y} = -\frac{[BC]}{B_2 G'} \tan\theta d\theta \quad (3.38)$$

This is a total differential equation where the two variables y and θ have been separated so that a simple numerical integration is possible for the shock shape, $y = f(\theta)$, giving a shock shape that is such that the pressure gradient behind it is everywhere zero. Equation (2.11)

implies that if the pressure gradient is zero then so is the velocity gradient and then Eqn. (2.13.a) requires that the enthalpy (temperature) gradient is zero also. It follows then that the Mach number gradient is also zero. The isobaric shock then is a surface that produces zero gradients not only in pressure but also in velocity, temperature and Mach number. With both pressure and temperature gradients being zero, it must be that the density gradient is zero also. Thus the isobaric shock is a particular shock shape that produces zero stream-wise gradients in most thermodynamic and dynamic variables. The isobaric shock is plotted in Fig. 3.11 for a range of Mach numbers from 2 to 8. Both acute and



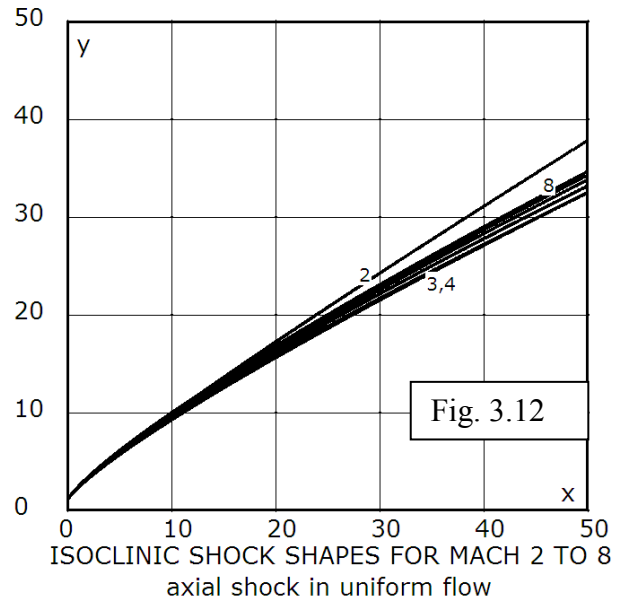
obtuse axisymmetric isobaric shocks can be produced. In planar flow there can be no isobaric shock surface, only an isobaric point at the Thomas shock angle.

A treatment that parallels that for the axisymmetric **isobaric** shock surface gives the equation for the axisymmetric **isoclinic** shock surface that has straight streamlines behind it everywhere. Requiring that $D_2 = 0$ in Eq. (2.67b) gives,

$$\frac{dy}{y} = -\frac{[CA]}{A_2 G'} \tan \theta d\theta \quad (3.39)$$

The expressions on the right hand sides of (3.38) and (3.39) are complicated functions of θ and have to be integrated numerically. The isoclinic shock profile, Fig. 3.12, is very similar to that for the isobaric shocks. Both acute and obtuse shocks can be produced. The body shapes that produce these shocks are axisymmetric. Finding body shapes involves some kind of finite difference approach that proceeds from the shock towards the body surface. Such calculations are sometimes *badly posed* in that the body surface is not necessarily unique; it may contain folds and cusps or it may not exist at all.

Isobaric and isoclinic shocks are dealt with here because, as incident shocks, they present unique flows to any potential reflected shocks. For example, if the $RR \rightarrow MR$ transition is thought to be influenced by pressure gradient or streamline curvature, then, by using incident isobaric and isoclinic shocks, it is possible to study transition when these gradients are absent, the notion being that, if neither pressure gradient nor streamline curvature is present, then there ought to be no effect of shock curvature on transition. Or, even further, if the gradients produced by the incident shock favour attachment of the reflected shock then transition ought to be delayed by their absence and conversely. It is important to realize that the isobaric and isoclinic-points can be made to lie anywhere behind the shock where the shock curvature ratio is such as to satisfy (3.37 c) for the isoclinic point and (3.37 d) for the isobaric point. It is only for planar flow that



the isoclinic point lies between the sonic point and the maximum deflection point and the isobaric point lies behind the strong shock between the maximum deflection and normal shock points.

3.7.2 Polar streamline slope for shocks with upstream uniformity

Equations for polar streamline slopes were presented in sections 2.4.4 and 2.5.3 for flow behind planar and conical shocks in a uniform freestream. Equations are presented here for shocks with compound curvature, also in a uniform freestream. Using equations (3.37 a) and (3.37 b), the polar streamline slope is,

$$\frac{P_2}{D_2} = \frac{[BC]S_a + B_2G'S_b}{[CA]S_a - A_2G'S_b} = \frac{[BC]\mathcal{R} + B_2G'}{[CA]\mathcal{R} - A_2G'} \quad (3.40)$$

This relation shows that, for a doubly curved shock, the polar streamline slope is a function of the upstream Mach number, the shock angle, and the ratio of shock curvatures. Any value of polar streamline slope between $-\infty$ and $+\infty$ can be obtained with a suitable choice of \mathcal{R} at a given Mach number and shock wave angle. Hornung [1997] has argued that the stability of steady-flow regular and Mach reflection is associated with the slope of the reflected shock pressure-deflection polar locus at the point where the locus intersects the pressure axis.

3.7.3 Polar streamlines for uniform post-shock flow

All examples of CST applications, presented so far, have involved either uniform or specified pre-shock flow as is the case for most aeronautical applications. However, in situations such as the design of air intakes it is useful to be able to specify the downstream or post-shock conditions, as determined by the combustor requirements. Typically, a **uniform** downstream flow is desired and specified as for Busemann flow in Ch. 4. If, in addition, the pre-shock flow is irrotational, such that $\Gamma_1 = 0$, then the two curved shock equations 2.30 a,b become,

$$\begin{aligned} A_1P_1 + B_1D_1 - (CS_a + GS_b) &= 0 \\ A'_1P_1 + B'_1D_1 - (C'S_a + G'S_b) &= 0 \end{aligned} \quad (3.41)$$

Solving these for P_1 and D_1 ,

$$P_1 = \frac{-B_1(C'S_a + G'S_b) + B'_1(CS_a + GS_b)}{A_1B'_1 - A'_1B_1} \quad (3.42)$$

$$D_1 = -\frac{-A_1(C'S_a + G'S_b) + A'_1(CS_a + GS_b)}{A_1B'_1 - A'_1B_1}$$

The polar streamline slope is then,

$$\bar{l} = \frac{P_1}{D_1} = -\frac{-B_1(C'\mathcal{R} + G') + B'_1(C\mathcal{R} + G)}{-A_1(C'\mathcal{R} + G') + A'_1(C\mathcal{R} + G)} \quad (3.43)$$

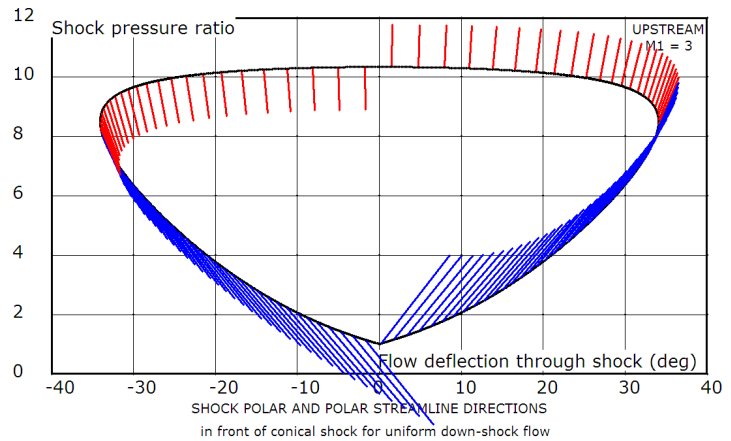
This is for the polar streamline in front of the shock. The over-bar is to distinguish the present l from the previous l which was for the **post-shock** polar streamline for a uniform **upstream** flow. For a planar shock, $\mathcal{R} \rightarrow \infty$ so that,

$$\bar{l}_{planar} = -\frac{-B_1C' + B'_1C}{-A_1C' + A'_1C} \quad (3.44a)$$

For a conical shock $\mathcal{R} = 0$,

$$\bar{l}_{conical} = -\frac{-B_1G' + B'_1G}{-A_1G' + A'_1G} \quad (3.44b)$$

The polar streamline slopes in the pre-shock flow, as given by Eqn. (3.44b) are shown on the $(p-\delta)$ shock polar as coloured line segments. Blue segments indicate supersonic post-shock flow and red segments indicate subsonic post-shock flow. The right half of the graph is for the acute Busemann shock and the left half is for the obtuse W-flow shock, both having uniform post-shock flow. Busemann and W-flows are discussed further in Ch. 4. If the acute shock is thought of as representing a reflected shock then its pre-shock streamline slope will have to match the post-shock streamline slope of an obtuse incident shock.



3.7.4 Conditions behind a reflected shock

The conditions P_2 , D_2 and Γ_2 , behind a curved **incident** shock, facing a uniform stream, are found from (3.12 a and b) and (2.31 c). These conditions now become the pre-shock conditions P_1 , D_1 and Γ_1 for the **reflected** shock. If the reflection takes place on a surface that has no streamwise curvature ($D_2 = 0$, a flat wall or a straight tube) the transverse curvature of the reflected shock is $S_b = -\cos(\theta - \delta)/y$ and then the curved shock equations for the reflected shock are Eqns. (2.30 a and b),

$$\begin{aligned} L_1 &= A_1 P_1 + B_1 D_1 + E_1 \Gamma_1 = A_2 P_2 + C S_a + G S_b \\ L'_1 &= A'_1 P_1 + B'_1 D_1 + E'_1 \Gamma_1 = A'_2 P_2 + C' S_a + G' S_b \end{aligned} \quad (3.45)$$

These are two simultaneous equations for P_2 and S_a . It will be shown in Ch. 6 that the pressure gradient, P_2 , plays a critical role in causing shock detachment from a wedge by *local choking*. It remains to be shown that the analogous RR→MR transition is similarly affected by the pressure gradient as calculated from Eqn. (3.45). The lateral surface curvature, S_b , will then have an influence on the transition. In a like manner a specified flow-wise curvature, D_2 , different from zero, would affect the pressure gradient and hence, detachment, directly.

3.8 Curvature and strength of characteristics

Shock waves form when compressive characteristics overtake one another. To determine if there exist regions behind a curved shock where there is a tendency for an embedded reflected shock to form we seek characteristics with positive strength (compressive) and positive curvature when acute and negative when obtuse, so as to be overtaking one another. Tools presented here are applied to the hyperbolic shock wave in Ch. 5.

3.8.1 Curvature of characteristics

Let the curvatures of the C^+ and C^- characteristics be denoted by S_a^+ , S_b^+ , S_a^- and S_b^- . As before, the a-subscript is for curvature in the flow plane and the b-subscript is for curvature in the flow-normal plane. The C^+ and the C^- characteristics are inclined at

$+\mu$ and $-\mu$ to the local streamline. In the weak shock limit, shocks become Mach waves or characteristics so that,

$$\begin{aligned} \delta &= 0 & \delta_2 &= \delta_1 & M_1 &= M_2 = M \\ q_2 / q_1 &= 1 & \theta &= \pm \mu \\ \sin \theta &= \pm 1 / M & \cos \theta &= \pm \sqrt{M^2 - 1} / M \\ \sin 2\theta &= \pm 2\sqrt{M^2 - 1} / M^2 & \cos 2\theta &= (M^2 - 2) / M^2 \end{aligned} \quad (3.46)$$

In reference to the characteristics on the downstream side of the shock, M is the Mach number on the back of the supersonic portion of the shock. With these limiting conditions the *shock curvature coefficients*, (2.30c), become the ***characteristics' curvature coefficients***,

$$\begin{aligned} A_1 &= \pm \frac{2\sqrt{M^2 - 1}}{(\gamma + 1)M} \left(3 - 4 / M^2 - (\gamma - 1) / 2 \right) \\ B_1 &= \pm \frac{2}{(\gamma + 1)M} \left(\frac{\gamma - 5}{2} + \frac{4 - M^2}{M} \right) \\ E_1 &= \pm \frac{2}{(\gamma + 1)M} \left(\gamma - 1 + \frac{2}{M^2} \right) \\ A_1' &= 2(M^2 - 1) / M^2 \\ B_1' &= -2\sqrt{M^2 - 1} / M^2 \\ (3.47) \\ A_2 &= \pm \sqrt{M^2 - 1} / M^2 \\ B_2 &= -1 / M^2 \\ E_1' &= 0 \\ C &= \pm 4\sqrt{M^2 - 1} / [(\gamma + 1)M^2] \\ G &= \pm 4\sqrt{M^2 - 1} \sin \delta_1 / [(\gamma + 1)M^3] \\ A_2' &= 2(M^2 - 1) / M^2 \\ B_2' &= \pm 2\sqrt{M^2 - 1} / M^2 \\ C' &= 0 \\ G' &= 0 \end{aligned} \quad (3.47)$$

so that,

$$[AB]=0; \quad [BC]=-\frac{8}{(\gamma+1)}\frac{M^2-1}{M^4}; \quad [CA]=\mp\frac{8}{(\gamma+1)}\frac{(M^2-1)^{3/2}}{M^4}$$

The upper sign of \pm or \mp is used with S_a^+ and S_b^+ and the lower sign is used with S_a^- and S_b^- . The subscript 1 variables, in the curved shock equations, are all relevant because the characteristics are facing non-uniform flow behind a curved shock. For axisymmetric flow,

$$S_b^\pm = -\cos(\mu - \delta) / y = \mp \frac{\sqrt{M^2 - 1}}{My} \quad (3.48)$$

Except for G , the characteristics' curvature coefficients are all functions of the local Mach number only. For the curved characteristics, using the above coefficients, the *curved shock equations*, (2.30 a,b) become,

$$\begin{aligned} A_1 P_1 + B_1 D_1 + E_1 \Gamma_1 &= A_2 P_2 + B_2 D_2 + C S_a^\pm + G S_b^\pm \\ A'_1 P_1 + B'_1 D_1 &= A'_2 P_2 + B'_2 D_2 \end{aligned} \quad (3.49)$$

If we apply these to finding the curvature of a characteristic on the downstream side of a shock then P_1 , D_1 and Γ_1 are the pressure gradient, streamline curvature and vorticity on the downstream side of the shock, as determined by the shock's curvature, and P_2 and D_2 are the pressure gradient and streamline curvature on the downstream side of the characteristic. From Eq. (3.49),

$$P_2 - P_1 = \pm (M^2 - 1)^{-1/2} (D_2 - D_1) \quad (3.50)$$

This shows that, across a characteristic, both streamline curvature and pressure gradient can be discontinuous and that the discontinuities are linearly related in proportions determined by the local Mach number. Note that the upper sign of \pm OR \mp is used with the C^+ characteristic and the lower sign with the C^- characteristic. Dividing Eqn. (3.50) by $2\sqrt{M^2 - 1}$ gives,

$$\frac{A'_1 P_1}{2\sqrt{M^2 - 1}} + \frac{B'_1 D_1}{2\sqrt{M^2 - 1}} = \frac{A'_2 P_2}{2\sqrt{M^2 - 1}} + \frac{B'_2 D_2}{2\sqrt{M^2 - 1}} \quad (3.51)$$

Subtracting Equations (3.51) and (3.50) gives,

$$S_a^\pm + S_b^\pm \sin \delta_1 = \frac{[(7-\gamma)M^2 - (\gamma+1)M - 8]}{[4M\sqrt{M^2-1}]} \left[\frac{\sqrt{M^2-1}P_1 \pm D_1}{\sqrt{\quad}} \right] \sqrt{\quad} \quad (3.52)$$

S_a^\pm and S_b^\pm are the curvatures of either the positive or negative characteristic depending on whether the upper or lower sign is used in the above equation. The subscript 1 denotes conditions immediately in front of the characteristic and, for the flow on the back side of a shock, M , P_1 and D_1 are then the values behind the shock, produced by the shock. If the flow is parallel to the axis then δ_1 is zero so that S_a^\pm can be determined from a knowledge of M , P_1 , and D_1 . Axisymmetric flow behind a regularly reflecting shock on a straight cylinder has both δ_1 and D_1 equal zero so that The C^+ and C^- characteristics have the same curvature in the flow behind the reflected shock. It is interesting to note that, for $\gamma = 1.4$ the term in the numerator $[(7-\gamma)M^2 - (\gamma+1)M - 8]$ is zero when $M = 1.4286$, so that the characteristic's curvatures are then very simply related by $S_a^\pm + S_b^\pm \sin \delta_1 = 0$. This is another example where *curved shock theory* yields a singular Mach number with curious properties. For axisymmetric flow $S_b^\pm = -\cos(\mu \pm \delta) / y$ so that the curvature of the characteristics in the flow plane is,

$$S_a^\pm = \frac{(7-\gamma)M^2 - (\gamma+1)M - 8}{4M\sqrt{M^2-1}} \left[\frac{\sqrt{M^2-1}P_1 \pm D_1}{\sqrt{\quad}} \right] + \sin \delta_1 \cos(\mu \pm \delta_1) / y \quad (3.53)$$

3.8.2 Strength of characteristics

In this section we define the strength of one characteristic as the pressure gradient in the direction of the other characteristic. This leads to a convenient formulation in terms of the local stream-wise pressure gradient and flow curvature. Using the formulas 2.42 for the gradients on the downstream side of a doubly curved shock gives the strengths of the incident and reflected characteristics and their ratio behind a shock - the *reflection coefficient*. The reflection coefficient has been used to gauge the strength of waves emanating from the back side of a curved shock as they hit the aft portions of a supersonic vehicle [Chernyi, 1961; Hayes and Probstein, 1966]. If the reflections are weak then it is possible to apply such approximate techniques as Shock-Expansion,

Tangent-Wedge and Tangent-Cone theory to the calculation of flow fields between body and shock.

The variation of any quantity across the C^+ characteristic, in the direction of the C^- characteristic, is,

$$\frac{\partial \bullet}{\partial \eta^-} = \cos \mu \frac{\partial \bullet}{\partial s} + \sin \mu \frac{\partial \bullet}{\partial n} \quad (3.54)$$

where η^- is the distance along the C^- characteristic and μ is the angle between the characteristic and the streamline. Similarly for the C^+ characteristic,

$$\frac{\partial \bullet}{\partial \eta^+} = \cos \mu \frac{\partial \bullet}{\partial s} - \sin \mu \frac{\partial \bullet}{\partial n} \quad (3.55)$$

Using these, we define the strengths of the C^+ and C^- characteristics in terms of their cross-characteristic pressure variation as,

$$\begin{aligned} \pi^+ &\equiv \frac{1}{\rho V^2} \frac{\partial p}{\partial \eta^-} = \frac{\cos \mu}{\rho V^2} \frac{\partial p}{\partial s} + \frac{\sin \mu}{\rho V^2} \frac{\partial p}{\partial n} \\ \pi^- &\equiv \frac{1}{\rho V^2} \frac{\partial p}{\partial \eta^+} = \frac{\cos \mu}{\rho V^2} \frac{\partial p}{\partial s} - \frac{\sin \mu}{\rho V^2} \frac{\partial p}{\partial n} \end{aligned} \quad (3.56 \text{ a,b})$$

π will be positive/negative for a compressive/expansive characteristic. Using Eqns. (2.16) and (2.17) these can be written in terms of the local pressure gradient and streamline curvature as,

$$\begin{aligned} \pi^+ &= \frac{1}{M} \left[\sqrt{M^2 - 1} P - D \right] \\ \pi^- &= \frac{1}{M} \left[\sqrt{M^2 - 1} P + D \right] \end{aligned} \quad (3.57 \text{ a,b})$$

These expressions are general in that they apply wherever the Euler equations are applicable.

3.8.3 Reflection Coefficient

The relative strength of the characteristics is,

$$\lambda \equiv \frac{\pi^+}{\pi^-} = \frac{\sqrt{M^2 - 1} P - D}{\sqrt{M^2 - 1} P + D} \quad (3.58)$$

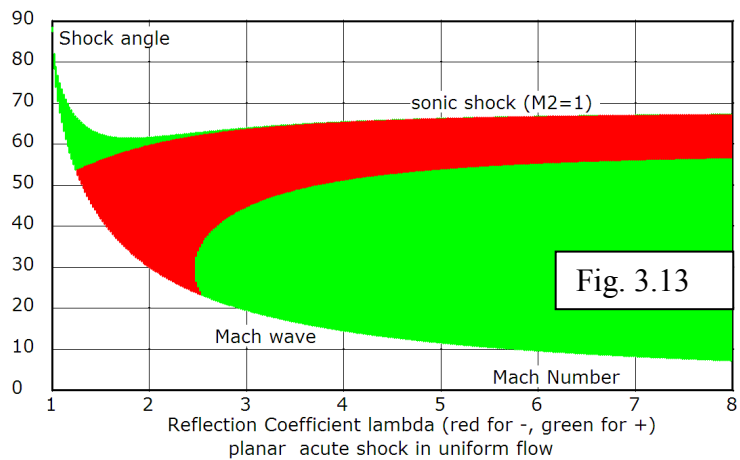
If the C^- characteristic is incident on the back of a shock and the C^+ characteristic reflects then λ is called the *reflection coefficient*. On the downstream side of a *planarly symmetric* shock with curvature S_a the pressure gradient and streamline curvature are from Eqn. (2.33),

$$P_2 = \frac{[BC]}{[AB]} S_a \quad D_2 = \frac{[CA]}{[AB]} S_a \quad (3.59 \text{ a, b})$$

so that the reflection coefficient for planar flow is,

$$\lambda_{\text{planar}} = \frac{\pi^+}{\pi^-} = \frac{\sqrt{M_2^2 - 1}[BC] - [CA]}{\sqrt{M_2^2 - 1}[BC] + [CA]} \quad (3.60)$$

This equation is plotted in Fig. 3.13. This is a plot of shock angle versus freestream Mach number showing where the reflection coefficient, λ_{planar} , is positive - green ('like' reflection) and where it is negative - red



(‘unlike’ reflection). The lower boundary of the coloured band is for the limiting weak shock – the Mach wave. The upper bound is where the post-shock Mach number $M_2 = 1$, the sonic condition. The reflection coefficient is zero at both the Mach wave and the sonic shock lines as well as at all boundaries between the green and red areas. At a very low Mach number, below 1.32, the reflection coefficient over the whole post-shock side is green – positive. This means that compression waves reflect as compression waves and expansion waves reflect as expansion waves – like reflection at all shock angles. Between Mach 1.32 and Mach 2.42 the weaker (red) part of the shock has a negative reflection coefficient, implying an unlike reflection, whereas the portion of shock nearest the sonic point is still in a like reflection (green) mode. There is a narrow region between Mach 2.42 and 2.55 where the reflection coefficient has four zones (- + - +). Above

Mach 2.55 there is (+ - +) sequence of zones. The upper green region, indicating like reflection near the sonic shock, becomes very narrow as it extends to higher Mach numbers. For positively curved shocks, be they acute or obtuse, the incident waves are compressive so that in this narrow region, next to the sonic shock, the reflected waves are also compressive. If a reflected shock forms here then its formation is compatible with the indicated presence of shock-causing compression waves. This will be applied and further discussed in Ch. 5 as it pertains to the formation of embedded shocks behind hyperbolic shocks.

For a *conical shock*, $S_a = 0$, and with the curvature $S_b = -\cos\theta / y$ Eqn. (2.30e) gives,

$$P_2 = \frac{B_2 G'}{A_2 B'_2 - A'_2 B_2} S_b \quad D_2 = \frac{-A_2 G'}{A_2 B'_2 - A'_2 B_2} S_b \quad (3.61)$$

This gives,

$$\pi^+ = -\frac{1}{M_2} \left[\sqrt{M_2^2 - 1} B_2 + A_2 \right] \frac{G' \cos\theta}{y} \quad (3.62 \text{ a,b})$$

$$\pi^- = -\frac{1}{M_2} \left[\sqrt{M_2^2 - 1} B_2 - A_2 \right] \frac{G' \cos\theta}{y}$$

and,

$$\lambda_{\text{conical}} = \frac{\pi^+}{\pi^-} = \frac{\sqrt{M_2^2 - 1} B_2 + A_2}{\sqrt{M_2^2 - 1} B_2 - A_2} \quad (3.63)$$

In conical flow, strengths of the characteristics both increase as $y \rightarrow 0$ but their ratio remains constant. The reflection coefficient in conical flow is uniformly positive for all Mach numbers and shock angles.

Behind a *doubly curved shock wave*,

$$P_2 = \frac{[BC]}{[AB]} S_a + \frac{B_2 G'}{[AB]} S_b \quad (3.64 \text{ a,b})$$

$$D_2 = \frac{[CA]}{[AB]} S_a - \frac{A_2 G'}{[AB]} S_b$$

Substituting in 3.58 gives the reflection coefficient for a doubly curved shock,

$$\lambda = \frac{\left\{ \sqrt{M_2^2 - 1} [BC] - [CA] \right\} \mathcal{R} + \sqrt{M_2^2 - 1} B_2 G' + A_2 G'}{\left\{ \sqrt{M_2^2 - 1} [BC] + [CA] \right\} \mathcal{R} + \sqrt{M_2^2 - 1} B_2 G' - A_2 G'} \quad (3.65)$$

where $\mathcal{R} = S_a / S_b$. This equation reverts to planar flow when $\mathcal{R} \rightarrow \infty$ and to conical flow when $\mathcal{R} \rightarrow 0$. Equation 3.65 shows that, although the strengths of the characteristics behind a doubly curved shock depend explicitly on the shock curvatures, the reflection coefficient depends only on the ratio of curvatures. The dependence on Mach number is complex, as seen in the above Fig. 3.13. The reflection coefficient and the strengths of the shock-reflected characteristics are important in the design of shock waves where one is concerned with coalescence of characteristics and the formation of embedded shocks behind a shock with given curvatures. Since the formation and existence of shock waves can be explained on the basis of overtaking (compressive) characteristics, it is possible that the appearance of a reflected shock wave behind a curved shock also comes about when the strengths of the reflected characteristics are positive. Equation (3.65) shows that at a sonic line ($M_2 = 1$), a characteristic reflects with the same strength but opposite sign irrespective of the ratio of the characteristic's curvature.

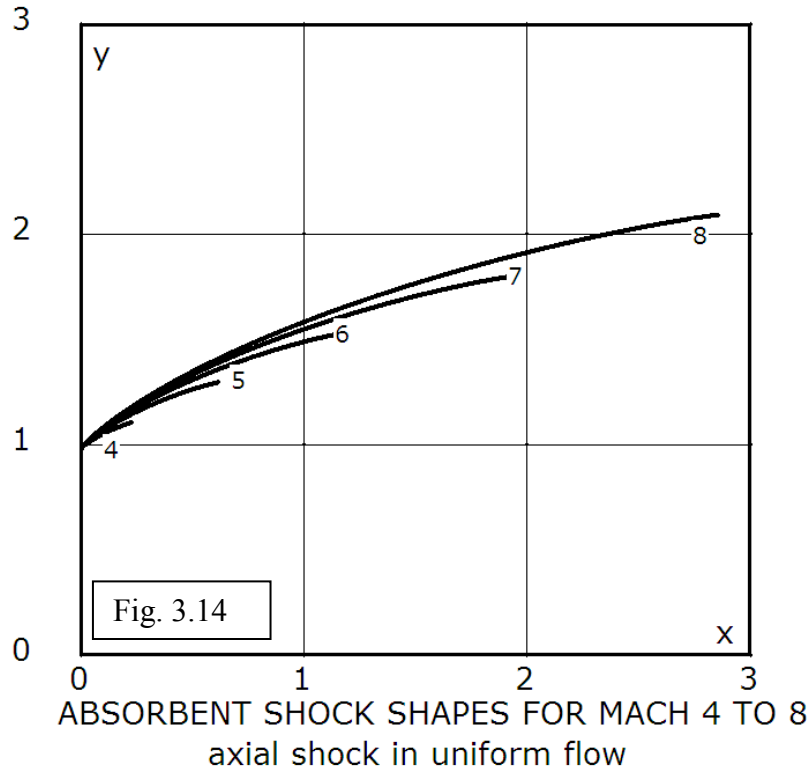
The back surface of a shock is perfectly absorbent to characteristics when $\lambda = 0$. From Eqn. (3.65) this occurs when the ratio of shock curvatures is,

$$\mathcal{R}_{\lambda=0} = -\frac{\sqrt{M_2^2 - 1}B_2G' + A_2G'}{\sqrt{M_2^2 - 1}[BC] - [CA]} \quad (3.66)$$

As with the isobaric and isoclinic shocks, the axisymmetric, perfectly absorbent shock, is found by numerically integrating,

$$\frac{dy}{y} = -\frac{\sqrt{M_2^2 - 1}[BC] - [CA]}{\sqrt{M_2^2 - 1}B_2G' + A_2G'} \tan \theta d\theta \quad (3.67)$$

Such shock shapes are plotted in Fig. 3.14, with the freestream Mach number as parameter. Shock shapes for a Mach number less than 4 are too small to appear on the scale of the plot. Sound, generated in the turbulent boundary layer on a body surface, would not be reflected from a surrounding, perfectly absorbent, shock wave, preventing sound reverberation between body and shock. Chernyi [1961] discusses further implications of the reflection coefficient at some length. As with the isobaric and isoclinic shocks, one is still faced with the task of finding the body shapes that produce the absorbent shock shapes.



3.9 Sonic line orientation

By its very nature the sonic line, in the post-shock flow, must impinge on the shock at the point where the post-shock flow is sonic. Orientation of the sonic line at the shock has an influence on the extent of subsonic flow behind the shock, which, in turn, must be compatible with the extent of supersonic flow. Any conflict, such as overlap of the two regions must mean that the proposed flow cannot exist. It will be shown in Ch. 5 that the orientation of the sonic line is critical to the existence of a concave smooth shock at the sonic point. Formulas will here be established for the angle between the streamline and the sonic line at the sonic point for planar and axial shocks in a uniform freestream in terms of the gradients behind the shock. Hints for developing the formula for the sonic line in case of a non-uniform upstream will be indicated.

The angle between a constant Mach number line, in this case the sonic line, and the streamline at the sonic point is α^* (Eqn. 2.22), where,

$$\tan \alpha^* = \frac{P^*}{D^* - \Gamma^*} \quad (2.22) \quad (3.68)$$

and where P^* , D^* and Γ^* are the pressure gradient, the streamline curvature and the vorticity, all evaluated at the sonic point behind the shock. This formula is valid for both planar and axial flows as well as for a non-uniform pre-shock flow. Expressions for the terms on the right-hand side of this formula vary, depending on the shock geometry and upstream conditions.

For a uniform upstream and **planar flow** ($S_a \neq 0$ and $S_b = 0$), using Eqns. (3.2 b,c,d,e,f),

$$\begin{aligned} P_2^* &= [BC]/[AB] \times S_a \\ D_2^* &= [CA]/[AB] \times S_a \\ \Gamma_2^* &= \left\{ \frac{C''}{E_2''} + \frac{[BC]A_2''}{[AB]E_2''} + \frac{[CA]B_2''}{[AB]E_2''} \right\} S_a \end{aligned}$$

so that,

$$\tan \alpha^* = \frac{P^*}{D^* - \Gamma^*} \quad (3.69)$$

becomes,

$$\tan \alpha^* = \frac{[BC]E_2''}{[CA]E_2'' + [AB]C'' + [BC]A_2'' + [CA]B_2''} \quad (3.70)$$

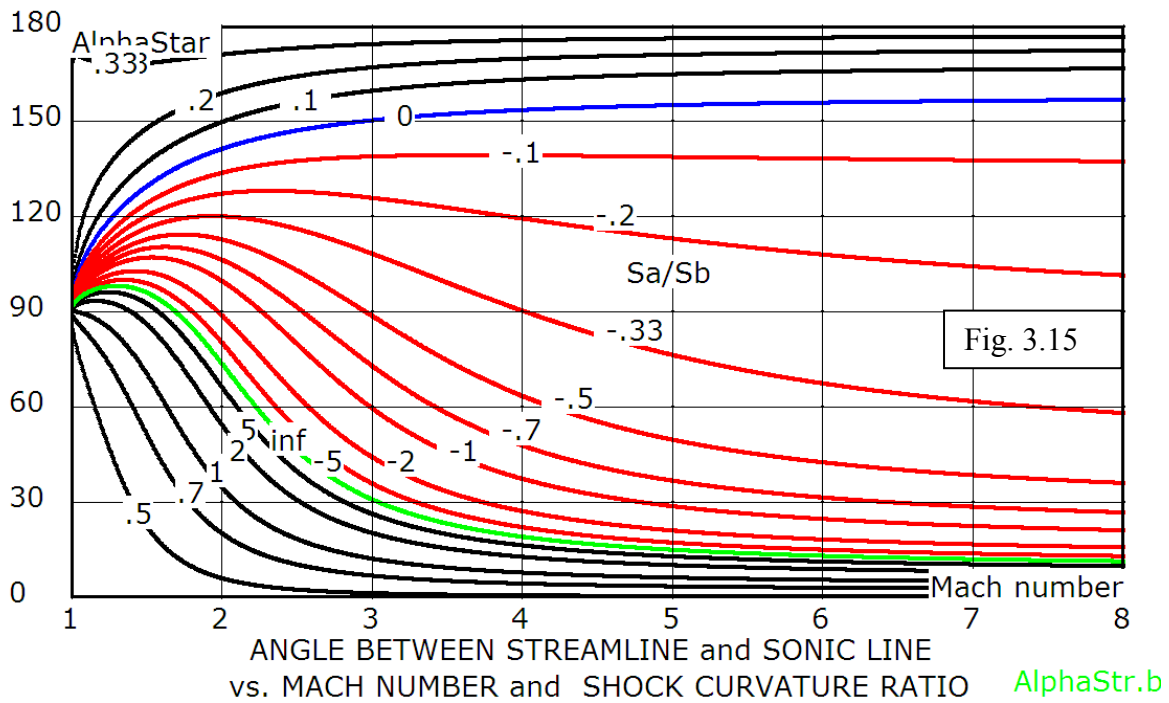
Note that, for planar flow, S_a cancels out, leaving α^* a function of the freestream Mach number only.

For a uniform upstream and **axial flow**, behind a **doubly curved shock** where $S_a \neq 0$ and $S_b \neq 0$, using equations (3.12 a and b) for P^* , D^* and Eqn. (2.40 b) for Γ^* , gives,

$$\tan \alpha^* = \frac{[BC]E_2''\mathcal{R}^* + B_2G'E_2''}{\{[CA]E_2'' + [AB]C'' + [BC]A_2'' + [CA]B_2''\}\mathcal{R}^* + \{[AB]G'' + [BG]A_2'' - [AG]B_2'' - A_2G'E_2''\}} \quad (3.71)$$

All coefficients on the right are evaluated at the post-shock sonic condition so that they are functions of Mach number only. This makes α^* a function of the freestream Mach number and \mathcal{R}^* only. The angle α^* is plotted in Fig. 3.15 against the freestream Mach number for a range of $\mathcal{R}^* = S_a / S_b$ as parameter, covering all the possible shock

shapes in Fig. 2.2. Black curves are for positive \mathcal{R}^* and red curves are for negative \mathcal{R}^* . The blue curve is for conical shocks and the green curve is for planar shocks. The green curve and its implications for planar shocks have been discussed by Hayes and Probstein [1966]. α^* and \mathcal{R}^* have critical roles in determining the nature of the flow behind hyperbolic shocks and shock detachment discussed in Ch. 5 and 6. Orientation of the sonic surface, as depicted by α^* , contributes greatly to the visualization of flow structure behind curved shocks, as further developed in Ch. 5.



With **non-uniform** pre-shock flow one would have to use the general expressions for P^* , D^* and I^* as in (2.30e) and (2.40b) in the formula (3.71). This situation occurs behind a regularly reflecting shock on a curved surface where the incident shock is curved. It occurs also for the reflected shock in Mach reflection with a curved incident shock.

3.10 Concluding remarks

This chapter has applied *curved shock theory* to calculate flow gradients near curved shocks on various simple aerodynamic surfaces as well as on shock surfaces with very specific properties. Most topics discussed are open to further investigation and elucidation. The following results have been deduced from curved shock theory:

1) The specific heat ratio, γ , upstream Mach number, M_1 , shock angle, θ , upstream flow inclination, δ_1 and the two shock surface curvatures, S_a and S_b , uniquely relate the flow properties as well as their gradients upstream and downstream of a doubly curved shock wave surface in steady flow of an ideal gas.

2) If S_b is constant along an isobar on the back side of the shock then the CST is applicable locally to a shock element in three-dimensional space.

3) In homenergetic flow lines of constant temperature, velocity, sound speed and Mach number are collinear.

4) Lines of constant pressure, temperature, density, velocity, sound speed and Mach number are collinear in homenergetic, irrotational flow.

5) There are singular positions behind doubly curved shock waves where the isoclinic and isobaric lines are collinear with the streamlines. At these locations the stream-wise flow gradients vanish. At any combination of Mach number and shock angle the positions exist for a specific value of shock curvatures ratio.

6) In planar flow the locations of the isoclinic (Crocco) point and the isobaric (Thomas) point are independent of shock curvature, being located at shock angles determined by Mach number only.

7) Curved shock theory predicts some curious results for curved normal shocks.

8) Shock stand-off distance and sonic patch extent can be approximated for convex and concave shocks.

9) Axisymmetric shock shapes are found such that the pressure gradient or streamline curvature vanish behind the whole shock surface. Also, shock shapes are found that do not reflect sound from their back surfaces. In all of these situations the pre-shock characteristics are those of the uniform free stream and the post-shock inclination and shapes of the characteristics are determined explicitly and uniquely by the local shock inclination and curvatures.

10) Curved shock theory predicts very high downstream flow gradients for oblique shocks approaching the axis of symmetry.

11) Curved shock theory predicts very high downstream flow gradients behind shocks near the Crocco point conditions for curved surfaces.

12) Orientation of the sonic surface behind a doubly curved shock is governed by the specific heat ratio, the pre-shock Mach number and the shock's surface curvature ratio at the sonic conditions on the shock.

13) It has been shown that CST can be used to find the doubly curved surface required to produce a given doubly curved shock or the inverse situation where the surface is given and the shock shape is found. This makes the theory useful as a predictive as well as an interpretive tool particularly since the analysis is algebraic in both directions.

CHAPTER 4

CONICAL FLOW AND TAYLOR-MACCOLL EQUATION(S)

Contents

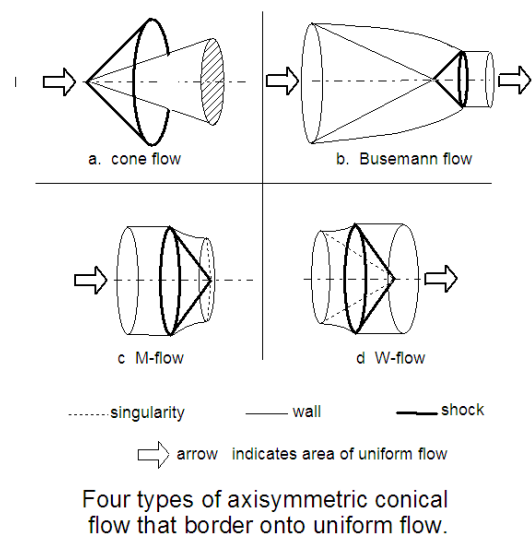
- 4.1 Introduction
- 4.2 The Taylor-Maccoll equations
 - 4.2.1 The first order equations
 - 4.2.2 Mach number variables
- 4.3 Conical flows with uniform upstream and downstream flows
 - 4.3.1 Cone flow and W-flow
 - 4.3.2 Busemann flow, experiments and CFD results
 - 4.3.2.1 Description of Busemann flow
 - 4.3.2.2 Busemann flow theory and intake performance
 - 4.3.2.3 Streamlines and radials in Busemann flow
 - 4.3.2.4 Numerical analysis of Busemann flow
 - 4.3.2.5 Characteristics and a centered axisymmetric compression fan
 - 4.3.2.6 Inflection point on the Busemann streamline
 - 4.3.2.7 Wind-tunnel tests on Busemann flow
 - 4.3.2.8 Busemann tests in the gun-tunnel at Mach 8.33
 - 4.3.2.9 Busemann tests in the wind-tunnel at Mach 3.00
 - 4.3.3 M-flow experiments and CFD results
 - 4.3.3.1 Characteristics on M-flow contour
 - 4.3.3.2 M-flow experiments in the gun tunnel and CFD results
 - 4.3.3.2(A) The 145 deg shock
 - 4.3.3.2(B) The 153.7 deg shock
 - 4.3.3.2(C) The 170.3 deg shock
- 4.4 Concluding remarks

4.1 Introduction

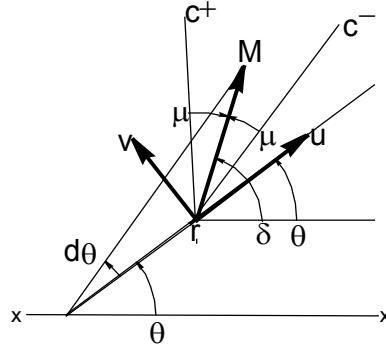
A preferred geometry for a scramjet combustor is a circular cross-section duct because of its superior ability to withstand both heat and pressure loads. Frictional losses are also at a minimum for such a duct since a cylinder has the smallest surface area for a given cross-sectional area. This leads to a cylindrical (axially symmetric) geometry as being desirable also for the intake that is attached to the front of the combustor duct. The same circular exit geometry for the intake is demanded by a gas turbine engine, this time because the axial compressor face is circular. In design selection of a suitable aerodynamic flowpath geometry, the requirement of high aerodynamic efficiency leads to the selection of intake flow types where any isentropic compression precedes shock compression so that the latter can occur at the lowest possible Mach number. Towards these ends, it is wise to study an axisymmetric flow and it is entirely fortuitous that axisymmetric, conical, Taylor-Maccoll flow provides a streamtube shape that satisfies the above intake design requirements, both geometric/structural as well as aerodynamic. In recognition of A. Busemann's work on such streamtube shapes, they are called Busemann flows and Busemann intakes. Enforcing conical symmetry for Busemann flow leads to flow quantities being constant on cones whose apices all lie on the same point and whose axes are all parallel to the free stream. Imposing conicality, restricts considerations to this specific class of flow while, at the same time, offering great simplicity in flow analysis where a wide variety of intake surfaces is available for selection - surface shapes that yield both a high compression and a high efficiency. Disappearance of the radial dimension as an independent variable, in conically symmetric flow, permits the depiction of results on the single remaining spatial variable – the conical angle. Furthermore, the use of conical flow means that all shocks are also conical and therefore of constant strength at any given angular position. The flows are not only uniform but also irrotational – generally, a desirable feature for flow that leaves the intake to enter a combustion chamber. These features of conical flow and, in particular, Busemann flow, which is by nature an internal flow, make the Busemann streamline shape an attractive candidate for an air intake of a hypersonic flight vehicle's engine.

This chapter is a self-contained treatment of supersonic conical flow. Later chapters will make reference to its various, seemingly disconnected, results. Four types of flow with conical symmetry are presented: a) cone flow, b) Busemann flow, c) M-flow and d) W-flow. The common feature of all four flows is that they abut uniform and parallel flow on either the up- or downstream boundary. In the case of Busemann flow both upstream and downstream flows are uniform. The flows were studied, as a set, by Godzowskii [1959]. Cone flow is a well-understood classical supersonic flow treated in many textbooks and it is here mentioned briefly for the sake of completeness. The much-less familiar W-flow is also treated briefly for completeness. It starts from an upstream singularity, expands and passes through a conical shock to become a uniform downstream flow. It has, so far, had no known practical utility in flow-path design. Busemann flow contains four unique fluid mechanical features that are treated in this chapter, a) internal flow with an inflected surface, b) a free-standing conical shock, c) an axisymmetric centered compression fan and d) a flow process from a uniform flow to another uniform flow. M-flow is another type of internal, conical flow that can represent part of an intake surface. It also contains some interesting fluid mechanical features – a) a singularity and b) an example of convergent flow with a decreasing pressure. It is suitable as a leading edge shape that produces a conical internal shock wave. Both Busemann and M-flow carry conical shocks that either diverge from or converge towards the centre line of symmetry. The study of such shocks is important in their applications to intake flows as well as to understanding the basics of reflection and interaction of curved shock waves. Busemann and M-flow are the main subjects of this chapter.

The first part of this chapter deals with conical flow theory as embodied in the Taylor-Maccoll equations and as applied to the four flows that are bounded on the up- or downstream side by uniform flow. The Taylor-Maccoll equations are recast and presented in terms of Mach number components; their



solution is applied to the calculation of internal, conical, axisymmetric flow. It is shown that the Taylor-MacColl numerical solution cannot be started at the free stream and that characteristics of Busemann flow, emanating from the surface, tend to focus close to the apex of the internal conical shock so that a substantial length of intake surface is required to determine a relatively short segment of the shock. An inflection point on the Busemann streamline is shown to have significance for starting of Busemann flows. The second part presents CFD and experimental results of Busemann flow and M-flow, the two types of conical flow that are significant for air intake design as well as to the understanding of shock reflection in axisymmetric internal flow.



4.2 The Taylor-Maccoll equation(s)

Flow which is both axially and conically symmetric is best described in spherical polar coordinates (r, θ) where r is distance measured radially out from the origin and θ is the angle measured from the downstream direction. In all cases the origin is at the apex of the conical shock, on the centre line of symmetry (xx). The flow velocity components in the radial and angular directions are designated as U and V . Drawing similar triangles along the streamline in the figure on the right gives the streamline equation:

$$dr / d\theta = rU / V \quad (4.0)$$

The original Taylor-Maccoll equation is a non-linear, second order total differential equation with the spherical polar angle, θ , as independent variable and the radial flow velocity, U , as dependent variable [Anderson 1982, Emanuel, 1994].

$$\frac{\gamma-1}{2} \left[1 - U^2 - \left(\frac{dU}{d\theta} \right)^2 \right] \left[2U + \frac{dU}{d\theta} \cot \theta + \frac{d^2U}{d\theta^2} \right] - \frac{dU}{d\theta} \left[U \frac{dU}{d\theta} + \frac{dU}{d\theta} \left(\frac{d^2U}{d\theta^2} \right) \right] = 0 \quad (4.1)$$

This is the model equation that governs steady, axisymmetric, conical flow of a perfect gas. No explicit algebraic solution has been found, nor are there any numerical schemes for solution of the **second order** equation (4.1) as given above. However, the equation can be converted to two **first order** equations, (4.2) and (4.3), at the price of acquiring

the additional dependent variable, V . The two equations are now amenable to standard numerical solution methods. Most of these solutions have been done with boundary conditions applicable to cone flow [Sims, 1964; Anderson, 1982; Emanuel, 1994;].

4.2.1 The first order equations

The first-order versions of equation (4.1) are the momentum equations, in polar coordinates, in the r and θ directions, [Thompson, p.488, 1972]:

$$dV/d\theta = -U + \frac{a^2(U + V \cot \theta)}{V^2 - a^2} \quad (4.2)$$

$$dU/d\theta = V \quad (4.3)$$

where a is the speed of sound that can be written in terms of the velocities and the total conditions through the energy equation. The second of these equations is also the irrotationality condition, implying that conical flows are necessarily irrotational. Explicit reference to the speed of sound and total conditions can be circumvented if the equations are recast so as to have the radial and angular Mach number components as dependent variables in place of the corresponding velocity components. The boundary conditions, when expressed as Mach number components at the up- and downstream sides of conical shocks are then applicable directly to the solution of the equations. Also, total conditions, which have no influence on the Mach number solution, do not have to be invoked.

4.2.2 Mach number variables

The Taylor-Maccoll (T-M) equations have been recast in terms of the radial and angular Mach numbers u and v , where $u = U/a$ and $v = V/a$ and a is the local sound speed:

$$\frac{du}{d\theta} = v + \frac{\gamma - 1}{2} uv \frac{u + v \cot \theta}{v^2 - 1} \quad (4.4)$$

$$\frac{dv}{d\theta} = -u + \left(1 + \frac{\gamma - 1}{2} v^2\right) \frac{u + v \cot \theta}{v^2 - 1} \quad (4.5)$$

These two equations seem more complicated than their parents (4.2) and (4.3). However, it will be shown that the use of Mach number components u and v leads to meaningful and useful physical interpretations from Eqns. (4.4) and (4.5)

The streamline equation is:

$$dr / d\theta = ru / v \quad (4.6)$$

The flow Mach number is:

$$M = \sqrt{u^2 + v^2}$$

Having the T-M equations in this form reveals their singular nature at $v = \pm 1$ where the singularity is caused by the $(v^2 - 1)$ -term in the denominators above.¹⁰ Absence of any explicit reference to total conditions, as well as the sound speed, leads to a more straightforward application of the boundary conditions. A standard, fourth-order Runge-Kutta scheme has been used to integrate the Mach number form of Eqns. (4.4) and (4.5). The solutions are identical, to eight decimal places, to similar solutions of (4.2) and (4.3) in the velocity variables. Previous reference to the T-M equations in Mach number form has not been found in the literature.

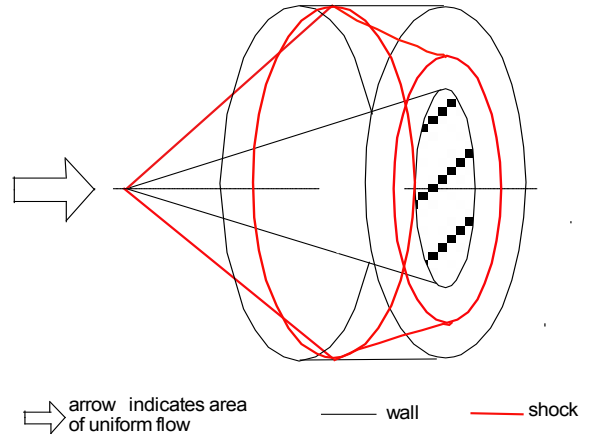
4.3 Conical flows with uniform upstream and downstream flows

The four types of Taylor-Maccoll (T-M) flow that are bounded on the up- or downstream side by a conical shock and/or uniform flow are of interest because, in each case, a uniform flow can be grafted onto the T-M flow to obtain a combined flow with some practical flight applications where the flow is joined onto a uniform and parallel freestream. The four flows are also of interest from a more fundamental viewpoint because they contain shock waves that appear to be incident on, or reflecting from, the centerline of symmetry and such reflections are pertinent to the study of reflection of curved shocks. Conical shocks, being of constant strength, aid in the understanding of causes and effects as pertaining to curved shock reflection. Integration of Eqns. (4.4) and (4.5) requires the starting values u and v at some specified value of θ . It is these boundary conditions that lead to the four different flow configurations.

¹⁰ Such singularities are discussed by Dadlizi [1946], Mölder [1967] and Rylov [1990]. Their appearance, in any given flow, should be taken as a warning that whatever symmetry assumption(s) have been made may not hold in the physical airflow.

4.3.1 Cone flow and W-flow

The most well-known numerical integration of the T-M equations is for the flow over an axisymmetric cone at zero angle of attack in supersonic flow. This is of some historical interest since it was one of the first applications of the digital computer, some 60 years ago. It is a classical compressible flow example found in most text books. Consideration of this flow is included here because the cone shape is a useful surface to form the centre-body of an axisymmetric intake. For an intake this is the situation where the shock from the centre-body reflects off the inside surface of the cowl as would be the situation when the engine operates at a Mach number higher than the design Mach number.



Axisymmetric conical flow with shock reflecting off the inside of a cylinder

Also, for more fundamental uses, the conical shock, produced by the cone, can be reflected from the inside surface of an enclosing circular cylinder. In applying CST to this reflection, the incident shock is conical so that $S_a = 0$ and $S_b = -\cos\theta$ for a *unit ring-wedge*. In this case all primitive variables as well as gradients and vorticity at the reflection point are analytically predictable by CST, as is the curvature of the reflected shock.

To calculate cone flow, we specify a free stream Mach number M_1 and a conical shock with aerodynamic shock angle θ_{12} where $\mu_1 < \theta_{12} < \pi/2$. The u and v components of Mach number immediately behind the shock are [Anon. NACA Rep. 1135 Eqns. 133 and 134]

$$u_2 = \frac{(\gamma + 1)M_1^2 \sin \theta_{12} \cos \theta_{12}}{\sqrt{[2\gamma M_1^2 \sin^2 \theta_{12} - (\gamma - 1)][(\gamma - 1)M_1^2 \sin^2 \theta_{12} + 2]}} \quad (4.7)$$

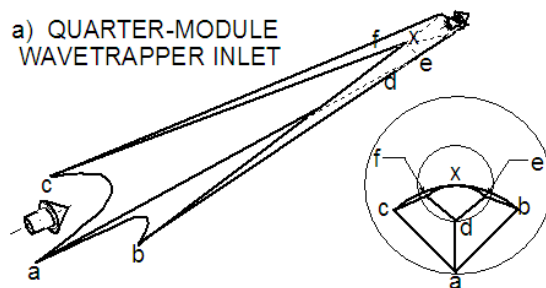
$$v_2 = \sqrt{\frac{(\gamma + 1)M_1^2 \sin^2 \theta_{12} + 2}{2\gamma M_1^2 \sin^2 \theta_{12} - (\gamma - 1)}} \quad (4.8)$$

These are the starting values, on the downstream side of the shock, for integrating Eqns. (4.4) and (4.5) numerically by decreasing θ until $v = 0$. At this value of θ the cone surface has been reached and the integration is complete. An iteration may have to be performed on θ_{12} if a specific cone half-angle is desired. The details of such integrations can be found in [Anderson, 1982 and Emanuel, 1994].

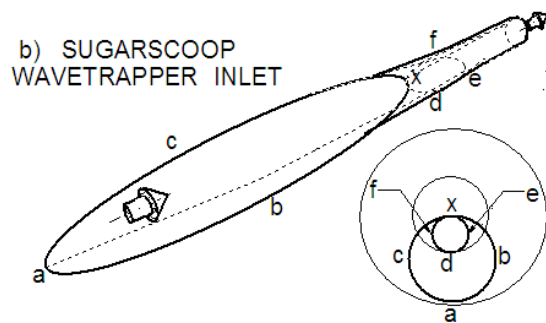
4.3.2 Busemann flow experiments and CFD results

Thermodynamic cycle calculations of high Mach number air-breathing engines, such as scramjets, have shown that these engines should have air intakes that contract and compress the flow by factors of 6 to 10 and 10 to 20 respectively and that this contraction and compression be done with the least loss of total pressure. Aside from high contraction and compression, the attainment of good intake performance is critically dependent on the free stream Mach number and the lateral and stream-wise contours of the intake surface.

Busemann [1944] demonstrated, analytically, the possibility of an axially and conically symmetric flow that starts as a supersonic and uniform free stream, compresses and contracts isentropically, finally passing through a conical shock wave to become parallel and uniform flow at a lower Mach number. The isentropic compression is contained between a Mach cone on the upstream side and a shock cone on the downstream side. Mölder and Szpiro [1966] proposed the Busemann flow as the basis for hypersonic air intake shape generation. A Busemann intake performance chart was presented which relates the intake's compression, contraction and efficiency. Using wave-rider methodology, Mölder and Romeskie [1968] presented the notion of selecting portions of the axisymmetric versions of Busemann flow to generate modular



abxc is the freestream capture tube
dexf is the exit stream-tube

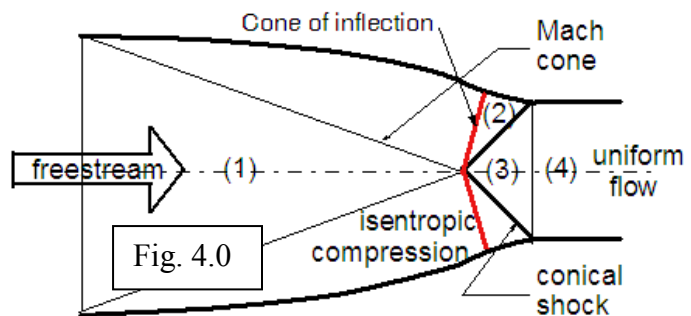


abxc is the freestream capture tube
dexf is the exit stream-tube (both circular)

“Wavetrapper” intake shapes with enhanced flow starting potential. Experimental results were presented for both full and modular (streamline traced) versions of the Busemann intake. Experimental performance of a full Busemann intake was compared by Mölder et.al. [1992] against a Prandtl-Meyer intake and an Oswatitsch type intake at a free stream Mach number of 8.33 and applications to flight vehicles were suggested by VanWie and Mölder [1992]. The above work has shown that, Busemann flow, which is axisymmetric, conical and bounded on the upstream by a Mach cone and on the downstream by a shock cone, does exist; and that it has characteristics which make it suitable for use as a basis for the design of supersonic and hypersonic air intakes. Some new analytical features of Busemann flow are presented in the following sections. Some new experimental results of Busemann flow at a freestream Mach number of 3.00 are found in Section 4.3.2.7 and 4.3.2.9, below.

4.3.2.1 Description of Busemann flow

In Busemann flow, compression from the high freestream Mach number is initially isentropic. Only at the lowest Mach number does the flow pass through a shock. The shock is weak and produces a downstream flow, which is irrotational, uniform and parallel to the free stream. High stream-wise pressure gradients occur *in* the flow as opposed to at the walls. High overall compression and substantial Mach number reduction is attained with a high efficiency. As an example: A Busemann intake reduces the Mach number from 8.33 to 2.8 with a total pressure recovery of 91%. In choosing a particular design, one can start by specifying the desired exit conditions and the efficiency – an approach suitable for preliminary design selection.



Alternatively, one can start by selecting a shock pressure ratio low enough to keep the boundary layer attached at the shock impingement point and then proceeding by considering all intakes satisfying this condition. Another virtue of the Busemann design approach is that the surface contours and intake operating conditions are very easily

calculable, allowing ready perusal of multiple design options. Recent CFD studies have shown that a given Busemann contour seems to produce a uniform exit flow at two distinctly different freestream Mach numbers. This discovery makes the intake suitable for use on dual-cycle engines that operate with subsonic or supersonic combustion, depending on the freestream Mach number. This possibility needs further analysis.

Schematics of Busemann flow contours are shown in Fig. 4.0. Uniform, parallel freestream flow, state (1), from the left, is isentropically compressed from a Mach cone up to the shock cone, state (2), and then the flow passes through the conical shock to become uniform and parallel flow at state (3). The flow is both axially and conically symmetric and irrotational throughout. In passing from state (1) to state (3), the flow is contracted and compressed and there is a loss of total pressure at the shock. Detailed examination of the shape of the Busemann streamline has shown that the upstream part of the streamline is curved towards the centre line and that this is followed by a downstream part that is curved away from the axis. These two portions are then separated by an inflection point. The heavy red lines indicate a cone whose base circle is at the inflection points of the Busemann streamlines. This inflection point cone has special significance to the starting of supersonic flow in the intake.

4.3.2.2 Busemann flow theory and intake performance

Busemann flow and its streamline shape are calculated from the T-M equations (4.4) and (4.5). These equations are integrated with respect to θ from the front of the conical shock (station 2) to the free stream (station 1). To do so requires the starting values: u_2 , v_2 and θ_2 . These have to be specified in such a way that the flow downstream of the shock will be parallel to the free stream – this is the most common requirement of flow entering a combustor. This condition must be applied to find the appropriate combination of u_2 , v_2 , and θ_2 . Using the Mach number in front of the shock, M_2 , and the aerodynamic shock angle, θ_{23} , the radial and circumferential Mach numbers are:

$$u_2 = M_2 \cos \theta_{23} \quad (4.9)$$

$$v_2 = -M_2 \sin \theta_{23} \quad (4.10)$$

The flow deflection through the shock is obtained from the equation relating Mach number, shock angle and flow deflection through the shock [Anon. NACA Rep. 1135, 1953, Eqn. 139a]:

$$\tan \delta_{23} = \frac{2 \cot \theta_{23} (M_2^2 \sin^2 \theta_{23} - 1)}{2M_2^2 (\gamma + 1 - 2 \sin^2 \theta_{23})} \quad (4.11)$$

The angular location of the shock which is the starting value for the variable of integration, is then:

$$\theta_2 = \theta_{23} - \delta_{23} \quad (4.12)$$

Equations (4.4) and (4.5) are then numerically integrated from θ_2 to $\theta_1 = \pi - \mu_1$. Since θ_1 is not known *a priori*, the integration is continued until the vertical or cross-stream Mach number ($u \sin \theta + v \cos \theta$) becomes zero, indicating that the free stream has been reached. Note that, prior to integration, we could calculate the intake's efficiency, using the total pressure ratio as measure,

$$p_{t3} / p_{t2} = \left[\frac{(\gamma + 1)k^2}{(\gamma - 1)k^2 + 2} \right]^{\frac{\gamma}{\gamma - 1}} \left[\frac{\gamma + 1}{2\gamma k^2 - \gamma + 1} \right]^{\frac{1}{\gamma - 1}} \quad (4.13)$$

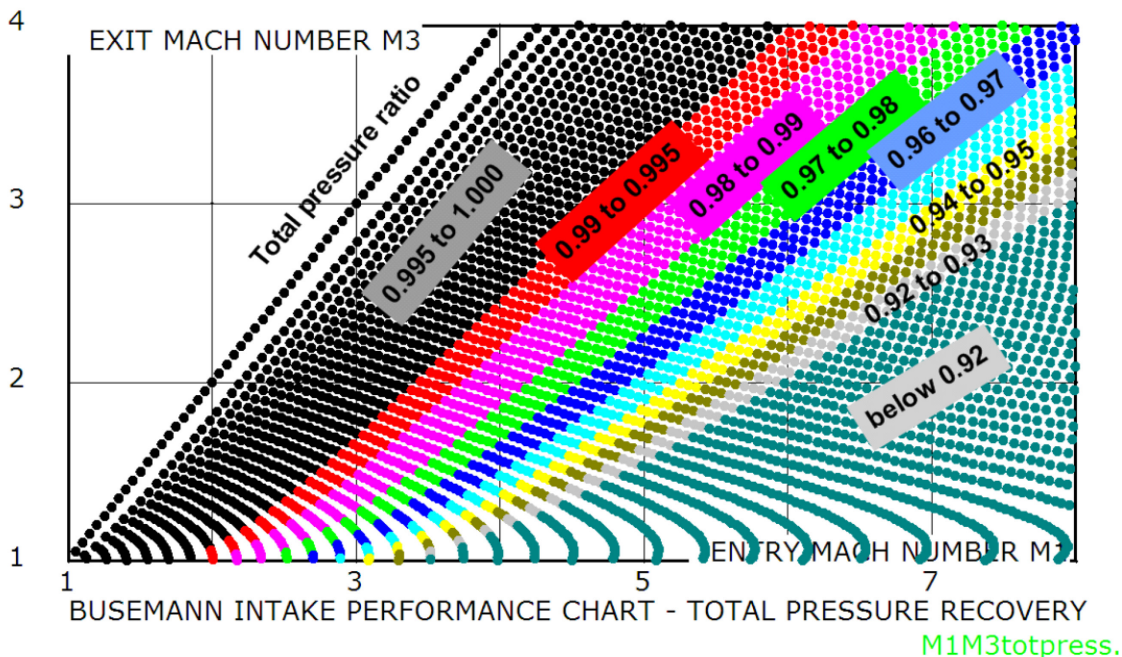
and the exit Mach number,

$$M_3^2 = \frac{(\gamma + 1)^2 M_2^2 k^2 - 4(k^2 - 1)(\gamma k^2 + 1)}{[2\gamma k^2 - (\gamma - 1)][(\gamma - 1)k^2 + 2]} \quad (4.14)$$

where $k^2 = M_2^2 \sin^2 \theta_{23}$. In fact, we could **prescribe** a desired efficiency; calculate k from Eqn. (4.13); **prescribe** the downstream Mach number M_3 and calculate M_2 by inverting (4.14). Then $\theta_{23} = \sin^{-1}(k/M_2)$, $u_2 = M_2 \cos \theta_{23}$ and $v_2 = M_2 \sin \theta_{23}$. After this, θ_2 and δ_{23} are found as above and the integration performed until $(u + v \cot \theta) \geq 0$. The ability to specify the downstream Mach number and an intake efficiency, **before doing the integration**, makes this approach particularly suitable for preliminary intake design selection. Note, however, that *all is not roses*, since the integration yields a free stream Mach number that may not be the desired one. An iteration, on the input conditions, p_{t3}/p_{t2} and M_3 , has to be performed to arrive at the desired design Mach number of the flight vehicle. This inconvenience is the direct result of, and the price paid for, the convenience and simplicity achieved by assuming a conical flow. At the free stream

condition an infinite number of different intakes are possible at any specified Mach number. This is in agreement with the appearance of the singularity at the freestream condition which makes it impossible to start the integration at a specific freestream Mach number – an infinite number of streamlines are possible. Proper boundary conditions cannot be specified for the freestream.

Proceeding with the integration of the TM-equations from the initial conditions, as chosen above, produces a free-stream Mach number M_1 . The results of many such calculations are shown in the figure below, each case represented by a dot. For each case, a value of M_2 is selected, in our case between 1 and 8 and k is cycled from 1 to M_2 . For each M_2 and k the total pressure ratio and M_3 are calculated; integration of the T-M equations then leads to the freestream at M_1 and a point is plotted on a graph of M_1 vs. M_3 with p_{t3}/p_{t1} as parameter, determining the point's colour.



Every point in this figure represents a Busemann intake calculation from the downstream shock to the freestream. This graph can be used to select a Busemann intake design based on the entry and exit Mach numbers and the total pressure ratio. Any two of these parameters can be used to determine the third. For example, a Busemann intake that reduces the freestream Mach number from 7 to 3 does so with a total pressure recovery of

0.95. This graph represents both components of intake performance, the capability by M_1 and M_3 and the efficiency by p_{t3}/p_{t1} .

4.3.2.3 Streamlines and radials in Busemann flow

When integrating equations (4.4) and (4.5) from the shock, in an upstream direction with increasing θ , we find the shape of the Busemann streamline, $r = f(\theta)$, by integrating the streamline equation, which, in spherical coordinates, takes the form:

$$dr/d\theta = ru/v \quad (4.15)$$

Equation (4.15) can be integrated separately from (4.4) or (4.5) since r does not appear in either (4.4) or (4.5). Although this equation is not coupled it is most conveniently integrated alongside (4.4) and (4.5). The integration is started by assigning a boundary value $r = r_2 = 1$ at $\theta = \theta_2$. The streamline (4.15) then originates from $(r, \theta) = (1, \theta_2)$. Other streamlines originate from lesser values of r_2 and, keeping in mind conical symmetry, are geometrically similar to each other, being scaled, at any θ , by their respective values of r_2 . This important property allows the construction of three-dimensional (modular) intake surfaces¹¹ by scaling the coordinates of a single Busemann streamline. [Mölder and Romeskie, 1968]. The inclination of the streamline ahead of the shock is $\delta_2 = -\delta_{23}$, from Eqn. (4.11). Progressing upstream, the inclination increases by a few degrees (typically 6 to 10) to the inflection point and then decreases to zero at the free stream. It is fortunate that all such integrations, done so far, have always terminated with a zero flow deflection, i.e. a parallel free stream flow. If this were not so, then the Busemann flow streamline surfaces would not be useful for compressing a uniform freestream and acting as the generators for air intake surfaces. No *a priori* reason has been discovered for this fortunate happenstance.¹² Note that in Eqns. (4.4) and (4.5) the term $(u \sin\theta + v \cos\theta)$ represents the Mach number component normal to the axis of symmetry. In the freestream this component is zero and also on a freestream Mach wave,

¹¹ The geometry of these intakes is such that overboard mass flow spillage is possible - allowing flow starting in high contraction intakes

¹² W-flow, which is briefly discussed below, is an example of Taylor-Maccoll flow that is limited in its usefulness because its upstream solution does not end at a uniform freestream but at a more-or-less useless singularity where the circumferential Mach number becomes sonic.

$v = 1$, so that in both equations the term $(u + v \cot\theta)/(v^2 - 1)$ becomes 0/0 in the freestream. Some algebra shows that Eqns. (4.4) and (4.5) then revert to,

$$du/d\theta = v \quad (4.16)$$

$$dv/d\theta = -u \quad (4.17)$$

which have the solution,

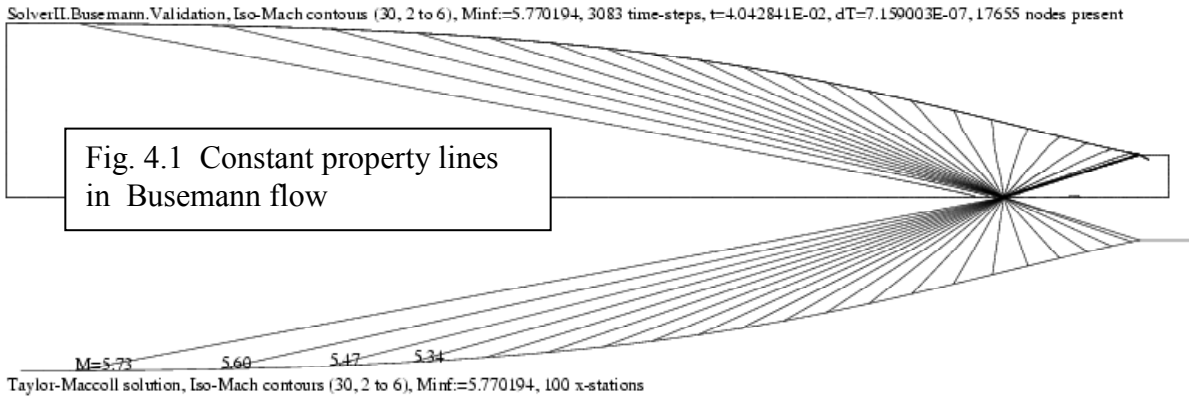
$$u = M_1 \cos \theta \quad \text{and} \quad v = -M_1 \sin \theta \quad (4.18)$$

These define a uniform flow in the freestream direction; thus, the Taylor-Maccoll equations are seen to allow a smooth merge of a variable, conical, Busemann flow with a uniform parallel flow. It is also apparent that the integration cannot be started in the freestream because equations (4.16) and (4.17) would continue giving the degenerate uniform flow represented by Eqns. (4.18). In fact there is an infinity of solutions starting from a given Mach number and a uniform parallel freestream and there is no rational way of specifying the boundary conditions at the freestream so as to arrive at a desired exit flow.

4.3.2.4 Numerical analysis of Busemann flow

The theoretical evolution of Busemann flow is determined by the conservation equations, equation of state, a high degree of imposed symmetry and flow steadiness, and the question arises as to whether such flow actually exists. We try to answer this by calculating the flow inside a Busemann intake with an independent method that is free of all the symmetry and steadiness assumptions. We have used SolverII which is a 2D, locally adaptive, unstructured Euler solver. Discretization has been performed using a 2D unstructured grid generator by Galyukov and Voinovich [1993]. The underlying numerical scheme and data structure were described by Saito et al. [2001]. This code knows nothing about conical symmetry or steady flow and we will examine its ability to simulate both of these features of the Busemann flow as well as of M-flow further down. We input the geometry of an axisymmetric Busemann intake duct as calculated by the Taylor-Maccoll equation integration, along with its calculated freestream Mach number. In the SolverII simulation, the duct geometry was inserted instantaneously into the supersonic, Mach 5.77, flow. An unsteady internal flow resulted that eventually settled into a supersonic steady internal flow. Upper half of Fig. 4.1 shows isobars as calculated

by SolverII. The lower half shows the constant property radials as calculated from the T-M solution. Similarity of the two sets of radials shows that the time-asymptotic SolverII solution has converged to the conical T-M solution, lending credibility to the existence of

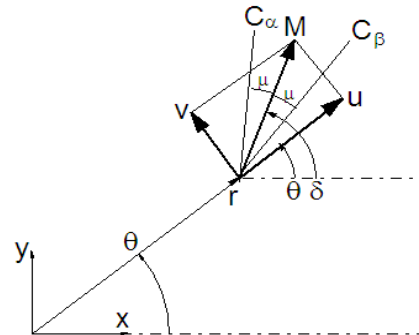


Busemann flow. Although the shock is straight and in its proper location, a short reflected shock emanates from the surface at the corner. This reflected wavelet is due to the finite thickness of the incident shock because the shock occupies two to three cell widths of computational space, some of which is ahead of the corner and some is behind. This leads to a reflected compression wave followed by a reflected expansion from the corner. The net result is a weak, decaying wave, which projects some distance into region (3). The insert is a zoomed-in view of the radials at the focal point showing that there is a loss of conicality, in the upstream flow, near the focus. This deficiency, due to the singular nature of the focal point, can be reduced, but not entirely eliminated, by progressive grid refinement in the SolverII code. The grid has been purposely left unrefined to show some difference between the benchmark Taylor-Maccoll flow and the SolverII results. Closeness of the leading radials at the focal point indicates a rapid change of flow properties in this area of flow. This feature of Busemann flow introduces a unique centered axial compression fan that will be discussed further below.

The results give us some assurance that steady, conical flow, as posed by the Taylor-Maccoll equation, exists in the Busemann intake. In a back-handed way, it is also reasonable to have confidence in the ability of SolverII to predict steady internal flow with freestanding shocks. Although the existence of such flows can conclusively be

proven only by experiment, it is not useful to use experimental results to verify CFD, because experimental error usually swamps the accuracy and resolution demanded of CFD. It is better to verify CFD against such exact solutions as the Busemann flow. Numerical integration of the Taylor-Maccoll equation by a technique such as fourth order Runge-Kutta can be made to have arbitrarily small errors and, in this sense, Busemann flow can be made exact in such features as adherence to conicality, irrotationality, shock location at the corner, streamline (body) shape and flow uniformity in the downstream flow state. The ability of CFD to replicate these features can then be used to judge the efficacy of the particular CFD technique.

Courant and Friedrichs [1948] pictured Busemann flow with straight radial lines from the focus to the surface, as shown in the Busemann Intake Figure 4.1 above. From our experience in dealing with centered Prandtl-Meyer fans, we might presume these radials to be characteristics. This is not so; the radials are lines of constant property value, isobars, isotherms, etc. – this being a necessary result of conical symmetry. The shape and location of characteristics is more complicated – the subject of the next section.



4.3.2.5 Characteristics and a centered axisymmetric compression fan

Characteristics are two sets of intersecting lines in supersonic flow. The characteristics carry a physical significance in that they delineate the region of space that influences flow conditions at a particular point as well as the region of space that depends on the flow conditions at a point. The characteristic lines are selected such that along these lines the governing partial differential equations become total differential, finite difference equations, allowing numerical solutions of the flow-field, [Zucrow and Hoffman, 1977]. Alternatively, once a supersonic flow has been established by some non-characteristic methods the characteristic lines can be calculated and superimposed and inferences about influences, causes and effects can be drawn. The α and β or $C+$ and $C-$ characteristics are inclined at $\pm \mu$ to the local streamlines where $\mu = \sin^{-1}(1/M)$. In polar coordinates the α and β characteristics' shapes are determined by integrating,

$$\left(\frac{dr}{d\theta}\right)_{\alpha,\beta} = r \cot(\delta - \theta \pm \mu)$$

Where the plus sign is for the α characteristic and minus is for the β characteristic. For x-y plotting one can integrate the α -characteristics:

$$(dx/d\theta)_{\alpha} = r \cos(\delta + \mu)/\cos(\pi/2 - \delta - \mu)$$

$$(dy/d\theta)_{\alpha} = r \sin(\delta + \mu)/\cos(\pi/2 - \delta - \mu)$$

and the β -characteristics,

$$(dx/d\theta)_{\beta} = r \cos(\delta - \mu)/\cos(\pi/2 - \delta + \mu)$$

$$(dy/d\theta)_{\beta} = r \sin(\delta - \mu)/\cos(\pi/2 - \delta + \mu)$$

Integration of the characteristics is easily performed inside the routine for integrating the T-M equations. This method was used to superimpose characteristics on the T-M solution

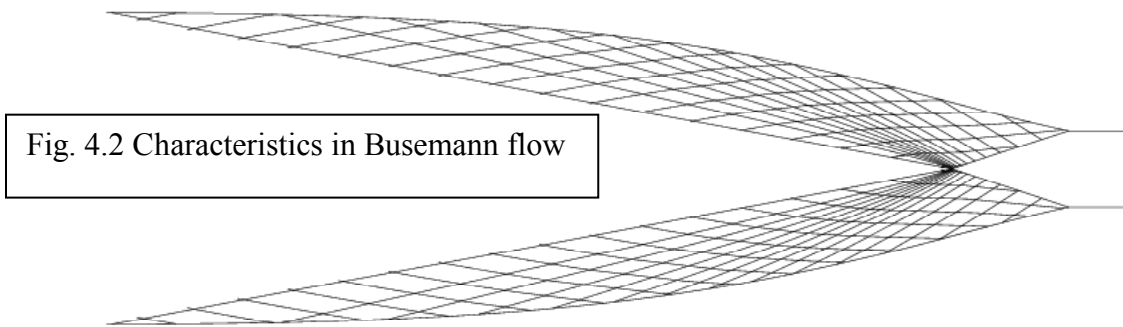
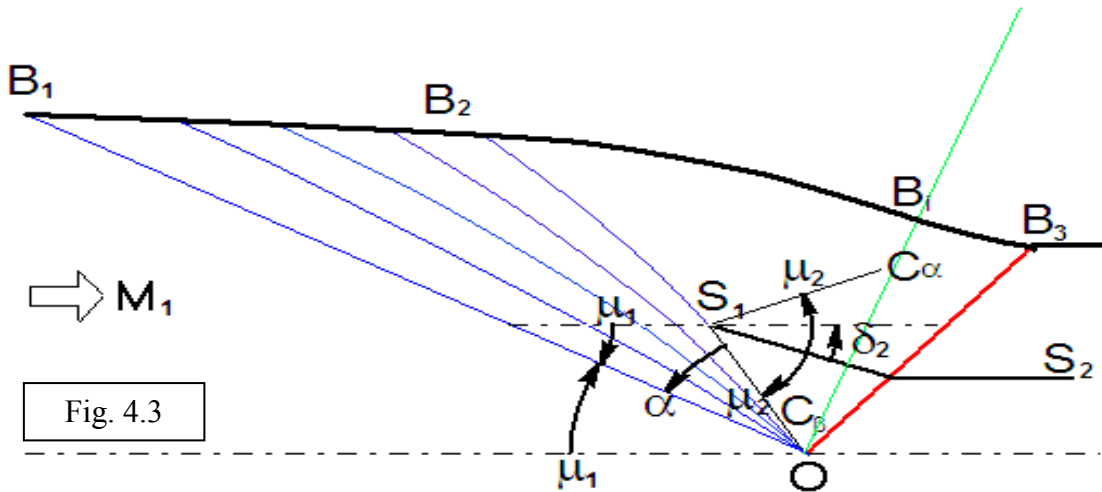


Fig. 4.2 Characteristics in Busemann flow

above. Resulting characteristic lines are shown in Fig. 4.2 for the same Mach 5.77 intake. The characteristics mesh is an overlay on the Busemann flow. The α -characteristics all start from the Mach cone and proceed away from the axis to intercept either the surface streamline or the front surface of the shock. The β -characteristics start at the surface and proceed towards the axis. The first of these is the free stream Mach cone itself, having an inclination μ_1 at the axis. At the shock the remaining characteristics have an inclination $\delta_2 + \mu_2$, different from μ_1 . Fig. 4.3 is a schematic showing a Busemann contour $B_1 B_2 B_3$ centered at O with a conical shock OB_3 and a streamline $S_1 S_2$ passing through the shock. Characteristics C_α and C_β emanate from S_1 and S_1 is so located on the streamline that the C_β characteristic passes through O. This characteristic intercepts the Busemann contour at B_2 .



An examination of the inclinations of the characteristics shows that $\alpha = \mu_2 + |\delta_2| - \mu_1$ which must be greater than zero, because $\mu_2 > \mu_1$ since $M_2 < M_1$. The angular region α is populated by β characteristics that fan out from O to the Busemann contour along B_1B_2 . The fan of β characteristics contained in OB_1B_2 is a centered, axisymmetric compression fan analogous to the Prandtl-Meyer fan in planar flow. The β -characteristics from the surface B_2B_3 (not shown) all intercept the shock OB_3 and it becomes apparent that a very small, near-apex segment of the shock, is determined by a relatively long length of the Busemann intake surface. This large surface-to-shock length ratio suggests that the leading edge shape is unimportant in determining the overall shock shape. We know, however, that a long leading edge surface length contributes to boundary layer growth and viscous losses, so that these two facts provide an incentive to truncate the leading edge so as to minimize the sum of leading edge shock and boundary layer losses on a practical intake surface. The results presented here give an indication of the extent (B_1B_2) to which the conical shock is influenced by a shortening of the intake surface. A study of viscous/inviscid efficiency loss tradeoffs is in order. Any treatment of the centered con-focal compression fan or the free-standing conical shock has not been

found in the open literature.¹³ An experiment, to expressly demonstrate this flow structure is described below.

B_i is an inflection point on the Busemann streamline and the green line OB_i contains all such inflection points. Rotating this line about the axis produces a conical surface containing all inflection points.

4.3.2.6 Inflection point on the Busemann streamline

Although the inflection point is mathematically a part of the general T-M flow, it is here discussed under Busemann flow because, of the four types of conical flow, it occurs only with Busemann type flow. An equation for the curvature of the T-M streamline is derived to show that the streamline can have points of zero and infinite curvature. The Busemann streamline has two points of zero curvature where one of these points has significance in the starting of a Busemann-type intake. A point of infinite curvature exists in M-flow as discussed below. The conical surface containing all inflection points in a typical Busemann flow is shown in green in the sketch above.

The defining equation of the T-M streamline is,

$$dr / d\theta = ru / v \quad (4.15)$$

where u and v are the radial and angular components of Mach number as used in the T-M equations. Taking another θ -derivative of (4.15) gives,

$$\frac{d^2r}{d\theta^2} = -r \frac{u}{v^2} \frac{dv}{d\theta} + \frac{r}{v} \frac{du}{d\theta} + \frac{ru^2}{v^2} \quad (4.19)$$

In polar coordinates the curvature of a planar curve is [Kreyszig, p.34, 1991],

$$D = \left(\frac{\partial \delta}{\partial s} \right) = \frac{r^2 + 2 \left(\frac{dr}{d\theta} \right)^2 - r \frac{d^2r}{d\theta^2}}{\left(r^2 + \left(\frac{dr}{d\theta} \right)^2 \right)^{3/2}} \quad (4.20)$$

Eliminating the derivatives of r with Eqns. (4.15) and (4.19) gives,

¹³ An analog of this flow exists in planar flow where the region B_1B_2O is a Prandtl-Meyer compression fan, the region B_2B_3O is then uniform, the shock OB_3 is plane and the flow in region 3 is again uniform.

$$D = \frac{r^2 + 2(ru/v)^2 + r^2 \frac{u}{v^2} \frac{dv}{d\theta} - \frac{r^2}{v} \frac{du}{d\theta} - (ru/v)^2}{(r^2 + r^2 u^2 / v^2)^{3/2}} \quad (4.21)$$

In this expression the derivatives $dv/d\theta$ and $du/d\theta$ are given by the T-M equations (4.4) and (4.5) so that the curvature can be written,

$$D = \frac{uv(u + v \cot \theta)}{r(v^2 - 1)(v^2 + u^2)^{3/2}} \quad (4.22)$$

This equation gives the curvature of the T-M streamline in terms of the polar coordinates, r and θ , and the radial and polar Mach number components, u and v . A number of very interesting and important features, about the T-M streamline, become apparent from an examination of its curvature as given by Eqn. (4.22):

1) D is inversely proportional to r so that when $r \rightarrow 0$ then $D \rightarrow \infty$. This means that streamlines near the origin of T-M flows are highly curved. This is a necessary condition for flow over a cone, where flow, near the tip and just aft of the conical shock, has to rapidly adjust to the inclination demanded by the cone since the flow deflection produced by the conical shock is insufficient for the flow to be tangent to the cone surface. Similar highly curved streamlines are to be expected near the origin of Busemann and M-flows. Conical flow is not conically symmetric (i.e. independent of r) when it comes to gradients of its dependent variables, such as streamline curvature, – the dependence being inversely proportional to r . This extends to other flow property gradients as well.

2) There is an asymptotic condition, ($D = 0$) in the T-M streamlines at $v = 0$. For flow over a cone, $v = 0$ at the cone surface. This confirms that the streamlines become asymptotic to the cone surface as they approach the surface. There is no $v = 0$ or $u = 0$ asymptotic condition in W-flow or M-flow and no $v = 0$ condition in Busemann flow.

3) When $u = 0$ then $D = 0$. This means that the streamline has a point of inflection at the place where the radial Mach number is zero. For flow over a cone and for M-flow the condition $u = 0$ never occurs, so that the streamlines are curved monotonically positive for these two flows. However, for Busemann flow there is a location, θ_o , where the streamline changes from being concave towards the axis (negative curvature) to being

convex (positive curvature). Numerical integrations of the T-M equations have shown that θ_o always lies in the interval θ_2 to $\pi/2$ (first quadrant) somewhat upstream of the Busemann shock as shown by the green line in Fig. 4.3. Every Busemann streamline has an inflection point and these points form a conical surface. At this angular location the flow is everywhere normal to the inflected flow cone surface, whose half-angle is θ_o and a conical normal shock can be placed here since the Mach number is supersonic! The shock could be coaxed into taking up this position by allowing enough mass spillage to occur upstream of the inflection location, [Fabri,1958] and by restricting the downstream contraction to that allowable by the Kantrovitz criterion for flow starting. Flow just downstream of the conical normal shock is inclined towards the axis. This is tolerable everywhere but not right at the axis since at the axis the flow must be aligned with the axis. This ($r \rightarrow 0$)-type singularity is similar to the cone-tip singularity described above; its existence, in the idealized form, has not seen confirmation by experiment or CFD. If the contraction downstream of the conical normal shock surface does not lead to choking, then the shock would move downstream and the intake would start spontaneously. This feature has not been appreciated for Busemann flow and it has some significance in the design of self-starting supersonic/hypersonic air intakes. It is a conical and axisymmetric example of the starting criterion proposed by Kantrovitz for one-dimensional flow, embodying the same principle of flow choking downstream of a normal shock where, in this case, the normal shock has a conical shape.

4) There is a point of inflection also when $(u + v \cot \theta) = 0$. The quantity $(u + v \cot \theta)$ is the component of Mach number normal to the flow axis. For Busemann flow it is zero only where the Busemann flow joins the free stream. Thus the leading edge of the Busemann flow has not only zero deflection but also zero curvature. Aerodynamically this means that the leading edge wave is neither compressive nor expansive but is a zero-strength Mach wave. The fact that the entering free stream flow is neither deflected nor curved by the Busemann leading edge means that the leading edge of a hypersonic air intake, based on Busemann flow, is totally ineffective in producing compression. This provides a clear incentive to truncate some length of the leading edge surface so as to decrease viscous losses without incurring serious inviscid flow losses. For M-flow the potential appearance of the condition $(u + v \cot \theta) = 0$ is prevented by the appearance of

the ($v = 1$)-singularity (described below) so that the down-shock flow never becomes parallel to the freestream. This is unfortunate from a practical viewpoint since it presents no possibility of grafting on any of the flows that have a uniform upstream such as cone or Busemann flows to the downstream of M-flow. From a fundamental viewpoint it presents an obstacle to the possibility of conical shock reflection at the centre line of symmetry.

5) When $v \rightarrow \pm 1$ then $D \rightarrow \infty$; the curvature is infinite and the streamline has a cusp or a corner. This indicates a *singularity* or a *limit line*. Neither cone nor Busemann flow exhibit such a limit line. However it does occur in both M- and W-flows.

6) The quantity $(v^2 + u^2)^{3/2}$, appearing in the denominator of (4.22), is just M^3 . It is always a positive quantity for all flows and has no drastic characterizing effect on D except to force streamlines to lose their curvature, to straighten out, at hypersonic speeds.

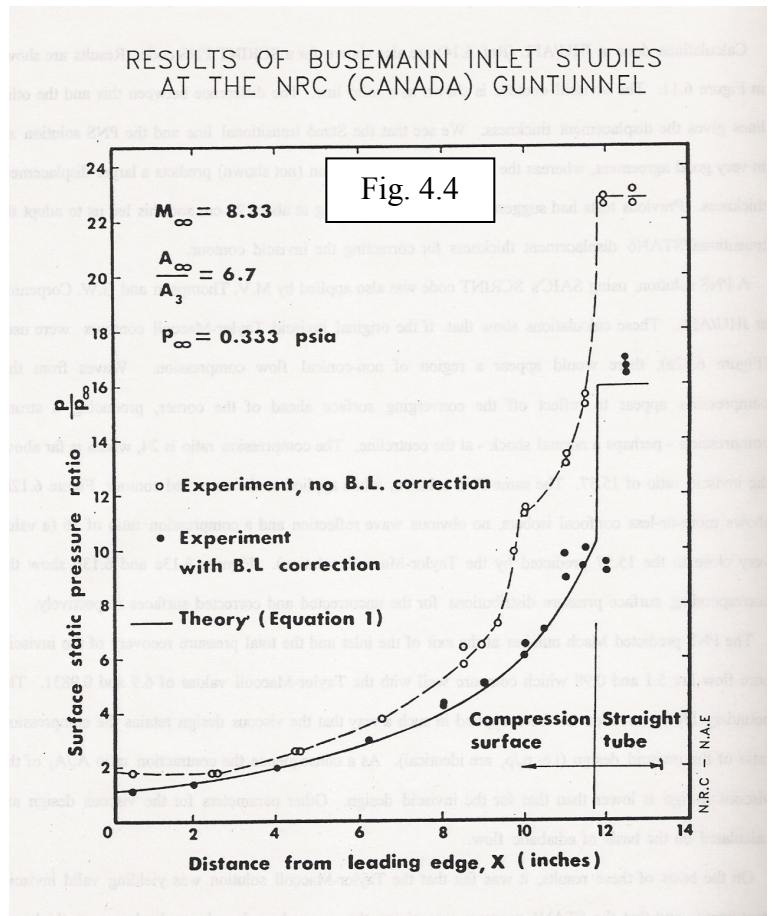
4.3.2.7 Wind tunnel tests on Busemann flow

Busemann flow was tested in the NRC/NAE hypersonic gun-tunnel at a Mach number of 8.33 and a Reynolds number of $15 \times 10^6/\text{m}$ and in the DRDC trisonic tunnel at a Mach number of 3.00 and a Reynolds number of $0.5 \times 10^6/\text{m}$. Tests on M-flow were also conducted in the NRC/NAE facility. Experiments on both the Busemann and M-flows were conducted in axisymmetric test models whose surface contours were calculated from the T-M equations for axisymmetric, conical and steady flow.¹⁴ Model contour shapes were corrected for laminar compressible boundary layer displacement. Both Busemann flow and M-flow, as modeled by both the T-M equation, as well as CFD analysis, predicted local high gradients in flow properties, including density. These density variations should be visible to any of the conventional optical flow visualization techniques used in supersonic tunnels. Evidence of such high gradients was sought in experiments and CFD results.

¹⁴ Attainment of flow with axial symmetry is advantageous in aerodynamic testing of internal flows because it eliminates the uncertainties caused by 'end effects' that plague experiments on shock interactions in planar flows. Its disadvantages are that it offers short optical light paths through density gradients so that weak disturbances become hard to detect and the axial solid surfaces are often impediments to optical flow visualisations.

4.3.2.8 Busemann tests in the gun-tunnel at Mach 8.33

An axisymmetric Busemann intake was constructed and tested in the NRC/NAE hypersonic gun-tunnel. The test model was designed for the tunnel Mach number of 8.33. It has a circular intake of 2.2 in. diameter and a Busemann contour length of 11.8 in. Its design exit Mach number is 5.39 with a compression ratio of 15.55 and an area contraction ratio of 6.71.¹⁵ Solid curve in Fig. 4.4 shows the theoretical surface pressure distribution. “Equation 1” refers to the T-M equation result. There is a smooth increase in pressure along the compression surface until the conical chock causes a pressure jump at 11.80 in. After the jump the pressure



levels off in the constant area section. First measurements (open circles) showed a higher-than-theoretical surface pressure distribution. A boundary layer displacement correction was applied and the pressures, now shown by solid circles, showed good correspondence with theory. The boundary layer effect on the exit pressure is significant in that it causes a pressure rise from 16 to 22 – a rise of 38%. Although the Busemann

¹⁵ This area ratio is far above the spontaneous starting value of 1.67 so that the intake would not start under steady-state conditions. However, the transient starting flow in the gun-tunnel nozzle is such that, in sweeping through the model, it causes supersonic flow starting in the model. This fortunate flow behaviour makes it possible to test high contraction intakes in gun-tunnels where they would not start in steady state wind tunnels.

wave structure had not been seen by any optical means, this was good evidence for Busemann type flow to exist.

4.3.2.9 Busemann tests in the wind-tunnel at Mach 3.00

A solution of the T-M equation for the Busemann flow shows a leading edge region of surface that causes a set of compressive confocal characteristics (CCC) to focus at the origin of the conical flow. This is followed by a region of non-uniform conical flow, in turn followed by a freestanding conical shock (as described above). Such axisymmetric flow structure has not been previously observed, at least not where it has been purposefully designed to meet specific criteria. This section describes an experiment to demonstrate the existence of CCC as well as the conical shock, both designed to specific criteria. The aim is to show that a reflected conical shock can exist at the centre line even though the incident wave is not a conical shock but a compression wave. Whatever prevents a conical shock/shock reflection is thus absent in the case of a CCC/shock reflection and one should then be able to compare the flows produced by a conical incident shock and by the CCC to see what prevents a conical reflected shock from forming in conjunction with a conical incident shock.

A solution of the T-M equations was performed as described above for Busemann flow above for the full Busemann intake. At the upstream side of the conical shock the Mach number was set at 1.800 and the aerodynamic shock angle at 42.88 degrees. These produced a normal-to-the-shock Mach number of 1.225. Integration of Eqns. (4.5) and (4.6) produced the Busemann streamline coordinates and the freestream Mach number 2.998. The coordinates were corrected for a laminar, compressible, axisymmetric boundary layer. Rotating the corrected streamline around the axis of symmetry created a leading edge portion of the Busemann intake surface.

A length of the leading edge portion of the surface was chosen such that the resulting internal contraction would allow the internal flow to start at a tunnel Mach number of 3.0 and such that the duct would be short enough to expose the focal point to the schlieren beam in the downstream flow. This required a 20 cm diameter duct with a length of 20 cm. The duct is shown mounted in the DRDC Trisonic Wind Tunnel on four swept support arms, Figs. 4.5 and 4.6.

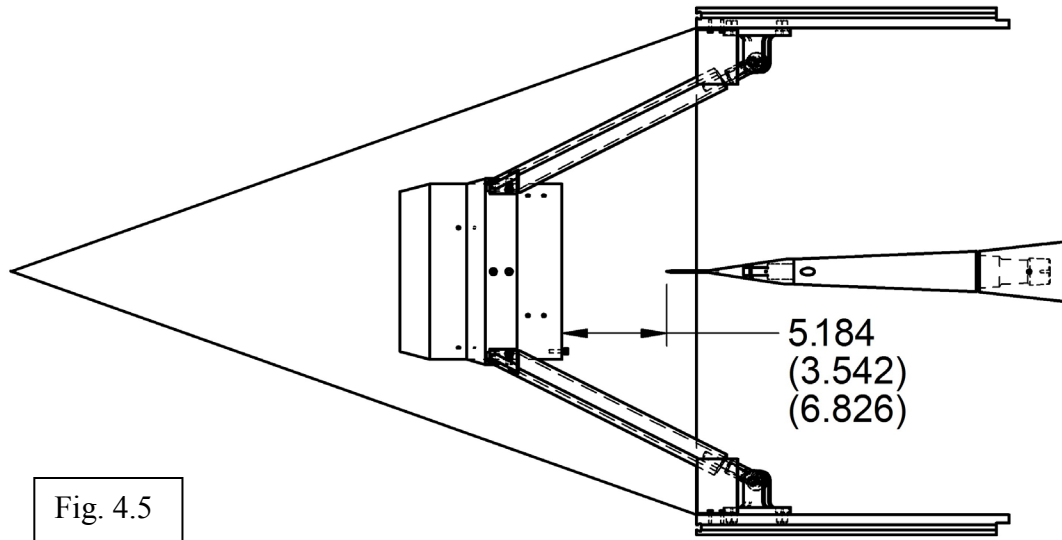


Fig. 4.5

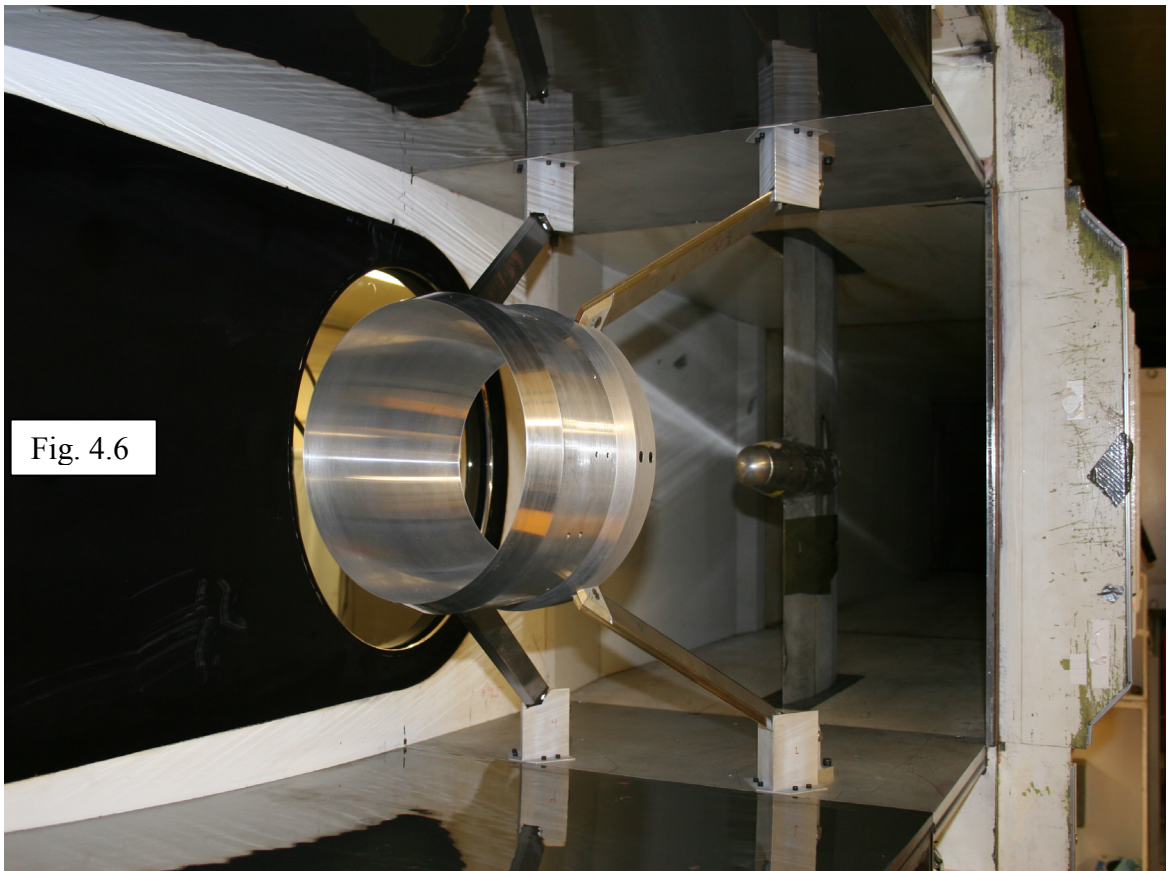
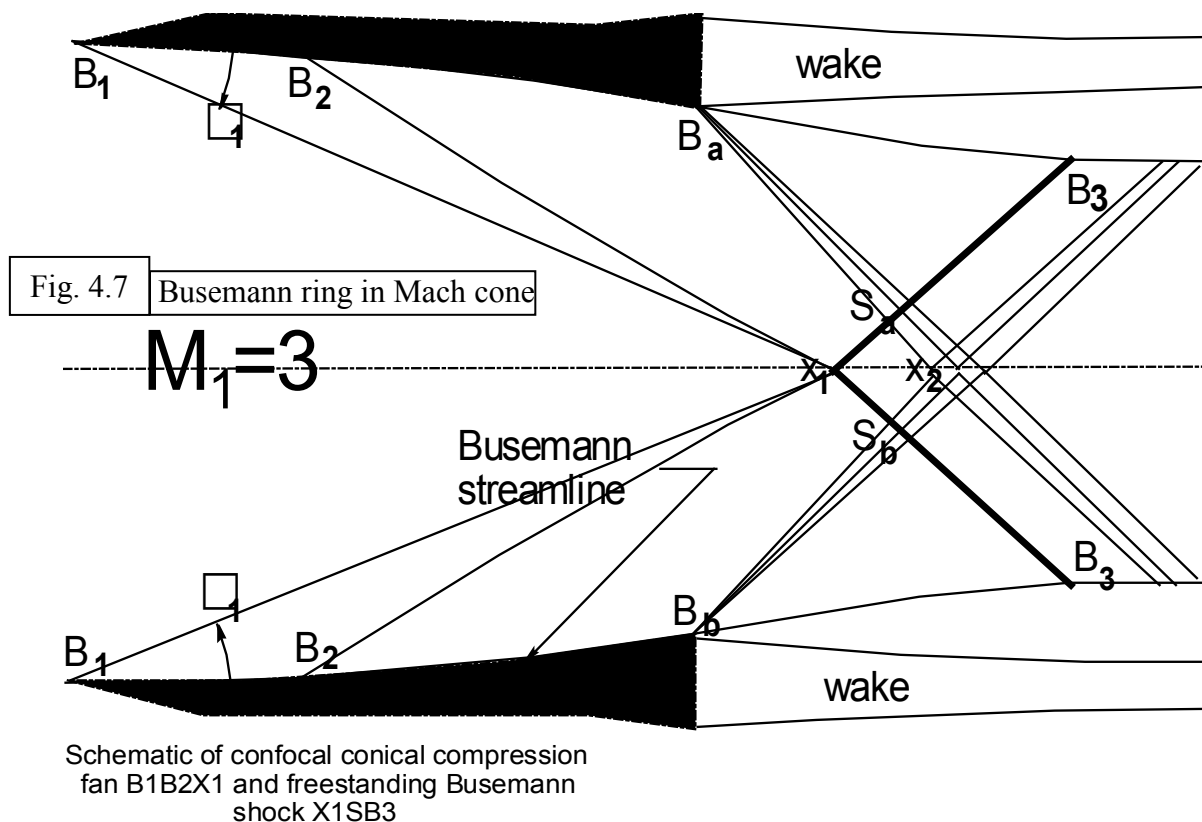


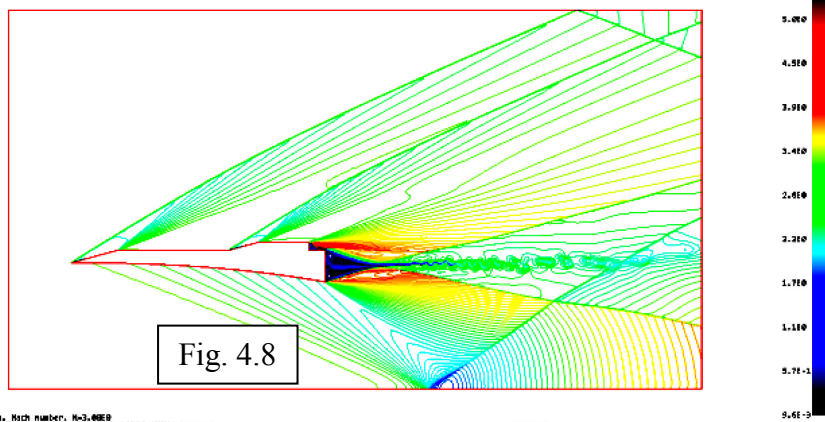
Fig. 4.6



Referring to the interpretive sketch, Fig. 4.7, CCC is contained in the region $B_1B_2X_1$. All the characteristics from B_1B_2 focus to X_1 . Characteristics from B_2 to B_a impinge on the front of the conical shock from X_1 to S_a . The calculated Busemann streamline is shown extending from B_a to B_3 . In the experiment there is no such streamline and a wake forms instead behind the base of the truncated profile. The whole flow is axisymmetric and, in the whole region $B_1B_2B_aS_aX_2X_1$, it is conical as well. The theoretical Mach number behind the apex of the shock is 1.48. The static pressure is 10.10 times the free stream pressure. The Mach number upstream of the shock is 1.80 (the flow is inclined towards the shock and the axis). The total pressure recovery across the shock is 0.992. Normal Mach number is 1.22. Figure 4.8 shows a CFD SolverII simulation of the flow-field in and around the model. At the centre line the shading shows an incident compression followed by a distinct conical shock. Figure 4.9 is a schlieren picture of the flow at the exit of the model at a tunnel Mach number of 3.00. Flow is from left to right. The exit diameter covers the height of the picture. Two X-shaped wave structures are apparent at the exit of the duct in the middle of the picture. The downstream structure has two left

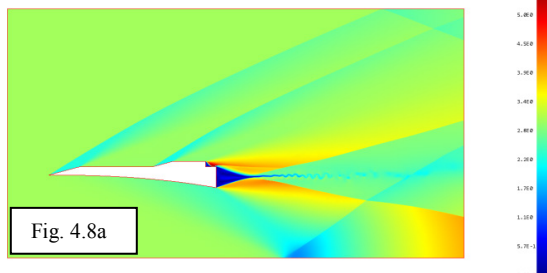
branches that represent the leading portion of an axisymmetric expansion emanating from the trailing edge of the Busemann ring. This wave reflects from the centre line as an axisymmetric expansion and it is of no direct interest. The upstream X-shaped wave structure emanates from the Busemann contour. The upstream branches represent the conical confocal compression fan. The leading wave of this fan originates at the leading edge of the Busemann ring and the trailing wave is the last wave of the CCC. Waves downstream of this do not go to the focal point but meet the conical shock along its length.

After 26246 time steps, $t = 4.085275E2$, $dt = 9.381E-3$, 153819 nodes present

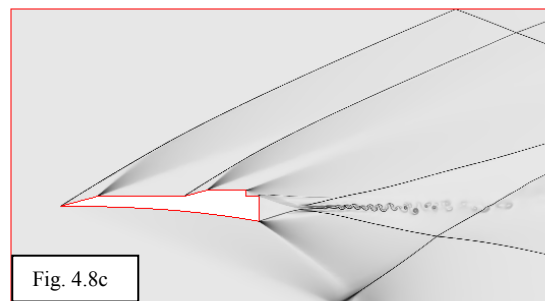


N/A, Mach number, $M=3.00E0$

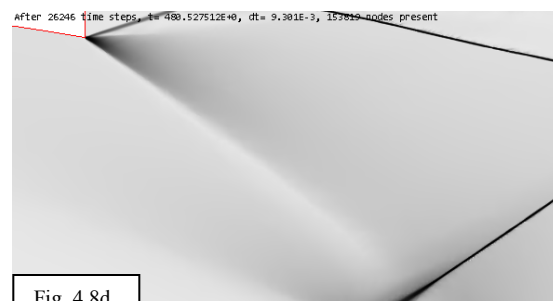
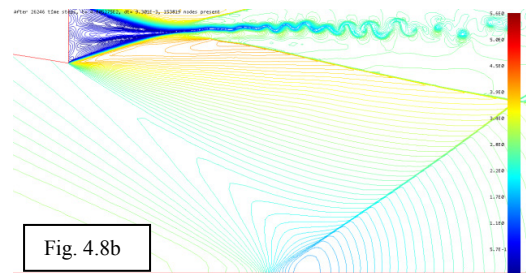
After 26246 time steps, $t = 4.085275E2$, $dt = 9.381E-3$, 153819 nodes present



After 26246 time steps, $t = 488.527512E+0$, $dt = 9.381E-3$, 153819 nodes present

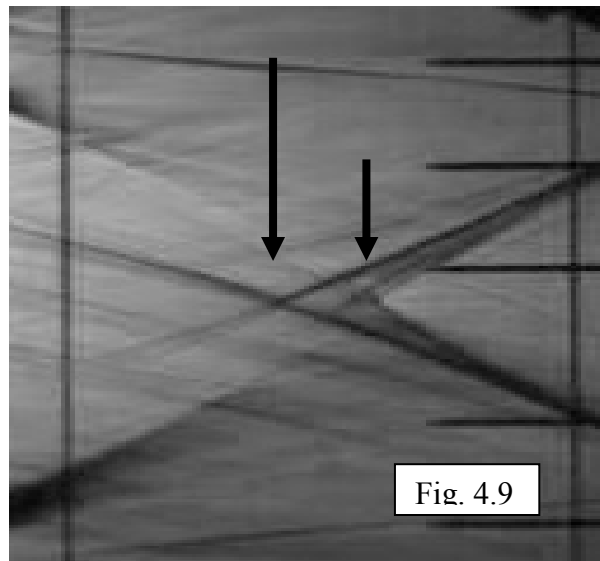


N/A, Mach number, $|M|$, $M=3.00E+0$



N/A, Mach number, $|M|$, $M=3.00E+0$

Figures 4.8a-d are CFD simulations of the Busemann ring as rendered in a simulated colour schlieren, constant Mach number contours, pseudo-schlieren and shadowgraph.



The long arrow points to the focal point where the converging compression fan and the free-standing conical shock meet. The short arrow points to the centered conical compression fan. The analytically predicted Busemann flow and its features have been confirmed by both CFD and experiment. The approach presented here is the only method for establishing a centered axial compression and a conical shock at the centre line in a steady flow.

4.3.3 M-flow experiments and CFD results

The leading edges of hypersonic air intakes are designed with some degree of bluntness to cope with high rates of heat transfer. Bluntness causes flow deflection and leading edge shock waves, which get captured by the intake, to focus at the centre line, producing flow distortion and efficiency losses in the intake flow. Converging and interacting shocks, particularly at centre lines of axisymmetric flow, produce Mach reflections and complex flow structures which are difficult to predict and control. The one-to-one correspondence that exists between a shock and its uniform, deflected flow for planar shocks does not exist as soon as the shocks become axisymmetric and curved. Curved shocks produce curved streamlines and flow property gradients. Internal flow theories of curved shocks are plagued by singularities. M-flow is a one-parameter, axisymmetric, conical, internal flow that has been discussed by Mölder (1967) and Rylov (1990). Its inherent axial and conical symmetry makes it simple to analyze and an ideal

candidate for generating intake leading edge surfaces for non-planar intakes. M-flow is examined in some detail because it is an example of flow and shock wave structure caused by flow deflection at the internal leading edge of an axisymmetric intake. A polar coordinate system (r, θ) is used where u and v are the Mach number components in the r and θ direction so that $M^2 = u^2 + v^2$. M-flow occurs behind an axisymmetric conical shock, with a downstream-pointing apex, sitting in a uniform upstream flow. It is supported by the inside surface of a ring that deflects the flow towards the axis of symmetry (see Fig. c in Sec. 4.1). This flow occurs at the sharp leading edge of an intake cowl where the leading edge angle is finite. Boundary conditions for M-flow are the same as those for cone flow except that the shock angle now lies in the second quadrant, in the angular range $\pi/2$ to $\pi - \mu_1$. The integration proceeds with a decreasing θ (clockwise) and, for all the cases calculated, always ends up at a singularity (limit line) where $v = -1$. At this value of θ the streamlines have a kink (corner) or a cusp where the flow turns back on itself.

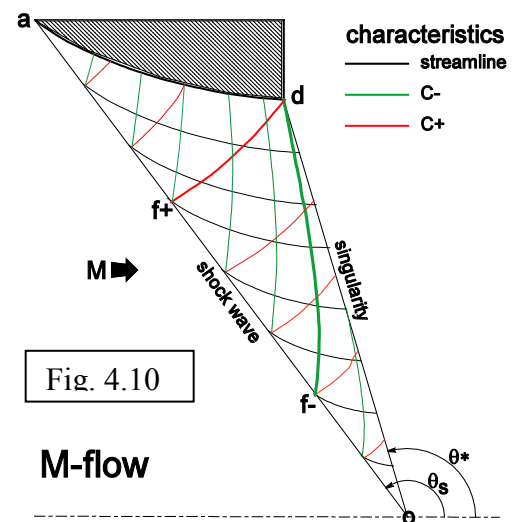


Fig. 4.10

M-flow

This is a physical impossibility, indicating that the assumptions of conservation of mass and energy, the momentum balance, the equation of state, inviscid flow, axisymmetric flow, conical flow and a smooth streamline cannot all be locally satisfied at some value of θ . At the singularity, Eqn. (4.22) predicts an infinite curvature – a sharp corner. A centered Prandtl-Meyer fan would normally occur at such a corner. We have named this type of flow ‘M-flow’ because the shock and the surface shape resemble the letter M when rotated 90 deg counter-clockwise. Computational and experimental M-flow results are in Sec. 4.3.3.

We assume the physical existence of an axisymmetric conical shock, in uniform flow, where the apex of the shock points in a downstream direction and the flow is directed into the shock cone, Fig. 4.10. Conical M-flow is in the region **oad**. Shock is at θ_s . M-flow streamline **ad** causes straight shock **oa**. Flow accelerates from **a** to **d** reaching $v = -1$ at the singularity at θ^* . **df⁺** and **df⁻** are the (+) and (–) characteristics through **d**.

Inclination of the shock with respect to the free-stream direction is everywhere the same, so that the shock is of uniform strength. Hence, conditions immediately behind the shock are everywhere the same and the downstream flow is irrotational and both conically and axially symmetric. Conicality implies that flow quantities remain constant on the surface of con-focal cones while changing from cone to cone in a downstream direction. As pointed out above, such flows are governed by the T-M equations and, for M-flow, their integration is started at the back of the shock, with θ in the second quadrant, at the shock angle θ_{12} and a free-stream Mach number, M_1 . The initial Mach numbers u and v are found from Eqns. (4.7) and (4.8) and they are both negative immediately behind the shock. Concurrent integration of the streamline equation, (4.6), produces a smoothly curving convex internal M-flow surface **ad**, with the surface Mach number slowly increasing in the downstream direction along the surface from **a** to **d**. All other streamlines in the M-flow region are similar to **ad** and scale geometrically linearly with distance from **o**. As the integration proceeds downstream from the shock, with decreasing θ , the v -Mach number soon reaches -1, leading to infinities in both $du/d\theta$ and $dv/d\theta$, at an angle θ^* , as is evident from Eqns. (4.4) and (4.5). Any forced continuation of the integration downstream of the singular cone, θ^* , leads to scattered results that depend on just exactly how the singularity is numerically over-stepped. The rapid change in v , at the singularity surface, suggests the presence of a shock wave where the Mach number component normal to the shock is discontinuous across the shock. However, the singularity surface cannot be a shock because its normal Mach number component is one and, furthermore, the rapid change of properties approaching the singularity is expansive rather than compressive. Concurrent integration of the C^+ and C^- characteristics is discussed below. The characteristics are also self-similar. The C^+ characteristic **df**⁺ forms one of the boundaries of the region **adf**⁺ whose disturbances can influence conditions on the surface **ad**. It intersects the singularity at an angle 2μ at **d**. The C^- characteristic **df**⁻ is a boundary to the region **adf**⁻ whose properties determine the shape of the shock **af**. The C^- characteristic intersects the surface at the point where the singularity intersects the surface and it is tangential to the singularity at this point. The shock from **f** to **o** is determined by the C^- characteristics originating on **od**; these all being tangential to **od**. In fact, it is the surface singularity point **d** that determines the shock

from **o** to **f** since no characteristics from downstream of **d** can penetrate the singular line **od** – at least not in conical flow. This peculiar behavior in supersonic flow casts some doubt on the existence of conical flow behind a concave conical shock. For this reason it is suspected that the problematics of the singularity and the questionable existence of regular shock reflection at the centre line are causally connected. If M-flow exists in the whole region **oad** then the conical shock has to proceed to the centre line, as shown in the figure above, and for conical flow to exist at the centre line there has to be a conical reflected shock there. Such ‘regular reflections’ are common in flow with planar shocks [see Ben-Dor, 2007]. Although regular reflection of shocks has been produced at the centre line for cylindrically collapsing shocks, in unsteady flow, and seemingly also for weak shocks in steady flow [Hornung (1999)], there are claims that RR is not possible at the centre line in steady flow [Rylov (1990)].

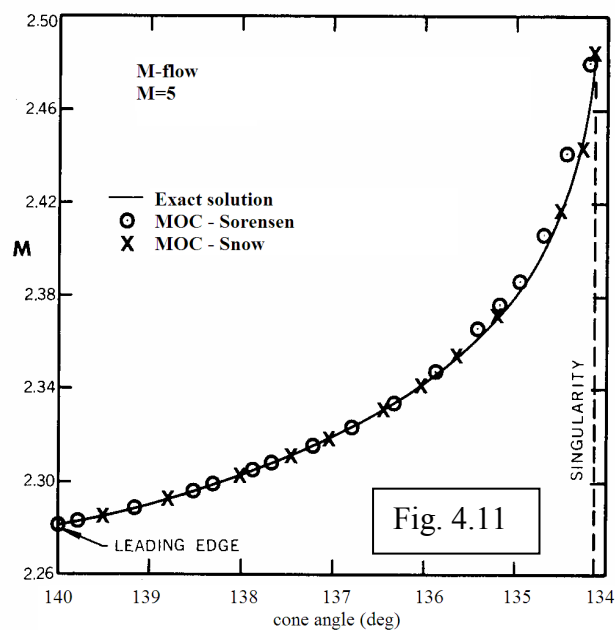
The first question then is, does the M-flow with a conical shock and a downstream conical flow really exist? In particular, does the shock extend from the leading edge all the way to the centre? The T-M equations pose no objections. One is also prompted to ask whether such singularities with high gradients really exist in the flow or are they just some kind of mathematical artifacts arising from the enforced symmetry or are the gradients inimical in themselves in forcing an end to the existence of downstream continuance of axial or conical symmetry or steady flow. The remainder of this section presents a T-M solution for the ideal M-flow including the surface shape and the surface pressure distribution. This surface shape is then used in the Method of Characteristics to calculate a new surface pressure distribution. As with the Busemann flow calculation, the MOC is not aware of the conicality assumption inherent in the T-M solution for M-flow. The Solver II code is used in a similar manner to calculate the surface pressure distribution as well as the internal flow over the M-flow contour. Solver II is not informed of either conicality or the existence of a final steady state M-flow. Only axial symmetry is imposed.

4.3.3.1 Characteristics on M-flow contour

In the previous section a characteristics mesh was superposed on an M-flow flow-field solution without asking whether such a flow existed in the first place. In this section

an MOC solution is done on an M-flow surface contour. The purpose is to seek a numerical confirmation of M-flow as calculated from the T-M equations. An M-flow surface was first calculated by a T-M solution for a shock angle of 140 degrees at a freestream Mach number of 5.

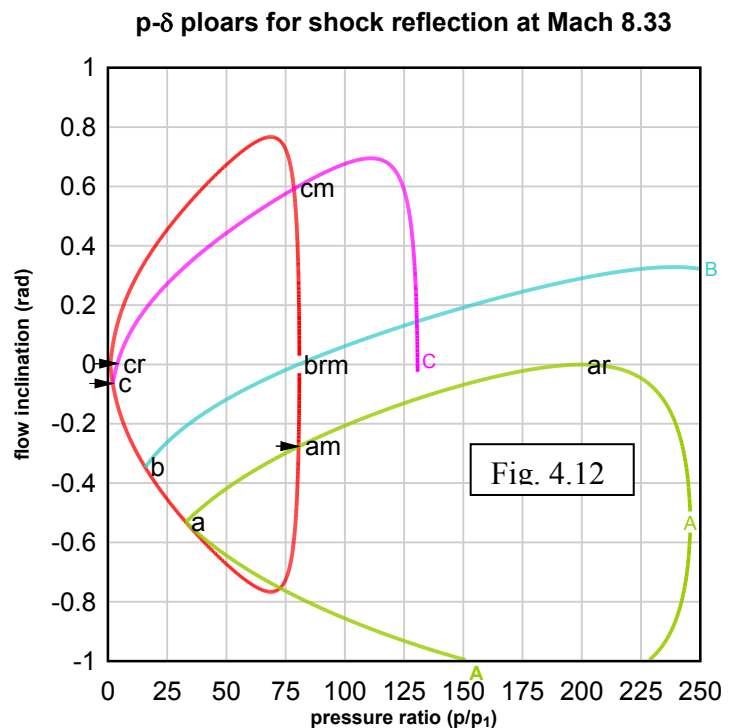
The surface coordinates were input into a Method of Characteristics program that had been developed by M. L. Snow (1966) of the Applied Physics Laboratory of The



Johns Hopkins University (JHU/APL) especially for the calculation of internal supersonic flows. A similar MOC code by V. L. Sorensen (1965) was used as well. The latter method had to be adapted for internal flow. The Mach number variations on the M-flow surface is labeled as 'Exact' when calculated by solving the T-M equations (4.4 and 4.5). The two characteristics methods of Sorensen and Snow are shown as circles and crosses. There is excellent

correspondence between the exact T-M and both MOC results for the surface Mach number distribution, differences being no more than 0.02 of a Mach number. All methods terminated at the predicted location of the surface singularity $\theta = \theta^*$. The T-M calculation stopped because both $du/d\theta$ and $dv/d\theta$ approached infinity. The MOC methods stopped and the calculation could not proceed because the characteristic from the surface singularity overtook the previous characteristic of the same family at the shock wave. The MOC stopped just before – typically 0.1 deg in front of the singularity. The MOC results have confirmed the T-M analysis for predicting the M-flow surface shape as well as the flow properties on it. But they have also indicated that there is a problem at the singularity – at least in continuing the calculation further with MOC as well as with T-M.

The point, on the shock, (R^-), where the overtaking occurred in the MOC methods of Snow and Sorensen, was short of the centre line and the singularity. This indicated that the region of influence of the M-flow surface was bounded by the surface s_1s_2 , the last calculated characteristic from the singularity, s_2R^- , and the shock, s_1R^- as in the figure above. More significantly, only the portion of the shock from s_1R^- was determined by the surface, the remainder, R^-o , up to the centre line was not influenced by the M-flow surface. The T-M solution predicted that the shock segment from R^- to o is determined by characteristics similar in shape to s_2R^- , starting from somewhere on the singularity between s_2 and o . Characteristics that started from a surface point just downstream of s_2 , overtook the previous characteristic at the shock, tending to form a secondary shock there. This shock would overtake and strengthen the straight shock coming from the leading edge. The leading edge shock would become curved and the flow behind it would become rotational. The two MOC methods were now trying to indicate that M-flow could be expected to be confined to the region $s_1s_2R^-$ and not to extend throughout s_1s_2o as predicted by the T-M solution. It was interesting to note that the two MOC's, that 'knew nothing' about the singularity proceeded through it without difficulty encountering a problem only at the shock.



4.3.3.2 M-flow experiments in the guntunnel at Mach 8.33 and CFD results

A series of experiments were conducted in the Mach 8.33 Gun Tunnel at the National Aeronautical Establishment of the National Research Council in Ottawa in an attempt to demonstrate the existence of M-flow and to discover the physical nature of the

flow near the singularity as well as at the centre line. The challenge was to discover what happens to conical shocks, reflecting off the centre line, at shock angles that produce well understood reflections of planar shocks at a plane wall. Three different M-flow surface rings were constructed that, at a free stream Mach number of 8.33, would produce shock angles of $A = 145.0$, $B = 153.7$ and $C = 170.5$ degrees with corresponding flow deflection angles of $a = -30.45$ deg, $b = -19.27$ deg, $c = -3.69$ deg. Figure 4.12 shows pressure-flow-inclination polars for regular and Mach reflection at Mach 8.33. Red polar is for the incident shock (I). Incident shock angles for the other polars are: (A) green 140.3; (B) blue 153.7; (C) purple 170.5. Conditions for regular reflections are indicated where the reflected shock polars cross the flow inclination = 0 axis, typically **ar**. Mach reflections occur where the reflected (A, B, C) and incident (I) polars intersect, typically **am**. These particular shock angles were chosen to produce for, A, a Mach reflection **am**; for B, the von Neumann reflection condition where both regular and Mach reflection can theoretically exist at **brm** with no flow deflection through the point of reflection; and for C, a very weak incident shock reflecting regularly as a very weak shock at **cr** or as a Mach reflection with a strong reflected shock at **cm**. The polar intersections are representative of conditions that occur with planar shocks. In our search for conical shocks that would regularly reflect at the centre line we would be on the look-out for conditions represented by **ar**, **brm** and **cr** since these yield zero net flow deflection as demanded by the centre line boundary condition.

Numerical values for the polar intersections are given in the following table where the subscripts 1, 2 and 3 refer to conditions in front of the incident shock, behind the incident shock (same as in front of the reflected shock) and behind a reflected shock. In all cases the reflected shock is assumed to deflect the flow back to the freestream direction. Conditions are based on reflection of planar shocks where the inter-shock space is uniform.

	SHOCK	A	B	C
M_1	I	8.33	8.33	8.33
θ_s (deg)	I	145.0	153.7	170.5
M_2	I	2.56	3.97	7.42
p_2/p_1	I	32.86	15.72	2.04
δ_1 (deg)	I	0	0	0
δ_{12} (deg)	I	-30.45	-19.87	-3.69
p_3/p_1	R	200 ar	80 br	4.0 cr
p_3/p_1	M	79 am	80 bm	75 cm
δ_2 (deg)	Rm	-30.45 arm	-19.87 brm	-3.69 crm
δ_3 (deg)	R	0 ar	0 br	0 cr
δ_3 (deg)	M	-16 am	0 bm	34 cm
δ_{23} (deg)	R	30.45 ar	19.87 br	3.67 cr
δ_{23} (deg)	M	14.45 am	19.87 bm	37.7 cm

4.3.3.2(A) The 145 deg shock

An axisymmetric M-flow tunnel model was constructed for a freestream Mach number of 8.33 to produce a conical shock with a shock angle of $A = 145.0$ deg. The model was tested in the National Research Council's Gun Tunnel. Polar A in Fig. 4.12 represents the possible pressure/deflection conditions behind the reflected shock. Figure 4.13a shows a schlieren picture of the flow as it emerges from the M-flow ring. Freestream flow comes from the left. The incident shock, generated by the M-flow surface, appears to be axisymmetric and conical. However, it does not extend to the centre-line but, rather, terminates at a triple-shock confluence off the flow axis and, clearly, the regular reflection condition **ar**, as demanded by the centre line, does not appear. The triple-point is the intersection of the incident shock, the reflected shock, a Mach shock (Mach disc) and a shear layer – a typical Mach interaction designated by **am**. The Mach disc appears to be flat and normal to the flow (more about this later). Both the reflected shock and the shear layer have a definite positive curvature – their angles increase with distance from the triple point. The shear layer is inclined towards the centre

line. No sharp density gradient is observed just downstream from the incident wave, where the singularity is predicted to lie. Dark and light shadings in front of the incident shock and elsewhere are not indications of density gradients but are merely optical effects of schlieren due to the circular shape of the discontinuities. Fine lines are contours produced by the CFD calculations of Solver II. Conical flow, mostly hidden by the ring, seems to come from the leading edge but it clearly breaks down at the centre line. Since the shear layer is angled towards the centre line at the triple point, it must be that the Mach disc is angled there as well and it cannot be normal to the free-stream flow. The Mach disc is of the strong shock family. That is why its inclination is small and hard to detect because a strong shock wave angle is close to 90 degrees, even for substantial flow deflections through the shock. The flow appears top-to-bottom symmetric so there is a good possibility that it is also axisymmetric.

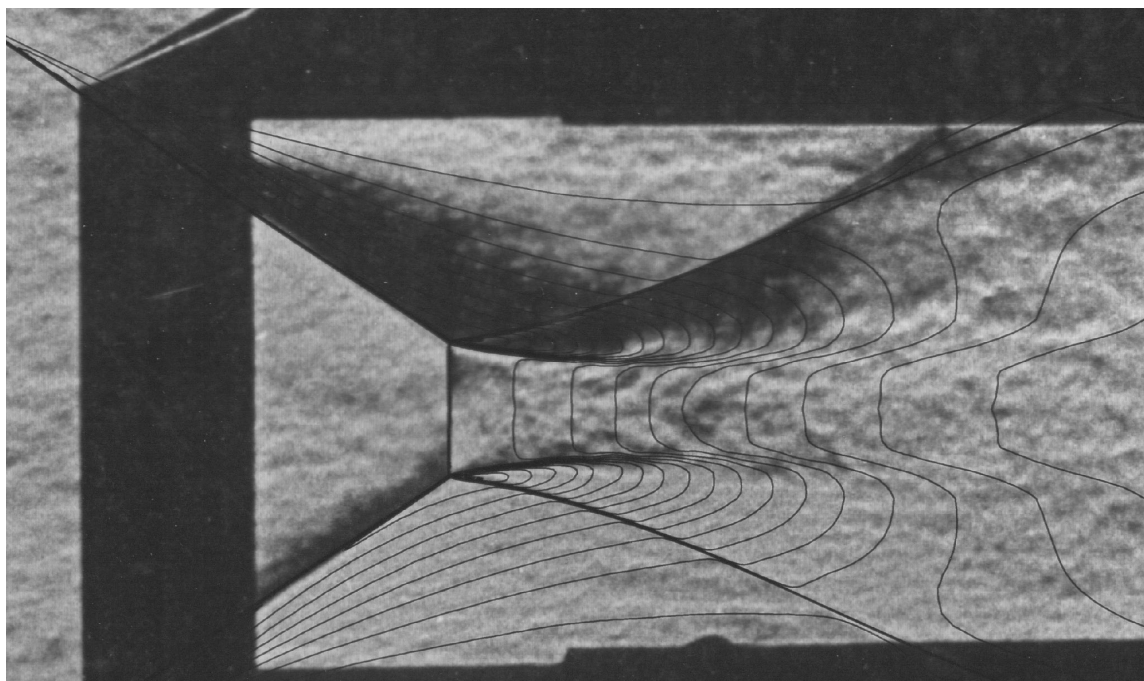


Fig. 4.13(A) M-flow at a free stream Mach number of 8.33, coming from the left and passing through a 145 deg conical shock. Superimposed contours are calculated constant density lines; their coalescence indicates shock waves. Picture shows a prominent Mach reflection with distinctive shear layer around the centre line. The density contours have been zoomed to fit the schlieren picture at the diameter of the Mach disk.

We conclude that a 145.0 deg conical shock does not reflect regularly off the symmetry axis. Instead, a Mach reflection is formed off the centre line. Flow at the triple point of this Mach reflection is turning towards the axis, as predicted by the triple point solution on the shock polar. There is good agreement between experiment and CFD, both showing that RR does not occur at the centre line for a conical incident shock.

4.3.3.2(B) The 153.7 deg shock¹⁶

If we think of moving the triple point closer to the centre line, without changing its geometry, then eventually, the inward flow turning at the triple point can no longer be tolerated by the centre line because axial symmetry requires that the flow inclination be zero right **at** the centre line. So, is this the reason for cessation of conical flow and regular shock reflection at the centre line? To answer this, we construct an M-flow surface that produces a shock that reflects in von Neumann reflection at the centre line (Molder 1967, Henderson 1990, BenDor 2007). The von Neumann reflection is a unique form of Mach reflection where the Mach disc is truly normal to the flow at the triple point and the flow deflection behind the triple point is zero, which makes it compatible with the zero flow deflection required by the centre line.

Von Neumann reflection occurs at a unique shock angle determined by the freestream Mach number. For Mach 8.33 the incident shock angle at the von Neumann reflection condition is 153.7 deg. The incident shock state is represented by polar B in the polar diagram Fig. 4.12. The von Neumann condition is at **brm** where the flow inclination aft of the reflected shock is zero. In this configuration, the triple point should be transportable to any location on the incident shock – including the centre line. The axisymmetric slip layer, now in the shape of a constant radius cylinder, would, in the limit, as the triple point is moved to the centre line, become a cylinder of zero diameter, to

¹⁶ For any kind of shock reflection to occur the incident shocks must always be in the ‘weak shock’ category because the flow behind strong shocks is subsonic and thus unable to sustain a reflected shock. That is, they must produce a pressure ratio that lies on the lower pressure branch of the pressure-deflection polar. For our purposes we further divide the lower pressure branch into ‘very weak’ and ‘weak’ shocks. The very weak are the shocks which, on Mach reflection, would produce a positive net flow deflection and the weak ones would produce a negative deflection. The two types are separated by the incident shock strength that produces no net flow deflection on Mach reflection. This condition is called the von Neumann (vN) condition.

merge smoothly with the centre line. For this as well as the previous case there is nothing derivable from the oblique shock relations that would indicate that RR is impossible at the centre line. An M-flow surface for this shock angle was calculated, machined and tested in the gun tunnel. The schlieren picture of the flow is shown in Fig. 4.13(B).

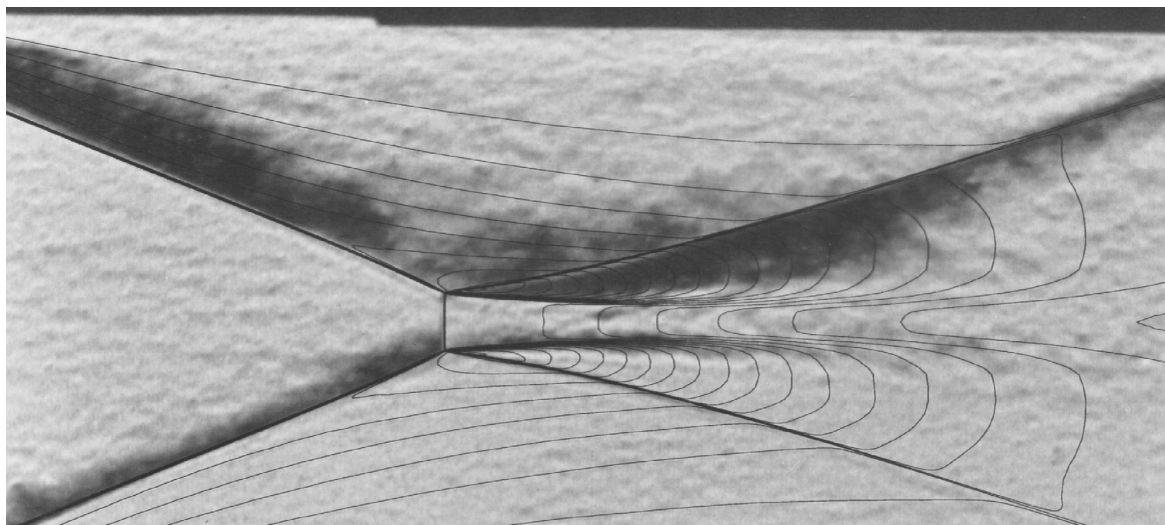


Fig. 4.13(B) M-flow at Mach 8.33 from the left passes through a shock at 153.7 deg. (the von Neumann angle). Contours are lines of constant density calculated by Solver II.

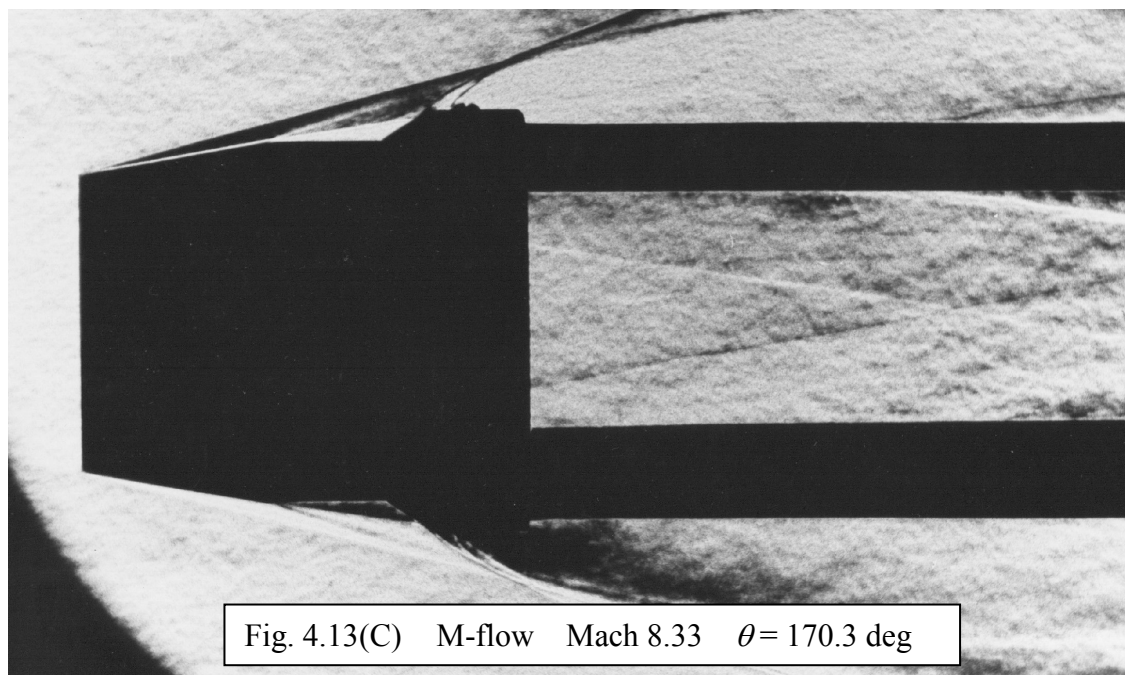
The Mach disk is now smaller than for case A, and the flow behind it appears to be less inclined to the centre line. However, there is a noticeable positive curvature on the incident shock, as it nears the triple point - it is no longer conical and so the flow behind it cannot be conical. Conical flow has broken down and the higher shock angle has taken us away from the von Neumann condition at the triple point. Axially the flow appears symmetric. Experiment and CFD are in good agreement in indicating that the attempt to experimentally coax the triple point to the centre line, by using the von Neumann shock interaction condition, has failed and there is still no appearance of any drastic density change at the predicted location of the singularity.

A number of questions arise: Where exactly does the conical flow break down? Why and how does it break down? Conicality does not vanish for cone flow or Busemann flow – why does it break down here? Why does conical and not axial symmetry break down? Since a singularity does not appear in cone flow or Busemann flow, is the breakdown caused by the singularity that occurs in conical flow theory for M-flow?

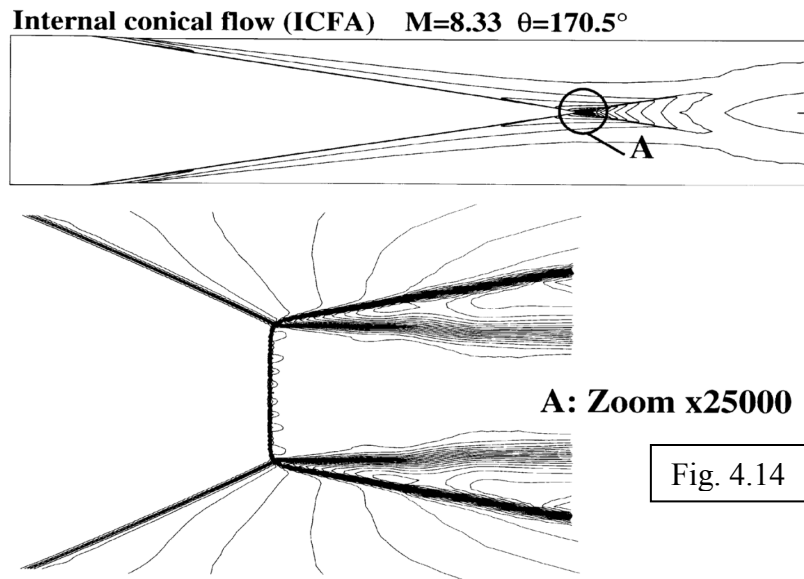
So far experiments have shown that both a conical shock of the weak family (A) and a von Neumann shock (B) reflect off the axis in Mach reflection. In both cases a Mach shock interaction has appeared at some distance from the flow axis of symmetry. The von Neumann shock curves towards the axis and acquires a strength above the von Neumann strength so that it deflects the flow toward the axis. No high flow property gradients are observed at the predicted location of the singularity. There is a definite discrepancy between experiment and predictions of the T-M conical flow analysis.

4.3.3.2(C) The 170.3 deg shock

Schlieren and shadowgraph pictures of supersonic flow exiting from axisymmetric nozzles have shown what appears like regular shock reflection at the centre line [Hornung (1999)]. Invariably, the nozzles have been fully or near-fully expanded, so that the shocks have been weak and the approach flow has been non-uniform. In a hypersonic air intake, the leading edge shocks should be weak also, so that the study of reflection of such shocks is relevant to hypersonic intake design. It was decided to produce a weak M-flow shock to see if it would reflect regularly at the centre line. An M-flow surface was constructed for Mach 8.33 and a shock angle of 170.5 deg, producing a shock-normal Mach number of $8.33\sin(170.5) = 1.36$ – a weak shock, yet strong enough to show up on schlieren. The pressure-deflection polar, for this shock angle, is the purple curve (C) on the (p, δ) -plot in Fig. 4.12. This polar shows that a very weak, regularly reflecting (zero net deflection), shock could occur at **cr** with an overall pressure ratio of 4.0 or a Mach reflection could occur with a net flow deflection of 0.593 rad (34 deg) and a pressure ratio of 78 at **cm**. The **cr** point is compatible with the apparent regular reflections at the centre line. The **cm** point indicates a flow deflection away from the centre line at the triple point. It could be compatible with the experimental observations only if the Mach disc would be ‘too small to be seen’. A Mach disc at **cm** would require a shock angle less than 270 deg at the triple point. In turn, this would force the Mach disc to be convex toward the upstream flow. We seek to discover what happens at weak conical shock reflection at the centre line by both experiment and CFD simulation - specifically to determine whether the reflection is regular (**cr**) or of the Mach type (**cm**) or possibly something else.



A schlieren picture of flow produced by the M-flow ring is shown in Fig. 4.13(C). The measured incident conical shock is at an angle of 170.3 deg, compared to the predicted value of 170.5 deg, showing that the calculated M-flow surface does produce the required strength axisymmetric shock. The calculated Mach number behind the shock is 7.42 and the flow deflection through the shock is -3.69 deg. If a planar reflected shock, with this Mach number in front of it, causes a flow deflection of +3.69 deg (back to the free stream direction), it would require a shock angle of 10.5 deg. The shock angle, measured off the schlieren picture, is 10.6 deg. Thus it appears that **weak conical shocks reflect off the centre line just as weak planar shocks** - at least so it appears in the far field where angular measurements of shock inclination can be made with some assurance of accuracy. On the schlieren picture, all shock traces appeared to meet at a single point and, in the near field, the experiment did not resolve a Mach disc. It remained for high resolution CFD to find the Mach disc, if it existed.



SolverII CFD code was used to simulate flow in the M-flow ring for the (C) model configuration. CFD calculations produced a quite straight incident shock cone at 170.3 deg and a reflected shock cone at 9.7 deg. The two shock cones appeared to reflect regularly at a point on the centre line with no trace of a Mach reflection. Further calculations with SolverII, at several levels of grid refinement, produced a 25,000-fold magnified picture of the zoomed-in centre-line region. This magnification shows a Mach reflection with a slightly curving incident shock with an angle of 153.4 deg! This is the von Neumann shock angle for Mach 8.33. The shear layer does not seem to deviate much from being parallel to the flow's axis of symmetry. It seems that the reflected shocks and the associated flow have by themselves sought out the von Neumann shock reflection configuration – the Mach reflection structure that is compatible with the boundary condition at the centre line. This allows us to predict the reflected shock angle for such weak shock reflections. In fact, the reflected shock angle is that predicted by the von Neumann triple point solution for the triple point at the von Neumann condition. Since the von Neumann condition is dependent only on the freestream Mach number, the reflected shock angle also does not depend on the initial shock strength for very weak incident shock waves in axisymmetric flow.

In axisymmetric internal flow, shocks approaching the axis of symmetry (centre line) always reflect as Mach reflections. Very weak shocks (those below vN strength) in

axisymmetric flow tend to strengthen as they approach the axis to become of vN strength. There they reflect at a very small ('too small to be seen') Mach reflection at vN strength, very near the axis, to give a reflected shock at the vN strength with a net flow deflection close to zero. Weak shocks, above vN strength, reflect also as Mach reflections but now of sizable (visible) proportions off the axis, producing a negative net flow deflection (towards the axis). CFD methods exist for the prediction of both very weak and weak shock reflections. Very fine computational grids have to be used to detect the 'too small to be seen' reflections of very weak shocks. No analytical or semi-analytical theories exist for predicting reflection of either very weak or weak shocks.

4.4 Concluding remarks

The Taylor-Maccoll equations are recast and presented in terms of Mach number components. Their solution is applied to the calculation of internal, conical, axisymmetric flow, which can be used as the basis for designing air intakes for high Mach number air breathing engines. Computational and experimental proof is presented for the existence of internal conical flows in the Busemann and M-flow configurations. The assumption of conical symmetry holds for flow over a cone and for Busemann flow, but it does not hold for M-flow near the axis of symmetry.

Busemann flow contains four unique fluid mechanical features: a) internal flow with an inflected surface, b) a free-standing conical shock, c) an axisymmetric centered compression fan and d) a flow process from a uniform flow to another uniform flow. All these features are significant if the Busemann streamtube is used as a basis for design of engine air intakes. M-flow is another type of internal flow that can represent part of an intake surface. It also contains two interesting fluid mechanical features: a) a singularity and b) an example of convergent supersonic flow with a decreasing pressure. It is suitable as a leading edge shape that produces a conical internal shock wave. Both Busemann and M-flow carry conical shocks that either diverge from or converge towards the centre line of symmetry. The study of such shocks is important in their application to intake flows as well as to understanding the basics of reflection and interaction of curved shock waves.

The Taylor-Maccoll equations point to the existence of a confocal, conical, compression fan - the axisymmetric analogue to a Prandtl-Meyer fan. Such a fan of coalescing characteristics, preceding a free-standing conical shock, is shown to exist experimentally as well as by CFD calculations.

Despite a focused search, no analytical, computational or experimental evidence was found for the possibility of regular shock reflection of incident shocks at the centre-line of symmetry.

CHAPTER 5

HYPERBOLIC SHOCK WAVE

Contents

- 5.1 Introduction
- 5.2 Geometry of the concave hyperbolic shock
- 5.3 Flow properties behind a curved shock
- 5.4 Streamlines behind hyperbolic shock
- 5.5 Orientation of sonic line behind the shock
- 5.6 CFD results
- 5.7 Conclusions

5.1 Introduction

In the design of supersonic airplane and air intake shapes, for specific performance, it is useful to begin with a known shock wave shape and flow-field and from these deduce the required wall shapes. These are design methods referred to as “Wave Rider” or “Wave Trapper” techniques. Questions then arise as to the nature and existence of flow behind a given known shock shape. This is particularly pertinent to supersonic air intake flows where doubly curved concave shocks are likely to exist and where the quality of the downstream flow is of importance but less well understood than external flows.

The left lobe of a hyperbola of revolution shape is proposed as a particular example of a doubly curved, concave axisymmetric shock surface. It offers an analytically simple surface for the study of pressure gradient and flow curvature effects on shock detachment and reflection where the cumulative effects of both shock curvatures are present. Such shock shapes are physically plausible for internal, converging flow and Mach disk shapes. Existence of simple analytical expressions describing the inclination and curvatures of the hyperbola lead to equally simple, explicit, analytical expressions for gasdynamic properties and their gradients downstream of the hyperbolic shock wave. The concave, hyperbolically shaped shock in both planar and axial flow is investigated analytically with oblique shock theory as well as curved shock theory to discover any tendency towards the formation of a shock wave in the flow immediately behind the hyperbolic shock. If such a shock appears, and impinges on the back of the hyperbolic

shock, then there would have to be a kink in the originally posed smooth shock and a Mach interaction would ensue. The onset of Mach interaction, at the sonic point is shown to depend on the freestream Mach number and the ratio of shock curvatures. Critical roles are attributed to both the subsonic patch of flow behind the strong portion of the shock and to the orientation of the sonic surface at the shock. There is much experimental evidence of the existence of strong concave shock waves in the studies of Mach reflection where such shocks constitute the Mach stem. No experimental or CFD examples of continuously curved concave shocks that span both the weak and strong shock range have been found, probably because the enclosing ducts have to have very special shapes. Such

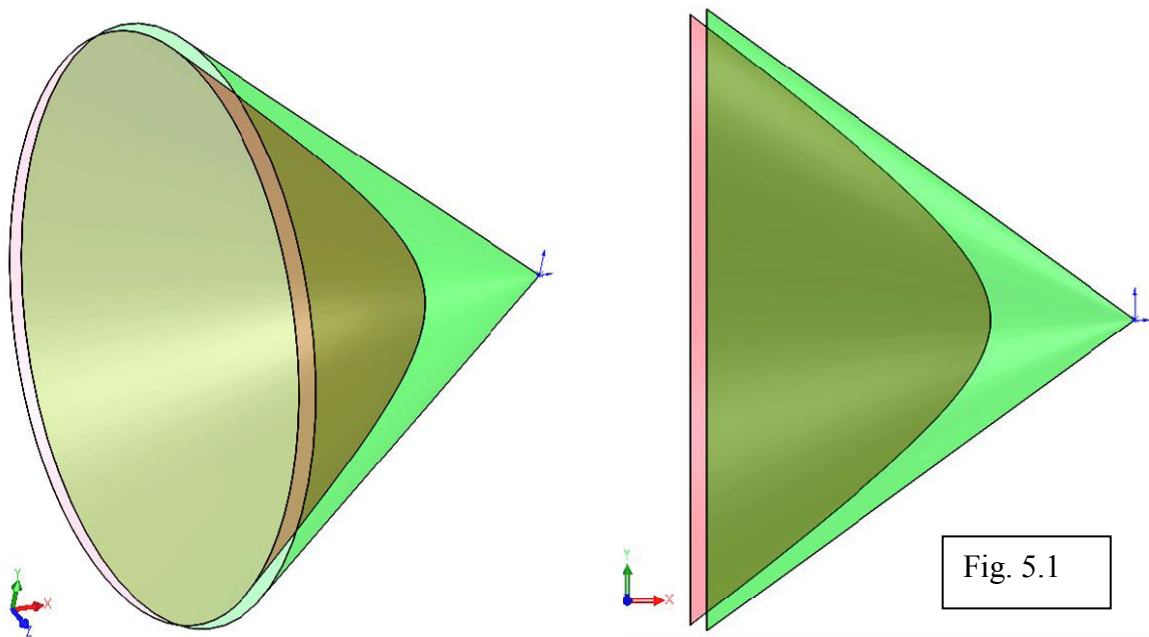


Fig. 5.1

surface shapes (both planar and axial) are presented here, together with their analytical and CFD-generated shock shapes. Background material, covering theory related to sonic line orientation for *convex*, planar shocks can be found in [Hayes and Probstein (1966)] and [Rusanov(1976)].

5.2 Geometry of the concave hyperbolic shock

In Fig. 5.1 the hyperbolic shock is shown as a purple surface. Its enveloping Mach cone is in green. In Cartesian coordinates the equation of a hyperbola of revolution, that has two lobes lying on the positive and negative x-axis, is,

$$\frac{x^2}{a^2} - \frac{y^2}{b^2} = 1 \quad (5.1)$$

The left lobe, which presents a concave surface to the left, towards the oncoming flow, has a shape that can be found from,

$$x = -a\sqrt{1 + y^2/b^2} \quad (5.2)$$

Setting, $a = M_1^2 - 1$ and $b = \sqrt{M_1^2 - 1}$ (5.3)

makes the far-out branches of the hyperbola asymptotic to the freestream Mach cones and the radius of curvature of the hyperbola at the horizontal axis equal to -1 (see Fig. 5.1 above and cross-section, Fig. 5.2).

Each freestream Mach number, M_1 , thus has a unique shock shape with the common radius of curvature -1 at the axis and with its extremities asymptotic to the Mach waves. Keeping the radius of curvature constant with Mach number is for convenience; it sets the problem's scale and facilitates comparison between shocks for various Mach numbers on the same plot. For any one Mach number the hyperbolic shock contains all possible shock angles

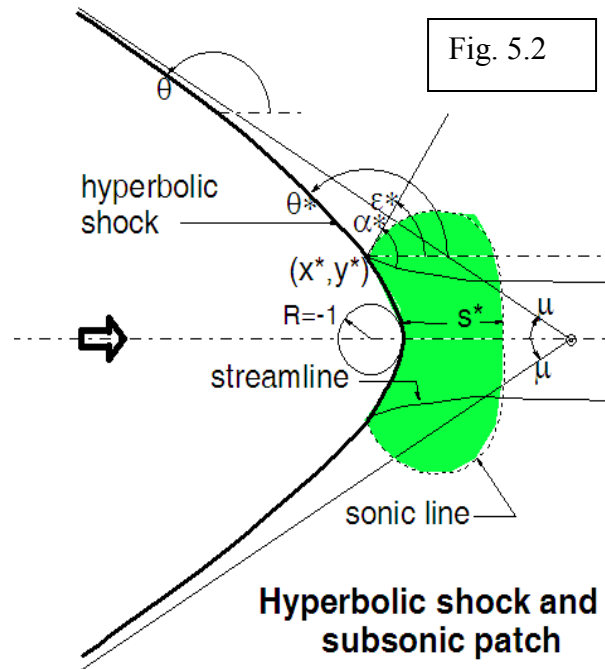
for that Mach number, from normal shock to Mach wave. The slope of the hyperbolic shock, at any point (x, y) on the hyperbola is (from Eqn. 5.1),

$$\frac{dy}{dx} = \tan \theta = n \frac{x}{y} \quad \text{where } n = \frac{b^2}{a^2} = \frac{1}{M_1^2 - 1} = \tan^2 \mu \quad (5.4)$$

and θ is the shock angle (obtuse in second quadrant). The second derivative is,

$$\frac{d^2y}{dx^2} = \frac{n}{y} \left(1 - n \frac{x^2}{y^2} \right) = \frac{1}{y} (\tan^2 \mu - \tan^2 \theta) \quad (5.5)$$

so that the left-lobe's shock curvature is,



$$S_a = \frac{\frac{d^2 y}{dx^2}}{\left[1 + \left(\frac{dy}{dx}\right)^2\right]^{3/2}} = \frac{n \left(1 - n \frac{x^2}{y^2}\right)}{y \left(1 + n^2 \frac{x^2}{y^2}\right)^{3/2}} = \frac{\tan^2 \mu - \tan^2 \theta}{y(1 + \tan^2 \theta)^{3/2}} \quad (5.6a)$$

This formulation for S_a matches our definition of shock curvature in the flow plane¹⁷ $S_a = d\theta / d\sigma$. Flow-plane shock curvature, S_a , is defined to be positive when the shock is concave towards the oncoming flow. The curvature in the flow-normal plane is,

$$S_b = -\cos \theta / y \quad (5.6b)$$

and the *ratio of shock curvatures*, S_a / S_b , for obtuse shocks, at any value of hyperbolic shock angle, is,

$$\mathcal{R} = \left(\frac{S_a}{S_b}\right) = (1+n) \sin^2 \theta - n \quad (5.6c)$$

On the shock surface \mathcal{R} varies from 0 to 1 as θ varies from μ to $\pi/2$. The shock intercepts the x-axis at $x = -a$ and $y = 0$ so that the shock angle there is $\pi/2$ and the ratio of curvatures is 1. Using Eqns. (5.1) and (5.2) enables a solution for x and y with the shock angle appearing as parameter,

$$x = \frac{a \tan \theta}{\sqrt{\tan^2 \theta - n}} \quad \text{and} \quad y = \frac{1}{\sqrt{\tan^2 \theta - n}} \quad (5.7)$$

The (x,y)-location of any significant shock angle, such as the angle for sonic post-shock flow, can then be determined directly using Equations (5.7) above. Positive square roots are taken in both cases resulting in a positive y and a negative x value for the upper-left branch of the hyperbola. At given value of x or y , on the shock, the steps to calculate the flow gradients behind the hyperbolic shock are as follows:

- 1) from a given M_1 calculate a and b using Eqn. (5.3);
- 2x) for a given $-\infty \leq x \leq -a$, calculate y from (5.1), or
- 2y) for a given $-\infty \leq y \leq \infty$, calculate x from (5.2); take the negative value of x for the left branch of the hyperbola;
- 3) find the shock angle θ from (5.4); or

¹⁷ The *flow plane* is the plane surface that contains the smallest angle between the down-shock flow vector and the shock surface; it also contains the upstream flow vector.

- 2) instead of steps 2x, 2y and 3, above, start with a given shock angle and calculate x and y from (5.7)
- 4) find the shock curvature in the flow plane, S_a from (5.6a)
- 5) find the curvature in the flow-normal plane, $S_b = -\cos\theta/y$, from (5.6b)

Since the shock has a vertical slope at the axis, it is better to take evenly spaced values of y rather than x , i.e. use option 2y) rather than 2x) above, when plotting or generating a CFD grid for the region behind the shock.¹⁸ The above has shown that, given a Mach number, a hyperbolic shock shape can be calculated and, given any shock angle, locates a point on the shock where the shock's surface curvatures are determinable. All of this applies to planar shocks as well as axial ones. For planar shocks $S_b = 0$ so that $\mathcal{R} \rightarrow \infty$.

5.3 Flow properties behind a curved shock

Having defined all relevant geometric properties of the hyperbola we now establish relations for flow properties behind the hyperbolic shock. The properties fall into two categories: the 'zeroth order' properties such as pressure, Mach number and the flow deflection angle; these requiring, as inputs, the ratio of specific heats, the shock angle and the freestream Mach number. The second category, the 'first order' properties, such as pressure gradient streamline curvature and vorticity, require the previous three inputs plus the shock curvature(s). The zeroth order quantities are obtained from the algebraic Rankine-Hugoniot equations and the first order quantities require the use of the Euler equations. The zeroth order relations as well as the Euler equations are given in all standard textbooks on gasdynamics [Liepmann and Roshko (1956)]. Curved shock theory (CST) for planar flow is derived in Ch.2 as well as by [Lin and Rubinoff (1948); Gerber and Bartos (1960); Thomas (1947); Truesdell (1952)]. Application of CST to axial flow and shocks with compound curvature is found in Ch. 2.

The streamline curvature, D_2 , pressure gradient, P_2 and vorticity, Γ_2 , behind the hyperbolic shock, are found from the curved shock equations (2.30e) and (2.31b),

¹⁸It is possible to study the flow behind a *convex* hyperbolic shock by taking the positive values of x as generated in step 2y) above.

$$\begin{aligned}
 P_2 &= \frac{[BC]}{[AB]} S_a + \frac{B_2 G'}{[AB]} S_b \\
 D_2 &= \frac{[CA]}{[AB]} S_a - \frac{A_2 G'}{[AB]} S_b \\
 \Gamma_2 &= -\frac{C''}{E_2''} S_a = \frac{\rho_2}{\rho_1} \left(1 - \frac{\rho_1}{\rho_2}\right)^2 \cos \theta \cdot S_a
 \end{aligned}
 \tag{5.8}$$

where the coefficients multiplying S_a and S_b are all functions of the freestream Mach number and the shock angle. These equations are general to any doubly curved, axial shock surface. All coefficient equations are found in Ch. 2.

5.4 Streamlines behind hyperbolic shock

For a given Mach number, the shock geometry, including the shock curvatures are calculated, at selected points, using equations (5.1) to (5.6) by the steps 1 to 5, above. Oblique shock theory gives the slope, $\tan \delta_2$, of the post-shock streamlines at any point on the shock. The *curved shock theory* equations (5.8) are then used to find the streamline curvature, D_2 , at the selected points, (x_s, y_s) along the shock and the streamline shape near the shock is calculated from a Taylor series approximation,

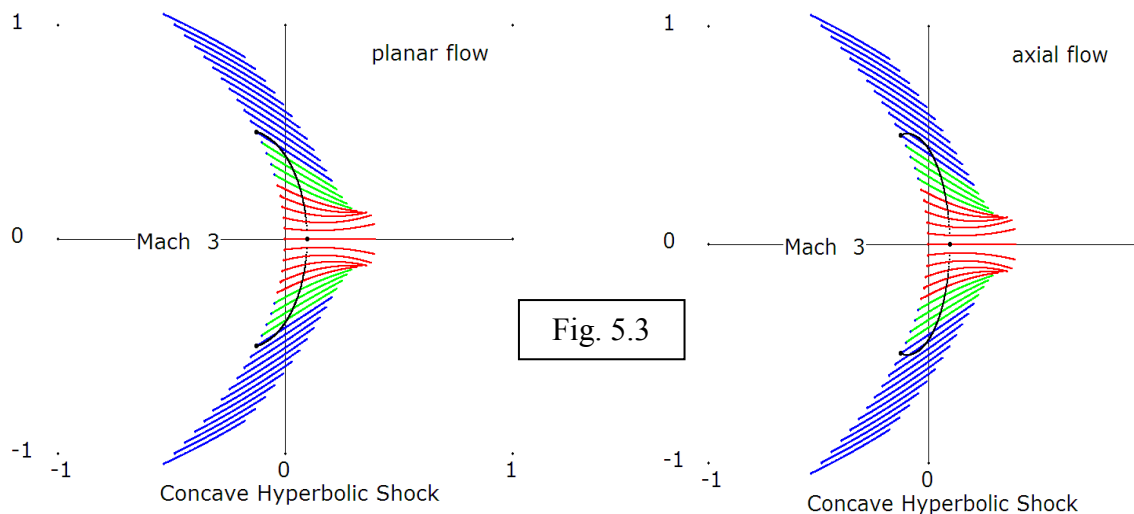


Fig. 5.3

$$y = y_s + (x - x_s) \tan \delta_2 + \frac{(x - x_s)^2}{2} D_2$$

where (x_s, y_s) is the starting point of the streamline, on the shock. The Figures 5.3 show streamline shapes behind a hyperbolic shock for axial and planar flows at Mach 3. Streamlines are red where the pressure gradient is negative, blue where the streamline curvature is negative and green where both are positive. The point on the shock where the streamline curvature is zero is the Crocco point and the point where the pressure gradient is zero is the Thomas point. The location of both points depends on the ratio of specific heats, the shock angle, the freestream Mach number as well as the shock curvatures. In each case, the approximate sonic line (to be further described in Section 4) is shown in black. The two pictures are quite similar because the cross sectional shock shapes are the same, the flow deflections are the same and the shock curvature, S_a , is the same at corresponding points. Differences arise from the transverse shock curvature, S_b , being zero for planar flow but non-zero for axial flow. This causes P_2 , D_2 and Γ_2 , as they appear in equations (5.8)¹⁹, to be different for the two flows. The difference is reflected in the not-so-easily discerned difference in streamline curvatures, D_2 , and the shape of the sonic line. The streamlines next to the centre line form a throat around the sonic point – indicated by the black dot on the sonic line. This is encouraging agreement between two essentially disparate downstream flow results of CST.

5.5 Orientation of sonic line behind the shock

The angle α^* , between the sonic line and the streamline is, from [Hayes and Probstein Eq.6.1.1 (1966)] and curved shock theory, Eqn. (2.22):

$$\tan \alpha^* = -\frac{(dM/ds)^*}{(dM/dn)^*} = \frac{P_2^*}{D_2^* - \Gamma_2^*} \quad (5.9)$$

This relation applies to both planar and axial flow. The asterisk indicates that the gradient quantities have been evaluated at the post-shock sonic condition. Hayes and Probstein present a formula for α^* for acute shocks in *planar* flow,

$$\tan \alpha^* = \frac{\tan^3(\theta^* - \delta^*) [3(\gamma + 1) \tan^2(\theta^* - \delta^*) + 5 - \gamma]}{[1 - \tan^2(\theta^* - \delta^*)] [(\gamma + 1) \tan^2(\theta^* - \delta^*) + 2]} \quad (5.10)$$

¹⁹ For planar flow, these quantities are not functions of shock curvature and for axial flow they are functions not of the individual curvatures but of their ratio.

Note that the right-hand side is a function of γ and M_1 only so that, for *planar flow*, the orientation of the sonic line does not depend on shock curvature. Eqn. (5.9) is valid for both planar and axial flow as are its components.

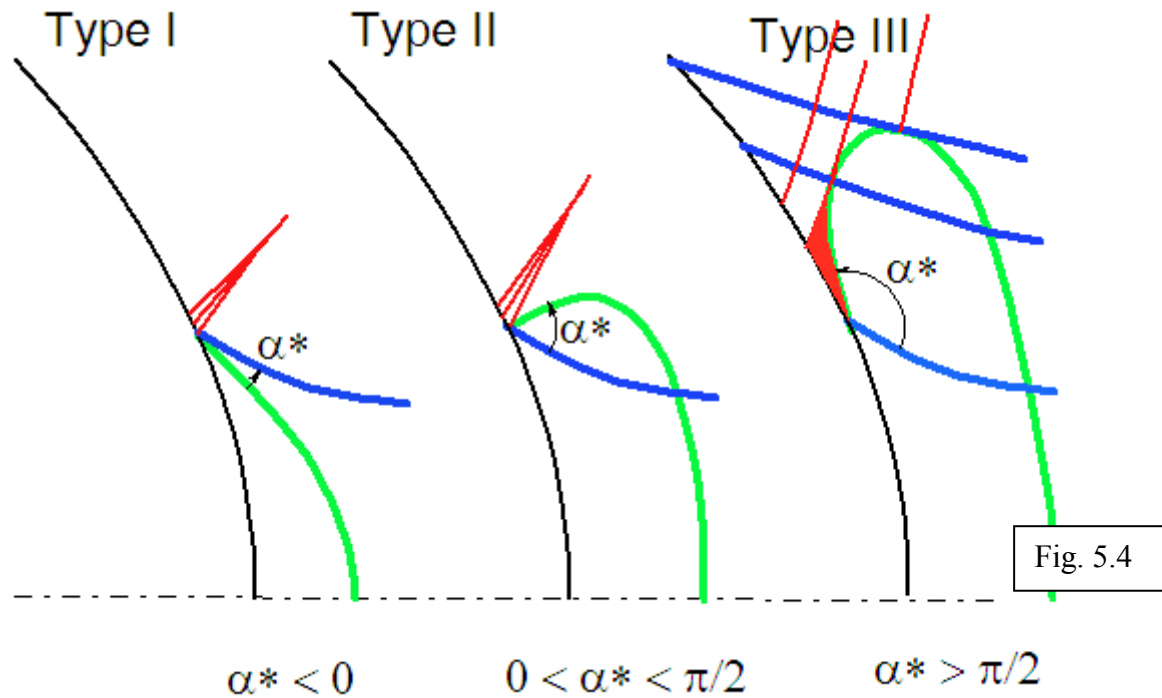
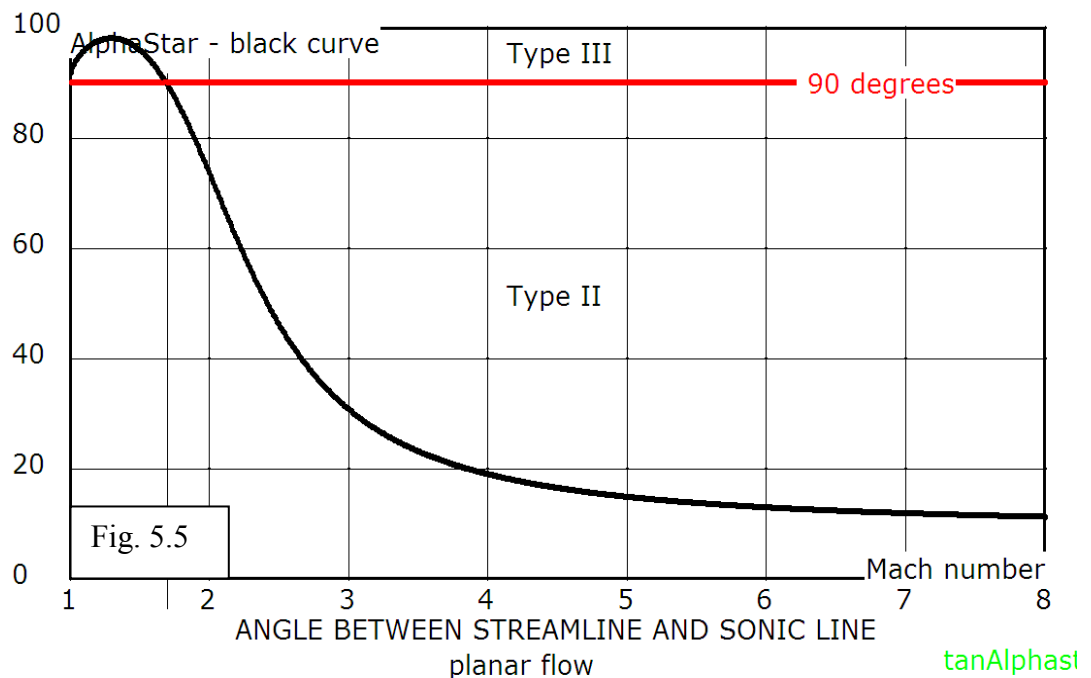


Fig. 5.4

For a shock with compound curvature, one of three types of flow can exist at the sonic point on the shock, depending on the orientation of the sonic line, α^* : Type I for $\alpha^* < 0$; Type II for $0 < \alpha^* < \pi/2$ and Type III for $\alpha^* > \pi/2$. Figure 5.4 illustrates the three types where shocks are black, streamlines are blue, sonic lines are green and the C+ characteristics are red. Flow is left-to-right. These three types determine the existence and nature of the flow at the sonic point. For Type I, supersonic flow, leaving the shock just outboard of the sonic point continues supersonically. For convex, planar shocks Hayes and Probstein [1966] have shown that Type I flow does not exist. For Types II and III the supersonic flow outboard of the sonic point has to cross the sonic line to become subsonic and then to accelerate to sonic at its second crossing of the sonic line. Types II and III are themselves further distinguished by the fact that for Type III the C+ characteristics, reflecting from the supersonic downstream side of the shock near the sonic line, become incident on the sonic line and are thus intercepted and blocked from coalescing to form a reflected shock. This occurs in the area shaded red on the Type III sketch in Fig. 5.4.

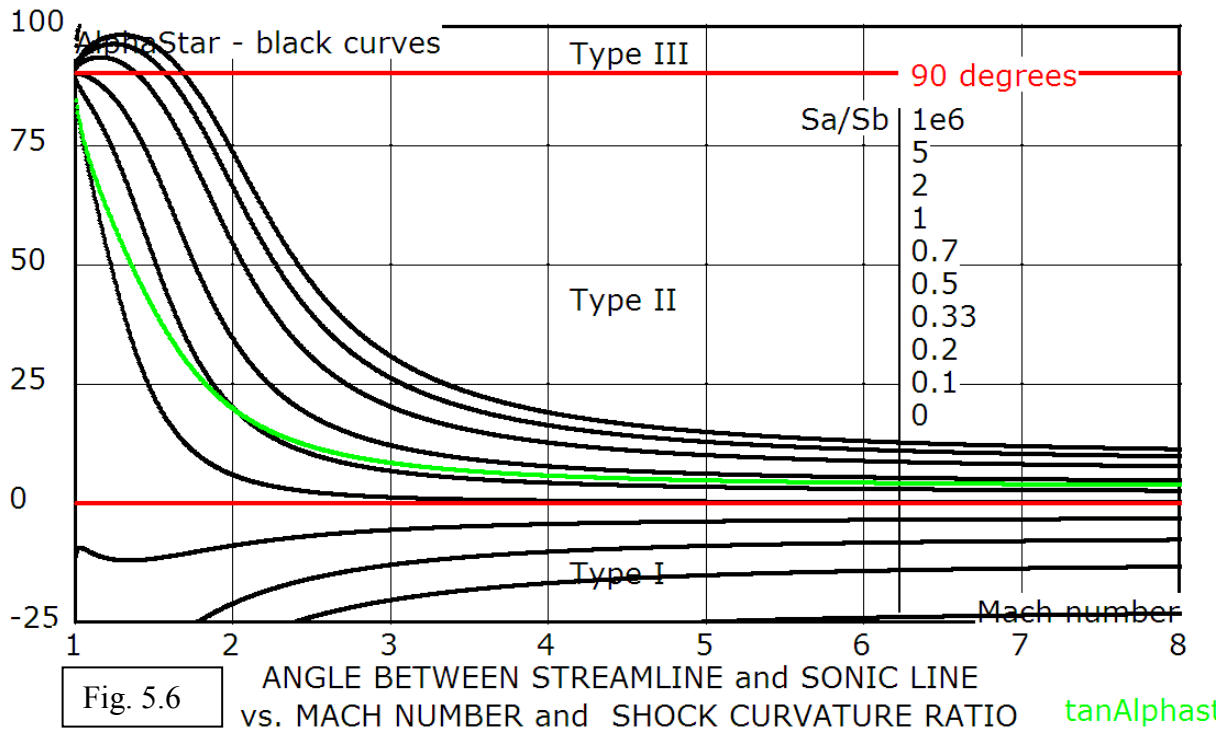
Thus Type III flow may have a continuous incident shock whereas Types I and II are likely to develop a reflected shock and Mach reflections. This will become more evident when considering the orientation of reflected characteristics and the sonic line. For planar flow, the angle that the sonic line makes with the streamline is shown in Fig. 5.5 which is a plot of Eqn. (5.10). Type III flow exists between Mach 1 and 1.7. Above Mach 1.7 only Type I or II flow is possible. This means that, in planar flow, a continuous shock can be expected only below Mach 1.7 and above that a Mach reflection will occur. Type I flow is not possible for planar flow since the curve never becomes negative. Shock curvature does not affect these results since the flow has planar symmetry. Similar results have been obtained previously for planar flows, involving *convex* shocks, by [Rusanov (1976)] and for planar shocks, Henderson (1987) has shown that Mach reflection cannot exist for very weak shocks.



The picture is more complicated when the shocks are axial (axisymmetric) with curvatures S_a and S_b , and curvature ratio $\mathcal{R}^* = S_a^* / S_b^*$ at the sonic point. In this case the curved shock theory Eqn. (5.10) for the sonic line orientation, α^* , takes the form,

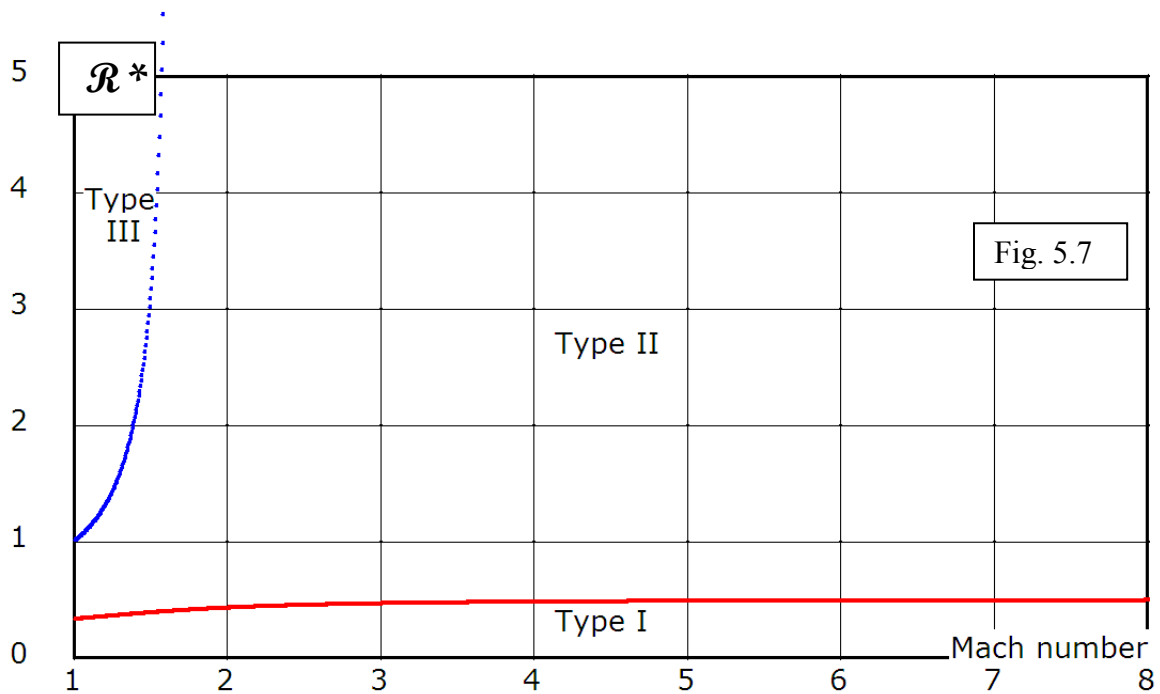
$$\tan \alpha^* = \frac{k_1 \mathcal{R}^* + k_2}{k_3 \mathcal{R}^* + k_4} \quad (5.11)$$

where asterisks denote values at the sonic point. The coefficients $k_{1...4}$ are all functions of the specific heat ratio and the freestream Mach number only. Formulas for the k's are found in Appendix 5A at the end of this chapter. The shock curvature ratio plays an



important role in determining the character of flow behind a doubly curved shock. The angle from the streamline to the sonic line α^* (AlphaStar), is plotted against the freestream Mach number in Fig. 5.6 with the shock curvature ratio, $\mathcal{R}^* = S_a / S_b$, at the sonic point, as parameter. The two red, horizontal lines, at zero degrees and 90 degrees, separate the regions for the three types of flow. The top-most curve, for $S_a / S_b = 1e6$ (i.e. 10^6) is effectively for planar flow as was presented in the previous figure. The bottom curve, for $S_a / S_b = 0$, is for conical flow. Type I flow, generally above Mach 2, appears for curvature ratios below 0.5. For a curvature ratio of 0.5, above Mach 3, α^* is approximately zero, indicating that the sonic line and streamline are collinear. This, in turn, means that the isobaric (Thomas) point is at the sonic point and that pressures in the supersonic/subsonic regions on either side of the streamline are increasing/decreasing. Type II flow is possible for curvature ratios between 0.5 and 10^6 for all Mach numbers. Type III ($\alpha^* > 90$ deg) flow is possible for curvature ratios above 1 and Mach numbers

between 1 and 1.7. Only for Type III conditions can a smoothly curving incident shock wave be expected for the whole range of shock angles from μ to $\pi/2$. The above conclusions apply to concave shocks of any shape - not only hyperbolic. For planar, concave, hyperbolic shocks the top-most curve applies, showing that both Types II and III flow are possible and that we can expect a single shock, without a reflected shock, at Mach numbers below 1.7. This lower limit to Mach reflection of 1.7 is only for planar incident shocks. For axial shocks the lower limit depends on the ratio of shock curvatures at the sonic point. For example for a ratio of 2 the lower limit is about Mach 1.4 and for a ratio of 1 there is no lower limit – implying that Mach reflection will appear for all Mach numbers as long as the ratio of shock curvatures is below 1. The green curve is for concave, *hyperbolic* shocks, showing that only Type II shocks are possible and we should not expect a complete **hyperbolic** axial shock at any Mach number. At the same time it does not mean that complete axial shocks (Type II) do not exist. If they do, they would have to have a ratio of shock curvatures at the sonic point higher than that provided by the present type of axial, **hyperbolic** shock. Figure 5.7 shows where the three types of sonic flow exist in the shock curvature ratio \mathcal{R}^* (Rstar) vs. Mach number space. Equations



(5.8) can be rearranged and substituted into Eqn. (5.9) so as to give,

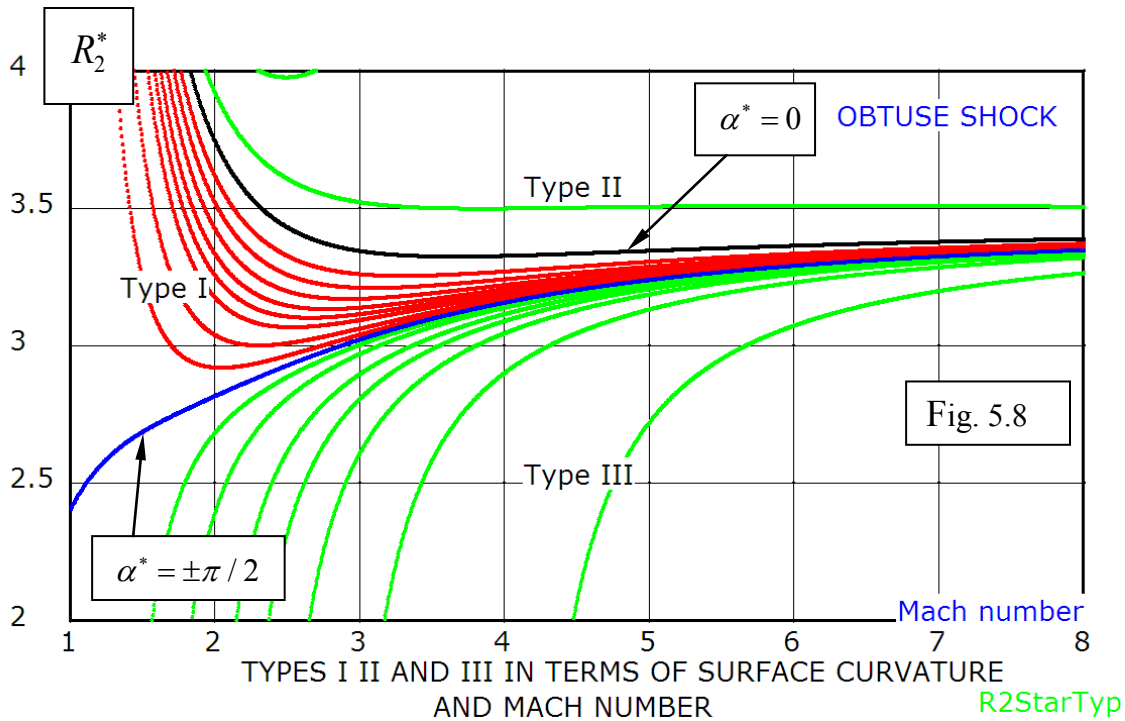
$$\tan \alpha^* = \frac{P_2^*}{D_2^* - \Gamma_2^*} = \frac{a_1 + \cos \theta^* (a_1 b_2 - a_2 b_1) R_2^*}{b_1 - c (1 + b_2 \cos \theta^* R_2^*)} \quad (5.12)$$

where,

$$\begin{aligned} a_1 &= [BC]/[AB] & a_2 &= B_2 G' / [AB] \\ b_1 &= [CA]/[AB] & b_2 &= -A_2 G' / [AB] \\ c &= -C'' / E_2'' \end{aligned}$$

are all evaluated at the sonic condition. The angle α^* in Equation (5.12) is now in terms of Mach number and the streamline radius of curvature behind the shock, R_2^* , where R_2^* has been normalized with respect to $y = y^*$ - the distance from the sonic point to the centre line. This shows that the inclination of the sonic line at the back of the doubly curved shock is controlled by the post-shock streamline/surface curvature. Consequently, so is also the shock type. Since the streamline curvature is also the curvature of the physical leading edge it is a more physically meaningful and realizable quantity than the ratio of shock curvatures, \mathcal{R}^* . Inverting Eqn. (5.12) to solve for R_2^* gives,

$$R_2^* = \frac{(b_1 - c) \tan \alpha^* - a_1}{\cos \theta^* (c b_2 \tan \alpha^* + a_1 b_2 - a_2 b_1)} \quad (5.13)$$



R_2^* is plotted against the freestream Mach number with α^* as parameter in Fig. 5.8. α^* is $\alpha^* = \pi/2$ positive on the green curves and negative on the red curves. It is zero on the black curve and $\pm\pi/2$ on the blue curve. In the region for Type III the sonic line is angled forward so that there is no reflected shock and therefore a smooth curved shock is possible in this region.

5.6 CFD Results

As described in Section 1, the shape of each concave, hyperbolic shock is defined completely by its freestream Mach number. At any point on the back of the shock a flow deflection and a post-shock streamline curvature is fixed and easily calculated. These are used for defining a curved surface as input to a CFD program for calculating the flow and the shock inside that annular surface. These input values of wall/streamline curvature are exact only right behind the hyperbolic shock surface so that the **constant curvature** wall surfaces used as input are only approximations to the true streamline/wall surfaces required to produce the hyperbolic shock. The length of curved wall is critical in the computations. Too short and it will not produce the proper hyperbolic shock shape; and too long a wall will cause premature Mach reflection - in some cases leading to total internal flow unstart (for reasons dealt with in the next chapter). Reasonably consistent results are obtained by selecting curved surface lengths which have one degree less turning than that required to produce sonic flow by Prandtl-Meyer turning from the post-shock conditions at the leading edge. This results in the trailing edges being just supersonic.

The aim of the CFD calculations is to show that the Type I, II and III flows do or do not appear where so predicted in Section 5.4. A time-asymptotic, finite difference scheme with automatic grid refinement, SOLVER II [2004] is used. Only the top half of the top-to-bottom symmetric flow is calculated. The centre line of symmetry and the top wall are shown in red. In each case the hyperbolic shock is shown as a black curve. Calculated shocks take their colour from adjacent contours. All figures show colour-coded constant Mach number lines and a black sonic line. Axial or planar symmetry and the freestream Mach number are denoted on the bottom text line of each figure.

Figure 5.9 is for planar flow at Mach 3. The calculated shock follows the hyperbola closely near the leading edge of the curved surface tending slightly forward as it nears the triple point of the Mach interaction. At the triple point the reflected shock is very weak and there is a small subsonic region between the reflected shock and the shear layer. The sonic flow for this case would be of Type II so that a continuously curving shock is not expected. The sonic line is shown in the flow downstream of the Mach disk.

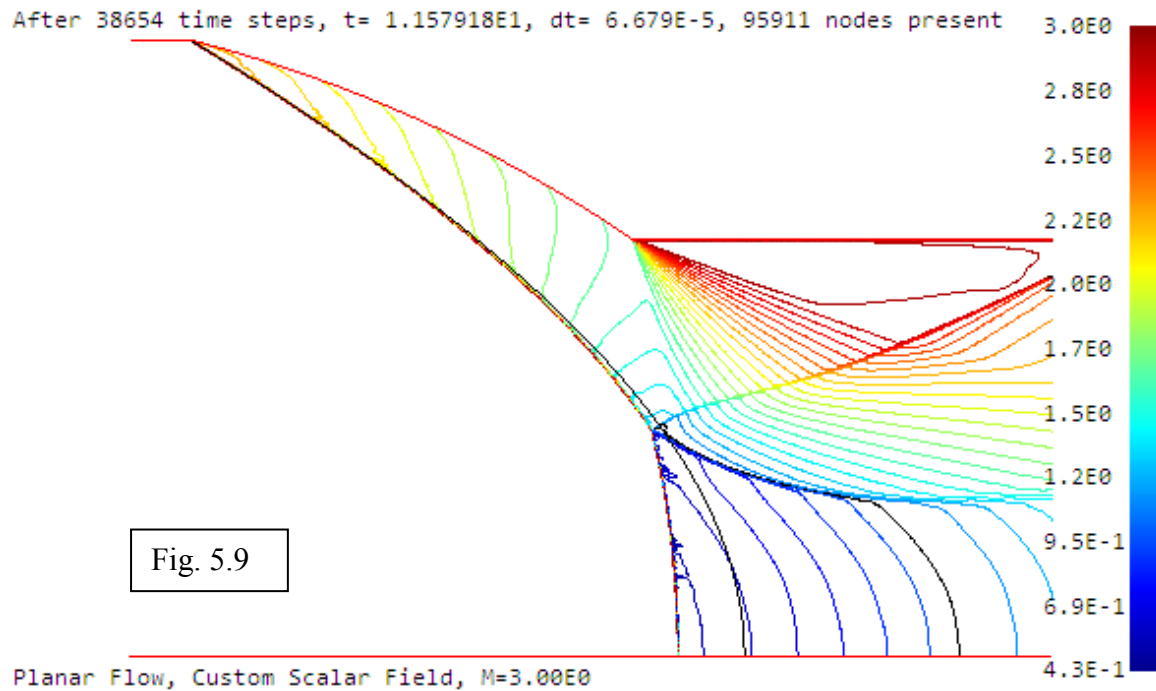
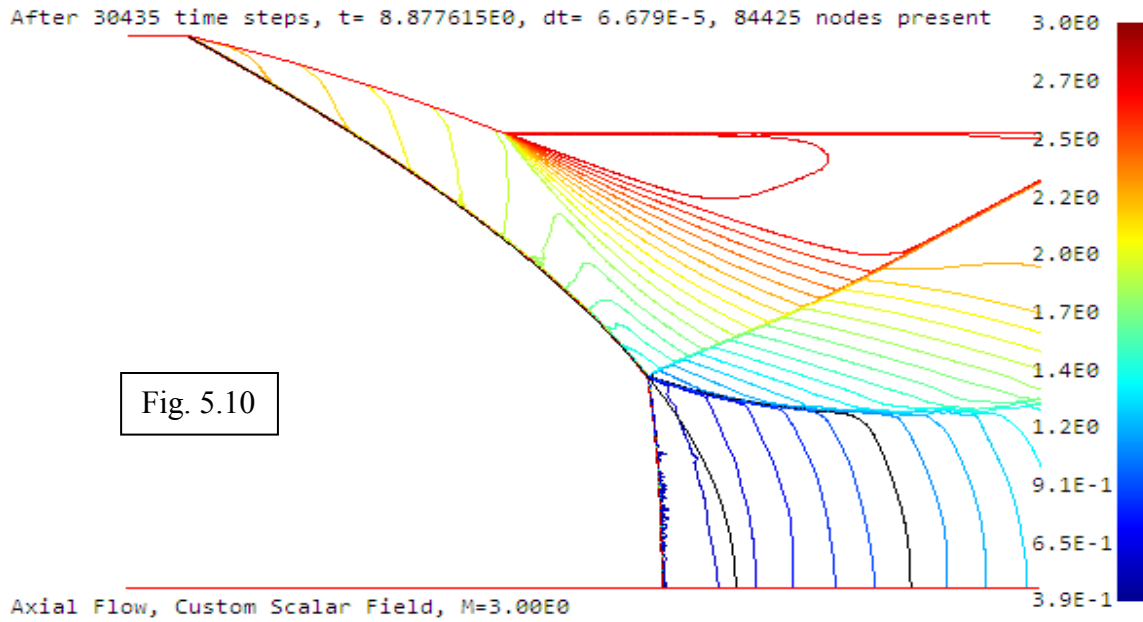
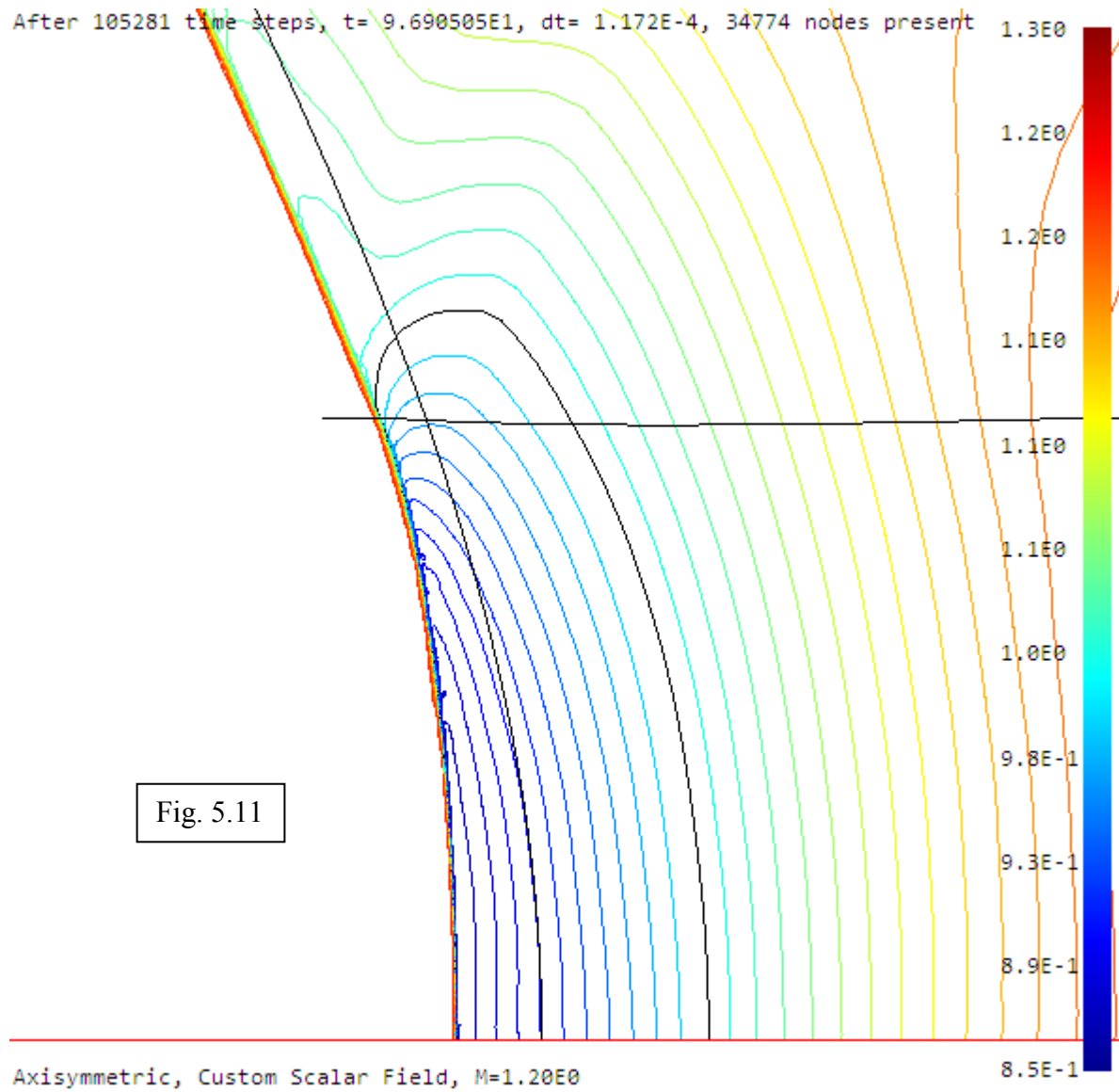


Figure 5.10 is for axial flow at Mach 3. The calculated shock agrees well with the hyperbola (thin black line) from the leading edge down to the triple point. The flow at the sonic point would be of Type II so that a continuously curving shock is not expected – Mach interaction appears, as with the planar flow above.



The zoomed-in Fig. 5.11 is for axial flow at Mach 1.2. The CFD shock is slightly ahead of the CST shock and it is no longer hyperbolic. The thin, black, kidney-shaped line is the sonic line with subsonic flow inside. A streamline runs through the sonic point on the back of the shock at what appears to be at a right angle to the sonic line. CFD shock curvatures measured off the figure, at the sonic point, give $S_a^* = 2.92$ and $S_b^* = 2.43$ giving a shock curvatures ratio $\mathcal{R}^* = S_a^* / S_b^* = 1.19$ at the sonic point. At Mach 1.2 this is just inside the Type III flow region, as confirmed by the lack of a reflected shock and the consequent continuously curving incident shock.



5.7 Conclusions

Analytical and computational results are presented for flow behind concave shocks. The existence of a reflected shock and hence the non-existence of a continuous smooth shock depends on the orientation of the sonic surface at the back of the shock. In turn, sonic surface orientation depends on the upstream Mach number and the ratio of shock curvatures at the sonic point. For planar shocks, a single, continuously curved shock is possible only below Mach 1.7 such that Mach reflection will occur at higher Mach numbers. For shocks with positive curvature ratio, \mathcal{R}^* , this Mach number limit is reduced until for $\mathcal{R}^* < 1$, no continuous concave shock is possible for any Mach number. A hyperbolic shock always reverts to Mach reflection. Both analytical and computational results show that the shock curvature ratio plays an important role in determining the character of flow behind a doubly curved shock. It is a determining factor, beyond shock polar intersections, as to what type of shock reflection can take place at any freestream Mach number when the incident shock is doubly curved.

Appendix 5A – Coefficients for the sonic line inclination

For **axial** flow the inclination of the sonic line with respect to the streamline, α^* , takes the form,

$$\tan \alpha^* = \frac{k_1 \mathcal{R}^* + k_2}{k_3 \mathcal{R}^* + k_4}$$

where,

$$k_1 = E_2''[BC] \qquad k_2 = E_2''B_2G'$$

$$k_3 = [CA]E_2'' + [BC]A_2'' + [CA]B_2'' + [AB]C''$$

$$k_4 = -A_2G'E_2'' + B_2G'A_2'' - A_2G'B_2'' + [AB]G''$$

and $\mathcal{R}^* = S_a^* / S_b^*$

CHAPTER 6

SHOCK DETACHMENT

Contents

- 6.1 Introduction
- 6.2 Preliminaries
 - 6.2.1 The Unit Ring Wedge (URW) and splitter tube
 - 6.2.2 Curved Shock Theory (CST)
- 6.3 Shock detachment from a sharp leading edge
 - 6.3.1 Detachment by excessive flow turning – δ_{max} criterion
 - 6.3.2 Shock detachment by overpressure
 - 6.3.2.1 Shock detachment by global choking
 - 6.3.2.2 Shock detachment by local choking
- 6.4 Analysis of detachment by local choking
 - 6.4.1 Pressure gradient at leading edge of curved surfaces
 - 6.4.2 Mach number gradient and choking length L^*
 - 6.4.3 Local choking on a flat plate
 - 6.4.4 Planar flow over a curved surface
 - 6.4.5 Flow in a URW with a conical surface
 - 6.4.6 Flow in a URW with curved surface
- 6.5 Computational examples
 - 6.5.1 Grid-independence
 - 6.5.2 Local and global choking
 - 6.5.3 Attachment/detachment hysteresis by CFD
 - 6.5.4 CFD vs. CST
 - 6.5.5 Abruptness of detachment
- 6.6 Conclusions

6.1 Introduction

“Transition from a shock attached to the leading edge of the wedge to a detached shock appears to introduce such a radical change in the flow field that one would expect quite abrupt changes in flow characteristics such as drag. The analysis of this particular change is of particular interest.”

G.K. Guderley in *The Theory of Transonic Flow*

Another reason for the **attached-to-detached shock analysis** to be of particular interest is that the termination of **regular reflection** of an oblique shock wave can have as its cause the same limiting flow conditions (e.g. excessive flow turning) as does the detachment of a shock from a wedge, so that the abrupt changes, referred to

by Guderley, for the detaching shock, should be expected to occur also at the termination of regular reflection. In the shock reflection situation the flow from the incident shock, approaching the reflecting surface, sees the reflecting surface as a freestream flow would see a flow-deflecting wedge. This implies that the fluid-mechanical process involved in the detachment of an oblique shock from a plane or curved surface and the termination of regular reflection on a plane or curved surface have the same underlying causes. The two phenomena are governed by the same equations and should, at their termination, have the same values of independent parameters and boundary conditions. Thus, an investigation of shock detachment from a plane or curved wedge should lead to an understanding of the more complicated regular reflection termination. Shock detachment occurs right at the leading edge, hence also right at the shock, so that CST, which also applies right at the shock, is the appropriate, precise analytical tool for tackling the shock detachment problem. In the study of detachment and transition, some resolution between differences in theory and experiment is required as noted by Sudani et al. [2000] who state that “**...transition from regular to Mach reflection occurs significantly below the maximum deflection condition**”. This justifies the study of shock detachment as a lead-in to understanding the regular-to-Mach reflection transition process.

It was the original intent to investigate the RR to MR transition, with CST, by using shock detachment from a wedge as a stepping-stone. However, it has turned out that the detachment of a shock from a curved wedge has enough substance and complexity to warrant clarification and that the proposed new mechanism needs investigation by a study of its own.

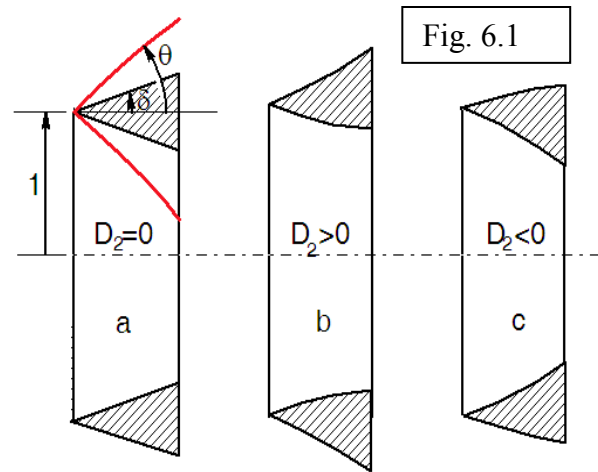
Section 6.2 of this chapter presents two useful concepts: the *unit ring-wedge with a splitter tube*, (URW), and some results of *curved shock theory* (CST). Section 6.3 discusses shock detachment from a sharp curved wedge. The concepts of *local and global choking* are introduced as possible causes for shock detachment. Section 6.4 shows the analytical conditions under which the above causes are present. Section 6.5 is a CFD confirmation showing flow field computations of shock attachment/detachment at the analytically predicted conditions.

6.2 Preliminaries

Two items are introduced to aid the development of discussion, theory and computation in subsequent sections: *the unit ring-wedge* and a short recapitulation of *curved shock theory*.

6.2.1 The Unit Ring-Wedge (URW) and splitter tube is an annular ring with a sharp leading edge that is everywhere at unit radius from the axis of symmetry ($y = 1$).

Three such rings are shown in Fig 6.1. At the leading edge, the outer surface of the ring turns the flow outward by δ_o and the inner surface turns the flow towards the axis by δ_i . The surface curvature, D_2 , in any meridian (flow) plane is zero when there is no curvature, positive when the flow turns away from the axis and negative when the flow turns toward the axis, as shown in the sketches a, b and c respectively.



THREE UNIT RING WEDGES (URW)

The shock has an acute angle on the outside and an obtuse angle on the inside; giving a positive/negative flow deflection on the outside/inside. Shock curvature in the meridian plane is S_a , defined as positive when the shock is concave towards the oncoming flow. In the transverse plane the shock curvature, at the leading edge, is $S_b = -\cos\theta/y$, which, for the URW, becomes simply $-\cos\theta$. All radii of curvature values such as $R_a = -1/S_a$, $R_b = -1/S_b$ and $r_2 = -1/D_2$ are normalized with respect to the *unit ring-wedge* radius $y = 1$. The URW thus provides the normalizing dimension and a convenient geometry for the study of doubly curved shock waves and surfaces in axial flow. The term *axial* is synonymous with *axisymmetric* and what is often called *two-dimensional* is referred to as *planar*; the latter being a limiting case of the former when $y \rightarrow \infty$. The term *wedge* is used to denote the URW and *Mach number* means freestream Mach number.

For some of the CFD calculations an infinitely thin tube is inserted into the computational mesh, extending forward from the leading edge into the free stream (see Fig. 6.20 and 6.24). Its purpose is to isolate the outer and inner flow calculations so that surface curvature effects appear separately on each side without spillage effects from detached flows on either side affecting the flow on the other side - yet the outer and inner flows have identical freestream conditions. Any differences between inner and outer flows becomes readily discernible and attributable to the local surface geometry only.

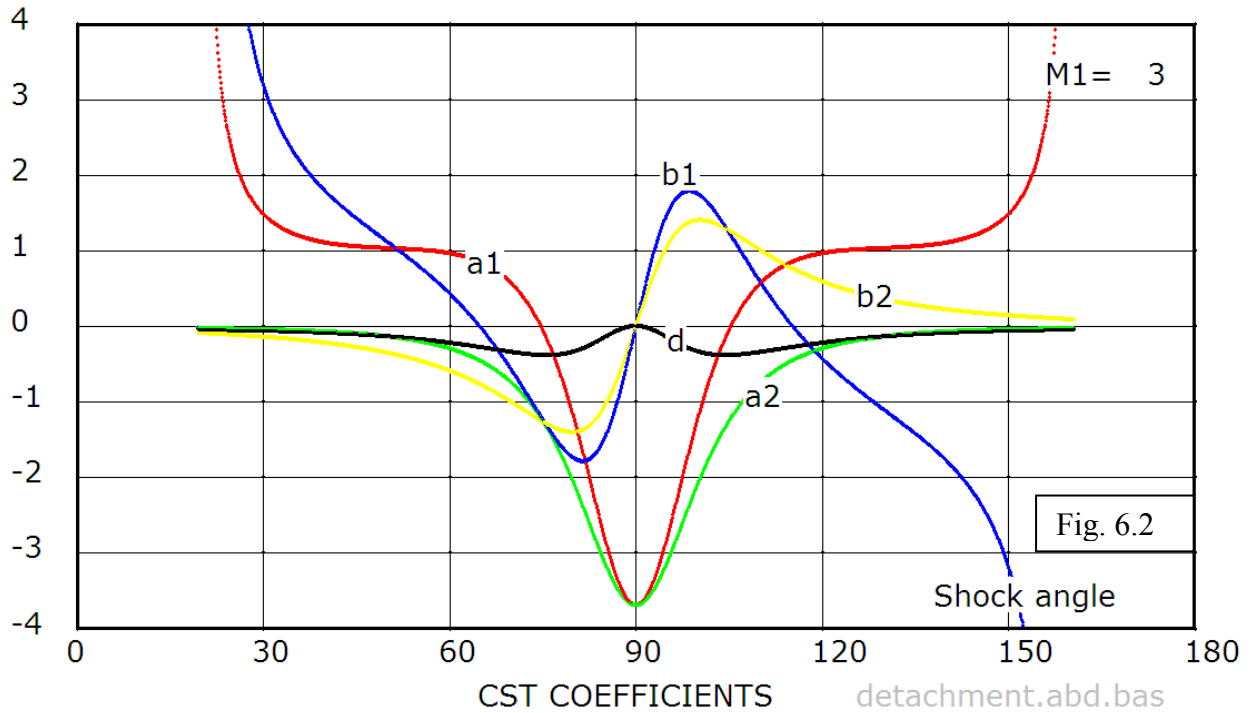
6.2.2 Curved shock theory (CST), presented in Ch.2, relates flow gradients on the up and downstream sides of a doubly curved shock wave. The theory is derived by taking derivatives of the oblique shock equations with respect to the distance along the shock. Equating the up- and downstream derivatives yields a set of simultaneous equations for the gradients of flow properties along the streamlines as a function of upstream Mach number, shock angle and the two shock curvatures. CST is applied in this chapter to find the **streamwise gradient of Mach number** behind a doubly curved shock wave. Two major results of CST, applicable to shock detachment formulations, are the algebraic expressions for **pressure gradient** and **streamline curvature** behind a doubly curved shock in terms of the shock's curvatures (see Eqn. 3.12 a and b):

$$P_2 = \frac{\partial p}{\rho V^2} = \frac{[BC]}{[AB]} S_a + \frac{B_2 G'}{[AB]} S_b \quad (6.1 \text{ a,b})$$

$$D_2 = \frac{\partial \delta}{\partial s} = \frac{[CA]}{[AB]} S_a - \frac{A_2 G'}{[AB]} S_b$$

where S_a and S_b are the shock's curvatures and their coefficients are all functions of shock angle and freestream Mach number. For convenience, write the equations as,

$$\begin{aligned} P_2 &= a_1 S_a + a_2 S_b \\ D_2 &= b_1 S_a + b_2 S_b \end{aligned} \quad (6.2 \text{ a,b})$$



These two equations will be used in Section 6.4 to derive an estimate of the length (L^*) of a curved surface, required to bring the flow to Mach one behind an attached shock. Coefficient values are plotted in Fig. 6.2, against both acute (<90) and obtuse (>90) shock angles, for Mach 3. The black curve refers to vorticity behind the shock from Eqn. (2.38g) when expressed as,

$$\Gamma_2 = dS_a$$

so that,

$$d = \left[\frac{C''}{E_2''} + \frac{[BC]}{[AB]} \frac{A_2''}{E_2''} - \frac{[AC]}{[AB]} \frac{B_2''}{E_2''} \right] \quad (6.2 c)$$

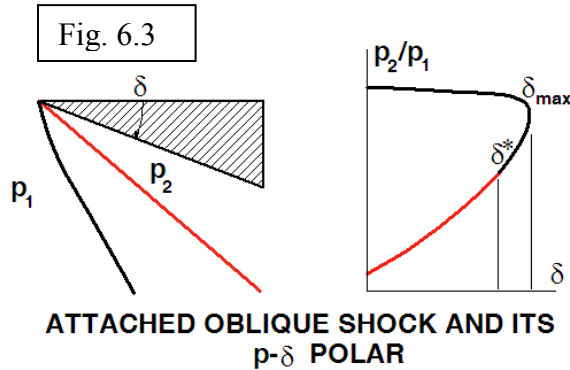
6.3 Shock detachment from a sharp leading edge

A shock wave will remain attached to a sharp wedge leading edge as long as the pressure ratio across the shock and the flow deflection demanded by the leading edge surface are related by the (p, δ) -relation for oblique shocks [Anon. NACA Rep.1135,

Eqn. 160].²⁰ A mismatch in pressure ratio and flow deflection will result in shock detachment. This chapter deals with how such mismatches can be produced.

6.3.1 Detachment by excessive flow turning – δ_{max} criterion

The oblique shock equations readily show that a shock, attached to the leading edge of a wedge, is incapable of turning the freestream flow into being parallel with the wedge surface beyond a certain maximum wedge angle. [Shapiro, 1954; Liepmann and Roshko, 1956; Owcharek, 1964]. This maximum turning angle, δ_{max} , depends on the ratio of specific heats and the freestream Mach number.²¹ Although other causes may preempt shock detachment at δ_{max} , this must be an



ultimate cause in that there are no analytical flow constructs for either a wedge-attached shock or of regular reflection beyond the δ_{max} criterion. Fig. 6.3 shows attached weak and strong shocks on a wedge surface and a typical polar diagram representing the necessary relation between the wedge angle and the shock pressure ratio for the shock to remain attached. On the red segment of the polar the flow behind the shock is supersonic and on the black portion it is subsonic. The shock will detach when either the wedge angle is made greater than δ_{max} or the pressure exceeds the top (black) part of the (p, δ) -polar curve. Since δ_{max} is a function of Mach number, shock detachment can also be brought about, on a fixed angle wedge, by a reduction of Mach number. As the Mach number in front of an oblique shock, on a plane wedge, is reduced, it becomes sonic behind the straight attached shock. A further reduction causes the shock to become curved and the Mach number to become

$$^{20} \tan^2 \delta = \left(\frac{\xi - 1}{\gamma M_1^2 - \xi + 1} \right)^2 \frac{2\gamma M_1^2 - (\gamma - 1) - (\gamma + 1)\xi}{(\gamma + 1)\xi + (\gamma - 1)} \quad \text{where } \xi = p_2 / p_1$$

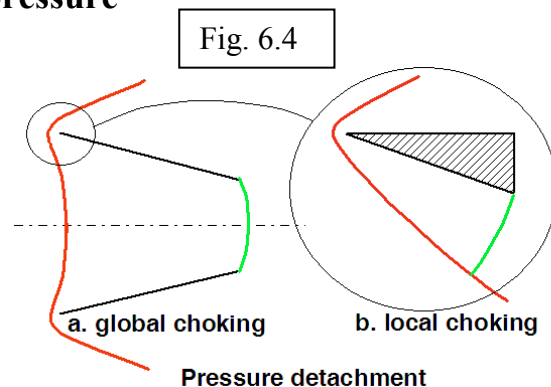
$$^{21} \xi_{\delta_{max}} = \frac{M_1^2 - 2}{2} + \sqrt{\frac{4}{\gamma + 1} + 2 \frac{\gamma - 1}{\gamma + 1} M_1^2 + \frac{M_1^4}{4}}$$

subsonic. The shock remains attached as long as the sonic line passes all the flow entering the subsonic portion of the shock. Flow behind the shock takes on the characteristics of subsonic flow in a concave corner. Such flow is shown in Fig. 6.20 where the shocks are just detaching from a wedge. Compressible corner flow is characterized by near-circular isobars, centered at the corner stagnation point. In the corner flow region, pressure decreases radially outward, compatibly with the curved bow shock which takes up a position that supplies the right mass flow to the sonic line downstream. Corner flow becomes fully established as the shock leaves the wedge at δ_{max} . It provides a smooth transition between attached shock and detached shock flow as long as the Mach number or wedge angle vary smoothly.

6.3.2 Shock detachment by overpressure

The appearance of detachment by excessive back-pressure is more likely in internal flows where it is easier to apply a back-pressure through downstream flow choking. Detachment by excessive backpressure is not causally dependent on the wedge

angle but on the pressure that is applied by the downstream flow exceeding the pressure indicated by the shock polar for that particular wedge angle. The downstream flow can exert this excessive pressure on the black portion of the polar where the flow is subsonic, allowing the increased pressure to be transmitted upstream to the attached shock at the leading edge. Although the detachment mechanism is local to the leading edge, the excessive back-pressure mechanism for shock detachment is of a global nature because the cause arises from choking of the downstream flow. Positively attributing detachment to the influence of downstream global flow requires calculation of the whole flow-field between the shock and the sonic line in the downstream flow. Two types of excessive pressure choking are possible in a convergent duct, as shown in Fig. 6.4. They are here referred to as *global choking* and *local choking*. Choking ($M = 1$) occurs at the green lines.



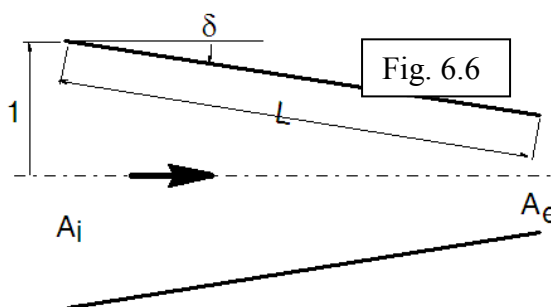
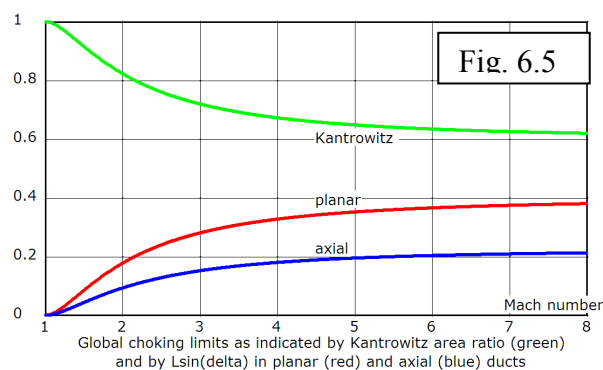
6.3.2.1 Shock detachment by *global choking* appears in internal flow when the mass outflow at the exit of a streamtube is restricted to such an extent that it is less than that passed into the inlet by an attached shock at the entrance. The excess flow must be spilled overboard and this is made possible by the shock detaching and moving upstream to allow a gap for flow spillage between the shock and the leading edge. When the shock detaches due to global choking the shape of the duct leading edge is immaterial. If the exit-to-entry area ratio is varied to choke and unchoke the flow, there appears a possibility for shock attachment/detachment at two different area ratios – a hysteresis is established. This is part of the shock swallowing/un-

swallowing process associated with supersonic air intakes for which analytical, one-dimensional flow area criteria were originally developed by [Kantrowitz and Donaldson, 1945]. Kantrowitz' one-dimensional theory predicts that the normal shock will stand at the

entrance of the duct when the exit-to-entry area ratio is less than that shown by the green curve in Fig. 6.5. A higher value of area ratio will cause the shock to move

downstream – be swallowed. For simple axial (conical) or planar (double-wedge) convergence of angle δ and surface length L it means that $L\sin\delta$ cannot exceed values that would yield an area ratio below the Kantrowitz area ratio, $(A_e/A_i)_K$ ²². A simple geometric

construction shows that if, for planar ducts, $L\sin\delta$ is greater than $1 - (A_e/A_i)_K$,



Simple converging axial or planar duct

$$\left(\frac{A_e}{A_i}\right)_K = \left[\frac{\gamma-1}{\gamma+1} + \frac{2}{(\gamma+1)M_1^2} \right]^{-1/2} \left[\frac{2\gamma}{\gamma+1} - \frac{\gamma-1}{(\gamma+1)M_1^2} \right]^{-1/(\gamma-1)} \quad [\text{Kantrowitz criterion}]$$

shown by the red curve, and if, for an axial ducts, $L\sin\delta$ is above $1 - \sqrt{(A_e/A_i)_K}$, the blue curve, global choking will take place and shock detachment will follow. The geometric relation $L\sin\delta$ gives a rule-of-thumb estimate of global choking, applicable best when L is large and δ is constant and small (Fig. 6.6). This $L\sin\delta$ relation was used to avoid global choking when setting conditions for CFD calculations of locally choked flow in Section 6.5.

6.3.2.2 Shock detachment by local choking appears near the leading edge when the sonic surface is not able to pass all the mass flow entering the portion of the shock between the leading edge and the sonic line behind the shock. As with detachment due to global choking, the shock then detaches, opening a gap between the leading edge and the shock for excessive flow spillage. As distinct from global choking, the conditions for detachment due to local choking depend on the geometric details of the leading edge surface. It is the purpose of this chapter to use CST to predict the conditions for local choking and to verify the predictions by CFD.

6.4 Analysis of detachment by local choking is based on CST. As such, its results are restricted to flow near the shock, i.e. near the leading edge of an attached shock. Local choking is greatly influenced by flow divergence or convergence that occurs in **axial** flow and it is therefore distinctly different from local choking in **planar** flow. This is the fundamental reason why detachment by local choking is different in planar and axial flows. An approximate analytical method, based on CST, is developed in this section for predicting the conditions necessary for shock detachment by local choking in axial flow. Planar flow will be treated as a special case. The underlying premise of local choking is that **a sonic line cannot exist on a surface if the flow area on that surface is contracting**. This principle is the same that applies to steady flow in a converging/diverging passage where the sonic surface can exist only at the throat and not in a convergent section of the passage. It is assumed that this is the driving mechanism that moves the sonic line forward in its attempt to satisfy the mass flow imbalance. Moving in an upstream direction, the

sonic line shifts itself and the imbalance to the leading edge, where detachment then occurs by local overpressure. For a wedge of given angle and curvatures, we attempt to find the wedge length required to choke the flow near the leading edge. Thus the conditions, determining shock detachment by local choking, at a given freestream Mach number, are: wedge angle, wedge curvatures and wedge length.

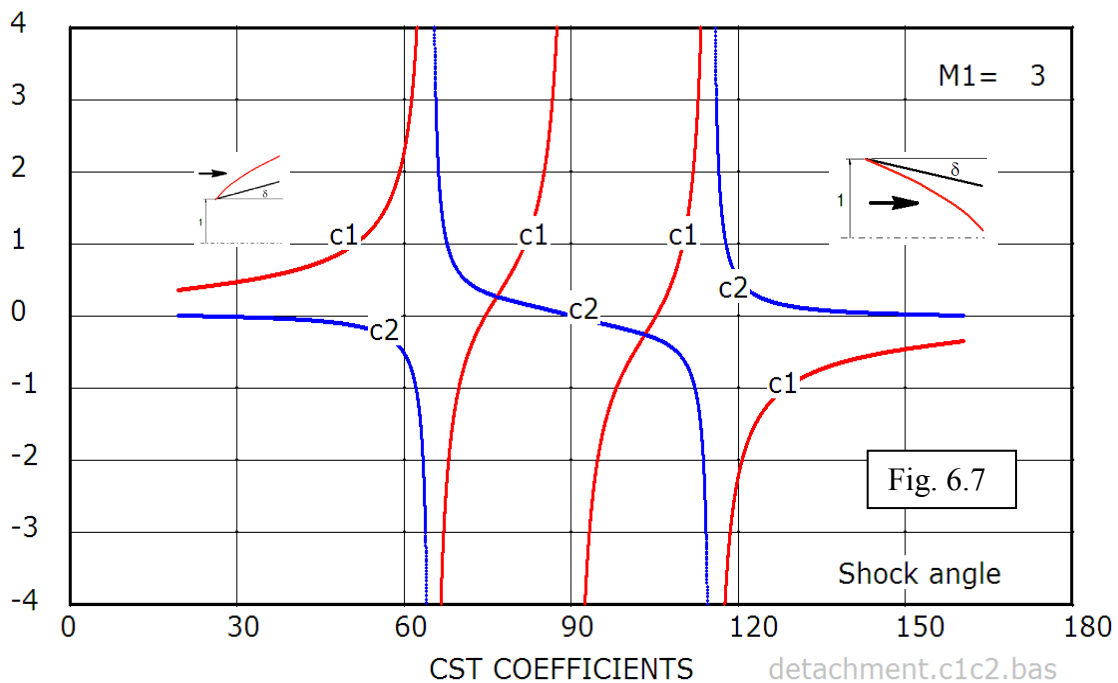
6.4.1 Pressure gradient at leading edge of curved surfaces

The starting point for local choking analysis is the curved shock equations (6.2 a,b) as applied to the URW. Using $S_b = -\cos\theta$ for the URW and eliminating S_a from the two Eqns. (6.2 a,b) gives,

$$P_2 = \frac{a_1}{b_1} D_2 + j \cos\theta (a_1 b_2 - a_2 b_1) / b_1 \quad (6.3)$$

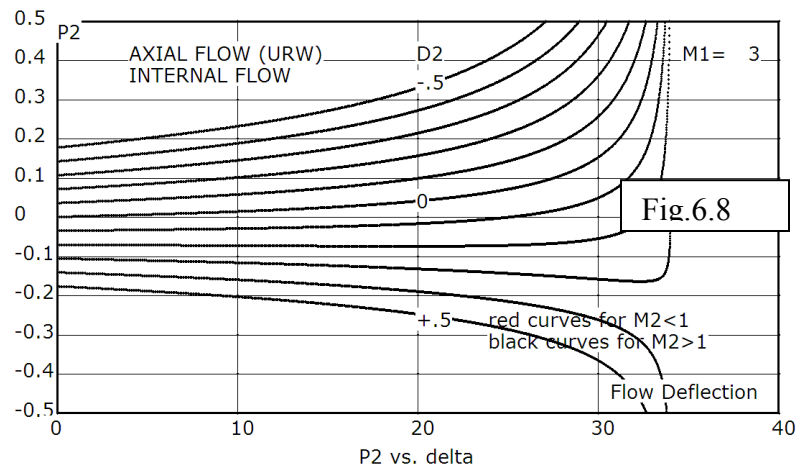
where

$$a_1 = \frac{[BC]}{[AB]} \quad a_2 = \frac{B_2 G'}{[AB]} \quad b_1 = \frac{[CA]}{[AB]} \quad b_2 = -\frac{A_2 G'}{[AB]}$$



This expression gives the normalized pressure gradient at the URW leading edge (both outside and inside) in terms of the leading edge curvature, D_2 , and the Mach number and shock angle, which are the only parameters contained in the a and b -terms in Eqn. 6.3. Outside/inside is determined by specifying the shock angle, θ , as acute/obtuse. The first term on the right hand side of Eqn. (6.3) is the contribution to pressure gradient from the streamwise curvature of the surface, D_2 , and the second term, which vanishes for planar flow, is the contribution of lateral surface curvature (divergence) in axial flow. The two terms are independent, being determined by the URW shape and freestream Mach number so that P_2 can be positive, negative, zero and infinite. Expressing P_2 from Eqn. (6.3) as, $P_2 = c_1 D_2 + j c_2$ (6.3.1) makes c_1 represent the **curvature** contribution to the pressure gradient and c_2 represent the **convergence** contribution. The distributions of the curvature and convergence coefficients are plotted against shock angle for Mach 3 in Fig. 6.7. At the Crocco values of shock

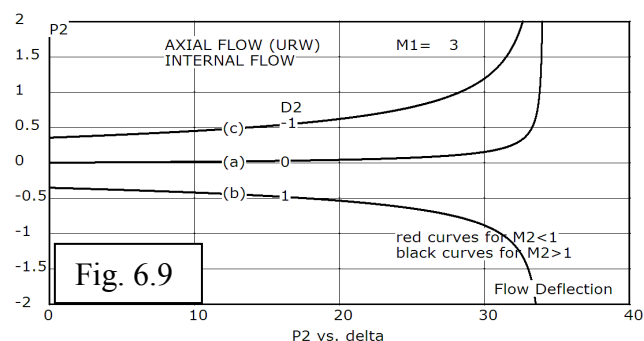
angle $[\text{CA}] = 0$, the coefficients go to $\pm\infty$, indicating that the pressure gradient can become very high at the Crocco point. The red curves cross the zero-lines at the



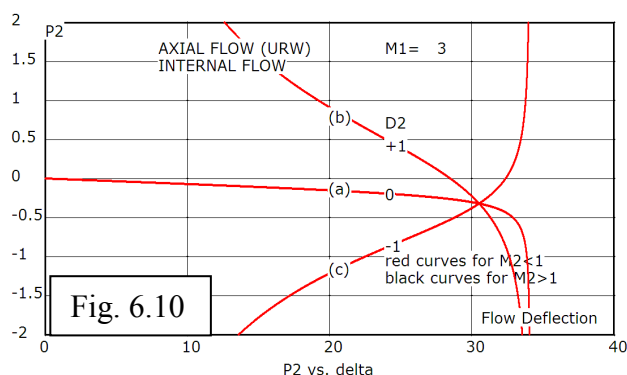
Thomas points showing that a zero pressure gradient can exist. The convergence contribution (c_2) is small in comparison to the curvature effect (c_1) over most of the

supersonic shock as well as the normal shock. It is only near the Crocco point where the reverse is true. Considering that D_2 also enters as a variable in determining the pressure gradient, the possible pressure gradient variation is complex. Figures 6.8 and 6.9 are for a supersonic post-shock flow showing the pressure gradient, P_2 , from Eqn. (6.3), at the leading edge of the **internal** surface of the URWs described in Section 6.2.1 for three streamwise

surface curvatures, $D_2 = +1, 0$ and -1 , plotted against wedge angle. The negative curvature (concave surface, case (c)) causes a positive pressure gradient. Such a gradient, applied to supersonic flow leads



towards flow choking. The zero curvature surface (straight conical duct; case (a)) carries a mild positive pressure gradient for small wedge angles. A convex surface (case (b)) has a negative pressure gradient.²³ Negative pressure gradients, applied to supersonic flow, lead towards higher supersonic Mach numbers and no flow choking for case (b).



The Figure 6.9 is the same as 6.8 but with an expanded P_2 -axis for P_2 values near zero and with D_2 ranging from -0.5 to $+0.5$ in steps of 0.1 . For negative values of D_2 (concave surfaces) the pressure gradient is positive, making local choking possible. For positive curvatures (convex surfaces) the pressure gradient is largely negative, hence no local choking occurs. However, for small positive values of curvature such as $+0.1$, P_2 is negative for small values of δ , becoming positive for $\delta > 25$ deg.

²³ Such surfaces can be calculated for conically symmetric M-flow from the Taylor-Maccoll equations. See Ch. 4

showing that, for more steeply converging ducts, local choking is attained by flow convergence and not by surface curvature. Figure 6.10 is for the same URW geometries (a), (b), (c), with a **strong** family attached shock carrying **subsonic post-shock flow**. In this case a negative pressure gradient moves the subsonic flow towards choking; again, it is configurations (a) and (c) that allow the internal flow in the URW to choke locally. More complicated behaviour is observed at higher values of **Flow Deflection** where (b) begins to support downstream choking by dipping into the negative P_2 region of the graph. At the same high values of **Flow Deflection** the (c) configuration rises into the positive P_2 region, showing that it no longer supports downstream flow choking. All curves meet at the Thomas point where $a_1 = \frac{[BC]}{[AB]} = 0$

so that the value of P_2 at this point is $P_2 = j \cos \theta (a_1 b_2 - a_2 b_1) / b_1$. The Thomas point occurs at a unique value of wedge angle for each freestream Mach number. At this unique value the pressure gradient and the length of surface required for choking, discussed below, are both insensitive to changes in surface curvature. The practical importance of this is unknown. The condition does not exist in planar flow.

In the investigation of boundary layer flow it may be of interest to examine the effects of surface curvature and divergence as isolated from the effects of a streamwise pressure gradient. Setting $P_2 = 0$ in Eqn. 6.3.1 gives the curvature of the required surface as, $D_{2P=0} = -c_2/c_1$. From Fig. 6.7 it appears that, for weak shocks, c_1 and c_2 have opposite signs so that the surface curvature is positive as in Fig. 6.1b. Between the two Thomas points c_1 and c_2 have opposite signs so that the surface curvature is negative as for the surfaces in Fig. 6.1c.

This section has presented the post-shock pressure gradient as the underlying cause of local choking near the leading edge of a doubly curved wedge surface and how this pressure gradient can be determined from freestream Mach number, wedge curvature and wedge angle. In the next section the pressure gradient is converted into a Mach number gradient to derive an approximate distance from the leading edge to the sonic point.

6.4.2 Mach number gradient and choking length L^*

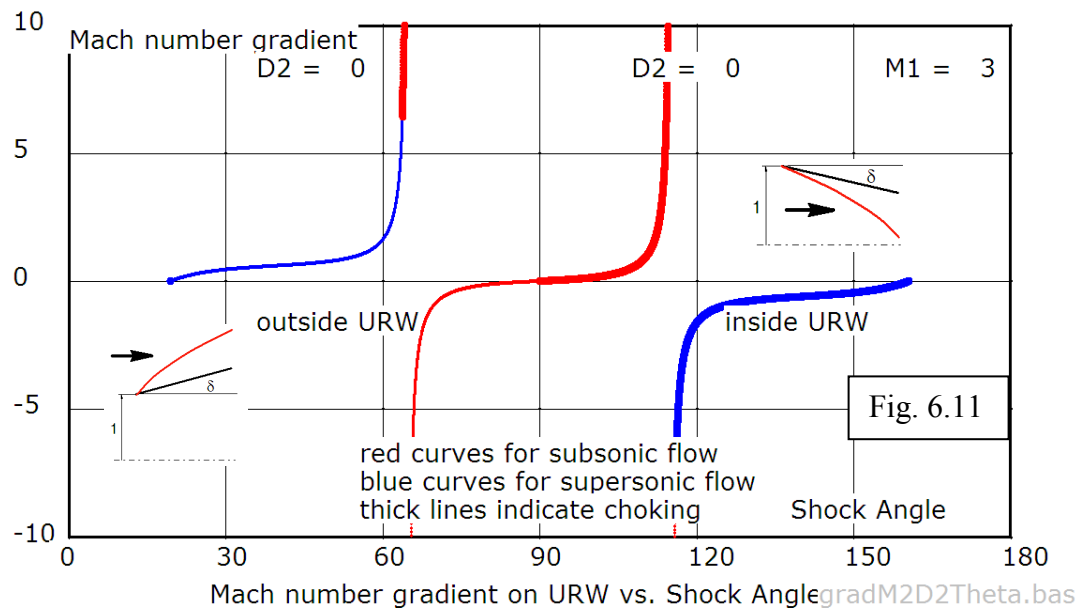
For the isentropic flow behind the shock (subscript 2), the Mach number gradient can be written in terms of the pressure gradient [Zucrow and Hoffman, Eqns. 4.50 and 4.51, 1977],

$$\frac{dM_2^2}{M_2^2} = -\frac{2 + (\gamma - 1)M_2^2}{\gamma M_2^2} \left(\frac{dp}{p} \right)_2 \quad (6.4)$$

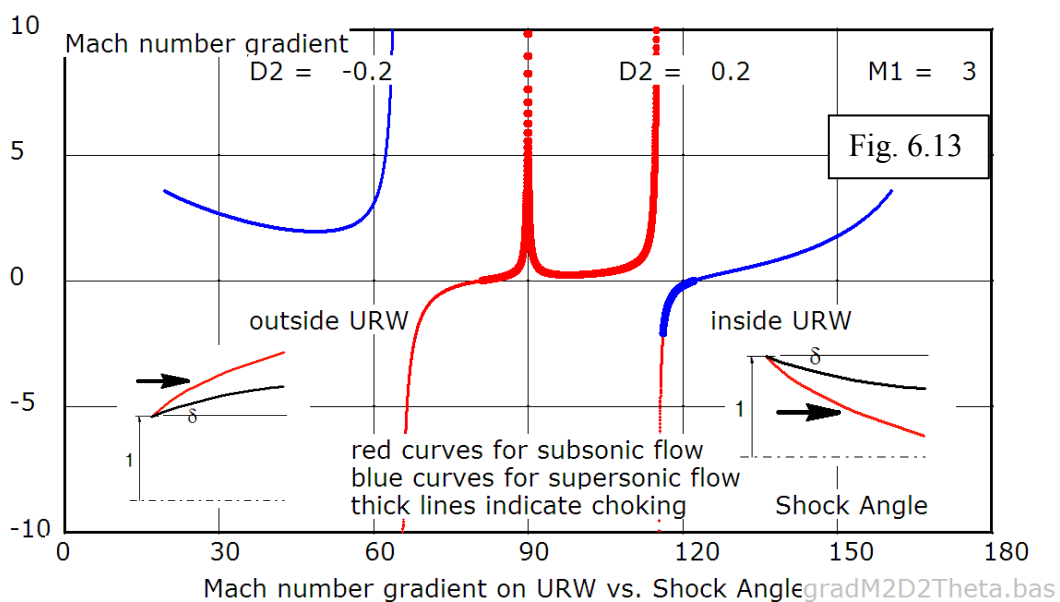
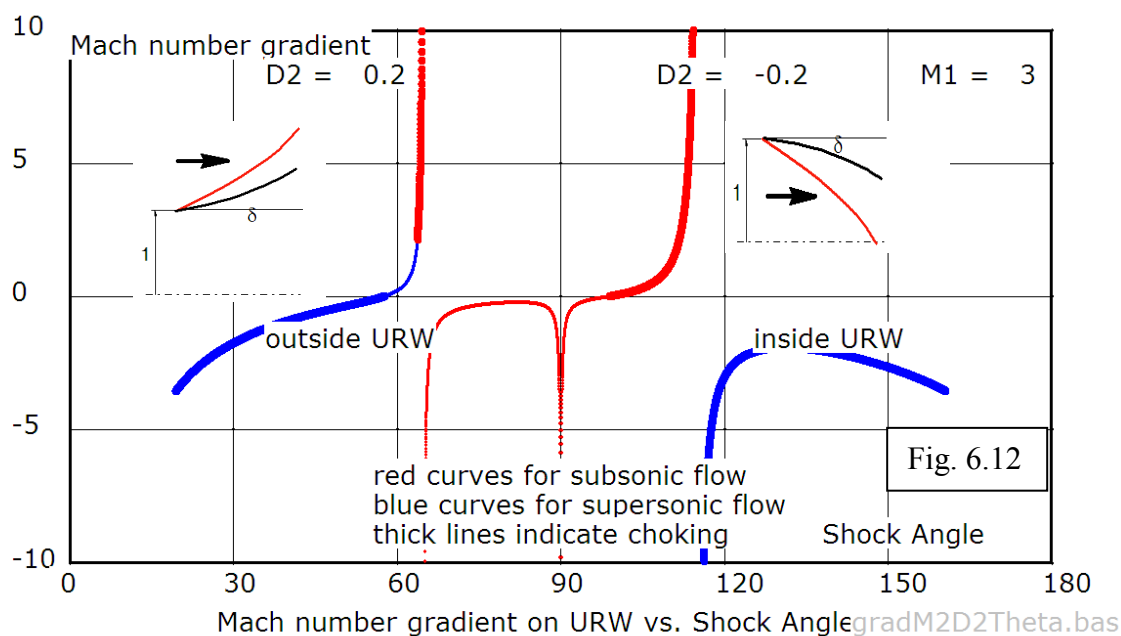
This enables the Mach number gradient to be expressed in terms of the normalized, CST, pressure gradient, $P_2 = (dp/ds)/(\gamma p M^2)$ as,

$$\frac{dM_2^2}{ds} = -[2 + (\gamma - 1)M_2^2] M_2^2 P_2 \quad (6.5)$$

where s is the distance along the wedge (streamline) in the flow direction. The Mach number will tend towards one if the flow behind the shock is subsonic and the Mach number gradient is positive or if the flow is supersonic and the Mach number gradient is negative. Given enough length, choking will occur behind a curved shock in both cases. The Mach number gradient is plotted against shock angle, for a URW with no streamwise curvature ($D_2 = 0$; i.e. conical surfaces) at Mach 3, in Fig. 6.11. Subsonic post-shock flow is shown in red and supersonic in blue. Both curves are rendered bold where local choking is possible. In the left side of the graph, for acute shocks, the supersonic flow goes sonic only at a shock angle near 65 deg. The situation is similar to what happens on a pointed cone at high cone angles. In the right side of the graph, for internal flow and obtuse shocks, the supersonic flow always chokes, only a short segment of subsonic flow (thin, red), having a negative Mach number gradient, does not. The strong shock curve, passing through the normal shock condition at a shock angle of 90 deg, shows that the subsonic flow on the external surface does not choke whereas it does choke on the internal surface. Although there is an obvious symmetry for the inside/outside Mach number gradient magnitudes, the flow types, in terms of their choking propensity, are quite different.



Opportunities for choking increase on a URW that is concave on its outer and inner surfaces as in Fig. 6.12. Supersonic flow, both inside and outside, tends to choke (bold, blue) except for a narrow band of acute angles in outside flow. Subsonic flow on the inside chokes, as it does in a narrow region in outside flow. A normal shock, facing uniform flow does not produce a curved streamline behind itself (Sect. 3.). Imposing such curvature causes anomalous results at a shock angle of 90 deg. There is a noticeable lack of symmetry due to divergence on the outside and convergence on the inside. It is this inside convergence that causes the inside flow to choke much more readily for all shock conditions.



Opportunities for choking decrease on a URW that is convex on its outer and inner surfaces. The curves, in Fig. 6.13 are for a URW with curved surfaces that are convex towards the oncoming flow both outside and inside. Only a short segment of the

weak inside shock (bold, blue) and all of the inside strong shock (bold, red) produce choking. There is a noticeable lack of symmetry due to divergence on the outside and convergence on the inside. Convergence causes the inside flow to choke and divergence prevents choking on the outside. For the convex URW choking is discouraged also by the expanding surface curvature.

This section has described the geometry of curved wedge surfaces that can produce shock detachment by local choking.

6.4.3 Curved surface length required for choking, L^*

Making the approximation that **the post-shock Mach number gradient equals the average gradient to the sonic surface** gives,

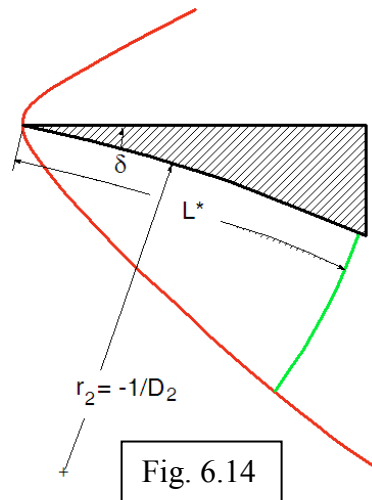
$$dM_2^2/ds = (1 - M_2^2)/L^* \quad (6.6)$$

where L^* is the distance from the shock (at the leading edge) to the sonic point on the wedge.²⁴ Using Eqn. (6.5) and P_2 from Eqn. (6.3), gives,

$$L^* = \frac{b_1(M_2^2 - 1)}{M_2^2 [2 + (\gamma - 1)M_2^2] [a_1 D_2 + j(a_1 b_2 - a_2 b_1) \cos \theta]} \quad (6.7)$$

where $j = 0/1$ for planar/axial flow. The post-shock Mach number, M_2 , is expressed in terms of M_1 and θ [NACA Rep. 1135, Eqn. 132],

so that the independent parameters that make up the right-hand side of this expression are the freestream Mach number, M_1 , the shock angle, θ , and the wedge curvature, D_2 . The shock angle can be traded for the wedge angle, δ , by the (M, θ, δ) -relation for oblique shocks [NACA Rep. 1135, Eqn. 138] so that the right side becomes an expression containing the freestream Mach number, M_1 , and wedge geometry as specified by



²⁴ An interesting variation would be to assume a linear decrease in Mach number instead of the square of the Mach number. In this case Eqn. (6.6) would read, $dM_2/ds = (1 - M_2)/L^*$. This equation would give a different value of L^* by at most a factor of 2.

(δ , D_2 , L^*). Equation (6.7) is the ‘*local choking equation*’. It places a limit, L^* , on the length of curved wedge surface that supports an attached shock, predicting that a value of $L > L^*$ will cause shock detachment by *local choking*. If $L^* = 0$, detachment will occur due to local choking conditions right at the leading edge. Detachment by local choking will not occur when $L^* \rightarrow \infty$. However, shock detachment can still occur by an excessive wedge deflection or by global choking. Shock detachment will also not occur by local choking when Eqn. (6.7) gives a negative value of L^* . A large positive surface curvature, D_2 , leads to local choking near the leading edge and shock detachment even for a small value of L . This will become more evident for planar flow where the combination L^*D_2 appears as a parameter. Equation (6.7) is the basis for judging the onset of local choking and the resulting shock detachment. Since it is based on CST, it applies strictly only right behind the shock for small values of $L^* \sim 0.1$. For values of L much larger than 0.1 one should look to *global choking* as the cause of shock detachment.

This section has produced an approximate length required to produce local choking on a curved wedge. The next four sections deal with the implications of Eqn. (6.7) for four types of leading edge shapes:

- planar flow over a flat surface where $j = 0$ and $D_2 = 0$;
- planar flow over a curved surface where $j = 0$ and $D_2 \neq 0$;
- axial flow over a URW with straight generators where $j = 1$ and $D_2 = 0$ (sketch (a) in Section 6.2.1);
- axial flow inside and outside a curved URW where $j = 1$ and $D_2 \neq 0$ (sketches (b) and (c) in section 6.2.1).

6.4.4 Local choking in planar flow over a flat plate ($j = 0$ and $D_2 = 0$)

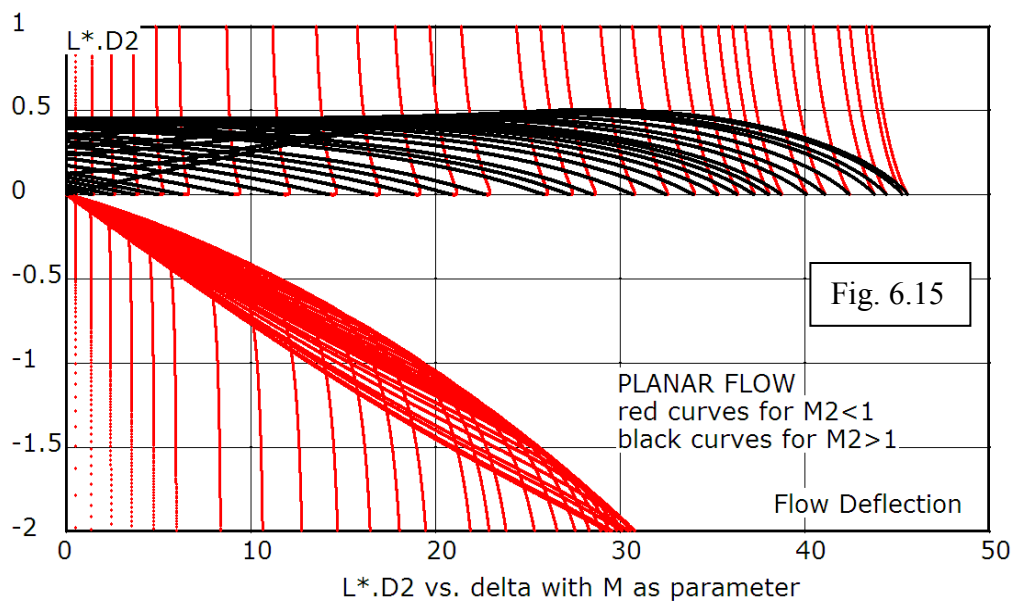
An examination of Eqn. (6.7) shows that for these conditions the third term in the denominator is zero so that $L^* \rightarrow \infty$. There is then no reason to expect local choking at any Mach number and shock angle, so that detachment would occur only when δ exceeds δ_{max} or $L \sin \delta$ is large enough for global choking to occur. Shock detachment by local choking does not occur for flat shocks and wedges. It is reassuring that CST

predicts what is known to be the correct result in the limiting case where surfaces and shocks have no curvature.

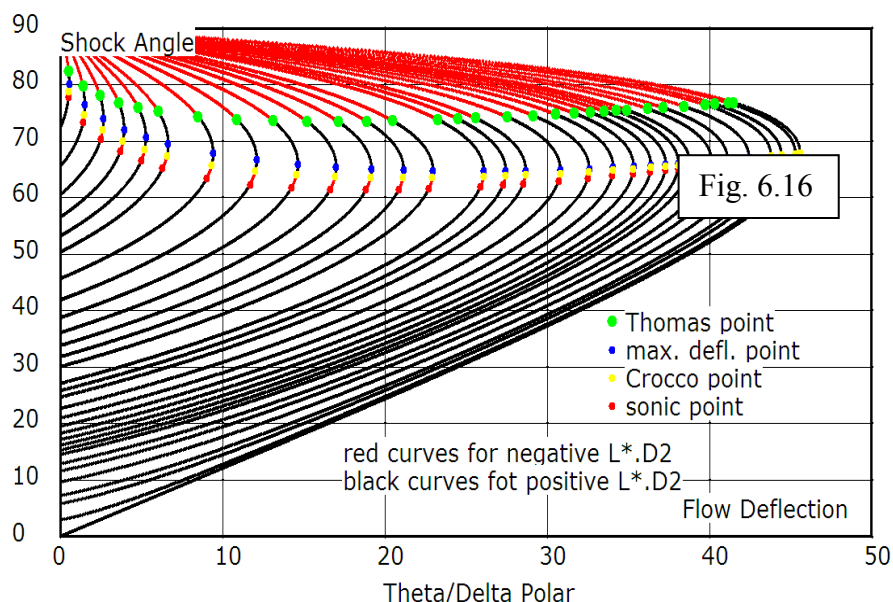
6.4.5 Planar flow over a curved surface ($j = 0$ and $D_2 \neq 0$)

For this case Eqn. (6.7) reduces to,

$$L^*D_2 = -\frac{L^*}{r_2} = \frac{b_1}{a_1} \frac{M_2^2 - 1}{M_2^2 [2 + (\gamma - 1)M_2^2]} \quad (6.8)$$



where r_2 is the radius of curvature of the concave surface. It states that the ratio of length of surface required to choke the post-shock flow to the surface radius of curvature is a function of freestream Mach number and wedge angle. So that Eqn.(6.8) places a limit on $L^*/r_2 = -L^*D_2$ (rad.) which is just the amount of post-shock flow turning. This equation, a function of M_1 and δ , is plotted in Fig. 6.15. Both this graph and Fig.6.16 plotted for a selection of Mach numbers, from left to right: 1.05, 1.1, 1.15, 1.2, 1.25, 1.3, 1.4, 1.5, 1.6, 1.7, 1.8, 1.9, 2, 2.2, 2.3, 2.4, 2.6, 2.8, 3, 3.2, 3.4, 3.6, 3.8, 4, 4.5, 5, 6, 8, 10, 20, 10000. This is the same set of Mach numbers that appears in the plots of NACA Rep. 1135. Black curves in Fig. 6.15 represent shocks with supersonic post-shock flow; red curves represent shocks with subsonic post-shock flow.



Each Mach number curve has a positive and a negative branch that meet at $\pm\infty$ at the Thomas point. The black curves for supersonic post-shock flow all give positive values of L^*D_2 ($= -L^*/r_2$) so that the supersonic post-shock flow chokes only when L^* is positive due to D_2 being positive (concave) also. It appears (black curves) that, on a planar wedge, a post-shock flow turning above approximately 0.5 radians will produce “supersonic” shock²⁵ detachment by local choking at any Mach number. All supersonic shock curves dip to $L^*D_2 = 0$ at values of their flow deflection angles corresponding to sonic post-shock flow. This indicates that detachment of a supersonic shock occurs when the flow behind the shock is sonic at any wedge curvature. Detachment from a planar wedge at δ_{max} occurs only on a wedge with zero or negative curvature. Detachment of a “subsonic” shock can occur for positive or negative D_2 on either side of the Thomas point as shown by the red curves. Detachment of a “subsonic” shock can not occur at the Thomas point since P_2 and hence the Mach number gradient, are both zero. Fig. 6.16 is on the familiar (θ vs. δ) polar for oblique shocks. It shows, by the black curves, where the L^*D_2 limit for an attached shock is positive and, by the red curves, where it is negative. A short portion

²⁵ The nature of local choking behind shocks is distinguished by the post-shock flow being either subsonic or supersonic. Hence the shocks are denoted as “subsonic” and “supersonic” in the two cases.

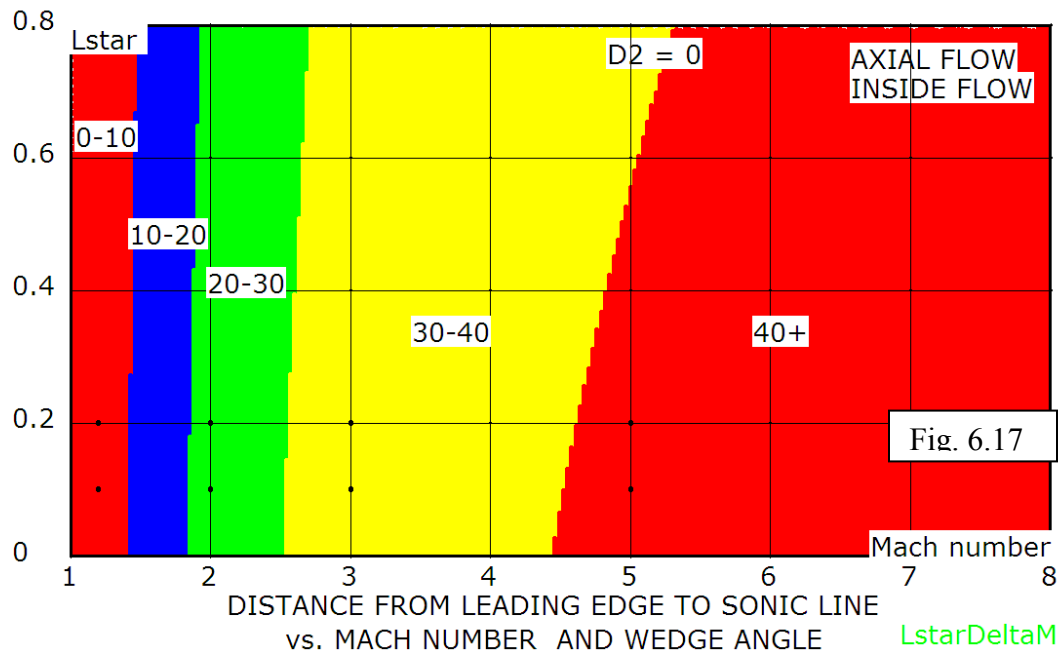
of each curve, between the sonic and Crocco points is also red so that L^*D_2 is negative in this region.

6.4.6 Flow in a URW with conical surface ($j = 1$ and $D_2 = 0$)

This is the URW (a) shown in Fig. 6.1. For this geometry Eqn. (6.7) becomes,

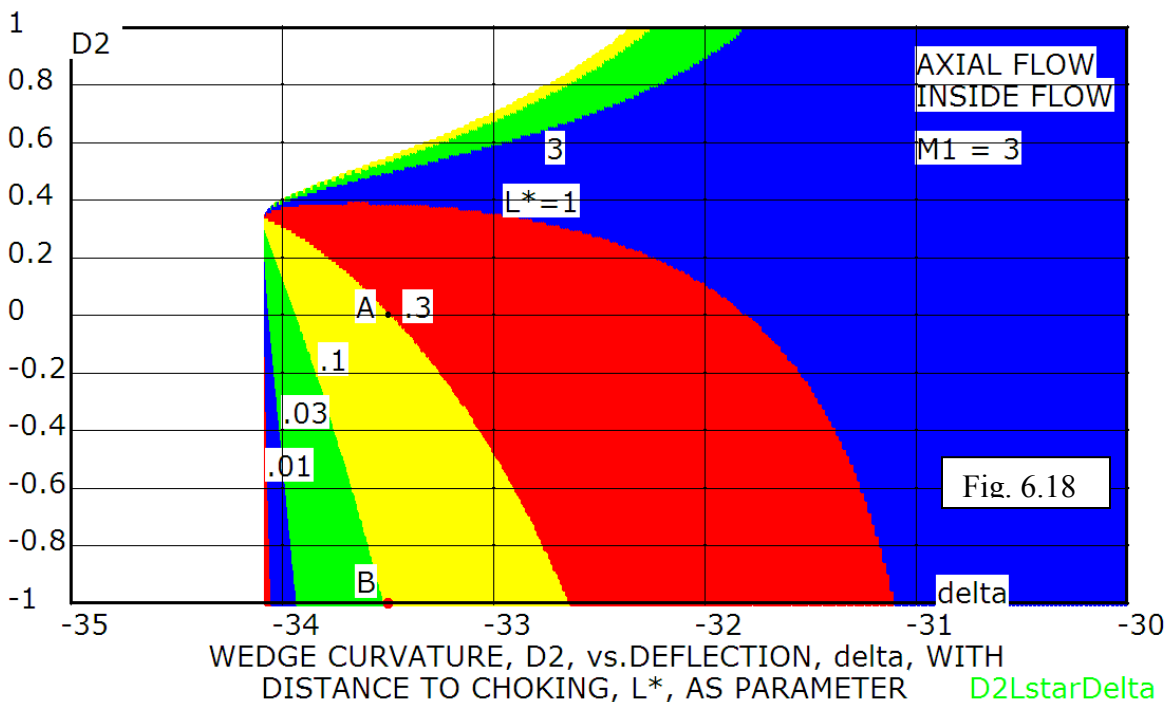
$$L^* = \frac{b_1(M_2^2 - 1)}{M_2^2 [2 + (\gamma - 1)M_2^2] [(a_1b_2 - a_2b_1)\cos\theta]} \tag{6.9}$$

This equation gives the flow-length of post-shock surface required to choke the flow. Since the outside and inside flows are different; the shocks are acute and obtuse respectively giving two different evaluations for L^* , for the outer and inner



flows. Figure 6.17 is a plot of Eq. (6.9) for L^* ($Lstar$)²⁶ against M_1 with the wedge angle as parameter for $D_2 = 0$, i.e an a -type URW, as described in Section 6.2.1, above with straight conically convergent inner surface. The various values of δ on the abscissa, where $L^* = 0$, are the δ_{max} values, indicating that, for $\delta = \delta_{max}$,

²⁶ L^* is normalized by the URW radius of $y=l$



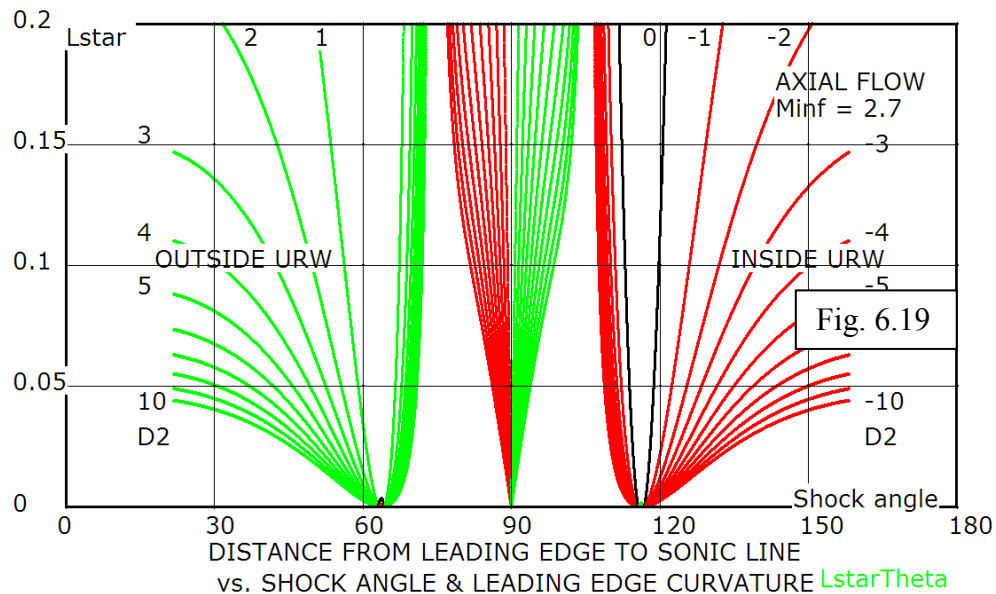
local choking occurs right at the leading edge, effectively requiring a very short duct length to cause detachment. An examination of this figure shows that moving to a smaller duct convergence angle increases the length of duct, L^* , required to produce local choking and hence detachment at that angle. At Mach numbers below ~ 2.5 the colour bands for δ are almost vertical so that the effect of local choking on shifting shock detachment away from δ_{max} is small. Figure 6.18 is a cross-plot of Eqn. (6.7) for the inside surface of a URW at Mach 3. At Mach 3 the deflection angle for sonic flow is -34.00835 deg and the maximum deflection is (-34.07344) deg, as represented by the vertical border of the coloured area. The surface curvature D_2 is plotted against the flow deflection through the shock at the leading edge with L^* , the distance from the leading edge to the sonic surface, as parameter. Since L^* is based on CST, and CST applies strictly only at the shock, then only small (fractional) values of L^* , predicted by Eqn. (6.7), are credible on this graph. Points at A(-33.5, 0) and B(-33.5, -1) are chosen for CFD verification. At the A-point, $L^* = 0.3$ and at the B-point, $L^* = 0.1$. CST predicts that shock detachment occurs with L -values larger than these in each case. The global choking measure, $L^* \sin \delta$, is 0.1655 and 0.0552 for points A and B, respectively; both values being below the global choking criterion of 0.23. Note that both of these

points are for a Mach number of 3 and a wedge angle of -33.5 deg, so that differences in shock attachment/detachment on the inner surface are due to wedge curvature as manifest by local choking.

6.4.7 Flow in a URW with ($j = 1$ and $D_2 \neq 0$)

This is the general case where the freestream Mach number and the wedge geometry, as specified by (M_1, δ, D_2), are given and L^* is then calculated from Eqn.(6.7).

$$L^* = \frac{b_1(M_2^2 - 1)}{M_2^2 [2 + (\gamma - 1)M_2^2] [a_1 D_2 + j(a_1 b_2 - a_2 b_1) \cos \theta]} \quad (6.7)$$



Positive values of L^* , as given by Eqn. (6.7), are plotted in Fig. 6.19, versus the wedge curvature and shock angle on the outside and inside surfaces of a URW, for Mach 2.7. Green curves indicate positive surface curvature (turning away from the axis), red curves indicate negative curvature (turning towards the axis). The black curve is for zero curvature (conical surface). Curves at and around a shock angle of 90 deg are anomalous because flow curvatures are imposed on a normal shock and a normal shock can not produce any curvature in a uniform free stream (see Section 3.5.1). All curves dip to $L^* =$

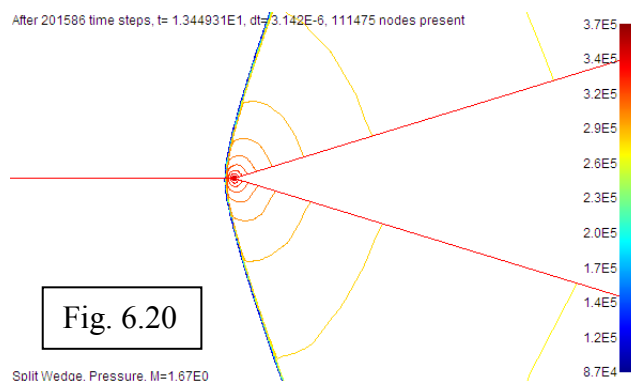
0 at the sonic shock angles and $L^* \rightarrow \infty$ at the Thomas shock angles. A conical inside surface will choke whereas a conical outside surface will not. Both sets of curves terminate on the left and right at the Mach angles for Mach 2.7. At these (weak shock) limits the surface curvatures determine the pressure gradients uniquely (see Section 3.8.1, Eqn. 3.50); the pressure gradient determines the Mach number gradient and the Mach number gradient determines L^* . This is the essence of local choking on a URW at Mach 2.7.

6.5 Computational examples²⁷

Curved shock theory (CST) applies exactly only to the curved shock and the conditions immediately in front of and behind the shock surface. It is capable of depicting conditions at shock detachment as they occur **right at the shock**. However, the cause of these conditions is not necessarily reachable and detectable by CST when the cause is some distance removed from the shock. Shock detachment by downstream choking is an example of where the higher-than-tolerable pressure behind the shock is created by conditions further downstream, conditions that are not in themselves predictable by CST. In these situations CFD has to be used to simulate the whole flow-field so as to include the effect of causes located away from the shock surface.

6.5.1 Grid-independence

The grid generator used by the CFD code produces a grid that is asymmetric with respect to the splitter tube. The code would then produce results that could not be compared if its calculations were at all grid-



²⁷Computer program SolverII is used in this paper to obtain steady state flows over URWs. SolverII is a finite-volume unstructured TVD Godunov-type Euler code with local grid refinement.

dependent. A test calculation was performed on two plane wedges with no stream-wise or cross-stream curvature on the top and bottom. For grid-independence the flows must be identical. The result is shown in Fig. 6.20 for Mach 1.67 and a wedge angle of 16 deg - just larger than the maximum deflection angle. The top and bottom flows show no grid-induced dissimilarity so that any grid refinement is unwarranted. As an added feature, the picture shows just-detached shocks where the post-shock flow has characteristics of corner flow with concentric near-circular isobars centered at the corner. Corner flow is an intermediate flow between an attached shock flow and detached shock flow. It allows a time-wise smooth transition between the two.

6.5.2 Local and global choking

This section illustrates the difference between global and local flow choking in an axial converging duct. Figure 6.21a shows Mach number contours on a URW as calculated by the CFD code Solver II. The freestream Mach number is 2.7 for which the maximum deflection angle is 31.7406 deg and the sonic shock deflection is 31.64294 deg. The upper (outer) and lower (inner) wedge angles are both 30 deg so that on a plane wedge the shocks would both be attached with slightly supersonic post-shock flow. Flow is supersonic on the outer wedge surface and the shock is attached. However, on the lower wedge the flow is subsonic and the shock is very close to detaching. This is an example of shock detachment by local choking where the sonic surface, appearing as a thin black line from the shoulder to the shock, is not able to pass the flow entering through the shock in front of it. Shock detachment is caused by the curved shape of the inside surface at the leading edge. Although there is a Mach disk at the centre line, the global (inside) flow is not choked and the detached flow is confined to the leading edge without being affected by downstream conditions – hence the term ‘local choking’.

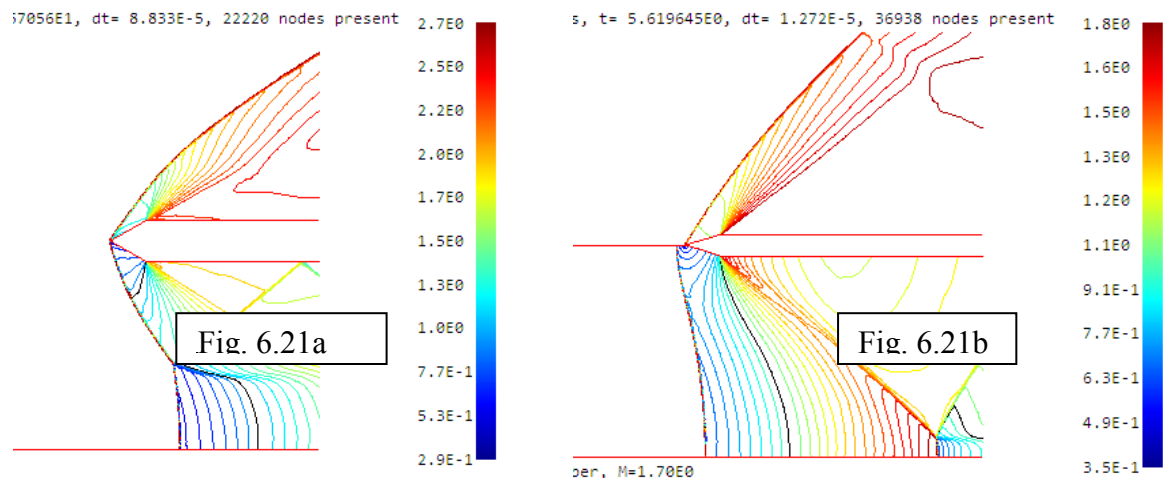
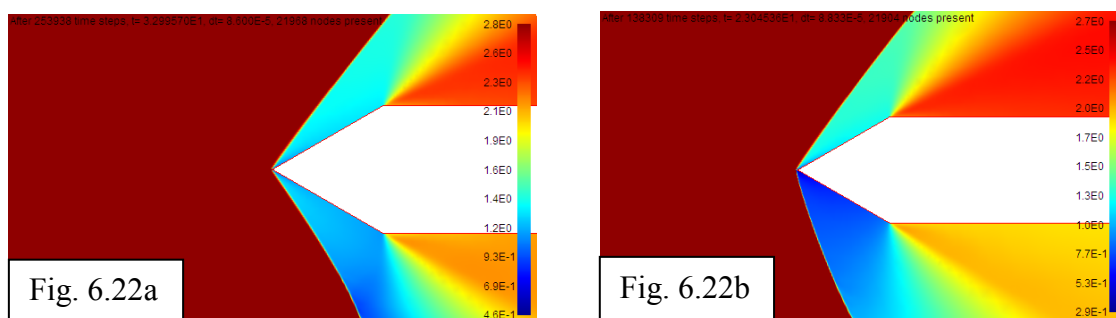


Figure 6.21b is for a URW at a freestream Mach number of 1.7. For Mach 1.7 the maximum deflection and sonic shock angles are 17.01194 and 16.63108. Both upper and lower wedge angles are 16.0000 deg. The splitter tube appears on this picture. In this case the outer shock is attached whereas the inner shock is detached from the leading edge. All of the inner flow is choked at the sonic surface and the shock has assumed a steady shape and position in front of the URW.

6.5.3 Attachment/detachment hysteresis by CFD

At supersonic speeds, two distinctly differing **global** flows can exist in a given converging duct, the so-called started and unstarted flows. These flows are subject to hysteresis when approached by increasing or decreasing Mach numbers. This section describes a similar hysteresis for **local** flow at the leading edge. The leading edge of a URW is shown in Fig. 6.22a,b with a ± 30 deg double wedge leading edge.

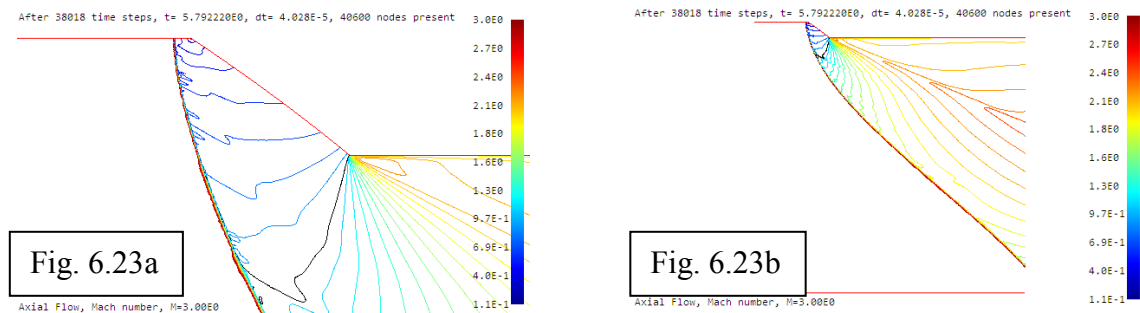


In the calculations for the left picture 6.22a the Mach number was very gradually brought down to Mach 2.7 from Mach 3. In the right picture 6.22b the Mach number was brought up to 2.7 from Mach 2.5. At Mach 2.7 the sonic angle is at 31.64294 deg and the maximum flow deflection is 31.7406 so it is not surprising that the flow on the outside wedges is supersonic with an attached shock for both cases. On the inside, however, the flows are markedly different. First of all they are different from their corresponding external flows because of the lateral curvature and secondly they are different from each other – this being the hysteresis. In the decreasing Mach number case the lower shock is attached and concave towards the on-coming flow. In the increasing Mach number case the lower shock is detached and convex with subsonic

downstream flow. This is in accord with Eqn. (6.7) which predicts differing values of L^* for weak and strong shocks.

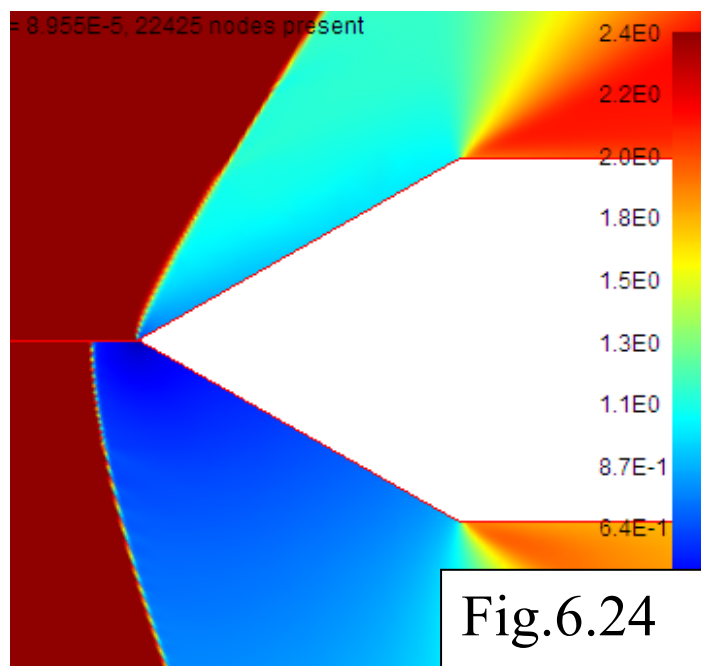
6.5.4 CFD vs. CST

CFD calculations are presented in this section for the CST predictions in Section 6.4 of Eqn. (6.7) at conditions for the two points A and B. All the results are for a Mach number of 3 and a wedge angle of 33.5 deg. At this Mach number the flow deflection angle for sonic flow is 34.00835 deg and for maximum deflection it is 34.07344 deg so that, on a plane wedge, the shock remains attached. The 0.5 degree difference in flow deflection angle represents a 1.5 degree difference in shock angle at this Mach number. CFD result for point B is shown in Fig.6.23b with constant Mach number contours. The axial wedge surface at the top is curved towards the flow with a radius of curvature of 1. The distance from the axis of symmetry at the bottom to the top of this figure is also unity. The doubly curved leading edge supports a detached shock with subsonic flow between the



shock and the surface and a sonic line from the corner to the shock. The diagram in Fig.6.23a is an enlarged view of the subsonic region where the detachment is clearly visible. This is an example of shock detachment occurring due to local flow choking as induced by wedge curvatures in both streamwise and transverse directions. Globally, the flow is unchoked. The conditions for point A led to global choking where the shock moved upstream out of the computational region.

Figure 6.24 shows Mach number colour grading over the leading edge of a URW with outer/inner deflection angles ± 30 deg in a Mach 3 freestream flow. An infinitely thin splitter tube is inserted, in the computational domain, projecting upstream from the leading edge, to keep the effects of the upper and lower curvatures from



interacting. The **streamwise** curvature for both surfaces is zero, $D_2 = 0$. For the upper/outer surface the **lateral** curvature is $-\cos(30) = -.8660$ and for the lower/inner surface it is $-\cos(150) = .8660$ with curvature radii 1.1547 and -1.1547 respectively. The negative and positive curvatures cause expansive and contractive flows on the upper and lower surfaces as specified by the second term of Eqn. (6.3). Expansive flow on the upper surface is supersonic whereas compressive flow on the bottom is subsonic. The bottom flow chokes at the corner causing detachment of the lower shock. This is an illustration of **shock detachment as caused by lateral surface curvature** through the action of local choking.

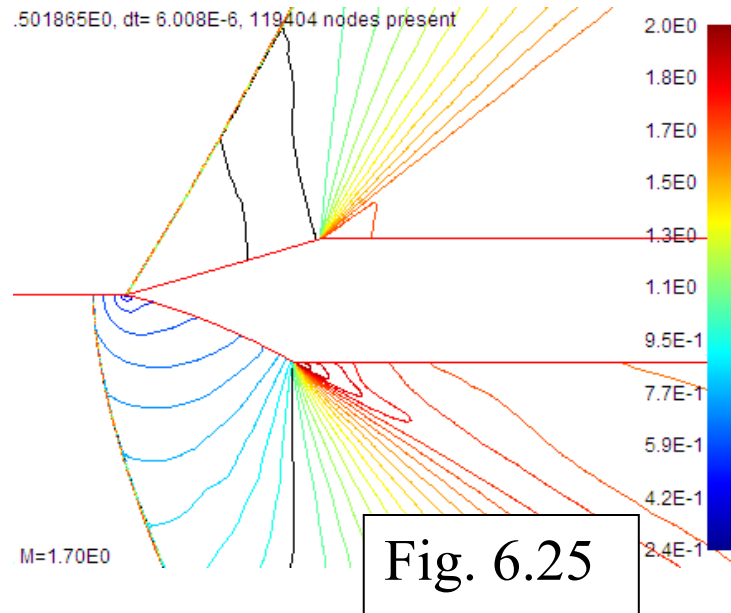


Fig. 6.25

Figure 6.25 is for **planar** flow at Mach 1.7, with constant Mach number lines, where the outer and inner wedge angles are ± 16.5 deg. At this Mach number the sonic and maximum deflection angles are 16.6311 and 17.0119, so that, on plane wedges the shocks would remain attached. In fact the upper wedge is plane and the shock is attached with a sonic line shown between the plane surface and the shock, indicating just-supersonic flow. The bottom wedge is curved towards the flow in the streamwise direction by $D_2 = -1$ so that, according to the first term in Eqn. (6.3), the flow is compressive. The thin black line shows where the **flow chokes locally by streamwise surface curvature, eventually causing shock detachment**. The last two figures have demonstrated that local choking can be caused by cross-stream as well as streamwise surface curvature and that local choking leads to shock detachment at flow deflection angles below sonic and δ_{\max} limits.

6.5.5 Abruptness of transition

Solver II's ability to simulate transient flow provided an opportunity to observe detachment evolution in time. Although, on a fixed geometry wedge, detachment occurred in a very narrow range of Mach number, there was no unsteadiness, instability or time-dependence in the flow and the detachment process could be

reversed by an increase in freestream Mach number at any point. The marked change in shock geometry was connected by steady corner flow. Any hysteresis was with respect to Mach number and not with respect to time. Guderlay's characterization of a "radical change" is confirmed but the "abruptness" is only as abrupt as the change in freestream Mach number. If the detachment process is fundamental to the RR to MR transition then a Mach number driven transition could be expected to be smooth.

6.6 Conclusions

Detachment by **global choking** is a flow area effect that occurs in the starting and unstarting of air intakes. It is due to the global mismatch of mass flow passing through the shock at intake entry and the sonic surface at the exit. If it occurs in a duct, it preempts **local choking**, where local choking is due to the same mismatch but now occurring at the duct leading edge. It has been shown that shock detachment can occur from a sharp leading edge that is curved either along or transverse to the freestream direction by **local choking** of the post-shock flow. Detachment by local choking is attributed uniquely to the shape of the leading edge and the freestream Mach number and occurs when the convergent flow is not globally choked. Both local and global choking can cause shock detachment from a sharp wedge whose angle is smaller than the maximum flow deflection angle as well as smaller than the angle for sonic down-shock flow.

Shock detachment from a sharp leading edge, as induced by **local choking**, depends on the freestream Mach number and the shape of the leading edge. Detachment by **global choking** depends on the freestream Mach number and the amount of downstream flow contraction, being largely independent of leading edge shape. In summary, a shock will remain attached to a curved leading edge if all of the following three conditions are satisfied:

- 1) - according to oblique shock theory, $\delta < \delta_{max}$
- 2) - no **global choking** according to the Kantrowitz criterion and as approximately stated by:

- a) $L \sin \delta < 1 - A_e / A_i$; for planar flow

$$\text{b) } L \sin \delta < 1 - \sqrt{A_e / A_i} ; \text{ for axial flow}$$

3) - no **local choking** according to Eqn. (6.7); $L < L^*$

If the mechanism for RR→MR transition has the same underlying cause as shock detachment from a curved wedge then the occurrence of transition depends on the curvature of the reflecting surface and hysteresis-induced flow duality becomes a possibility. Mach number driven hysteresis is possible for both global and local choking. Extension of present results to studies of the RR→MR transition is straightforward to planar flow when a plane (flat) incident shock impinges on a surface that is curved behind the shock. Conditions in front of the reflected shock are uniform and all detachment conditions are then applicable. A curved incident shock causes non-uniform, vortical flow ahead of the reflected shock so that a more elaborate version of CST has to be applied where the pre-shock flow gradients are finite for the reflected shock. The same local and global choking conditions should be applied to flow behind the reflected shock as causes for regular to Mach reflection to substantiate Sudani et al. [2000] who state that “...**transition from regular to Mach reflection occurs significantly below the maximum deflection condition**”.

CHAPTER 7

CLAIMS, CONCLUSIONS, DISCUSSION AND RECOMMENDATIONS

7.1 Claims

The Author claims originality in the following specific discoveries, developments and applications:

- 1) Derivation of the curved shock equations in a general form which makes them applicable to doubly curved shocks in non-uniform flow.
- 2) Recasting the curved shock equations into an influence coefficient form.
- 3) Derivation of the vorticity jump equation in the influence coefficient form for a non-uniform upstream flow.
- 4) Unique equations (3.3a) and (3.4) for the Thomas and Crocco points in planar flow.
- 5) An exact solution for Eqn. (3.3a).
- 6) Shock polar streamline slopes and their compatibility requirements.
- 7) Application of CST to find shock stand-off distances on bluff bodies.
- 8) Application of CST to find length of subsonic flow behind concave normal shock.
- 9) Application of CST to swept leading-edge flow.
- 10) Establishing Thomas and Crocco shocks for doubly curved shocks.
- 11) Reflection coefficient equation for doubly curved shock.
- 12) Sound-absorbent shock shapes.
- 13) Sonic line and surface orientation behind doubly curved shocks.
- 14) Taylor-McColl equation in Mach number variables.
- 15) Application of Busemann flow to air intakes.
- 16) An inflection point on the Busemann streamline; its significance to intake starting.

- 17) Initiating and monitoring critical wind-tunnel and gun-tunnel experiments to prove existence of Busemann flow.
- 18) Initiating and monitoring critical wind-tunnel and gun-tunnel experiments to prove existence of M-flow.
- 19) Discovering (analytically) the focused, axial compression fan and initiating experimental work to prove its existence.
- 20) Discovering (analytically) the free-standing conical shock and proving its existence experimentally.
- 21) Initiating and monitoring gun-tunnel experiments to discover regular shock reflection at the centre line.
- 22) Initiating and monitoring CFD calculations to complement 17) to 21), above.
- 23) Suggesting the hyperbolic shock shape for study of flow behind doubly curved concave shocks.
- 24) Identifying three types of doubly curved concave shocks critical to the formation of a reflected shock.
- 25) Identifying the shock's curvatures ratio as a critical parameter for the formation of a reflected shock.
- 26) Identifying three distinct causes for shock detachment from a doubly curved wedge surface.
- 27) Presenting *local choking* as a cause for shock detachment and formulating the geometric detachment conditions from curved shock theory.
- 28) Demonstrating by CFD that local choking pre-empts the sonic and detachment conditions in causing shock detachment from a doubly curved wedge.
- 29) Suggesting that, by analogy, *local choking* causes transition from regular to Mach reflection of curved shocks.

7.2 Conclusions

Detailed conclusions are presented at the end of each of the previous chapters. This chapter focuses on aspects of this report that are both novel and significant. Each

such aspect is discussed with respect to its novelty, its potential application and, where appropriate, its further development.

The historical development (1938 to 2011) of curved shock theory has been reviewed. Extensions have been made for CST to apply to axial shocks in non-uniform flow. A general formula has been derived for the vorticity jump across a doubly curved shock in non-uniform flow. Influence coefficient forms of equations for the gradients and vorticity show the effect of changing pre-shock conditions and shock geometry.

CST has been applied to a series of simple shock flows including the orientation of the sonic surface at the rear face of a doubly curved shock. This orientation is significant in determining the occurrence of embedded shocks in the post-shock flow. Application of CST to curved, concave, normal shocks allowed the derivation of an explicit relationship between the shock's curvature and the length of down-shock subsonic flow. This aspect of the structure of Mach reflection and its associated triple-shock confluence are important components of many air intake flows. The direct relationship deserves further investigation, by a combination of CST and CFD, to help construct an incident and reflected shock structure around a given Mach disk/stem – an inverse approach to the Mach reflection problem.

Investigations of M-flow by analysis, CFD and experiment all failed to demonstrate the existence of regular reflection at the centre line of axial flows. Both experiment and CFD have shown that the analytically predicted conical shock, on the calculated streamline, does not extend all the way to the centre line but terminates in Mach reflection. It appears that the existence of an analytical Taylor-Mccoll solution is not in itself a guarantee of the physical existence of a conical flow in all cases. Mathematical singularities appear in the equations of fluid mechanics as a result of idealizations of fluid behaviour and imposition of symmetry. These singularities are not approachable by real flow because the mathematical streamlines have cusps or corners at the singularities. Real or artificial viscosity would smooth out singular behaviour. Of the two imposed symmetries, it is the conical symmetry that breaks down whereas experiment shows that axial symmetry is preserved.

The Taylor-Maccoll equations predict the existence of an axisymmetric centered compression fan, analogous to the Prandtl-Meyer fan in planar flow. A free-standing

conical shock is located downstream of the compression fan. Both features have been shown to exist by CFD as well as experiment. Busemann flow is the only flow where these wave structures can exist. It is seen that, although regular reflection of shocks at the centre line is not possible, it is possible to reflect an incident, centered compression as a conical shock. Investigations have also shown that it is possible to place an upstream pointing solid cone behind the conical shock, in which case the ‘reflected’ shock becomes stronger and the Busemann flow exits through an annulus. Such flow passages have applications to air intakes that feed annular passages of axial compressors.

Discovery of an inflection point on the Busemann streamline has an important implication to spontaneous starting of Busemann intakes. If the normal shock, at the entry, can be coaxed to come to the inflection point (surface) and if the post-shock flow is not contracted beyond the Kantrowitz starting limit, then the shock will move downstream from the inflection point and the intake will start – at least so predicts inviscid theory.. The shock can be coaxed to move to the inflection point by spilling the post- and pre-shock flow. The performance (attainable compression and contraction) of such spontaneously starting intakes needs investigation.

Three types of flow can exist behind a doubly curved concave shock. Only one type can exist as a continuously curved shock from the Mach angle to the normal shock. The other two develop an embedded reflected shock, most likely reverting to Mach reflection. The three types are characterized by the orientation of the sonic surface which, in turn, is determined by the pre-shock Mach number and the shock curvatures ratio. Post-shock flows, which in themselves are shock-free, may be applied to avoid the often troublesome shock-boundary layer interaction of the reflected shock.

Shapes of special axial shock surfaces, with straight post shock streamlines, (Crocco shocks) or vanishing streamwise pressure gradient (Thomas shocks), have been calculated. They have no known application but to demonstrate the ability of CST to produce “designer shocks”. Similar calculations produce curved shocks that have post-shock surfaces with specific sound reflectivity (zero, if desired). Application to boundary layer generated noise abatement is a possibility.

Local flow choking, near the leading edge, is shown to lead to shock detachment from a curved wedge. Such detachment depends on freestream Mach number, the wedge

angle, the wedge curvature and the wedge length. It would pre-empt detachment by excessive flow deflection. If the mechanism for regular reflection termination is the same as shock detachment from a wedge then there is a need to apply CST to the prediction of regular to Mach reflection transition for curved shocks on curved surfaces. This is planned as the Author's next project.

CST, as presently formulated, is applicable to shock surfaces with planar and axial symmetry. It also applies at ridge and trough lines of left-right symmetric shocks such as would occur on symmetric swept leading edges - even if the sweep is variable. The criterion is that the post-shock, constant property lines be normal to the freestream vector so that there be no cross flow derivatives. For a uniform pre-shock flow it means that CST applies locally on a 3D shock wherever the lines of constant shock angle are normal to the freestream flow vector. For a smooth shock element in 3D space, it is possible to identify a *flow plane* as well as a *flow-normal plane* where the shock traces have curvatures S_a and S_b . These curvatures, together with the pre-shock Mach number and the shock angle, are sufficient to calculate the post-shock gradients using CST, as it presently stands. However, this approach is not valid for general 3D flow and shocks because the post-shock flow curvature's osculating plane is no longer in the flow plane and there is a pressure gradient across the flow plane. Dr. Emanuel has spent a considerable effort in analyzing this very complicated problem, with the aim of extending CST to 3D shock surfaces. Extension of CST to 3D flow would be an important attainment as no 3D CST is known to exist.

REFERENCES

Ames Research Staff, *Equations, Tables and Charts for Compressible Flow*, NACA Rep. 1135, 1953

Anderson, J.D., *Modern Compressible Flow with Historical Perspective*, McGraw-Hill, 1982

Ben-Dor, G., *Shock Wave Reflection Phenomena*, Springer, 2007

Bianco, E., Cabannes, H., Kuntzmann, J., Curvature of attached shock waves in steady symmetric flow. *Journal of Fluid Mechanics*, vol.1, no.6, 1960.

Billig, F.S., Shock-Wave Shapes around Spherical- and Cylindrical-Nosed Bodies, *J. Spacecraft and Rockets* 4, 822, 1967

Busemann, A., Die achsensymmetrische kegelige Überschallströmung. *Luftfahrtforschung* 19, No. 4 137-144, 1944

Chernyi, G.G., *Introduction to Hypersonic Flow*, Academic Press, 1961.

Clutterham, D.R. and Taub, A.H., Numerical Results on the Shock Configuration in Mach Reflection. [source missing] 1953

Courant, R and Friedrichs, K.O., *Supersonic Flow and Shock Waves*, Interscience, 1948

Crocco, L., Singularita della corrente gassosa iperacustica nell' interno di una prora adiedro, *Atti del 1° Congresso dell Unione Matematica Italiana*, vol. 15, pp.597-615, 1937.

Curran, E.T., Scramjet Engines: The first forty years. ISABE Paper 97-7005; XIII ISABE Conf. Sep. 1997

Curran, E.T. and Murthy, S.N.B. *Scramjet Propulsion*; AIAA series Progress in Astronautics and Aeronautics; Vol. 189, 2000

Dalitz, R.H. *SOME MATHEMATICAL ASPECTS OF COMPRESSIBLE FLOW*, Report ACA-20, Australian Council for Aeronautics, 1946

Darden, C.M., Spatial Derivatives of Flow Quantities Behind Curved Shocks of All Strengths, NASA TM 85782, 1984.

Eckert, D., Über gekrümmte gasdynamische Wellen in stationären ebenen und rotations-symmetrischen Überschallströmungen, *ZAMM* 55, issue 6, pages 281-289, 1975

Emanuel, G., Liu, Min-Shan, Shock wave derivatives, Phys. Fluids 31 (12), December 1988

Emanuel, G., Analytical Fluid Dynamics, CRC Press, 1994

Emanuel, G., Private e-mails, 2009 to 2012

Fabri, J. (ed.) AIR INTAKE PROBLEMS IN SUPERSONIC PROPULSION, AGARD Combustion and Propulsion Panel Meeting, Paris, Dec 1956; AGARDograph No. 27; Pergamon Press, 1958

Gadd, G.E., The possibility of Normal shock waves on a body with convex surfaces in inviscid transonic flow, Kurtze Mitteilungen, ZAMP, Vol XI, p 51-58, 1960

Gerber, N., Bartos, J.M., Tables for determining flow variable gradients behind curved shock waves. U.S.A. Ballistics Research Laboratories Rep. 1086. 1960.

Glass, I.I., *Shock Waves and Man*, Univ. of Toronto Press, 1974.

Grodzovskii, G.L., Supersonic axisymmetric conical flow bordering on a symmetrical parallel flow through a shock wave. RAE translation of Prikladnaya Matematika i Mekhanika, XXIII 2, pp. 379-383, 1959

Guderley, K.G., *The Theory of Transonic Flow*, Pergamon Press, 1962

Hayes, W.D., The vorticity jump across a gasdynamic discontinuity, J.Fl.Mech. 2, p. 595-600, 1957

Hayes, W.D., Probstein, R.F., *Hypersonic Flow Theory*, Academic Press, 1966

Henderson, L.F., Regions and Boundaries for Diffracting Shock Wave Systems. Zeitschrift für Angewandte Mathematik und Mechanik, Vol.67, No.2, 1987.

Hornung, H.G., Non-equilibrium ideal-gas dissociation after a curved shock wave. J. Fluid Mech. 74:143, 1976.

Hornung, H.G. & Robinson, M.L., Transition from Regular to Mach Reflection of Shock Waves, Part 2, The Steady-Flow Criterion. J. Fluid Mech. 123, 155-164, 1982

Hornung, H.G., On the stability of steady-flow regular and Mach reflection. Shock Waves J., vol.7: 123-125, 1997

Hornung, H.G., Gradients at a curved shock in reacting flow. Shock Waves J., vol.8, pp.11-21, 1998.

Hornung, H.G., Oblique shock reflection from an axis of symmetry, J.Fl.Mech. 409 1-12, 5, 2000

Hsu, C.T., On the Gradient Functions for Nonequilibrium Dissociative Flow Behind a Shock, Jour. Aerospace Sci. p. 337, Apr. 1961

Ivanov, M.S., Gimelshein, S.F., Kudryavtsev, A.N, Markelov, G.N., Transition from regular to Mach reflection in two- and three-dimensional flows, Paper 2960, 21st International Symposium on Shock Waves, Great Keppel Island, Australia, 1997

Kaneshige, M. J., Hornung, H.G., Gradients at a Curved Shock in Reacting Flow, Shock Waves, 9, 219, 1999

Kanwal, R.P., On Curved Shock Waves in Three-Dimensional Gas Flows, Quart. Of Appl. Mathematics, Vol.16 (1958) p.361-372

Kanwal, R.P., Determination of Vorticity and the Gradients of Flow Parameters behind a Three-Dimensional Unsteady Curved Shock Wave, Archive for Rational Mechanics and Analysis, Vol.1, Nr.1, 225-232

Kantrowitz, A., Donaldson, C.D., Preliminary Investigation of Supersonic Diffusers, NACA Rep. ACR L5D20, Langley, VA, 1945

Kreyszig, E., *Differential Geometry*, Dover Publications, 1991

Liepmann, H.W., Roshko, A., *Elements of Gasdynamics*, John Wiley. 1956

Lighthill, M.J., Dynamics of a Dissociating Gas, Part 1, Equilibrium Flow, J.Fl.Mech., 2, 1-32, 1957

Lin, C.C., Rubinov, S.I., On the Flow Behind Curved Shocks, Jour. of Math. and Phys. vol. XXVII, no. 2, pp. 105-129, 1948

Mel'nikov, D.A., Shock reflection from an axis of symmetry, Izv. Akad. Nauk. SSSR, Mekh. Mashinostr., No. 3, 24 1962

Molder, S. and Szpiro, E.J., Busemann Inlet for Hypersonic Speeds. J. Spacecraft and Rockets, Vol.3, No. 8, 1966

Mölder, S., Internal, Axisymmetric, Conical Flow, AIAA J. Vol.5, No.7, July 1967

Mölder, S. and Romeskie J.M.; Modular Hypersonic Inlets with Conical Flow. AGARD Conference Proceedings No. 30 (1968)

- Mölder, S., Reflection of Curved Shock Waves, 7th Congress of the International Congress of the Aeronautical Sciences, ICAS paper 70-11, 1970.
- Mölder, S., Reflection of Curved shock Waves in Steady Supersonic Flow, CASI Transactions, vol.4, no.2 pp.73-80, 1971.
- Mölder, S., Polar Streamline Directions at the Triple Point of Mach Interaction of Shock Waves. CASI Transactions, vol.5, no.2, 1972.
- Mölder, S., Particular conditions for the termination of regular reflection of shock waves, CASI Transactions, 25, 44-49, 1979
- Molder, S. et. al. Investigations in the Fluid Dynamics of Scramjet Inlets, Ryerson Polytechnic Institute, University of Toronto. USAF Contract Report F33615-87-C-2748 and JHU/APL Contract APL602235-0, 1992
- Mölder, S., Gulamhussein, A., Timofeev, E.V., Voinovich, P., Focusing of conical shocks. Paper 5601, International Symposium on Shock Waves. Great Kepple Island, Australia, 1997
- O'Brien, T.F., Colville, J.R., Analytical Computation of Leading-Edge Truncation Effects on Inviscid Busemann-Inlet Performance, AIAA J. Propulsion & Power, Vol. 24, No. 4, July-August 2008
- Oswatitsch, K., and Zierep, J., Das Problem des senkrechten Stosses an einer gekrümmten Wand, ZAMM, Vol. 40, p.43, 1960
- Owczarek, J.A. *Gas Dynamics*, International Textbook Company, 1964
- Pant, J.C., Some aspects of curved shock waves, Int.J.Eng.Sci. vol.7, pp. 235-245, Pergamon Press, 1969.
- Pant, J.C., Reflection of a Curved Shock from a Straight Rigid Boundary, Physics of Fluids, vol.14, no.3, 1972.
- Shock Wave Re Rylov, A.I., On the issue of impossibility of regular reflection from the axis of symmetry for stationary shockwave. Applied Mathematics and Mechanics, Vol.54, issue 2, 1990 (translated from Russian by E.V.Timofeev).
- Saito, T., Voinovich, P., Timofeev, E., and Takayama, K., Development and Application of High-Resolution Adaptive Numerical Techniques in search Center. Toro E.F. (ed) Godunov Methods: Theory and Applications. Kluwer Academic/Plenum Publishers, NY, pp. 763-784, 2001
- Sedney, R. Some Aspects of Nonequilibrium Flows. Jour. Aerospace Science, Mar. 1961

Shapiro, A.H., *Compressible Fluid Flow*, Vol. 1, Ronald Press, 1954

Sims, J.L. *Tables for Supersonic Flow Around Right Circular Cones at Zero Angle of Attack*, NASA SP-3004, 1964

Smith, L.G. *Photographic investigation of plane shocks in air*, USA/OSRD Tech. Rep. 6271, 1945

SolverII, Software Package, Ver. 2.30.2385, RBT Consultants, Toronto, 2004.

Sudani, N., Saito, M., Karasawa, T., Noda, J., Tate, A., Watanabe, M. Irregular effects on the transition from regular to Mach reflection of shock waves in wind tunnel flows, *J. Fluid Mech.* Vol. 459, pp. 167-185, 2000

Thomas, T.Y., On curved shock waves, *J. Math. & Phys.* Vol. 26, pp 62-68, 1947.

Thomas, T.Y., The consistency relations for shock waves, *J. Math. & Phys.* vol. 28, no.2, pp. 62-90, 1949a.

Thomas, T.Y., On conditions with steady plane flow with shock waves, *J. Math. & Phys.* Vol.28, no.2, pp.91-98, 1949b.

Thomas, T.Y., The Determination of Pressure Behind on Curved Bodies behind Shocks, *Comm. Pure and Appl. Math.*, vol.3, pp.103-132. 1950

Thomas, T.Y., The Extended Compatibility Conditions for the Surfaces of Discontinuity in Continuum Mechanics. *J. Math. & Mech.*, vol.6, no.3, pp.311-322, 1957a. (See also correction in vol.6, no.6, pp.907-908.)

Thomas, T.Y., On the Propagation of Spherical Blast Waves, *J. Math. & Mech.*, vol.6, no.5, 1957b.

Thompson, P.A., *Compressible-fluid dynamics*. McGraw-Hill, 1972

Truesdell, C., On Curved Shocks in Steady Plane Flow of an Ideal Fluid. *J. Aero. Sci.* vol.19, pp.826-828, 1952.

Van Wie, D.M. and Mölder, S. Application of Busemann Inlet Designs for Flight at Hypersonic Speeds; 1992 Aerospace Design Conf.; AIAA 92-1210 (1992)

Van Wie, D.M. *Scramjet Inlets* in [Curran and Murthy, 2000]

Voinovich, P.A., Satunina, E.L., Timofeev, E.V., Numerical modeling of the reflection of an annular shock wave from the symmetry axis and a plane solid surface or gas layer, *Am. Inst. of Physics, Tech. Phys.*41 (2) , Feb 1996

Von Neumann, J., Oblique reflection of shocks, Explos. Res. Rep. 12, Navy Department, Bureau of Ordnance, Washington, D.C, U.S.A. 1943

Zierep, J., Der senkrechte Verdichtungsstoss am gekrümmten Profile, Zeitschrift für Angewandte Mathematik und Physik, Vol. 9b, p.764, 1958.